Geosynthetics 2007

January 16-17, 2007 • Washington, D.C.

TRANSPORTATION CONFERENCE PROCEEDINGS

IFAI GMA Geosynthetic Materials Association nags igs

SPONSORED BY

Table of Contents

Transportation Technical Session Papers
Geosynthetics 2007 Conference
January 16-19, 2007
Washington D.C.

Erosion Control

Reinforced Soils

Roads & Highways

- Laboratory Test Studies of Concrete Slab Over Drainage Geocomposite, Jianjun Leng, Design Engineer, Tenax Corporation
- Geotextiles as a Dust Control for Unpaved Roads, John Bowders, Professor of Civil Engineering, Univ of Missouri
- Enhancing and Analyzing a Bending Stiffness Test and Relating its Results to Geogrid Reinforced Base Materials of Pavements, Ayman Halim Abusaid, Professor, The University of Texas at Austin

Testing

- Understanding and Minimizing Uncertainty in Geosynthetic Testing, Rich Lacey, Laboratory Director, Geotechnics
- Filtration Performance of Geotextiles in Cyclic Flow, Jonathan Fannin, PhD, University of British Columbia
- Mechanistic Response Measurements of Geogrid Reinforced Flexible Pavements to Vehicular Loading, Erol Tutmuler

Soil Improvement & Foundations

- Reducing The Seismic Earth Pressures on Retaining Walls By EPS Geofoam Buffers - Numerical Parametric Analyses, G. A. Athanasopoulos, Professor, University of Patras
- Performance of Electrically Conductive Vertical (wick) Drains in Treatment of Soft Clay, Eng Choy Lee, Emas Kiara Marketing Sdn. Bhd.

NAGS Student Paper Competition

- Development of Low Altitude Aerial Photometry Techniques to Quantify Geomembrane Wrinkles, Melissa Chappel, Graduate Student, R. W. I. Brachman and W. A. Take, GeoEngineering Centre at Queen's-RMC
- Effect of Wet-Dry Cycles on Capillary Break Formation in Geosynthetic Drainage Layers, John McCartney, Doctoral Candidate, University of Texas at Austin
- Assessment of Geotextile Filament Properties and Size Variation During Interface Shearing, Duhwan Kim, Graduate Research Assistant, Georgia Institute of Technology

Erosion Control

Geocell and Reinforced Soil Restoration of Eroded Steep Slopes

Stan Boyle, Ph.D., P.E., Shannon and Wilson, Inc.; Kathy Robertson, P.E., L.E.G., Pickets Engineering, LLC

ABSTRACT

In October 2003, stormwater overflows from an intense, short-duration storm eroded approximately 20,000 cubic yards of soil from the bottom and side slopes of a ravine between the Tacoma Narrows Bridge and a subdivision near Tacoma, Washington. The erosion ruptured two storm drains and left undermined slopes that continued to ravel and retreat. Measures were implemented to help stabilize the eroded slopes and prevent further retreat that could impact the Tacoma Narrows Bridge expansion project and a residence above the opposite ravine slope. The measures also addressed regulatory agency concerns about sediment-laden water discharging from the ravine into the Narrows that could damage sensitive sand lance habitat on the beach at the mouth of the ravine.

Ravine restoration measures consisted of constructing unreinforced soil, flexible geocell-faced reinforced soil, and geocell-geogrid reinforced soil slopes that mimic the former steep ravine. After slope construction, a mixture of drought tolerant and native vegetation was planted to provide erosion protection and restore the natural ravine environment. The geocells had the flexibility to fit against, and transition between variable slopes and create steep slopes with planting benches for trees, pockets for smaller plants, and terraces that slow stormwater runoff. The perforated geocell walls allowed roots to spread. The geocell ravine repair design was an effective, economical solution that saved the client the cost of potential litigation, satisfied regulatory requirements, and expedited construction, which was completed in less than 5 months during the 2004 construction season.

This paper presents project history, features, and challenges, and discusses design and construction of the geocell-faced reinforced-soil slopes and vegetation restoration.

INTRODUCTION

On Monday, October 20, 2003, during an intense rainstorm, stormwater overflowed into a ravine along the north side of the west anchorage being excavated for the Tacoma Narrows Bridge expansion project, approximately 6 miles west of Tacoma, Washington (Figure 1). The rain event exceeded the intensity of the 100-year storm by about 20 percent and overwhelmed the 24-hour/10-year stormwater controls for the bridge expansion project and drainage systems in the vicinity. As flooding continued, concern rose about the safety of the existing bridge abutment and anchorage, which could be undermined if stormwater overflowed and eroded the bluff above the Tacoma Narrows, a fast flowing tidal channel between Tacoma and Gig Harbor, Washington. Stormwater was diverted into the ravine to protect these structures. Figure 2 presents a project site plan.

The diverted stormwater overflows added to runoff already in the ravine from adjacent roads. The resulting high discharge eroded the ravine bottom to the level of the Narrows beach, ruptured two storm drains buried in the ravine bottom, gullied and undermined the south slope next to the bridge, and undermined the north slope below the subdivision and an access road used for the bridge construction. The erosion also ruptured an old storm drain on the south slope and removed an old gravel road in the ravine used as a trail to the beach by the subdivision residents. Flows from the ruptured storm drains contributed to the erosion.

The storm event eroded approximately 20,000 cubic yards of soil from the ravine, some of which was deposited as an alluvial fan at the Narrows shoreline. The ravine bottom was lowered by approximately 12 vertical meters. Ravine sideslopes were left undermined and over-steepened, continuing to ravel and slope retreat in subsequent storm events. This continued erosion threatened the east abutment of the Tacoma Narrows Bridge expansion and a residence above the north side of the ravine. The erosion also created sediment-laden discharges from the ravine into the Narrows, potentially degrading sensitive sand lance habitat. Figure 3 shows post-event conditions.

If unrepaired, the ravine would continue to degrade, impacting public safety, creating economic loss, and damaging the environment. Recognizing these hazards, the regulatory agencies, permitting authorities and bridge expansion design-build contractor (Tacoma Narrows Constructors) set a deadline for ravine stabilization by November 1, 2004. Earthwork had to be completed by mid-September 2004.

While permanent stabilization measures were designed and permits for their implementation obtained, temporary erosion and sediment control measures were installed to reduce sediment delivery to the Narrows. These measures included constructing a sediment trap about 18 meters from the ravine mouth, above the beach (see Figures 2 and 3); temporarily piping stormwater past the site; and removing sediment deposited on the beach.

PROJECT GOALS

The primary goals of the ravine repair were to (1) prevent further erosion that could impact the bridge construction project and the residence above the opposite ravine slope and (2) avoid damaging sensitive sand lance habitat on the Narrows beach at the mouth of the ravine. The project was not intended to prevent naturally occurring erosion, such as the bluff retreat occurring above the Narrows shoreline. Completing the project before November 2004 was critical, but because of the wet ravine conditions, work could not begin until mid-June 2004. With the support of stakeholders (i.e., subdivision residents, Tacoma Narrows Constructors, Washington Department of Transportation, the general public, and various permitting and regulatory agencies) , the project team was able to:

1. Obtain environmental and building permits in less than 6 months.
2. Design a flexible, low maintenance, cost-effective solution that rebuilt the eroded, steep ravine in 3 months.
3. Complete the project without complaints from landowners, the general public or agencies in 5 months.

SITE CONDITIONS

The damaged area extended approximately 80 meters inland from the beach and measured approximately 55 meters from top of south slope to top of north slope. The approximately 25-meter-high south ravine slope was eroded to approximately 45 degrees with locally steeper areas at the toe. The eroded portion of the north ravine slope varied from approximately 35 degrees in the lower 6 vertical meters and upper 12 meters, with the intermediate 12 meters steepened to about 70 to 80 degrees, with locally vertical areas. The top of the north slope had eroded to within approximately 3 meters of a sport court for the residence above the north slope.

Pieces of stormwater pipes and concrete plus quarry spalls (i.e., 8-inch minus angular rock) placed early during the storm event, were on the surface and buried in debris in the ravine after the storm event. Fallen trees covered the ravine bottom, see Figure 3.

Dense sand with varying amounts of silt and gravel was exposed in the lower two thirds of the north slope. The sand is overlain by a 3 to 4.5-meter-thick layer of hard, interbedded silt and clay, which is itself overlain by 0.3 to 0.6 meters of colluvium.

Soil exposed on the south slope consists of loose silty sand, which records indicate was fill placed during construction of the existing Tacoma Narrows Bridge. Approximately 1.5 to 3 meters of very loose sand, silt, and gravel was deposited in the ravine bottom and along the toes of the slopes near the end of and following the storm event.

Despite being plugged and diverted uphill of the site, the ruptured storm drains leaked and continued contributing flow into the ravine after storm events. Small seeps observed on the lower section of the south slope added to the flow that kept the ravine bottom conditions wet.

Steep slopes and existing roads cut off upland ravine access except at one location along a construction access road that was being used for the bridge expansion project. Primary access for ravine repair was via this access, while access from the shore could be used only for emergencies.

PROJECT ELEMENTS

As mentioned above, the ravine repair project focused on improving slope stability and reducing long-term erosion. The repair backfilled the ravine bottom and buttressed the failed sideslopes. Finish slopes vary from about 1H:1V (horizontal to vertical) to flatter than 2H:1V.

Repair measures included:

1. Constructing an access road into the ravine.
2. Removing debris, vegetation, topsoil, loose soil, and concrete from areas where fill would be placed.
3. Installing subsurface drains to collect and drain natural seeps.
4. Backfilling the bottom of the ravine with clean sand and gravel (Figure 4).

5. Building 1.5H:1V to 2H:1V slopes using geocell-reinforced soil (Figure 5).
6. Building 1H:1V to 1.5H:1V slopes using geogrid-reinforced soil with geocell slope face stabilization (Figure 6).
7. Replacing damaged stormwater conveyance pipes and systems.
8. Replacing the old trail with a forest-type path.
9. Covering unreinforced soil with a biodegradable turf reinforcement mat (TRM), protecting the slope against surface erosion until vegetation is established.
10. Planting drought-tolerant and native ground cover, shrubs, and small trees that will provide short- and long-term erosion protection, reduce the need for watering, and help reestablish vegetation in the ravine.

The flexible design accommodated the complex, variable site conditions, which changed with each storm event; allowed rapid field modifications; and reduced potential construction delays. Workers could readily shape the geocells and geogrids to match existing terrain.

MATERIALS

The Washington State Department of Fish & Wildlife required that the ravine backfill and slope fill be clean sand and gravel to reduce the amount of fines washing out onto the beach and into the Narrows. Table 1 presents the gradation the agency approved for fill and backfill, which also conforms to WSDOT (2002) requirements for backfill for reinforced soil and gravel borrow. Fill was compacted to a minimum 92 percent of its maximum Modified Proctor (ASTM D1557) dry density. To enhance plant growth, organic soil was mixed with the fill material placed on the surface of unreinforced slopes and in the exposed cells of geocell-reinforced slopes.

Table 1: Fill Gradation

Sieve/particle size (mm)	Percent Passing
32 mm*	100
U.S. No. 4 Sieve: 4.75 mm	50 – 80
U.S. No. 40 Sieve: 0.43 mm	30 max
U.S. No. 200 sieve: 0.075 mm	5.0 max

* Maximum particle size of 100 mm was allowed for fill not in geocells or adjacent to geogrid reinforcement.

Confinement at the slope face was required for slopes steeper than 2H:1V (Figures 5 and 6). Geocells, 200 mm high by 200 mm nominal dimension with perforated cell walls, were selected because they:

- Were easily transported into the confined work areas.
- Had the flexibility to fit against, and transition between, variable slopes.
- Could be used to create steep slopes with planting benches for trees, pockets for smaller plants, and terraces to slow stormwater runoff.
- Allowed roots to spread via the cell wall perforations.
- Allowed waster to water drain between cells.

To limit erosion and potential soil loss, geocell walls exposed at the slope face were not perforated. The contractor, Quigg Brothers, Inc., used GeoProducts (2004) EGA 30P geocell. Geocell-faced slopes 1.5:1V and steeper (Figure 6) were reinforced with geogrid.

Reinforced slope design was based on procedures presented in Elias and Christopher (2000).

Long-term design tensile strengths of 37 kN/m and 72 kN/m were specified for geogrids placed within 3.6 meters of the top of slope and geogrids at greater depth, respectively. For ease of construction, the contractor used a single geogrid, Fortrac 80/30-20 (Huesker, 2004), which satisfied the higher strength requirement for the project.

High density polyethylene (HDPE) pipe was used in the subgrade drains, to replace the ruptured storm drains, and for new storm drain pipes. This pipe type was selected for its ease of handling, durability, and strength. Pipe joints were fusion-welded for strength.

CONSTRUCTION

The contractor mobilized on site June 14, 2004. Work was performed 10 to 12 hours per day, 6 days a week, except for approximately 30 days in August while an outfall pipe for the bridge expansion project was installed through the area. Earthwork and storm drain repair were completed mid-September 2004. Vegetation and planting operations were completed in October 2004. The access road that the contractor constructed down the center of the ravine to reach the work area was restored to a narrow forest trail upon construction completion.

Before placing fill, the Contractor removed debris, loose material, and the temporary sediment trap that had been installed near the ravine mouth. Subsurface drains were installed at the base of the fill and along the toe of the south ravine slope to collect and convey seepage to the Narrows. Fill was delivered to the site by backing dump trucks down the 15 to 18 percent grade of the access road or dumping material from the trucks over the top of the south ravine slope. A wheel-loader and excavators transported the fill to placement locations. Unreinforced material in the bottom of the ravine was spread with a bulldozer and compacted using a smooth drum vibratory roller. New, continuously welded HDPE storm drain pipe was buried in the fill, connecting existing upgrade catch basins to the existing outfall pipe. New storm drain catchbasins, pipe and outfall were installed to collect runoff from the bridge site to avert a similar future occurrence. The outfall for the subgrade drains discharged onto a rocked-reinforced section of the slope rebuilt across the mouth of the ravine above the beach.

Workers placed and stretched the geocells and geogrid material to fit the variable terrain, and used walk-behind compactors to compact soil placed within geocells and the reinforced zone. The lightweight, flexible geocells and geogrid reinforcement allowed workers to place and field-adjust them on variable steep slopes within confined area (Figures 7 and 8), achieving continuous coverage and smooth transitions. An excavator placed fill material in geocells and over geogrid (Figure 8) and workers raked the fill into place. The fill kept the geocells shaped and positioned. Where the design minimum specified lengths would have required excavating into steep ravine slopes, geogrids were extended to the natural slope face, reducing earth

pressures assumed to act on the back of the reinforced zones, and the tails wrapped back, providing pullout resistance.

Planting benches formed by the geocell-faced slopes were relocated, modified, or eliminated, as necessary, to match actual conditions and expedite work progress. After completing the earthwork and storm drain repairs, workers placed the TRM on the unreinforced slopes faces, and then planted mostly drought tolerant, but also native, ground cover, small shrubs, and trees that have good root holding capability. Geocell cell walls were cut or removed to create large planting pockets shrubs and trees and room for roots to expand. Riprap was placed at the mouth of the erosion channel, above the ordinary high tide line and vegetation planted either side of the riprap to protect the slope toe.

Photographs of the project soon after planting (October 2004) are presented in Figures 7 through 9.

SUMMARY

A combination of unreinforced soil and geocell- and geogrid-reinforced soil were used to repair an erosion-damaged ravine and reduce slope retreat that could potentially impact adjacent structures. These techniques were selected because they could be adapted to variable, changing slope geometry, constructed in confined work areas on steep slopes; rapidly installed; and provided for erosion control and easy planting. The repaired slopes include an approximately 27-meter elevation difference between toe and top of the easternmost geocell- and geogrid-reinforced slope. The slopes have performed well during the two years since construction.

The successful partnering of the bridge expansion project and ravine repair contractors and designers, the bridge owner [Washington State Department of Transportation (WSDOT)], regulatory and permitting agencies, and neighboring homeowners were integral to the timely completion of the project. The professionalism, high level of communication, coordination, and trust between all parties averted potential litigation, expedited project approvals, and reduced project costs.

This project exemplifies the adaptability and flexibility of geocell- and geosynthetic-reinforced soil construction, and the value of stakeholder partnering.

REFERENCES

Elias, V. and Christopher, B.R. (2000), Mechanically Stabilizeed Earth Walls and Reinforced Soil Slopes Design and Construction Guidelines, U.S. Department of Transportation Federal Highway Administration, FHWA Demonstration Project 82, FHWA-NHI-00-043, 393p.

GeoProducts, LLC. (2004), EGA 30P geocell product information, www.geoproducts.org

Huesker, Inc. (2004), Fortrac 80/30-20 geogrid product information, www.hueskerinc.com

Washington State Department of Transportation (2002), Standard Specifications, M41-10.

ACKNOWLEDGEMENTS

Success of this project and its timely implementation was the result of partnering, cooperation, and coordination of a number of interested and affected parties, including: SvR Design Company (SvR) the civil engineer, landscape architect, and project manager for the project; Shannon & Wilson, Inc. which provided geotechnical engineering, geology, natural resource, and environmental services; St. Paul Travelers, the insurer; J. Walling Associates, insurance adjustor; Quigg Brothers, Inc., the general contractor for the ravine repair; Terra Dynamics, the landscape subcontractor; Tacoma Narrows Constructors (TNC), the design-build team for the bridge expansion project; Shipwatch Homeowners Association; Washington State Department of Transportation, which owns right-of-way in the ravine; Duane Hartman & Associates, surveyors; and Pierce County and Washington State Departments of Ecology, Fish & Wildlife, and Natural Resources, the regulatory agencies.

CONTACT:

Stanley R. Boyle, Ph.D., P.E.
Vice President
Shannon & Wilson, Inc.
P.O. Box 300303
Seattle, WA 98103
Phone: 206-632-8020
Email: srb@shanwil.com.

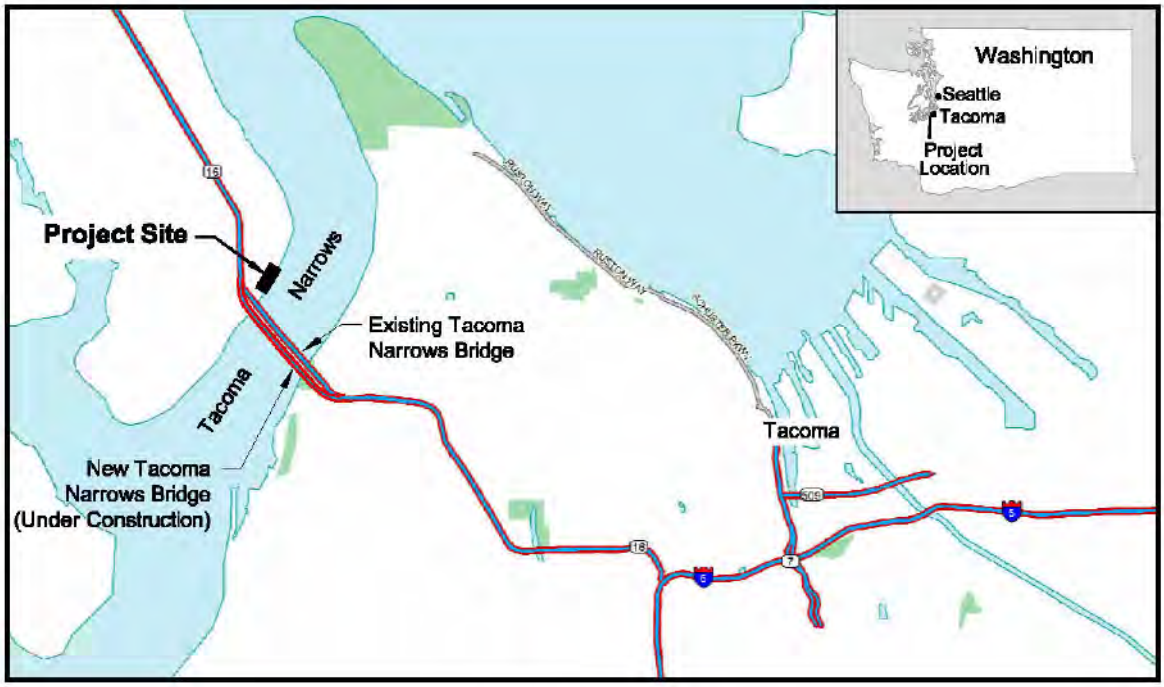

Figure 1: Project location.

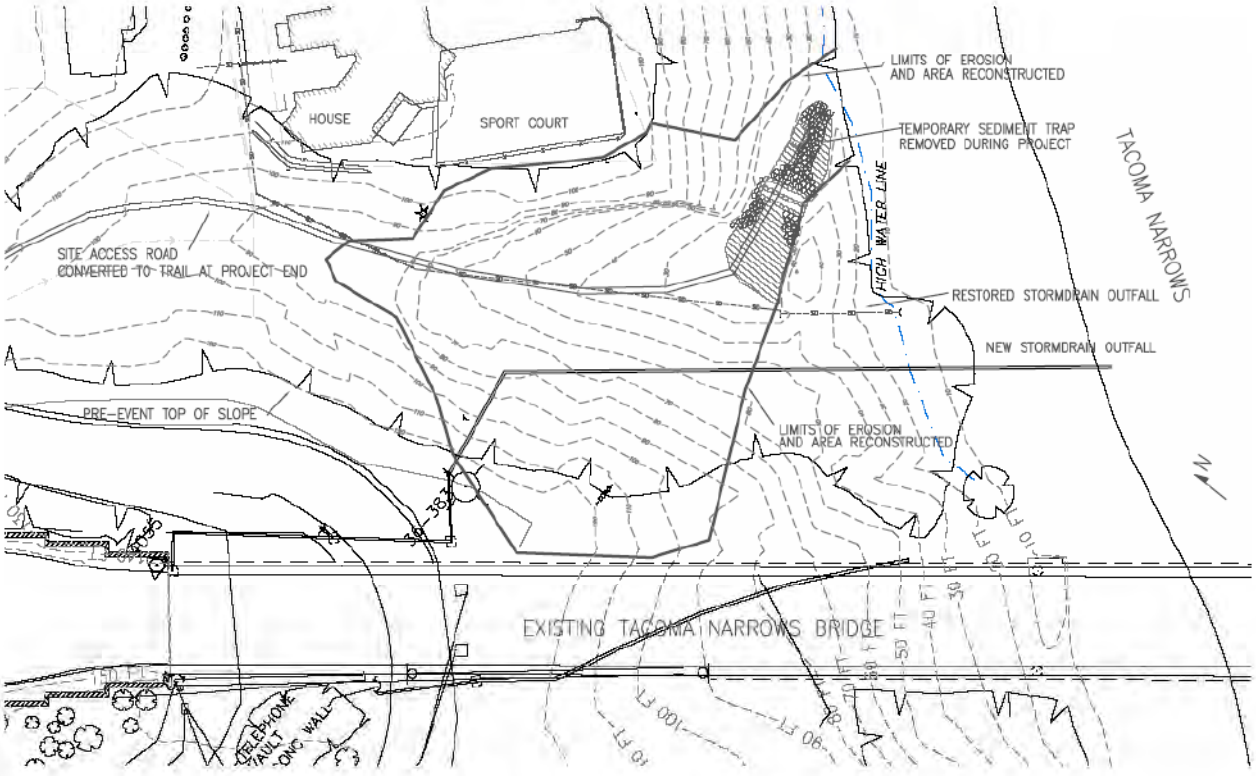

Figure 2: Site plan. (contour interval = 3 meters)

Figure 3: Ravine erosion, note sediment trap at ravine mouth. (used with permission of Shannon & Wilson)

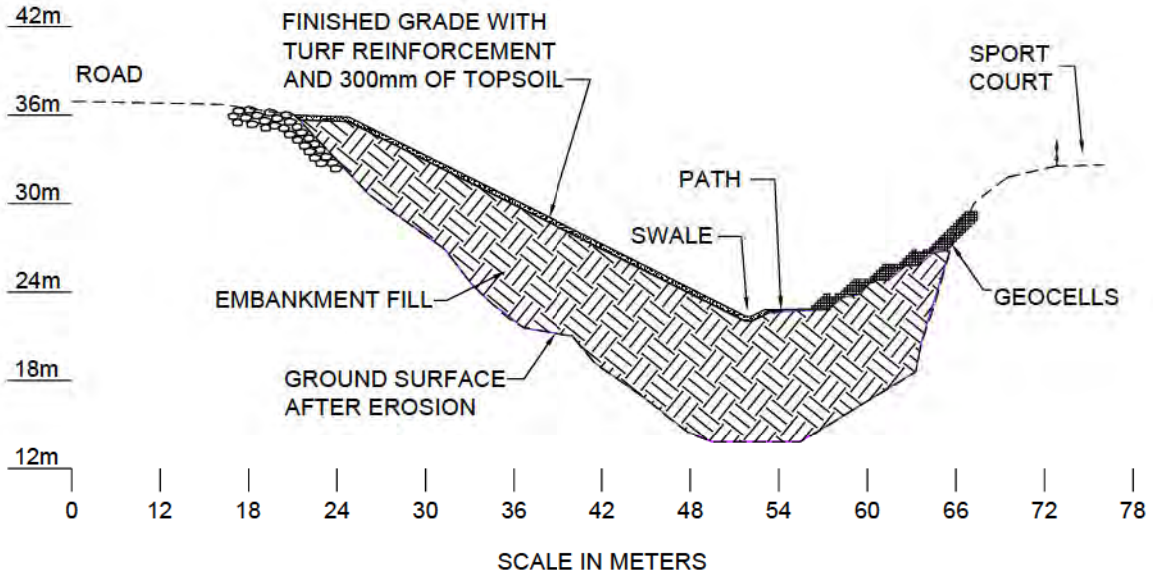

Figure 4: General ravine section. (used with permission of SvR).

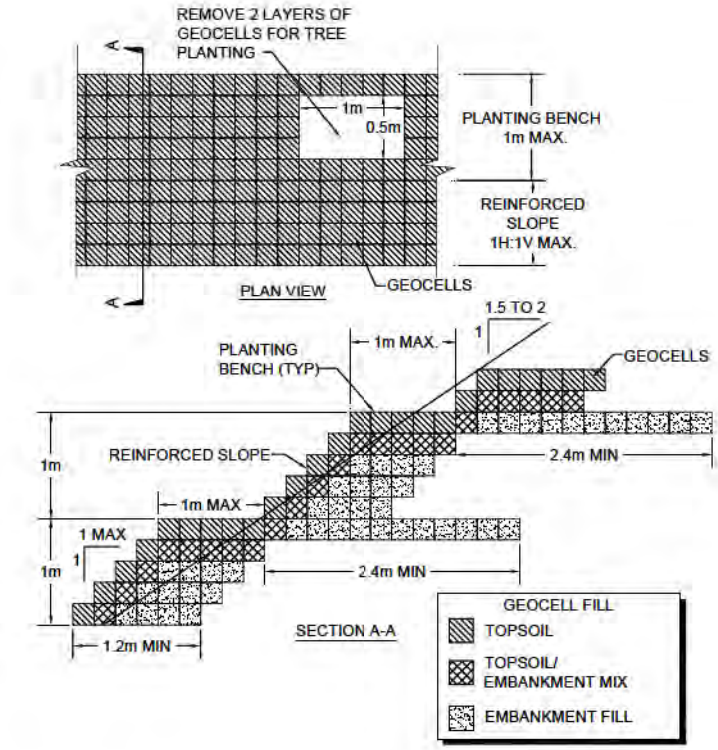

Figure 5: Geocell section. (used with permission of SvR)

DEPTH FROM TOP OF FILL SLOPE	GEOSYNTHETIC LENGTH	GEOSYNTHETIC LONG TERM DESIGN STRENGTH
0-3.6 m	2.4m MIN.	37 kN/m
3.6 - 7.6 m	4.8m MIN.	72 kN/m
7.6 to 12 m	6.0m MIN.	72 kN/m

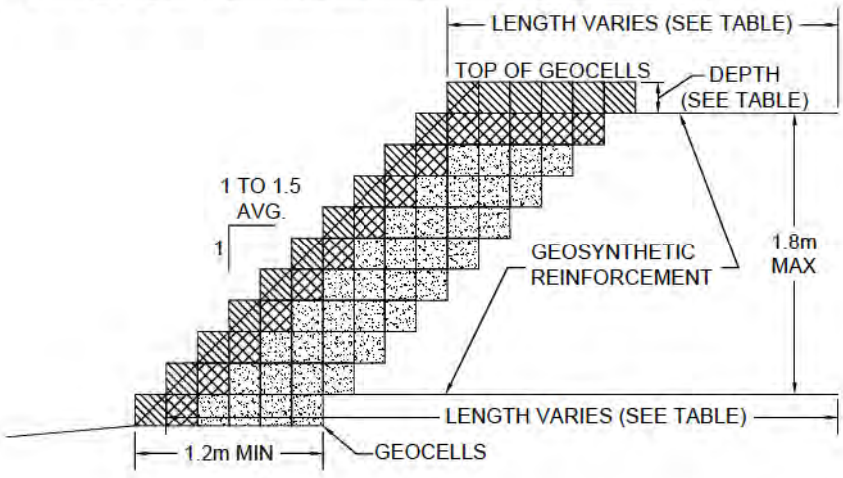

Figure 6: Geogrid reinforced section. (used with permission of SvR)

Figure 7: Geocell placement on steep slope with confined work area. (used with permission of Shannon & Wilson)

Figure 8: Completed slopes. Note variable spacing of geocell panels to match existing slope (left) and geocells placed between existing trees (right). TRM slope protection and plantings on flatter terrain (right). (used with permission Shannon & Wilson)

Figure 9: Completed 30 m high geocell slope. (used with permission Shannon & Wilson).

Use of Geocell Retaining Walls for Slope Stabilization and Erosion Control

D. Wade Anderson, P.E.,USDA, Natural Resources Conservation Service

ABSTRACT

The Natural Resources Conservation Service (NRCS) often repairs slope failures and eroded stream banks as part of the Emergency Watershed Protection (EWP) Program. Right-of-Way is often limited due to constraints from environmental agencies or fish and wildlife concerns and due to the presence of critical infrastructure such as roads on the top of the slope. The use of reinforced concrete walls are often not accepted by resource agencies and are often cost prohibitive. Geocell Retaining Walls have been used on EWP projects for slope stabilization and erosion control adjacent to small rivers and county roads by the NRCS.

This paper will provide a brief case history of two geocell retaining wall projects highlighting the design methodology, construction specification methods along with lessons learned for future projects using geocell retaining walls. One project is located on the banks of a river with a sensitive fish habitat and critical county road at the top of the slope and is designed to provide erosion protection from the river flows and support the slope and road above. A second project is designed to support the slope between an upper county road and lower road that provides access to a residence.

SAWMILL RIVER BANK STABILIZATION

Site Description

The site is located on the outer bank of a 90 degree curve in the Sawmill River near Montague, Massachusetts. The slide occurred as the river level dropped following a long period at a higher river stage. Continual sloughing of sandy slopes is common when the base of the slope has become or remains saturated. The moist, but unsaturated materials overlying them tend to be more stable due to negative pore pressures. The Sawmill River bank instability appears to have been caused by the rapid drawdown of the river, and the resulting erosion due to seepage out of the slope. A photograph of the slide is shown in Figure 1.

The bank is approximately 35 feet high and consists of loose to medium dense silty sand, sands, and gravelly sands. The initial stabilization design included a steel sheet pile driven near the toe with backfill and a vegetated slope above the sheet pile. However, bedrock was encountered near the river bed elevation in the two borings, preventing the use of a cantilevered sheet pile wall. Bedrock was encountered at a depth of approximately 20 feet at the top of the slope and dips to approximately 7 feet below the existing river bottom.

Figure 1 Sawmill River Bank Failure

Extending the toe of the retaining structure out into the river was not allowed due to the potential negative environmental and wildlife impacts. These limitations required the use of a near vertical retaining structure at the toe of the bank and an upper slope of 1.6H:1V to 2.4H:1V.

Bank Stabilization Design

The design consisted of stability analyses of the geocell wall as a retaining structure and the global stability of the entire slope including the geocell wall. An erosion control blanket was installed along the upper slope above the geocell wall to provide surface erosion protection until the vegetation was established.

Geocell Wall Stability

Evaluation of the external and internal geocell wall stability was completed by an installer using software developed by a major geocell supplier. The final design was completed by the contractor. The final design was required to meet the minimum factors of safety discussed under Construction Drawings and Specifications below.

A drainage system was included to prevent development of hydrostatic pressures behind the wall from bank seepage or a rapid drop in the river level following an extended period of high water.

Global Slope Stability

A global slope stability analysis was conducted using SLOPE/W. The soil profile was based on data collected from 2 soil borings and associated laboratory testing. The results of the analysis are shown in Figure 2.

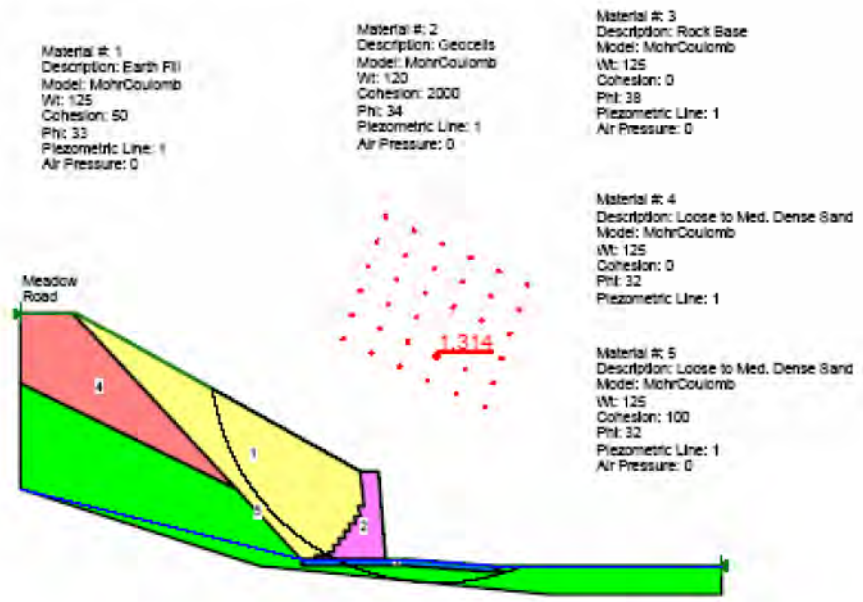

Figure 2 Sawmill River Global Stability Analysis Results

Construction Drawings and Specifications

The contract specified the geocell material characteristics listed in Table 1. The material density and sheet thickness where chosen to ensure a stiff material would be provided to allow compaction of the geocell infill. The carbon black content provides UV protection until the vegetation is established, while the environmental stress crack resistance ensures the material will not degrade with time. The cell depth, area, and seam strength facilitates compaction of the infill.

A sketch of a typical section is shown in Figure 3.

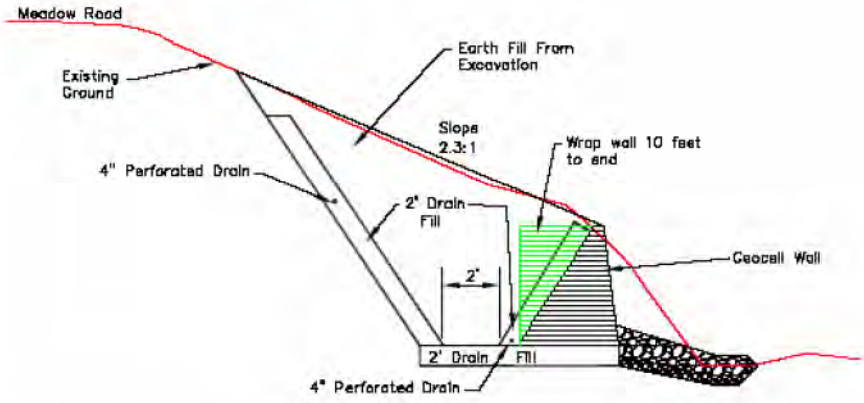

Figure 3 Sawmill River Typical Section

Table 1 – Sawmill River Geocell Properties[1]

Property	Test Method	Requirement
Material Density, g/cm^3	ASTM D 1505	0.935
Material Carbon Black Content, %	ASTM D 1603	1.5 – 3
Environmental Stress Crack Resistance of Material, hours	ASTM D 1693	2,000
Sheet Thickness, mil	ASTM D 5199	50 ±5
Cell Depth (expanded), in.		6
Cell Area (expanded) in.^{2}		38.5
Cell Seam Strength, lbs.	See Note 2	330

Note 1: All values, unless otherwise specified, are minimum average roll values as reported for the test method.
Note 2: U.S. Army Corps of Engineers Technical Report GL-86-19, Appendix A

The geocell retaining wall was designed by the manufacturer with the following soil properties and actual versus the required factors of safety:

Unit Weight of Geocell Infill = 130 pcf
Internal Friction angle of Geocell Infill = 34 degrees
Cohesion of Geocell Infill = 0 psf
Unit Weight of Retained Fill = 125 pcf
Internal Friction angle of Retained Fill = 32 degrees
Cohesion of Retained Fill = 0 psf
Unit Weight of Foundation = 130 pcf
Internal Friction angle of Foundation = 34 degrees
Cohesion of Foundation = 0 psf

$FS_{\text{external sliding}} = 1.53 > 1.5$
$FS_{\text{external overturning}} = 2.6 > 2.0$
$FS_{\text{external bearing capacity}} = 5.8 > 2.0$
$FS_{\text{internal sliding}} = 1.52 > 1.5$
$FS_{\text{internal overturning}} = 2.5 > 2.0$

The contractor's design required the bottom width of the geocell wall to be 10.5 feet. The global stability analysis required a minimum bottom width of 12 feet to achieve a factor of safety of 1.3. Therefore, the lower three rows of the geocell wall were 12 feet wide.

Massachusetts DPW Specification M1.04.01 was specified for the drainfill and M1.03.0 type c (2-inch maximum) for the geocell infill. The gradations for the materials are shown in Figure 4. The outer cell was filled with topsoil rather than the geocell infill and seeded with a variety of grasses and fertilized.

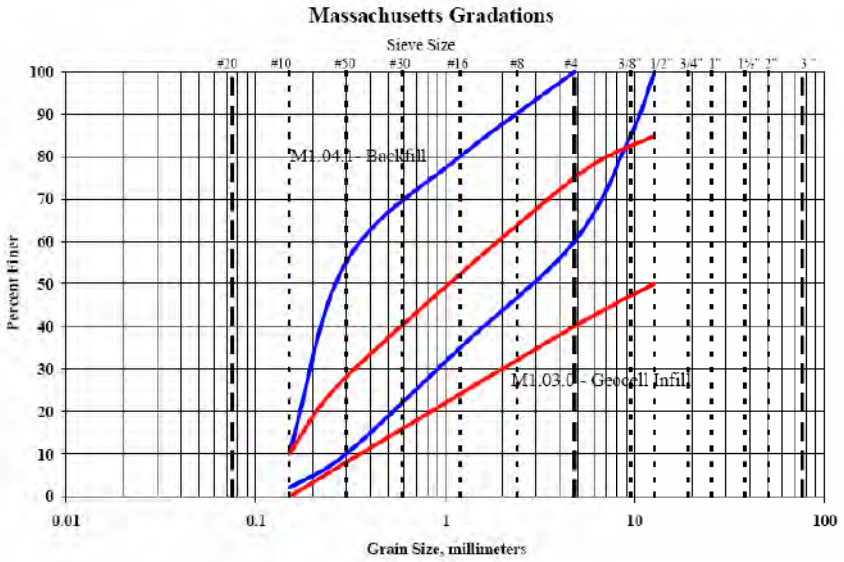

Figure 4 Massachusetts Gradations

Construction

Construction of the bank stabilization was completed in the fall/early winter of 2002. Access to the site was difficult and required excavation of an access ramp as shown in Figure 5. The temporary shoring to allow placement of the geocell is shown in Figure 6. Completion of the final rows of geocell before winter is shown in Figure 7. Figure 8 shows the completed project with the erosion control blanket installed on the upper slope.

The geocell retaining wall has performed well for four years. The construction of the geocell wall had minimal impact on the Sawmill River fish habitat and allowed construction in the river to be minimized. Figure 9 show the project one year after completion and Figure 10 shown the project fours years after completion.

Figure 5 Access Ramp

Figure 6 Temporary Shoring at Sawmill River

Figure 7 Finishing Geocell wall at Sawmill River

Figure 8 Completed Project at Sawmill River

Figure 9 Sawmill River Project after One Year

Figure 10 Sawmill River Project after Four Years

RABUN EWP SITE 3 SLOPE REPAIR

Site Description

Heavy rainfall from hurricanes in the fall of 2004 resulted in numerous slides. The Rabun EWP Site 3 project is located on a road slope in Rabun County, Georgia. The bank is approximately 20 feet high and consists of loose to medium dense silty sand, and sands. A private drive along the toe of the slope limited the right of way to approximately 26 feet from the edge of the upper road. A photograph of the slope failure is shown in Figure 11. Flattening to a stable slope was not possible within the available right of way. A geocell earth retaining wall was selected to provide support to the upper road and slope without encroaching on the driveway near the toe of the slope.

Figure 11 Rabun County EWP Site 3 Slope Failure

Stability Analyses

Design consisted of stability analyses of the geocell wall as a retaining structure and the global stability of the entire slope including the geocell wall.

Geocell Wall Stability

Evaluation of the external and internal geocell wall stability was completed by the NRCS using a spreadsheet developed to evaluate overturning and sliding of the entire geocell structure and that of individual rows of the geocell wall. The factors of safety along with the minimum required values were:

$FS_{\text{external sliding}} = 1.5 > 1.5$

$FS_{\text{external overturning}} = 3.7 > 2.0$

$FS_{\text{internal sliding}} = 1.9 > 1.5$

$FS_{\text{internal overturning}} = 3.2 > 2.0$

Global Slope Stability

A slope stability analysis was conducted using SLOPE/W. The soil profile was based on visual descriptions of the soils and estimated soil strength parameters. Groundwater was not observed in the slope soils and therefore not considered as a hydrostatic load on the geocell wall. The results of the analysis are shown in Figure 12. A minimum factor of safety of 1.3 was required for the global slope stability.

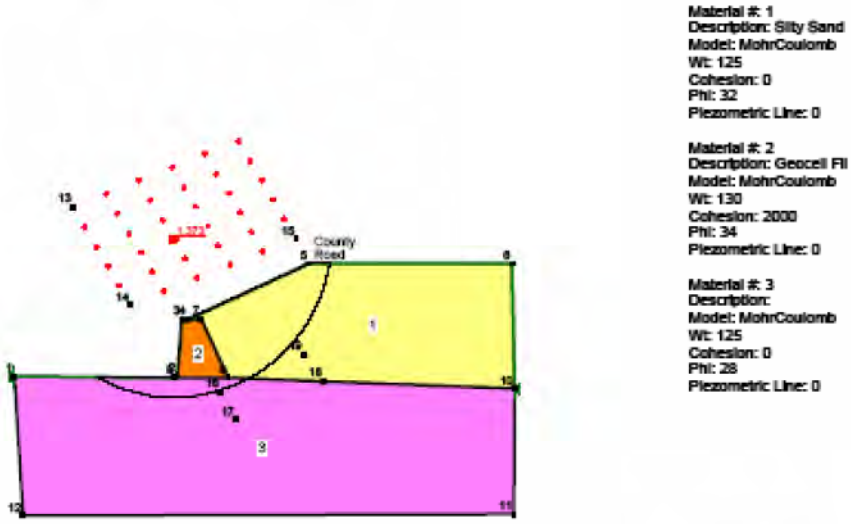

Figure 12 – Rabun County Site 3 Global Slope Stability Results

Construction Drawings and Specifications

The contract specified the geocell material be Presto Products GW30V, Geoproducts EGA30, or approved equal. The cells were required to be 6-inches in depth and be fabricated of high density polyethylene (HDPE). The products specified are typical geocell products used for geocell retaining structures. The cell depth allows adequate compaction throughout the depth while the HDPE material provides long term durability.

The Georgia Department of Transportation (GA DOT) has a very broad gradation in Section 812-Backfill Materials, 812.2.04 Mechanically Stabilized Embankment (MSE) Backfill. This gradation was required for the geocell infill material. The gradation is shown in Figure 13.

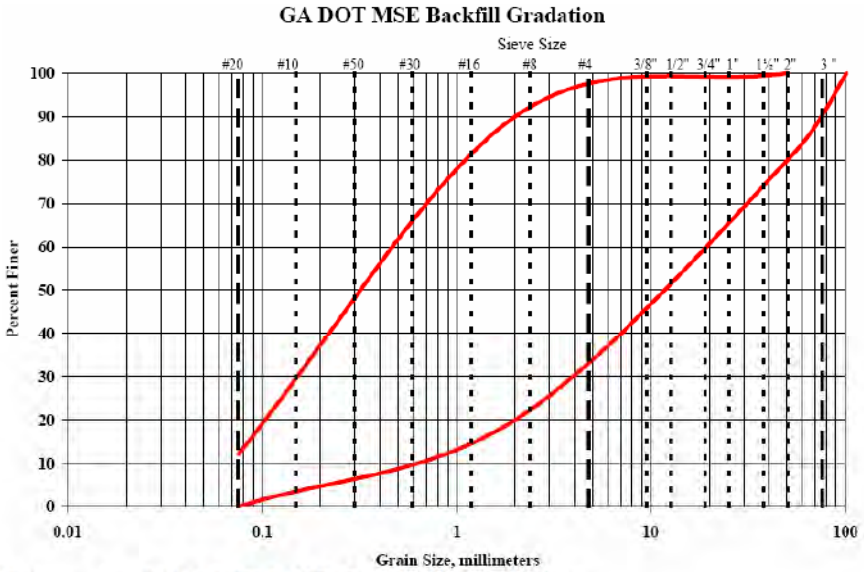

Figure 13 GA DOT MSE Backfill Gradation

The drawings provided the minimum dimensions of the wall as shown in Figure 14.

GeoCell Retaining Wall	
Section Number	Length (feet)
21	3.5
20	3.5
19	3.5
18	3.5
17	3.5
16	4.375
15	4.375
14	5.25
13	5.25
12	6.125
11	6.125
10	7
9	7
8	7.875
7	7.875
6	8.75
5	8.75
4	9.625
3	9.625
2	9.625
1	9.625

Note: Section number 1 is the bottom geocell. Section number 21 is top geocell.

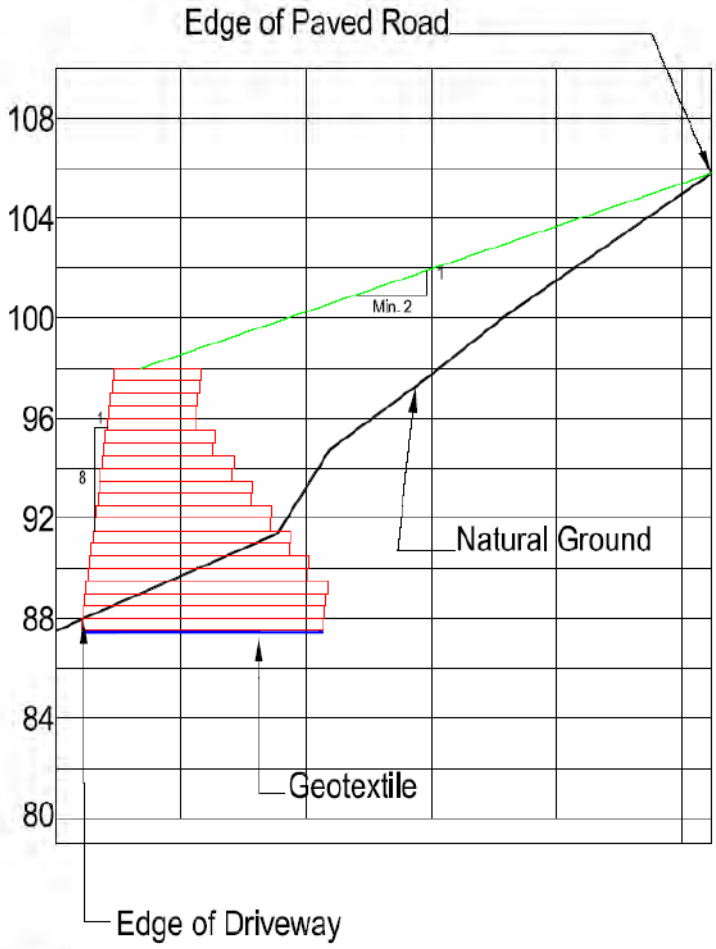

Figure 14 Rabun County Site 3 Design Drawing

Construction

Construction of the slope repair was completed in the summer of 2005. Placement of granular infill material is shown in Figure 15. Connection of adjacent section of geocell with staples and the steel spreader bar are shown in Figure 16. Figure 17 shows the project once construction of the geocell wall is complete and Figure 18 shows the completed project.

Figure 15 Granular Material for Geocell Infill

Figure 16 Attaching adjacent section of Geocell

Figure 17 Rabun County EWP Site 3 Near Completion

Figure 18 Rabun County EWP Site 3 Completed

The geocell retaining wall has performed well for over one year with minor problems near the ends of the wall discussed in Lessons Learned below. Figure 19 shows the project one year after completion.

Figure 19 Rabun County EWP Site 3 after One Year

LESSONS LEARNED

Design software provided by the manufacturer analyzes the external stability of the geocell retaining wall and the internal stability of each layer of cells. It does not evaluate the global stability of the slope. A global stability analysis should be conducted on all projects, in particular those with steep upper slopes or deep soil foundation materials. The Sawmill River site would not have had a global slope stability factor of 1.3 had the wall been designed to only meet the required factors of safety for the geocell wall stability.

Geocell retaining wall design often assumes the material retained by the wall is adequately drained and will not produce hydrostatic pressures on the wall. If the retained material is not adequately drained, an adequate drainage system must be designed and constructed. If drainage features are not included, the geocell wall should be designed considering the potential hydrostatic pressure behind the structure.

For sites that repair or stabilize a portion of a slope, the transition into the adjacent natural slopes is critical. Extension of the geocell walls into the adjacent slope will help prevent localized slope failure or erosion at the ends of the retaining structure. Figure 20 shows the results of not extending the geocell around the ends of the wall.

Figure 20 Slope Failure at the end of the Geocell Wall

On projects with wall heights of 10 to 15 feet and overall lengths less than 100 feet, such as the Rabun County Site 3, detailed and specific wall dimensions and material specifications are recommended to expedite construction. External and internal stability analyses may be conducted during design using hand calculations or spreadsheets. For larger projects, submittal of a wall design by the contractor/supplier may lead to cost savings. Minimum wall dimensions may be necessary to provide the global slope stability as this is often not evaluated by wall manufacturers.

ACKNOWLEDGMENTS

These projects were completed by the Natural Resources Conservation Service and the Emergency Watershed Protection Program. Final engineering plans and specifications and construction contract administration were provided by local NRCS staff. Mr. Carl Gustafson and Mr. Dave Nelson of Amherst, Massachusetts and Ms. Deena Roberts of Athens, Georgia coordinated these efforts for the Sawmill River site and Rabun County site, respectively.

REFERENCES

Geo-Slope International.1991-2006. SLOPE/W Computer Program, Calgary, AB, CA.
Presto Products Company. 2001. The Geoweb Earth Retention System Technical Overview. Appleton, Wisconsin.
Presto Products Company. 2001. The Geoweb Earth Retention System Product Specification. Appleton, Wisconsin.
WebTec, Inc. 2001-2004. TerraCell Cellular Confinement System. Charlotte, North Carolina.
Geotechnical Fabrics report. 2001-2005. Specifiers Guide. Roseville, Minnesota.

CONTACT:
D. Wade Anderson
USDA-NRCS-NDCSMC
501 W. Felix, Bldg. 23
Ft. Worth, TX 76115
Phone: 817-509-3764
Email: wade.anderson@ftw.usda.gov

Reinforced Soils

Offsetting Lateral Loads and Moments at the Top of Segmental Retaining Walls

James A. McKelvey, III, Earth Engineering Incorporated; Ward McMasters, Earth Engineering Incorporated

ABSTRACT

In the design of commercial developments, civil engineers are required to maximize parking areas to support the commercial buildings proposed. This requirement often leads to the necessity of retaining walls to provide the necessary horizontal area for the project. Similarly, residential developments often require retaining walls to allow building pad geometry. As geogrid-reinforced segmental block walls are very cost effective, this type of wall is often specified for commercial and residential developments. However, segmental block walls have limited lateral resistance to offset loads imposed by features required at the top of the wall, such as fences, guide rails and lighting foundations. This paper will discuss common lateral loads and moments typically imposed at the top of retaining walls and present several design methods and construction techniques to provide acceptable lateral resistance for these features.

INTRODUCTION

Retaining walls are a common occurrence in the development of commercial and residential properties, where horizontal area is required for development. Usually the costs of segmental retaining walls are much less than reinforced concrete walls in these applications, hence their popularity. However, using segmental retaining walls can pose problems for wall designers, as segmental retaining walls may not have sufficient lateral rigidity to offset lateral loads and moments induced by site features at the top of the wall. For residential developments, fencing is typically required by code at the top of the wall. In commercial developments, site features such as fencing, guide rail or vehicle barriers, and light foundations are commonly located at the top of the wall.

The most popular method to provide resistance for these lateral loads is to offset the site features from the face of the retaining wall, allowing the retaining soils the passive resistance without inducing stress on the segmental wall units. Guidance documents (National Concrete Masonry Association (NCMA), 1997) and segmental block manufacturer's literature suggest that an offset 36in (914mm) to 40in (1,016mm) from fence and guide rail posts to the front of the wall will provide adequate passive resistance to these lateral loads. However in many commercial development plans, areal constraints dictate that these site features be located closer to the face of walls. Even if adequate setback can be provided at the top of the wall for fencing, safety issues could result if landscaping requiring maintenance is planted between the fence and the top of the wall.

The currently available analysis software programs for segmental retaining walls do not allow for consideration of lateral loads and moments at the top of the walls. Accordingly, analyses of these loads need to be evaluated separately. While many of the segmental blocks used in engineering applications have block-to-block and block-to-geogrid connection strengths exceeding many of the lateral loads that will be discussed herein, the segmental blocks have inadequate overturning resistance to offset the associated moments induced by the lateral loads. Accordingly, both the shear resistance and overturning resistance of the segmental blocks need to be evaluated as appropriate.

Transient loads and lateral displacements are typically evaluated at the service limit state (American Association of State Highway and Transportation Officials (AASHTO), 2004). Accordingly, acceptable results are obtained when performance ratios exceed 1 with LRFD reduction factors set at 1, and lateral displacements are within tolerance. AASHTO suggests (AASHTO, 2004) that maximum allowable displacements at the service limit state in geotechnical applications be limited to 1.5in (38mm) while the NCMA guidance document suggests (NCMA, 1997) service limit state displacements be limited between 0.16in (4mm) to 0.75in (19mm), depending on if block-to-block or block-to-geogrid connection strength is evaluated, respectively. For demonstration purposes in this paper, a maximum allowable displacement of 0.5in (13mm) at the service limit state will be considered acceptable.

Discussed herein are design methods and construction techniques that can be considered to offset lateral loads and moments associated with fence, guide rails and vehicle barriers, and light foundations. Some of the features discussed will provide lateral load and overturning resistance independently of the segmental block wall, eliminating the need to evaluate shear and overturning resistance of the segmental blocks.

LATERAL RESISTANCE FOR FENCE

For both residential and commercial developments, fencing is required at the top of retaining walls by the International Building Code for walls having an exposed height greater than 30in (762mm) (International Code Council, 2002). This code requires that the fence form a protective barrier at least 42in (1,076mm) above the ground surface at the top of the wall and withstand a load of 50lb/ft (730N/m) or a concentrated load of 200lb (890N) applied at the top of the fence. The design of fence for residential developments only has to consider the concentrated load, while fence design for commercial developments needs to consider both loading conditions, but not concurrently. To develop the appropriate lateral resistance for the fence load, the spacing of fence posts needs to be known.

Shown in Figure 1 is the minimum offset for fence posts from the segmental retaining wall such that the fence supports acts independently from the retaining wall. The minimum offset can be determined using Equation 1.

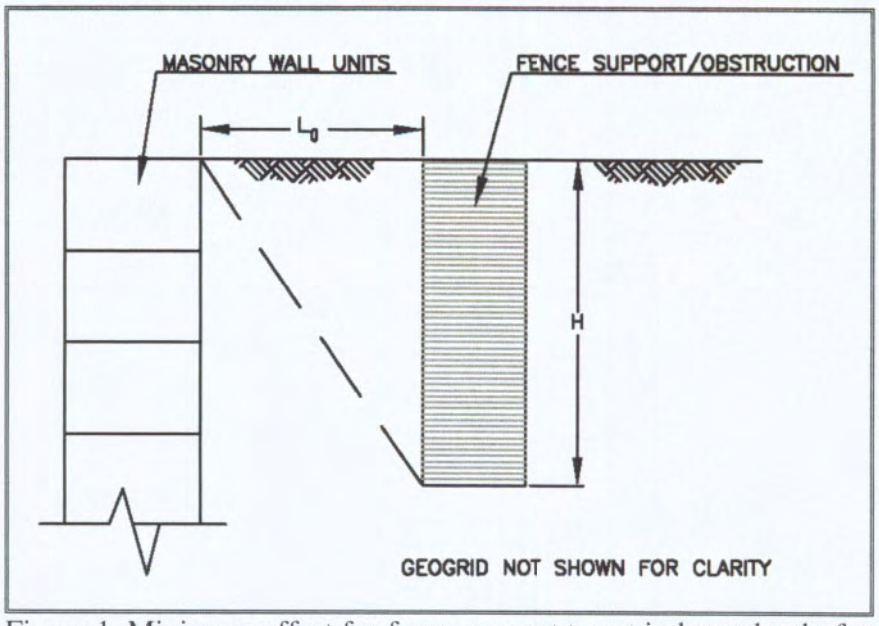

Figure 1 Minimum offset for fence support to act independently from the retaining wall.

$$L_o = H \tan\left(45 - \frac{\phi}{2}\right)$$

(Equation 1)

Where:

Lo = offset from back of segmental blocks of retaining wall (ft or m)
H = embedment of fence post (ft or m)
□ = effective stress internal angle of friction (degrees)

If the minimum offset can be provided, analysis of the segment block stability doesn't need to be evaluated, as the fence will act independently of the wall. Many fence manufacturers have data suggesting the building code load criteria can be offset if the fence posts are driven 36in (914mm) to 42in (1,067mm) below grade. If areal constraints or safety/maintenance concerns require placement of the fence within the minimum offset, several options are available.

Placing the fence post directly into the segmental blocks has been used to secure fence posts in the past. Here the upper courses of segmental blocks that will support the fence are filled with low-strength concrete, and the posts installed either in the uncured concrete or later cored into the cured concrete. Competent design of this system requires evaluation of the system using appropriate masonry analyses, which are beyond the scope of this paper. While adequate resistance can be provided for fence loads with this system, this system can be costly, will render the somewhat flexible segmental retaining wall to be locally rigid, and usually requires several trades to construct.

Another common technique to providing support for fencing is to place 12in (305mm) diameter circular forms behind the wall at the locations to receive fence posts. The forms are typically either sections of plastic pipe or prefabricated cardboard embedded 36in (914mm) below grade. After wall construction, the fence posts are placed within the forms and low-strength concrete. Figure 2 shows lateral load resistance provided for typical size concrete filled forms embedded 36in (914mm) in a medium dense sand and dense gravel. Results shown in Figure 2 were computed using the COMP624P (Reese and Wang, 1993) subroutine featured in the AllPile computer program (CivilTech, 2005). This computer program will be subsequently referred to herein as the lateral resistance software. The medium dense sand was modeled having a unit weight of 125lb/ft3 (2,002kg/m3), an effective stress internal friction angle of 34°, and a subgrade modulus of 77lb/in3 (2,131g/cm3). Assumed to have a relative density of 75%, the dense gravel was modeled having a unit weight of 135lb/ft3 (2,163kg/m3), an effective stress internal friction angle of 38°, and a subgrade modulus of 210lb/in3 (5,813g/cm3).

The lateral load resistance provided at the service limit state (i.e., top displacement of 0.5in (13mm)) for the 12in (305mm) diameter form can be seen in Figure 2 to be approximately 310lbs (1,379N) when embedded in medium dense sand and approximately 500lbs (2,224N) when embedded in dense gravel. By inspection of Figure 2, the concentrated load of 200lb (890N) required by the building code can be achieved with this system for the soils shown. However, as the spacing of fence posts is usually 8ft (2,438mm) or 10ft (3,048m), the distributive load of 50lb/ft (730N/m) required by the building code for commercial developments would result in fence post loads of 400lbs (1,779N) to 500lbs (2,224N), which exceeds the lateral resistance provided by embedment within the medium dense sand. Accordingly, to use this system in commercial developments, the circular form would need to be embedded in the dense gravel.

The shear and overturning resistance of the portion of the segmental retaining wall within the embedment zone of the circular form needs to be evaluated. While the shear resistance of the block-to-block and block-to-geogrid interfaces to be evaluated may exceed the additional lateral load imposed by the circular form during fence loading, computations of overturning moments would yield unsatisfactory results for most segmental blocks. The overturning resistance of the effected segmental blocks could be increased by filling the blocks with low-strength concrete, but this would have the same disadvantages as described previously.

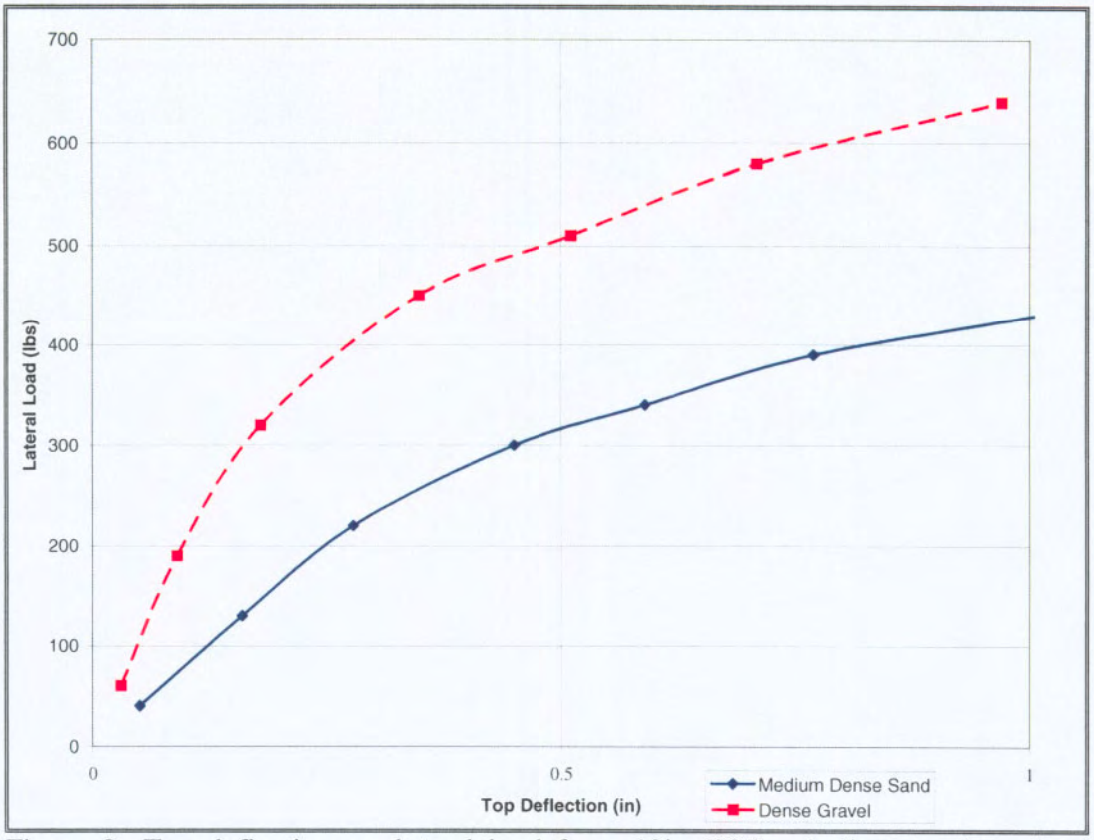

Figure 2 Top deflection vs. lateral load for a 12in (305mm) diameter form for fence support embedded 36in (915mm) below grade.

Another solution would be to reduce the overturning moment imposed on the segmental blocks by wrapping geogrid around the circular form as shown in Figure 3. A portion or the entire lateral load imposed on the segmental wall could be transferred to the geogrid. As can be seen in Figure 3, the geogrid is placed "standing up" from the subgrade elevation at the base of the form, and wooded stakes or steel reinforcement bars temporarily support the embedment end of the geogrid.

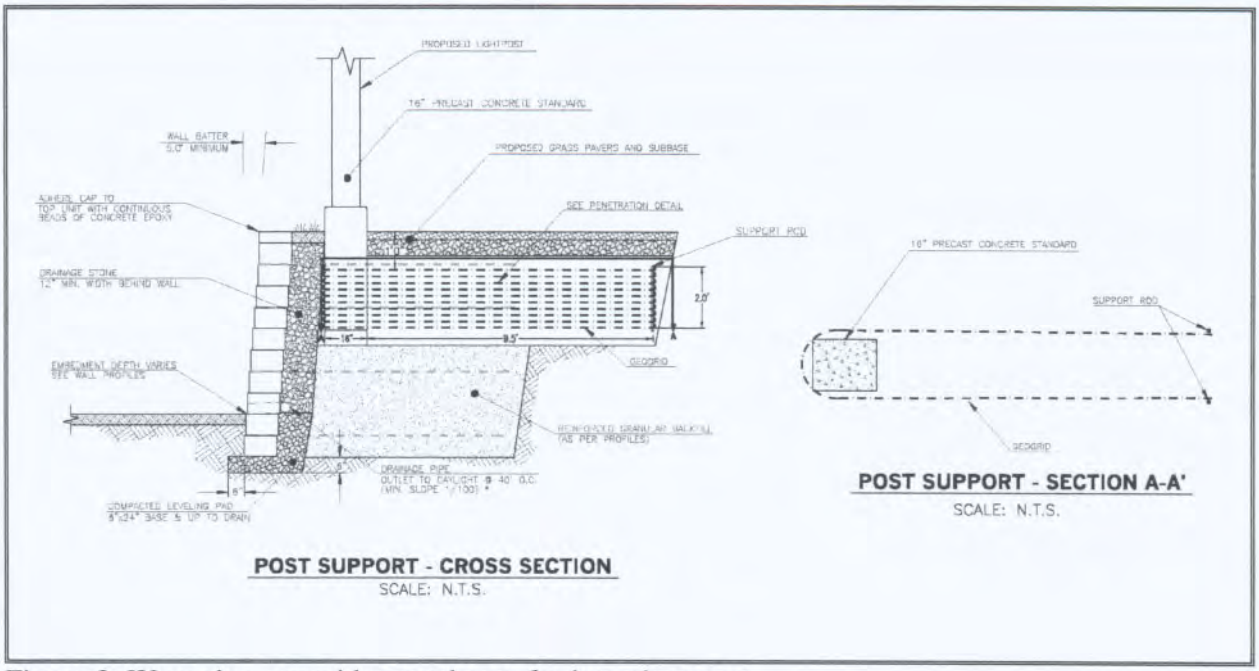

Figure 3 Wrapping geogrid around post for lateral support.

The length of embedment for the geogrid can be determined using Equation 2, which is derived by using the well published equation for horizontal embedment and using horizontal normal stress instead of vertical normal stress. The earth pressure exerted on the geogrid should approach the at-rest earth pressure, however since the influence of compaction effort on either side is not known, the active earth pressure is conservatively assumed to be acting on the geogrid. The tensile strength used in this equation is a portion or the entire lateral load imposed by the fence support on the segmental wall. Geogrid is then selected using long-term allowable strength; however, no reduction factor is required for creep due to the transient nature of the load.

$$L_e = \frac{T/2}{\left(H_t + \frac{W}{2}\right)\gamma\, K_a W\, C_i \tan\phi}$$

(Equation 2)

Where:

Le = length of embedment past form (ft or m)
T = Tensile strength required for lateral support (lbs or N)
Ht = depth to top of geogrid (ft or m)
W = width of geogrid (ft or m)
□ = unit weight of soil (lb/ft3 or kg/m3)
Ka = active earth pressure coefficient (dimensionless)
Ci = coefficient of geogrid interaction (dimensionless)
□ = effective stress internal angle of friction (degrees)

Another fence support system has recently been developed that can withstand the lateral loads required by the building code and not impose unacceptable stress on the segmental block retaining wall. The components of this proprietary fence support system are shown in Figure 4, which features two half sections of polyethylene circular form, which when assembled are 12in (305mm) in diameter, and 24in (610mm) long. The fence support system features quick assembly and can be placed directly behind the segmental block retaining wall.

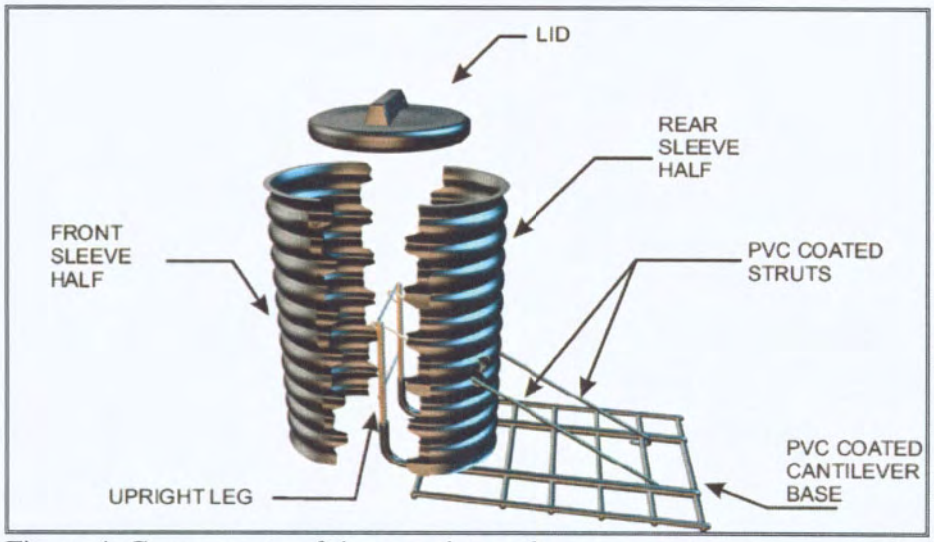

Figure 4 Components of the proprietary fence support system.
(© Advanced Hardscape Solutions LLC, 2006. Used by permission.)

The manufacturer of the proprietary fence support system has conducted full-scale testing of this system installed at the top of a geogrid-reinforced segmental block retaining wall. The wall used in the tests was 51in (1,295mm) high, constructed using non-proprietary segmental blocks having typical dimensions for segmental blocks used in engineering applications. Soil backfill for the wall consisted of a 12in (305mm) width of poorly graded gravel directly behind the segmental blocks and a silty sand for the remainder of the reinforced zone. The silty sand was had a maximum dry density of approximately 108lb/ft3 (1,730kg/m3), an effective stress internal friction angle of 28°, and effective stress cohesion of 295lbs/ft2 (1,440kg/m2) as determined by direct shear and standard Proctor tests. Placed in 8in (203mm) lifts, the soil backfill was compacted to 95% of the materials maximum dry density. One layer of polyester geogrid having a long-term allowable strength of approximately 980lbs/ft (14,301N/m) was placed on top of the third layer of segmental blocks, 24in (610mm) above the toe of the wall. Figure 5 shows compaction of the soil backfill during the full-scale tests of the proprietary fence support system.

Figure 5 Compaction of soil backfill during full-scale testing of the proprietary fence support system. The fence supports can be seen in the foreground, placed directly behind the segmental blocks.
(Photograph courtesy of Advanced Hardscape Solutions LLC, 2006. Used by permission.)

Upon completion of the segmental wall construction, W6x15 steel beams were installed in the fence support system, and then the circular form of the fence support system was filled with concrete. The size of the steel beams was selected such that the flexural rigidity of the members would exceed the maximum loads anticipated in the tests. After the concrete in the circular forms was allowed to cure, a hydraulic ram and instrumentation to measure the applied load and deflection of the top segmental block was setup as shown in Figure 6.

Loading of the fence post was then performed with the hydraulic ram located 48in (1,219mm) above the top of the retained fill behind the test wall. The load was applied to the fence post in 50lb (222N) increments until excessive wall deformation was measured. Figure 7 shows the results of three tests performed on the proprietary fence support system. By inspection of this figure, it is seen that the building code requirements for lateral support of fences was obtained when wall deformation is limited to 0.5in (13mm). The manufacturer has begun further testing the proprietary fence support system using proprietary segmental blocks and has obtained similar results.

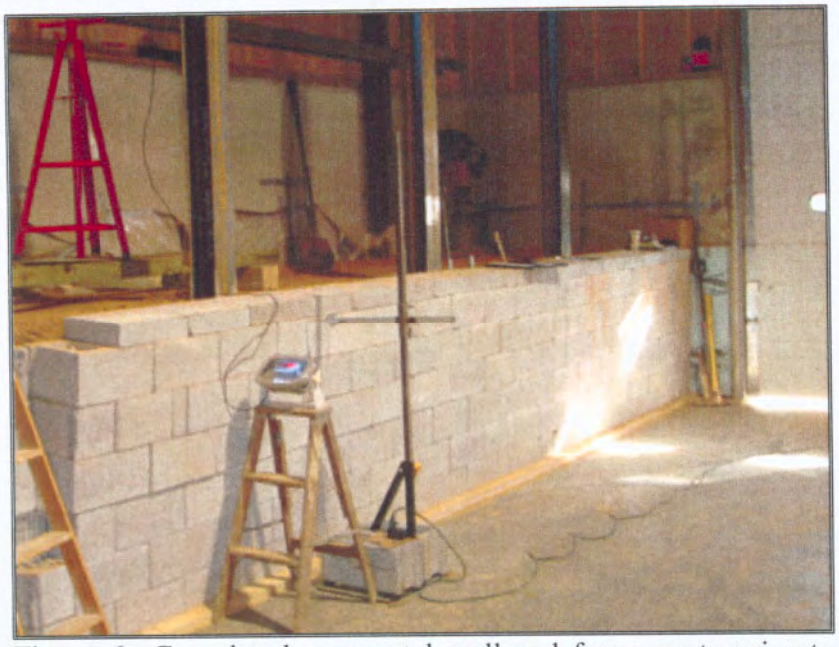

Figure 6 Completed segmental wall and fence posts prior to full-scale testing of the proprietary fence system. Instrumentation, hydraulic ram and the reaction frame can also be seen.
(Photograph courtesy of Advanced Hardscape Solutions LLC. Used by permission.)

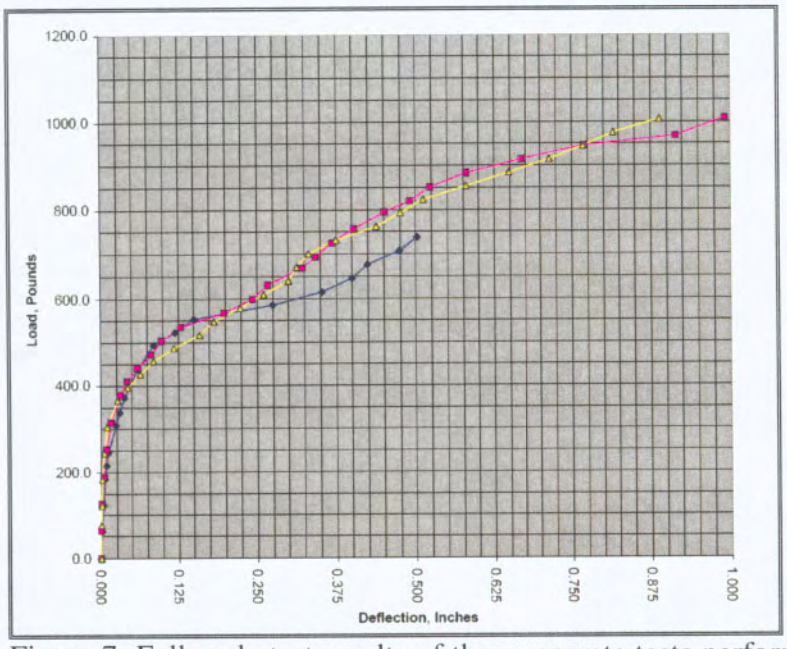

Figure 7 Full-scale test results of three separate tests performed on the proprietary fence support system.
(© Advanced Hardscape Solutions LLC, 2006. Used by permission.)

As a comparison to the performance of the proprietary fence support system, the manufacturer conducted full-scale tests on fence posts supported by 12in (305mm) diameter circular forms behind the wall. The forms used in the tests were prefabricated cardboard embedded 24in (610mm) below grade. Limiting wall deformation to 0.5in (13mm), the lateral resistance of the 12in (305mm) by 24in (610mm)-deep prefabricated circular form was found to average approximately 100lbs (444N). Using the lateral resistance software, the authors were able to predict the lateral resistance of the 12in (305mm) by 24in (610mm)-deep prefabricated circular form within 5 percent of that measured in the full-scale testing.

LATERAL RESISTANCE FOR GUIDE RAILS AND VEHICLE BARRIERS

To protect vehicular traffic at the top of a retaining wall, guide rail is typically specified in commercial developments between the traffic and the retaining wall. In some cases, particularly where the retaining wall supports roadways, vehicle barriers similar to parapets on modern bridges are specified. As the design criteria for guide rails and vehicle barriers vary appreciably, the lateral loads that may be imposed on the retaining wall, if any, will vary as well.

Design criteria for guide rail is stipulated by AASHTO for various vehicle characteristics and the crashworthiness of the proposed guide rail system as determined by full-scale crash tests. As the expense of such testing is typically beyond the budgetary constraints of commercial developments, development engineers often rely on standard details for guide rails developed by the transportation agency of the state the project is located in. The resulting design criterion is vague, as the development engineer does not know the impact load imposed on the guide rail system. The argument for design is that if it is good enough for highway applications, it will suffice for commercial development. So how does the wall designer know if the guide rail will negatively impact the segmental retaining wall?

While it is acknowledged that guide rail details may vary from state to state, the general size and spacing of guide rails is reasonably consistent in the United States. To ascertain the lateral load guide rail may impose on segmental retaining walls, the service limit state lateral resistance of a standard strong post guide rail was estimated using the lateral resistance program. The guide rail system considered consists of W6x9 steel beams driven 50in (1,270mm) below grade at 75in (1,905mm) centers, consistent with the requirements stipulated by one transportation agency (Commonwealth of Pennsylvania Department of Transportation, Bureau of Design, 2004). The center of the railing portion of the guide rail is positioned approximately 22in (559mm) above grade. The medium dense sand and dense gravel described above for fence support was also considered for guide rail post embedment in the lateral resistance program.

Figure 8 shows that the lateral resistances at the service limit state offered by the medium dense sand and dense gravel are approximately 750lbs (3,336N) and approximately

1,150lbs (5,115N), respectively. At the strength limit state (where deformation at the top of the pile is limited to 1in (25mm)), the lateral resistances offered by the medium dense sand and dense gravel are approximately 980lbs (4,359N) and approximately 1,500lbs (6,672N), respectively. The lateral resistance program predicts that the center of rotation exists below the pile tip for both soil types. Such low lateral resistance in comparison to vehicle weight supports the conclusion that the intent of guide rail systems is to redirect traffic back onto the roadway and not to prevent vehicles from going over the retaining wall. Accordingly, the development engineer must carefully consider the appropriateness of this system for use at the top of retaining walls.

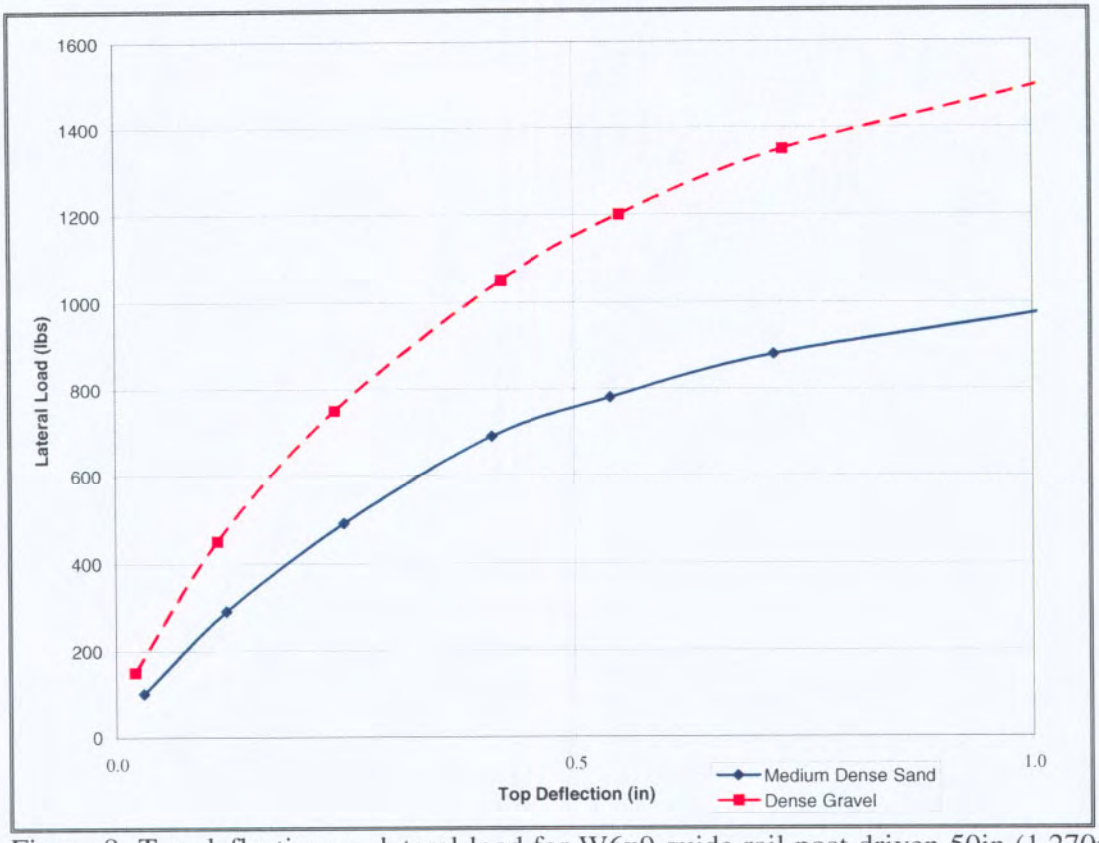

Figure 8 Top deflection vs. lateral load for W6x9 guide rail post driven 50in (1,270mm) below grade.

The most desirable method to resist the guide rail load would be to drive the posts at the minimum offset distance defined by Equation 1. If this is not possible, then 12in (305mm) diameter circular forms can be placed behind the wall at the locations to receive guide rail posts. To reduce the shear and overturning moment imposed on the segmental blocks of the retaining wall, geogrid can be wrapped around the circular form. The embedment length for the geogrid can be determined using Equation 2. Geogrid is selected using long-term allowable strength; however, no reduction factor is required for creep due to the transient nature of the load. The guide rail posts are then positioned in the circular forms and the forms filled with concrete.

While not intended for guide rail support, the test results of the proprietary fence support system in Figure 7 suggest that this system may provide sufficient lateral resistance for guide rail if the site soils are of weaker strength. Accordingly, this system may be considered for guide rail support if it can be demonstrated it provides equivalent lateral resistance to guide rail posts located away from the retaining wall on the project. However, it must be emphasized again that guide rail systems will not prevent vehicles from going over the wall. If the wall is high enough to introduce a significant hazard to public safety in the event of a high impact collision with the guide rail, vehicle barriers need to be specified at the top of the retaining wall.

Both the building code and AASHTO prescribe design criteria for vehicle barriers. The building code stipulates that vehicle barriers shall be able to resist a load of 6,000lbs (26.70kN) when applied at a minimum height of 18in (457mm) above the grade (ICC, 2002). AASHTO stipulates that the upper layers of soil reinforcement of a geogrid-reinforced retaining wall be able to resist a concentrated lateral load of 10,000lbs (44.48kN) distributed over a length of 5ft (1,524mm). The vehicle barrier shall have sufficient mass to resist overturning moments and have adequate space shall be provided between the barrier and the back of the retaining wall to preclude direct transmission of lateral load to the top segmental blocks (AASHTO, 2004).

Whichever design criteria is considered relevant for the project (i.e., the building code or AASHTO), the prescribed lateral load is resisted by the upper layer(s) of geogrid. The long-term allowable strength and embedment length is determined by typical geogrid design practices. To provide adequate overturning resistance for the vehicle barrier, a moment slab consisting of reinforced concrete is typically required. The moment slab needs to have sufficient length to transmit the lateral load to the underlying soils without sliding and have sufficient structural rigidity to resist the overturning moment, the design of which is beyond the scope of this paper.

LATERAL RESISTANCE FOR LIGHT FOUNDATIONS

Foundations for light posts typically consist of 18in (457mm) to 24in (610mm)-diameter caissons embedded 5ft (1,524mm) to 6ft (1,829mm) below grade. The vertical load imposed by the light posts is typically negligible in comparison to applied moment, but still needs to be considered in the retaining wall design as an applied bearing pressure. Due to the similarity in geometry, the light post foundation is merely an extension of the fence post, albeit with much larger loads.

For illustration purposes, a typical light foundation was evaluated using the lateral resistance program. The light foundation considered was 24in (610mm) in diameter, embedded 60in (1,524mm) below grade. The medium dense sand and dense gravel described above for the fence and guide rail support was also considered for light foundation embedment in the lateral resistance program. As shown in Figure 9, the lateral resistance of the light foundation at the service limit state varies between

approximately 3,700lbs (16.46kN) and approximately 5,950lbs (26.47kN) for the two soil types considered.

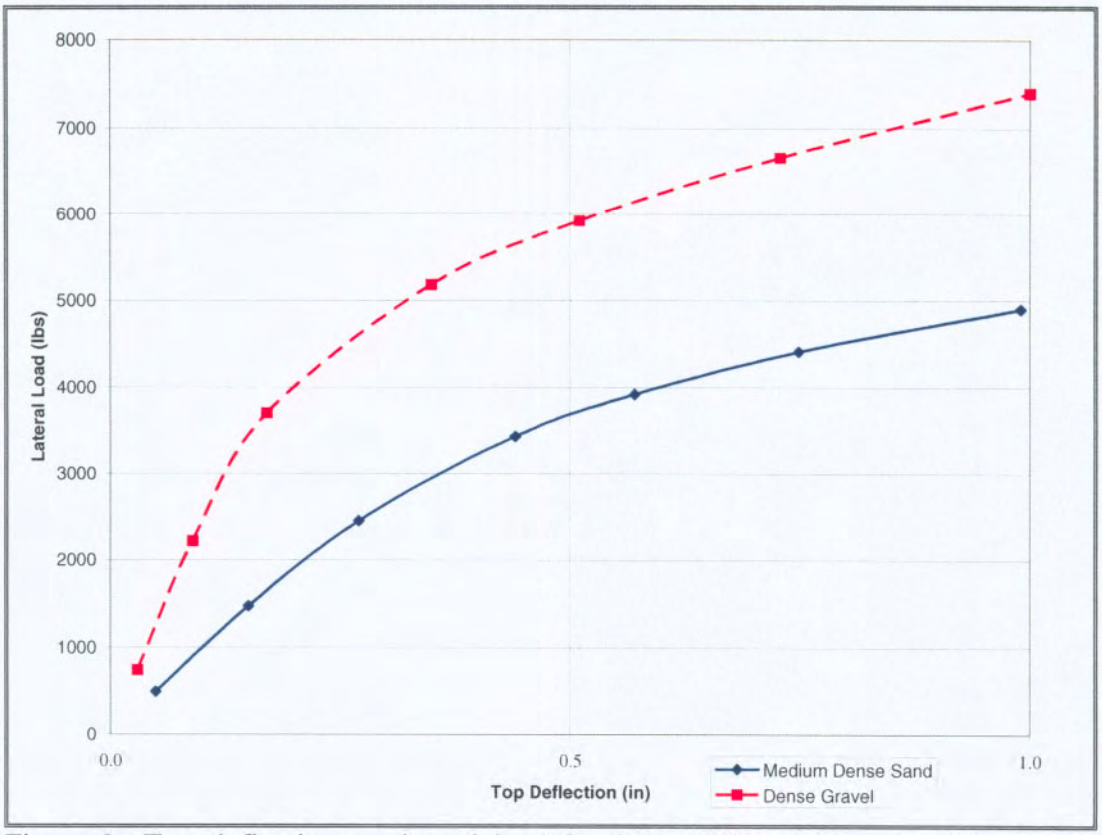

Figure 9 Top deflection vs. lateral load for 24in (610mm) diameter light foundation embedded 60in (1,524mm) below grade.

Again it would be ideal to locate the back of the light foundation at the minimum offset distance from the retaining wall as defined by Equation 1. If this is not possible, the shear and overturning moment imposed on the segmental blocks of the retaining wall can be reduced by wrapping geogrid around the circular form used for the light foundation. The embedment length for the geogrid can be determined using Equation 2. Geogrid is selected using long-term allowable strength; however, no reduction factor is required for creep.

SUMMARY

Site features such as fence, guide rail and vehicle barriers, and light foundations are commonly located at the top of retaining walls. Due to the limited lateral resistance of segmental retaining walls, design of the retaining wall must carefully consider the presence of these site features. As the currently available analysis software programs for segmental retaining walls do not allow for consideration of lateral loads and moments at the top of the walls, analyses of these loads need to be evaluated separately. Several

design methods and construction techniques were presented to provide adequate lateral resistance for fence, guide rail and vehicle barriers and light foundations.

While the solutions presented offer a method to resist lateral loads and overturning moments associated with typical site features located at the top retaining walls, the presence of these features within a geogrid-reinforced soil mass will result in considerable penetrations of the upper layers of reinforcement. Accordingly, the impact of these features on the internal stability of the retaining wall needs to be carefully considered during design, and additional layers of geogrid be specified as required.

The full-scale testing presented in the paper provides needed insight into the lateral loads imposed by fence at the top of segmental retaining walls. Using the lateral resistance program, the results of the full-scale testing could be replicated, which is encouraging. Additional research is needed to further substantiate the design methods and construction techniques presented.

Finally, it is common practice in the design of segmental retaining walls to stipulate on construction drawings that site features located at the top of the retaining wall are to be "designed by others". Considering the potential impact on the retaining wall stability by these features, the responsibility for engineering of the site features and foundations of same needs to be fully identified between the wall designer and the development engineer. As the paper presented the limited performance of guide rail in resisting impact loads, the practice of specifying guide rail at the top of retaining walls needs to be carefully scrutinized by the responsible engineers such that adequate safety is provided to the public.

ACKNOWLEDGEMENTS

The authors would like to thank Mr. Jon Calle of Advanced Hardscape Solutions LLC, Glenmoore, Pennsylvania for sharing laboratory data of the proprietary fence support system presented in the paper. For further information on Advanced Hardscape Solutions LLC's fence support system, contact Mr. Calle at 866.843.0500 or visit www.fencesleeve.com. Appreciation is expressed to Ms. Lisa Christ, Mr. Rick Smith and Mr. Vince Ruelas of Earth Engineering Incorporated for their assistance in figure presentation and to Mr. Bob Follett of Earth Engineering Incorporated for reviewing the manuscript.

REFERENCES

American Association of State Highway and Transportation Officials, (2004), AASHTO LRFD Bridge Design Specifications, Customary U.S. Units, Third Edition, Washington, District of Columbia: AASHTO.

CivilTech Corporation, (2005), AllPile Version 7 User's Manual, Bellevue, WA: CivilTech.

Commonwealth of Pennsylvania Department of Transportation, Bureau of Design (2004), Standards for Roadway Construction, Series RC-1M to 100M, Publication 72M, April 2004 Edition, Harrisburg, Pennsylvania: PENNDOT.

International Code Council, Inc., (2002), 2003 International Building Code, Falls Church, Virginia: ICC.

National Concrete Masonry Association, (1997), Design Manual for Segmental Retaining Walls, Second Edition, J.G. Collin, Editor, Herndon, Virginia: NCMA.

Reese, L.C, and S.T. Wang, (1993), COM624P-Laterally Loaded Pile Analysis Program for the Microcomputer, Publication No. FHWA-SA-91-048, U.S. Department of Transportation, Federal Highway Administration, Washington, D.C.: FHWA.

CONTACT:

James A. McKelvey
Earth Engineering Incorporated
115 West Germantown Pike
East Norriton, PA 19401
Phone: 610-277-0880 ext. 261
Email: JayM@EarthEngineering.com

GEOTEXTILE WRAP-FACE WALL USING MARGINAL BACKFILL

Brandon Parrish, Graduate Research Assistant; John J. Bowders, University of Missouri, Department of Civil & Environmental Engineering; Allen Thompson,Associate ProfessorBiological Engineering at the University of Missouri-Columbia

ABSTRACT

A concrete retaining wall was constructed during October/November 2005. The height of the wall was 9 feet with a stem width of 0.83 ft, while the width of the base was 1.83 ft. The backfill was a low plasticity clay (CL). As a result of this design, the wall was not able to withstand the lateral pressures from the backfill and noticeable cracks in the wall developed within one month after backfilling. The backfill soil was then removed to relieve pressure on the wall until a remediation scheme could be developed and implemented. A geotextile wrap-face wall was chosen to reinforce the soil mass behind the existing concrete wall, which now acts as a facade. The geotextile wrap-faced wall was designed with a high strength woven geotextile with seven layers of reinforcement. The in-situ soil (CL), a marginally suitable material, was used for the backfill. Extensive drainage was incorporated in the design and construction of the geotextile wrap-face wall to reduce positive pore water pressures in the backfill. A gap between the face of the geotextile wall and the back of the concrete wall allows for deformation of the wrap-face wall without contacting the concrete wall. Index and compaction tests were performed on the backfill soil and interface shear tests were conducted with the geotextile and soil to provide design parameters. The geotextile wrap-faced wall was constructed in July 2006, and the performance is being monitored. To date, four months post construction, no significant lateral, nor vertical movements have occurred, and the drainage system has successfully handled significant flows.

INTRODUCTION

Throughout the world there is an increasing lack of available prime development space due to increasing population and associated land development. As a result, structures enabling maximum land utilization, such as retaining walls and mechanically stabilized earth (MSE), are becoming increasingly popular. Retaining walls are built to accomplish exactly what their name implies, retain, or reinforce, a mass of soil, rock, or other material. Many different types of retaining walls exist, and include gravity and cantilever concrete retaining walls, and MSE retaining structures constructed using geosynthetics or metallic reinforcement. According to MSE wall design manuals by FHWA (1997) and AASHTO (2000), the MSE backfill soil must be of high quality, i.e., contain less than 15 percent fines. Limiting the amount of fines (particles passing #200 (0.075 mm) sieve) ensures proper drainage throughout the backfill, mitigates the buildup of positive pore water pressures in the backfill soil and dramatically reducing the stress on the wall face. Positive pore water pressures produce seepage forces on the reinforced fill that decreases the stability and reduces the shear resistance of the reinforced soil fill. Studies show that forces against a retaining wall with poor drainage can be twice those of a properly drained reinforced fill soil (Christopher and Stulgis 2005). Well-draining backfill is considered high quality but can be difficult and/or expensive to obtain. Koerner (1998) provided a comparison of wall costs for various types of retaining walls. His survey showed MSE geosynthetic retaining

structures to be the least costly and on the order of one-third as costly as reinforced concrete cantilever walls. High quality or permeable backfill can cost two to three times that of low quality, high fines backfill (Christopher and Stulgis 2006). As a result, the use of MSE wall backfill soil located on-site has positive attributes including: close proximity to the construction site and minimal cost. Although the use of in-situ backfill soils is convenient, they are often of marginal quality, defined as having greater than 35 percent fines, or a plasticity index greater than 20 (Sandri 2006). MSE walls can be constructed using marginally suitable backfill soil and still perform properly if adequate drainage is incorporated in the design and construction of the wall. The segmental retaining wall design manual, developed by the NCMA (1997), includes the use of backfill soils containing more than 35 percent fines, as well as addressing the drainage of such structures (NCMA 2002). However, few full-scale MSE walls using marginal backfill have been performance monitored and documented

A concrete retaining wall was constructed during October/November 2005 at a residential property to establish an elevation difference between the front yard area and the adjacent lower level garage (Figures 1 and 2). The project site is located in Boone County, Missouri, USA. The concrete wall was constructed with number four (0.5 in. diameter) vertical and horizontal rebar spaced vertically and laterally every two feet and has a height of eight feet (2.4 meters) (Figure 3). The nine-foot tall retaining wall ties into the existing wing wall of the house and extends westward approximately 29 feet then makes two 45-degree angles and extends 14 ft. north. At this point the wall height reduces to four feet and the wall continues for about 10 more feet before turning back to the east.

Figure 1 - Existing concrete retaining wall constructed October/November 2005 (February 2006)

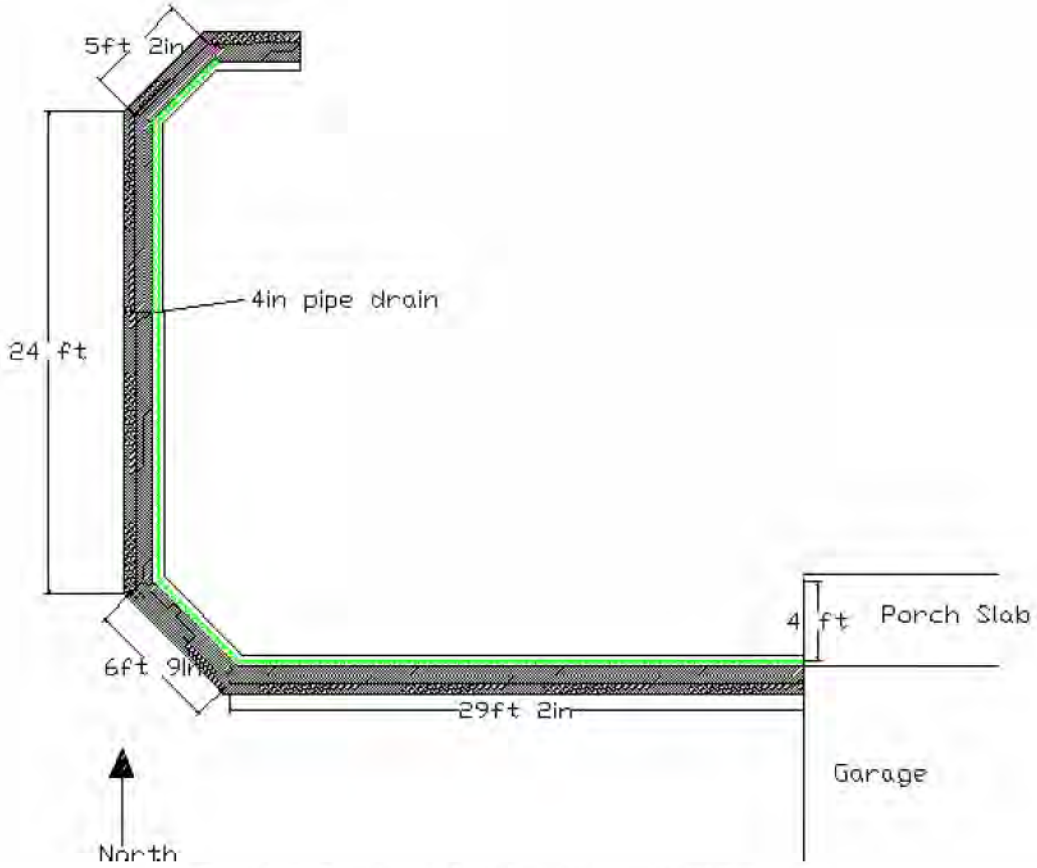

Figure 2 - Plan view of existing concrete retaining wall

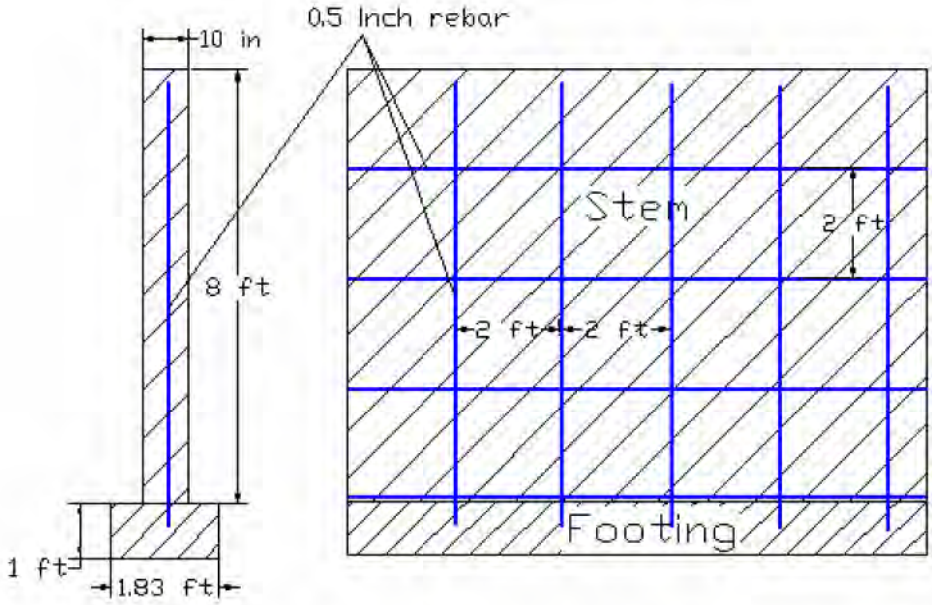

(a) Profile view of concrete wall (b) Elevation view of concrete wall

Figure 3 - Profile and elevation view of existing concrete wall

Noticeable cracks in the concrete wall developed on the south face of the wall approximately one month after the backfilling. The backfill was removed to protect the wall from further deformation. Stability analyses of the existing concrete wall were performed *after* the backfill had been removed.. The results confirmed that the existing concrete wall was not stable in the backfilled condition (Table 1). The factors of safety for overturning and sliding indicate imminent failure. To mitigate the potential for failure of the wall, a geotextile wrap-face wall was designed to reinforce the backfill soil and reduce, or relieve, the lateral load on the existing concrete wall. The geotextile wrap-face wall was constructed and instrumented to allow performance assessment, and further our knowledge of walls incorporating marginally suitable backfill.

Table 1 - Calculated and desired factors of safety of existing concrete wall

Factory of Safety Condition	Desired Value	Calculated Value
Overturning	>2.0	0.2
Sliding	>2.0	0.4
Bearing Capacity	>2.0	5.7

GEOTEXTILE WRAP-FACE WALL DESIGN

A wrap-face retaining wall was chosen to reinforce the soil mass immediately behind the existing concrete retaining wall. The wrap-face retaining wall consists of layers of compacted backfill with a reinforcing geotextile or grid between each soil layer that wraps around the exposed face of the layer and is embedded within the soil mass to form a wrap-face. The reinforcing material and earthen backfill are two integral components that are key to wall performance. The strength of an MSE wall comes from the fill and the reinforcement. The fill provides 80-85% of the wall's strength, while the reinforcement provides 15-20% of the strength. As a result, the type of fill chosen for construction has a great effect on the overall strength of the MSE wall (Lawson 2005). The backfill material available for this project was the on-site soil, a light brown silty clay (liquid limit 42, plasticity index 16, 100% passing 0.075 mm), and classified as a low plasticity silty clay (CL), (Unified Soil Classification System ASTM D2487). It was considered a marginal backfill soil.

A moisture-density relationship was developed by performing variations of the standard Proctor test (ASTM D698). Two compaction energies were used to perform the tests, standard Proctor energy (12,400 ft-lb/ft^3), and 50 percent standard Proctor energy (6,200 ft-lb/ft^3). The maximum dry unit weight and optimum moisture content obtained using standard Proctor energy was 105 pcf, and 17%, respectively. Using 50 percent standard Proctor energy, a dry unit weight of 94 pcf and an optimum moisture content of 23% were obtained. The reinforcement material was a woven polypropylene geotextile with an ultimate strength of 400 lbs/inch (wide-width). The allowable tensile strength was calculated to be 120 lbs/in. The interface friction angle, δ, between the geotextile reinforcement and backfill soil was further measured using a tilt table and by direct interface shear tests. The tilt table results indicated $\delta = 45$ degrees. Direct shear test configurations included shear in the geotextile's machine direction, cross-machine direction, and cross-machine direction with specimens submerged in water. The normal stresses used for each configuration were 1, 5, and 10 psi, chosen to bracket the stresses expected in the field. Each direct shear test was performed until peak friction between the soil and geotextile occurred or

until reaching horizontal movement limitations (approximately 0.7 inches). The interface friction angles determined for each testing configuration are shown in Table 2.

Table 2 - Direct shear interface friction angle for woven geotextile and on site soil (low plasticity clay).

Testing Configuration	Cohesion Intercept (psi)	Interface Friction Angle (degrees)
Shear in geotextile machine direction	2.5	50
Shear in geotextile cross-machine direction	3.5	32
Shear in geotextile cross-machine direction while submerged in water	1.0	30

The internal and external stability of the wrap-face retaining wall was analyzed and a design produced using the measured material properties. Internal stability of the wall was first addressed. To achieve internal stability, geotextile spacing, length, and overlap distance were determined. Assumptions in the wrap-face wall design included a backfill total unit weight of 115 pcf and an effective friction angle of 25 degrees. The interface friction angle was assumed to be 15 degrees. This value is lower than the values that were found during interface shear testing; however, it was assumed that construction practices will not be as controlled as in the laboratory, thus a reduction in the interface friction angle might better approximate the field case. A cohesion value of 2 psi was originally used in the design, which falls within the range of cohesion values obtained during the direct shear tests; however, the cohesion was assumed to be zero for long-term analyses and calculation of the geotextile lengths. The friction angle of the backfill was assumed to be zero degrees for purposes of locating the failure plane and determining the length Lo. The ultimate tension for the geotextile reinforcement was assumed to be 400 lbs/in. (wide-width tension), (Propex Fabrics 2006). The allowable tesile strength of the geotextile when accounting for damage due to installation, biological effects, and chemical effects as well as creep, was calculated to be 120 lb/in. and this strength was used in the design.

External stability of the geotextile wrap-face wall was analyzed by determining the safety factor with respect to overturning, sliding, and bearing capacity (Table 3). The factor of safety with respect to overturning for the reinforced mass was calculated at 5.0. This value is significantly increased compared to the same value for the existing concrete retaining wall. The factor of safety with respect to sliding was calculated at 1.5. Although this value is less than the desired value of 2.0, a conservative analysis was utilized while performing the calculation because the existing concrete wall was not incorporated in the stability analyses. The actual wrap-face wall will have a greater sliding resistance due to the base of the concrete wall located directly in front of the base of the reinforced mass (Figure 4) . The external stability of the wrap-face wall is significantly higher than the external stability of the existing concrete wall when in the backfilled position. The final design of the geotextile wrap-face wall included seven layers of geotextile

reinforcement ranging in thickness from one to two feet. Geotextile runout lengths increased with wall height and ranged from 4 to 10 feet from the face of the geotextile wall (Figure 4).

Table 3 - Calculated and desired external stability analysis of the designed geotextile wrap-face wall

Factor of safety condition	Desired Value	Calculated Value
Overturning	>2.0	5.0
Sliding	>2.0	1.5
Bearing capacity	>2.0	4.8

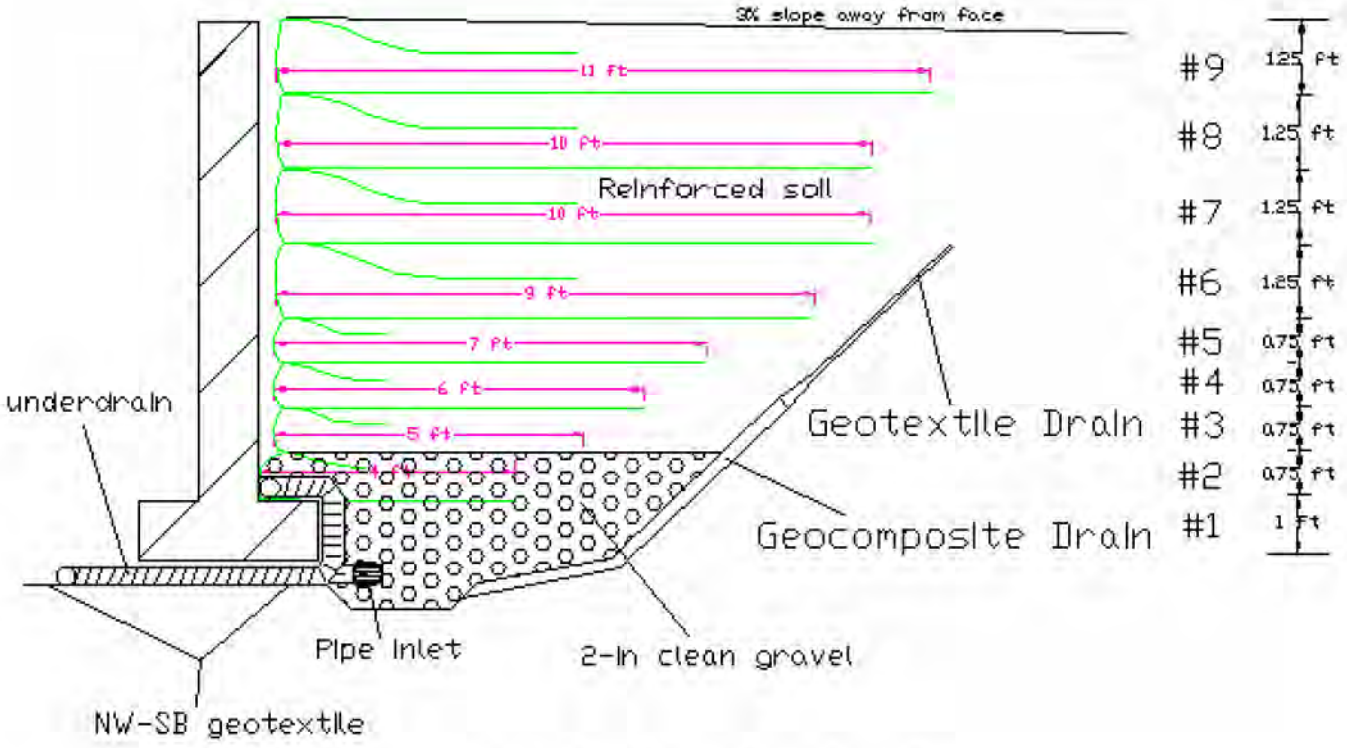

Figure 4 - As-designed profile view of wrap-face wall

CONSTRUCTION OF GEOTEXTILE WRAP-FACE WALL

Construction of the geotextile wrap-face wall using marginal backfill took place on July 17 – 24, 2006. Project conditions encountered at the site varied slightly from expected conditions. As a result, minor changes in construction as compared to the original design were needed to facilitate the conditions present. Upon arriving on-site, a survey of the existing drainage system was performed. Inspection of the perforated pipe drainage system revealed that the pipe was clogged (Figure 5), nearly level and presented an indirect route for drainage of water behind the wall.

Figure 5 – Clogged existing perforated pipe drain along top of the concrete wall footing (July 17, 2006)

These drainage deficiencies were removed by installing an exit pipe beneath the concrete wall footing and exiting down to the adjacent driveway down slope. Completion of the drainage system was followed by placement of backfill. In order to produce a firm and level base for the wrap-face wall and aid in drainage, a nonwoven-spunbonded geotextile separator was placed on the subgrade and 2-inch clean gravel was placed with a skid-loader to a height that was even with the top of concrete wall footing (Figure 6).

Figure 6- Placement of the gravel leveling pad (July 17, 2006)

Once a level surface was obtained, a drainage blanket was installed on top of the excavation working surface that ties into the non-woven geotextile underneath the gravel. The bottom drainage blanket consisted of a geonet between two layers of nonwoven, needle-punched geotextile. This blanket was then rolled up to provide a working surface for the skid-loader.

The second layer of the wrap-face wall consisted of geotextile reinforcement with gravel backfill (Figure 7). This layer was placed and compacted using the skid-loader. The geotextile reinforcement was wrapped around the existing perforated pipe drain and rested on the concrete footing in order to provide some downward load on the footing of the concrete wall.

Figure 7 - Placement of 2nd layer with geotextile reinforcement and gravel backfill (July 17, 2006)

After installation of the second layer it was apparent that the rolled up drainage blanket was slowing progress, and difficult to work around. As a result, the blanket was cut and placed under each lift separately thereafter. Before installation of the third lift was possible, timber face forms were constructed and placed on top of the second lift.

Geotextile reinforcement was cut to the correct length, placed for the third lift, tucked behind the timber face forms, and backfilling began using the on-site soil (CL). The method for backfilling included filling up to the lift height at the wall face, then sloping the backfill away from the face of the wall. The geotextile reinforcement was wrapped around and placed on top of the backfill and tensioned. Backfilling continued until a level lift was achieved, and compaction using the skid loader was performed. Nuclear density tests of the compacted backfill were performed, and showed an average dry unit weight of 97 pcf, and a moisture content of 18 percent, which correlate to approximately 75% standard Proctor energy.

Gravel was used for the backfill along the far west side of the excavation to facilitate drainage along the wall face. The fourth through eighth lifts were constructed in this manner with proper geotextile reinforcement lengths and lift thicknesses (Figure 8).

Figure 8 - Installation of CL backfill on geotextile reinforcement - 5th lift (July 19, 2006)

Completion of lift #8 included placing nonwoven geotextile along the existing 4-ft tall wall and repairing the drainage system that rested on the footing. This area was then backfilled with gravel and covered with on-site soil.On Friday July 21st, only the final lift reminaed to be placed and a heavy precipitation event occurred. Surface run-on water infiltrated the reinforced soil mass, traveled through the drainage system and exited in the drainage ditch (Figure 9) providing evidence that the drainage system constructed throughout the wrap-face wall was working.

Construction of the final lift, #9, was completed on Monday, July 24, 2006. The addition of the lift brought the geotextile wrap-face wall height even with the concrete retaining wall. The final lift of the geotextile wrap-face wall was graded and compacted so that precipitation will flow away from the reinforced soil mass, not through it (Figure 10). This area will be sodded to increase evapotranspiration thereby further reducing infiltration into the reinforced soil mass. A permanent cover will be placed over the gap between walls, to mitigate exposure of the geotextile ultra-violet radiation.

GEOTEXTILE WRAP-FACE WALL DESIGN VS. FIELD CONSTRUCTION

Several differences between the initial wall design and actual field construction (Figure 11) are present due to the on-site conditions. The total number of soil/gravel layers was increased from 7 to 9. The bottom layer was utilized as a leveling pad and constructed using 2- inch clean gravel. The second layer, first reinforcing layer, was also constructed using gravel and rested on the footing of the concrete wall. The geotextile reinforcement wrapped around the 3-inch diameter perforated pipe.

Figure 9 – Example of water in drainage excavation beneath footing

Figure 10 - Grading of finished geotextile wrap-face wall (July 24, 2006)

Geotextile overlaps of 3 feet were used for layers 2, 3 and 4 while 5-ft overlaps were used for the remaining layers. The overlaps were increased midway through the wall construction to facilitate efficient construction. Lateral overlaps were increased from 1-ft, to approximately 2 feet to maintain desired lateral overlap.

Several differences between the design and as-built geotextile walls were found in the drainage system. The original drainage system consisted of perforated drainage pipe resting on the concrete wall footing and exiting on the west side. The underdrain would tie into a proposed sand layer that would allow infiltrated water to enter the drainage pipe and flow out of the reinforced soil mass. The as-built drainage system also consists of a perforated pipe running on top of the concrete wall footing, but the pipe exit is at a lower elevation, below the footing enabling infiltration to drain down slope (Figure 12). The bottom 2 feet of the geotextile wall were constructed of 2-inch clean gravel to permit infiltrated water to enter the drainage pipe and exit the reinforced soil mass. Nonwoven geotextile was also placed on the east and west wall of

the geotextile wall to provide drainage and minimize infiltration in the reinforced soil mass. The west side of the concrete wall was backfilled with gravel and wrapped in geotextile to further increase the flow to the drainage pipe, and decrease positive pore water pressure buildup behind the wall.

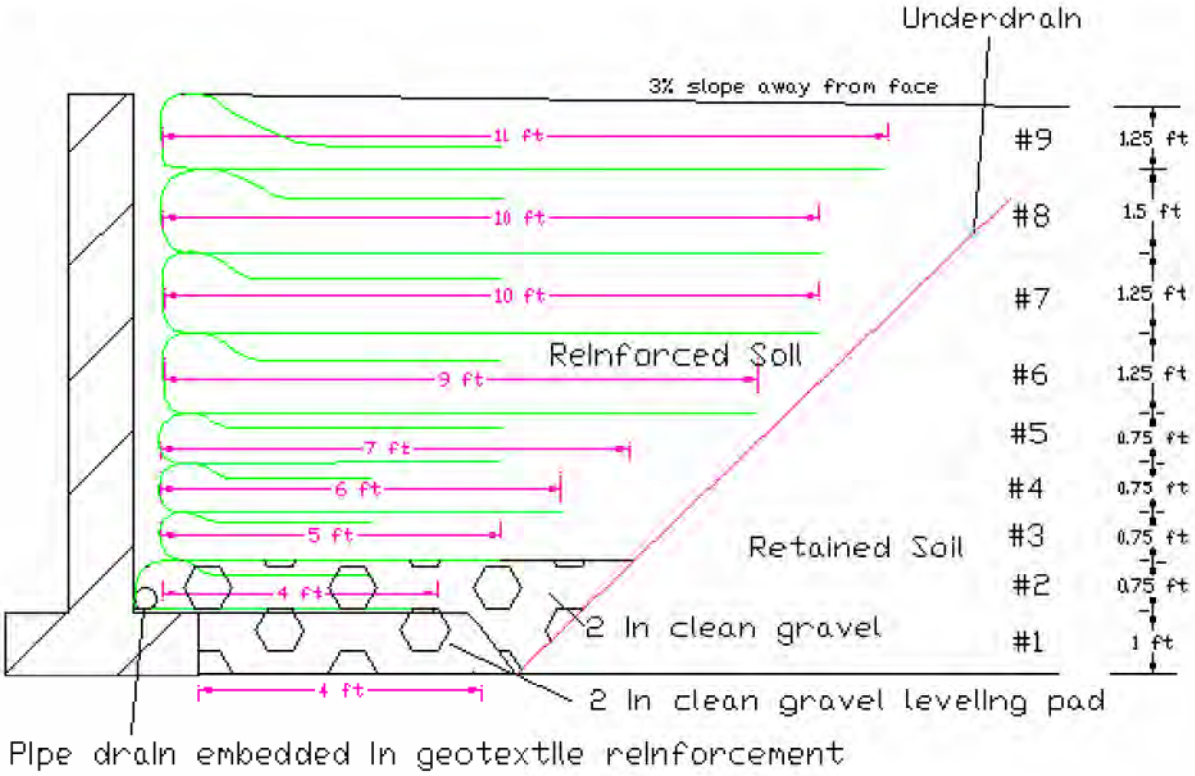

Figure 11 – As-built geotextile wall design

As a result of these differences, an additional factor of safety was incorporated in the construction of the geotextile wrap-face wall. The increased number of geotextile layers decreases the tension force in each geotextile layer. Increased geotextile overlaps decrease the potential of failure of the wrapped geotextile face due to unraveling. The drainage system modifications reduce the lateral stress of reinforced fill.

INSTRUMENTATION AND FIELD PERFORMANCE

The deformations of the wrap-face wall and existing concrete retaining wall are being monitored. Installation of the geotextile wall allowed for some deformation of the wrap-face wall prior to contacting the concrete wall. After the completion of each layer, a gap between the concrete wall and geotextile wall remained when the timber face forms were removed (Figure 13). The gap has closed or reduced in some areas along the wall face due to the geotextile being tensioned by the deforming soil Tell-tale® crack gauges (Figure 14) were installed over the existing cracks on the concrete wall face to monitor the concrete wall crack widths. An existing concrete wall survey was performed prior to construction of the geotextile wall. The survey included wall inclination, crack location and width, and wall translation.

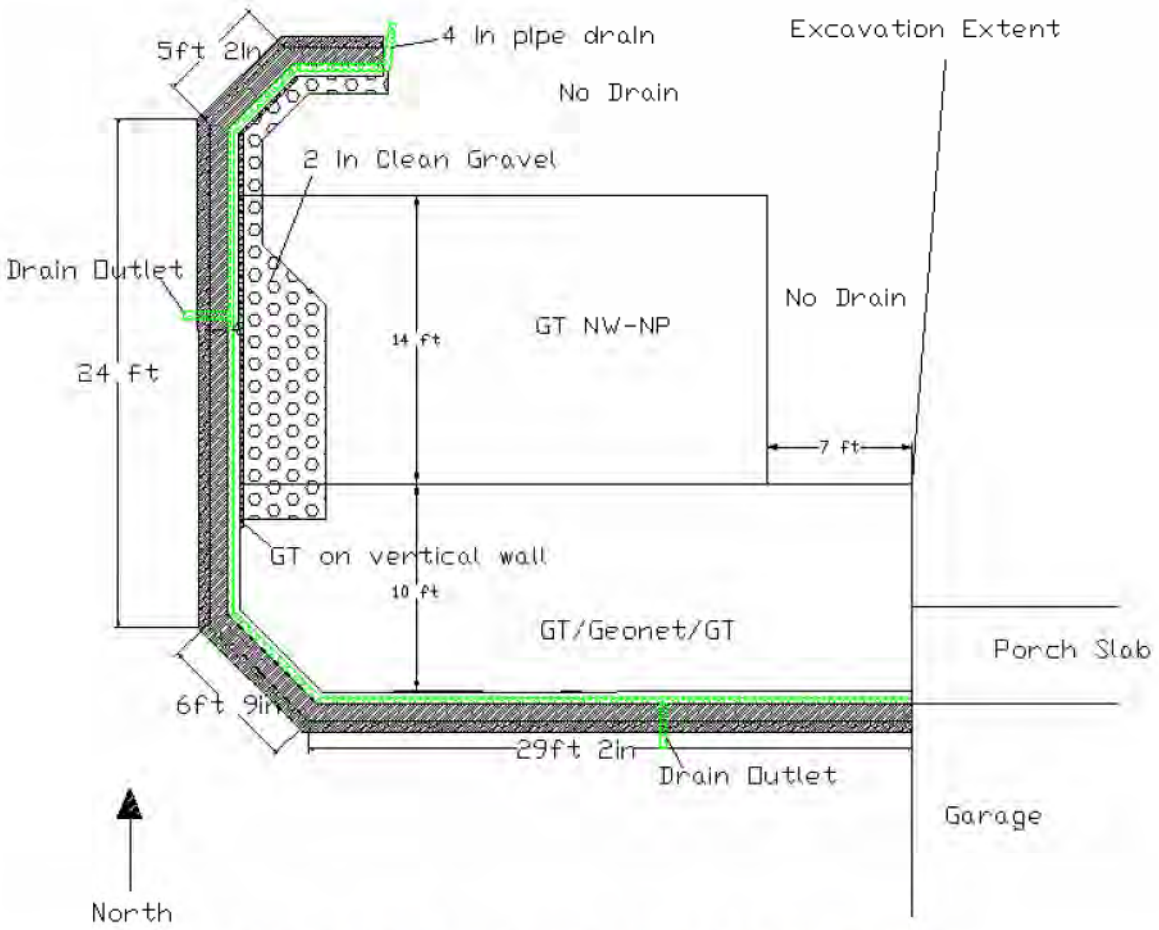

Figure 12 - As-built geotextile wrap-face wall drainage system

Figure 13 - Gap between concrete wall and geotextile wall in lift #9 (July 24, 2006)

Figure 14 – Existing corner crack on concrete wall face with crack gauge (July 24, 2006)

The crack gauge data indicate little movement or crack enlargement in the existing concrete wall has taken place over four months after geotextile wrap-face wall construction. Maximum crack movements of 1 mm have been recorded in the gauges.

CONCLUSIONS

A 9-foot tall geotextile wrap-face wall was constructed using marginal backfill material. The backfill soil classified as a low plasticity clay. An extensive drainage system was installed beneath and around the sides of the backfill. The surface of the backfill was graded to promote surface runoff in a direction away from the wall. Monitoring of lateral and vertical deformations of the wall has shown some movement in the wrap-face owing to tensioning of the geotextile; however, the wall appears to be performing well. Several significant precipitation events have occurred and the drainage system was observed to be performing well. The wall has been in place for approximately four months and performance monitoring will be continued to observe the performance over a full compliment of seasons.

ACKNOWLEDGEMENTS

The authors greatly appreciate the support and assistance of all those who contributed to the success of this project including: Andy Carrigan, Missouri Petroleum; William Hawkins, BBA Nonwovens; Dhani Narejo, Caro Consultants (formerly of GSE); Jeff Bertell, Paul Koenig, Andy Boeckmann, Jianhua Li, Peng Li, Nathan Textor, University of Missouri; Neal Kaplan, North

Carolina; Young Kim, Korea; Brad Parrish, Palmerton and Parrish; and Erin Sutton, Missouri State University.

REFERENCES

AASHTO, (2000), *Standard Specifications for Highway Bridges,* American Association of State Highway and Transportation Officials, Seventeenth Edition, Washington, D.C., USA

Christopher BR and Stulgis RP (2005) "Low Permeable Backfill Soils in Geosynthetic Reinforced Soil Walls: State-of-Practice in North America," *Proceedings* of GRI 19 Las Vegas, NV.

FHWA (1997), *Mechanically Stabilized Earth Walls and Reinforced Slopes Design and Construction Guidelines*, Federal Highway Administration Demonstration Project 82, FHWA-SA-96-071, 371p.

Koerner RM (1998) *Designing with Geosynthetics,* 4th Ed., Prentice Hall, Englewoood Cliffs, NJ, 768pp.

Lawson (2005) "Geosynthetic Reinforced MSE Walls and Slopes with Fine-Grained Fills: International Perspectives," *Proceedings* of GRI 19 Las Vegas, NV.

NCMA (1997) *Design Manual for Segmental Retaining Walls.* 2nd Edition., National Concrete Masonry Association, Herndon, Virginia, 289p.

NCMA (2002) *Segmental Retaining Wall Drainage Manual,* National Concrete Masonry Association, Herndon, Virginia, CD-ROM.

Propex Fabrics (2005) "Product Specification Data: Propex 2044" March 2005.

Sandri D (2005) "Drainage Recommendations For MSE Walls Constructed with Marginal Fills," *Proceedings* of GRI 19 Las Vegas, NV.

CONTACT:

John Bowders
University of Missouri
Professor of Civil Engineering
E2509 Lafferre Hall
Columbia, MO
Phone: 573.882.8351
Email: bowders@missouri.edu

STATE-OF-THE-PRACTICE DESIGN OF SEGMENTAL RETAINING WALLS: NCMA'S THIRD EDITION MANUAL

James G. Collin, PhD, PE, The Collin Group; Mark S. Meyers, PhD, PE, University of Wisconsin-Platteville;Ryan R. Berg, PE, Ryan R. Berg and Associates

ABSTRACT

The National Concrete Masonry Association (NCMA) published the First Edition of the Design Manual for Segmental Retaining Walls (DMSRW) in 1993 to provide a standardized engineering approach for the analysis and design of conventional and reinforced soil segmental retaining walls (SRWs). The Second Edition of the DMSRW was published in 1997 and the companion NCMA Segmental Retaining Wall Drainage Manual was published in 2002; the latter provided general guidelines for incorporating surface and subsurface drainage details and systems into SRW design and construction to minimize the potential for hydrostatic forces to develop and to provide guidance for including hydrostatic forces when drainage alone will not eliminate the potential for water to load the SRW. The Third Edition of the DMSRW, completed in 2007, incorporates significant changes in the state-of-the-practice regarding MSEW and SRW topics. This paper summarizes these changes and discusses the rational for each. This paper will serve as a useful guide for practioners, particularly those designing with the aid of software based upon the earlier Second Edition of the DMSRW. The paper is directed towards designers and specifiers of the materials and methods used for SRWs.

INTRODUCTION

A segmental retaining wall (SRW) is constructed from dry-stacked units (without mortar) that are usually connected through concrete shear keys or mechanical connectors. SRW units may be dry-cast machine produced or wet-cast concrete products. A variety of proprietary SRW units are available from various suppliers. SRWs may be constructed as gravity structures or as geosynthetically reinforced soil segmental retaining walls. Reinforced SRW systems are composite facing-mechanically stabilized earth (MSE) retaining wall structures that have unique features and design requirements.

The Third Edition of the Design Manual for Segmental Retaining Walls (DMSRW) (NCMA 2007) was published by the National Concrete Masonry Association (NCMA) in 2007 to provide a state-of-the-practice engineering approach for the analysis and design of segmental retaining walls (SRWs). The First Edition of the DMSRW was published in 1993 and the Second Edition was published in 1997. In 2002, a companion manual, the Segmental Retaining Wall Drainage Manual (SRWDM), was published. The Third Edition of the DMSRW incorporates the design recommendations of the DMSRW and the design principles for the inclusion of hydrostatic forces and surface and subsurface drainage details and systems presented in the SRWDM into one document.

There are several changes that have been made in the DMSRW with respect to previous editions. These changes include the deletion of the: (i) hinge height concept; (ii) bulging calculation at the face of the wall; and, (iii) serviceability requirements for connection strength between the geosynthetic reinforcement and SRW units. Changes also include: the addition of recommended minimum factors of safety for specific design cases and design soil shear strengths for cohesive (i.e., clayey) soils; enhanced specifications; and recommended reinforced fill and drainage fill gradations for use when water is present in the SRW system. The DMSRW adds an emphasis on the effect of water on wall stability and provides an expanded discussion and design equations for determination of bearing capacity under various groundwater conditions and for sloping toe conditions. This paper summarizes these changes and discusses the rational for each change.

DISCUSSION OF CHANGES TO MANUAL

Deletion of Hinge Height Concept

In the previous editions of the DMSRW, the hinge height concept was implemented in all local facing stability calculations. The hinge height limited the maximum weight applied to any SRW unit interface for calculation of shear capacity and facing connection strength based on the geometry of the system and shape of the SRW unit.

Research over the last decade has demonstrated that the concept of hinge height does not realistically predict the vertical load on an SRW unit within a wall. Friction that develops between the reinforced soil and SRW unit effectively transfers vertical load to the SRW units equivalent to the height of the wall above the unit regardless of hinge height.

Deletion of Bulging Calculations at the Wall Face

Bulging of a SRW in the vertical plane occurs when a SRW unit does not maintain its relative position with respect to the SRW units above and below it. The relative position of one course to the next is maintained by shear resistance. Therefore, for reinforced soil SRWs, all units must possess sufficient shear capacity to resist the theoretical horizontal earth pressure being applied between layers of geosynthetic reinforcement. Consequently, resistance to bulging is controlled by: the magnitude of applied pressure; the vertical spacing of geosynthetic reinforcement; and, the shear capacity between SRW units.

In previous editions of the DMSRW, the shear force applied to the SRW units was thought to vary with location along the height of the wall. For analysis of bulging, the dry-stacked SRW units were modeled as a continuous beam subjected to a continuous distributed load (i.e., earth pressure) using a simplified equivalent beam method as proposed for flexible tied-back steel sheet pile retaining walls.

The bulging calculation presented in the previous editions of the manual does not model the failure mechanism associated with bulging of the SRW. The Third Edition of the manual has replaced the previous bulging calculation with the more rigorous compound stability analysis, which models the actual failure mechanism when bulging occurs.

Deletion of Serviceability Requirements for Connection Strength

The facing between the geosynthetic reinforcement and SRW unit at each reinforcement placement elevation must have sufficient connection strength to preclude rupture or slippage of the reinforcement due to the applied tensile force. In previous editions of the DMSRWs, there were two criteria to be addressed when designing the connection of a geosynthetic reinforced SRW: (i) the limit state strength of the connection at failure; and (ii) a serviceability state, which is the strength of the connection at a specified deformation. The recommended maximum allowable movement of the connections to minimize wall face deformation was 3/4 inch, based on the successful construction of hundreds of SRWs with the connection design considering 3/4 inch deformation.

The serviceability requirements for connection strength have been eliminated in the Third Edition of the DMSRW. When following the construction guidelines provided in this manual, the connection between the SRW unit and geosynthetic reinforcement is pre-stressed. This pre-stressing eliminates the serviceability issue for currently available combinations of SRW units and geosynthetic reinforcements. If, in the future, more flexible reinforcements are used to build SRWs, the serviceability requirement provided in the Second Edition of the DMSRW may be appropriate.

Hydrostatic Loads

Previous editions of the DMSRW included limited discussion of the impact of groundwater on the design of an SRW system and design and analysis methods were not presented for cases where groundwater was present. The stability calculations presented in the Third Edition of the DMSRW cover a range of groundwater table locations and the methodology for incorporating the hydrostatic forces from these water levels into the design of the SRW.

In many cases, the groundwater table is located well below the base of the wall (i.e., greater than $\mathbf{0.66}\boldsymbol{H}$ where $\boldsymbol{H}$ is the height of the wall). For this case, all stresses are computed as total stresses and do not have to be modified for the influence of porewater pressure. In addition, the destabilizing effect of hydrostatic pressures or seepage forces is not a concern when the groundwater table is at this depth.

There are also many cases when surface and internal drainage can not effectively remove the groundwater from an SRW system. The design of the SRW in these cases must consider the destabilizing affects of the hydrostatic pressure from the water. Figure 1 illustrates the conditions where water pressure affects the design of an SRW. There are three different water levels that should be considered in the design. For external stability calculations the height of the groundwater is defined as H_{we}. For internal stability, the height of the groundwater within the reinforced soil mass is defined as H_{wi}. For facing stability, the height of the groundwater table within the drainage aggregate is defined as H_{wd}.

Failure Modes

The external, internal, and local stability failure modes presented in the previous editions of the DMSRW remain unchanged with the exceptions that the hinge height concept, the bulging

calculation, and the serviceability requirements for connection strength have been eliminated in the Third Edition of the DMSRW. The Third Edition of the manual adds particular emphasis on the design cases to be analyzed for each failure mode, the shear strengths to be used for each design case, and a more rigorous table of minimum required factors of safety.

External stability analyses include base sliding, overturning, bearing capacity, and global stability (Figure 2). These analyses determine the minimum length of geosynthetic reinforcement. The Third Edition of the DMSRW addresses the impact of the groundwater level with respect to the elevation of the leveling pad on the bearing capacity of the SRW system. An additional bearing capacity analysis improvement is a discussion of the impact of a sloping toe in front of the SRW on the bearing capacity of the SRW system. The Third Edition of the DMSRW places particular emphasis on the use of the global stability analysis when weak soils are present as retained fill and/or as foundation soils.

Internal stability analyses include tensile overstress, pullout, internal sliding, and compound stability (Figure 2). The internal stability analyses determine the minimum strength, minimum number, and required vertical spacing of reinforcement layers. The Third Edition of the DMSRW places particular emphasis on the use of the compound stability analysis to improve the efficiency of the internal stability design.

Local stability analyses include facing connection and maximum unreinforced height (Figure 2). The unique dry-stacked construction method using SRW units and the connection of the SRW units to the geosynthetic reinforcement layers requires that these local stability analyses be carried out to ensure the column of SRW units remains intact.

Global/overall slope stability failure is a mass movement of the entire reinforced soil SRW structure including the soil adjacent to the structure (Figure 2). Generally, the reinforced soil SRW is assumed to act as a coherent structure in the overall rotating mass (Figure 2). The Third Edition of the DMSRW recommends that the responsibility for ensuring adequate global/overall slope stability shall be coordinated between the retaining wall designer, project civil engineer, and project geotechnical engineer.

Compound stability is similar to global stability except the failure surfaces pass through both the unreinforced and reinforced zones (Figure 2). For simple structures with rectangular geometry relatively uniform reinforcement spacing, and a near vertical face, compound failure surfaces passing through both the unreinforced and reinforced zones will not generally be critical. However, if complex conditions exist, such as changes in reinforcement soil types or reinforcement lengths, high surcharge loads, sloping faced structures, significant slopes at the toe or above the wall, or stacked structures, compound failures must be considered and analyzed. The Third Edition of the DMSRW recommends that the responsibility for ensuring adequate compound stability rests with the retaining wall designer.

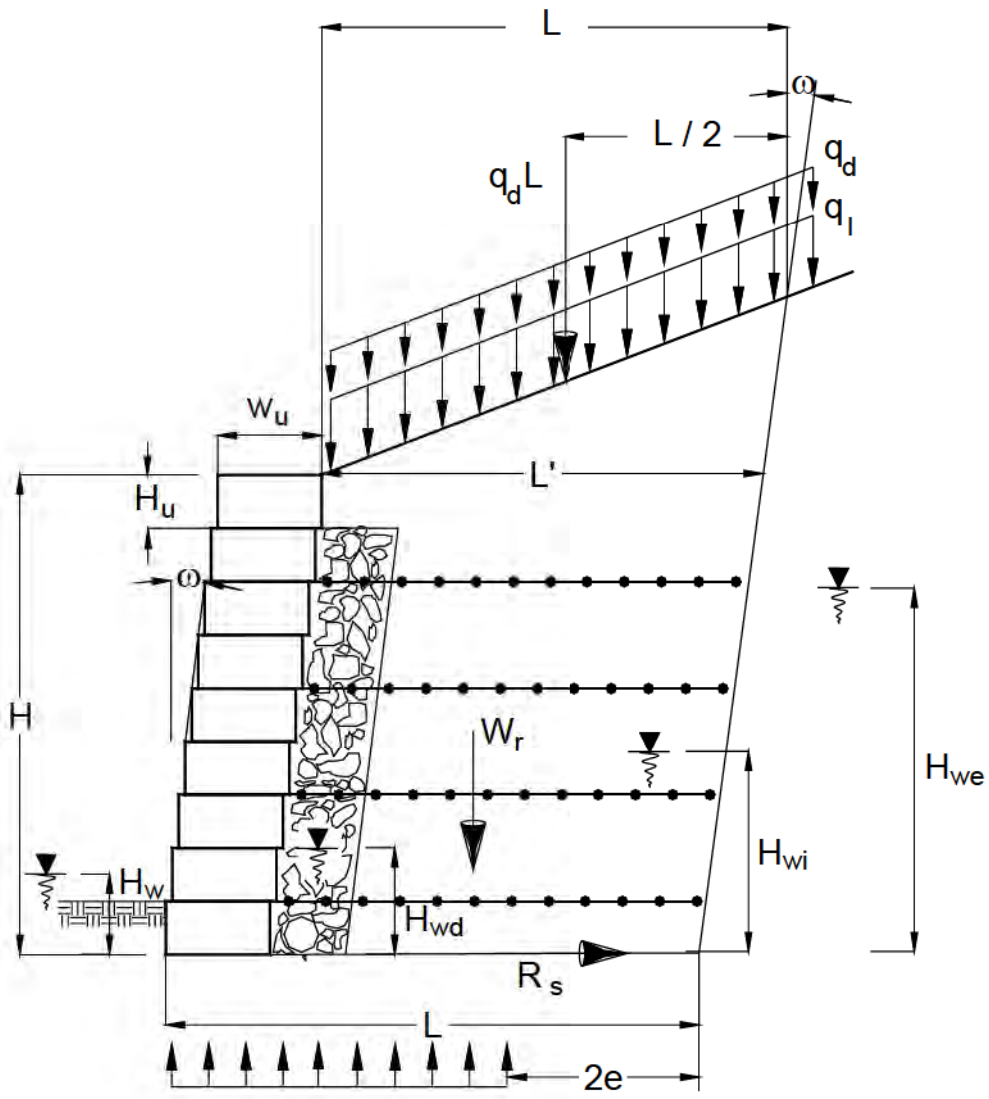

Figure 1. Definition of height of groundwater

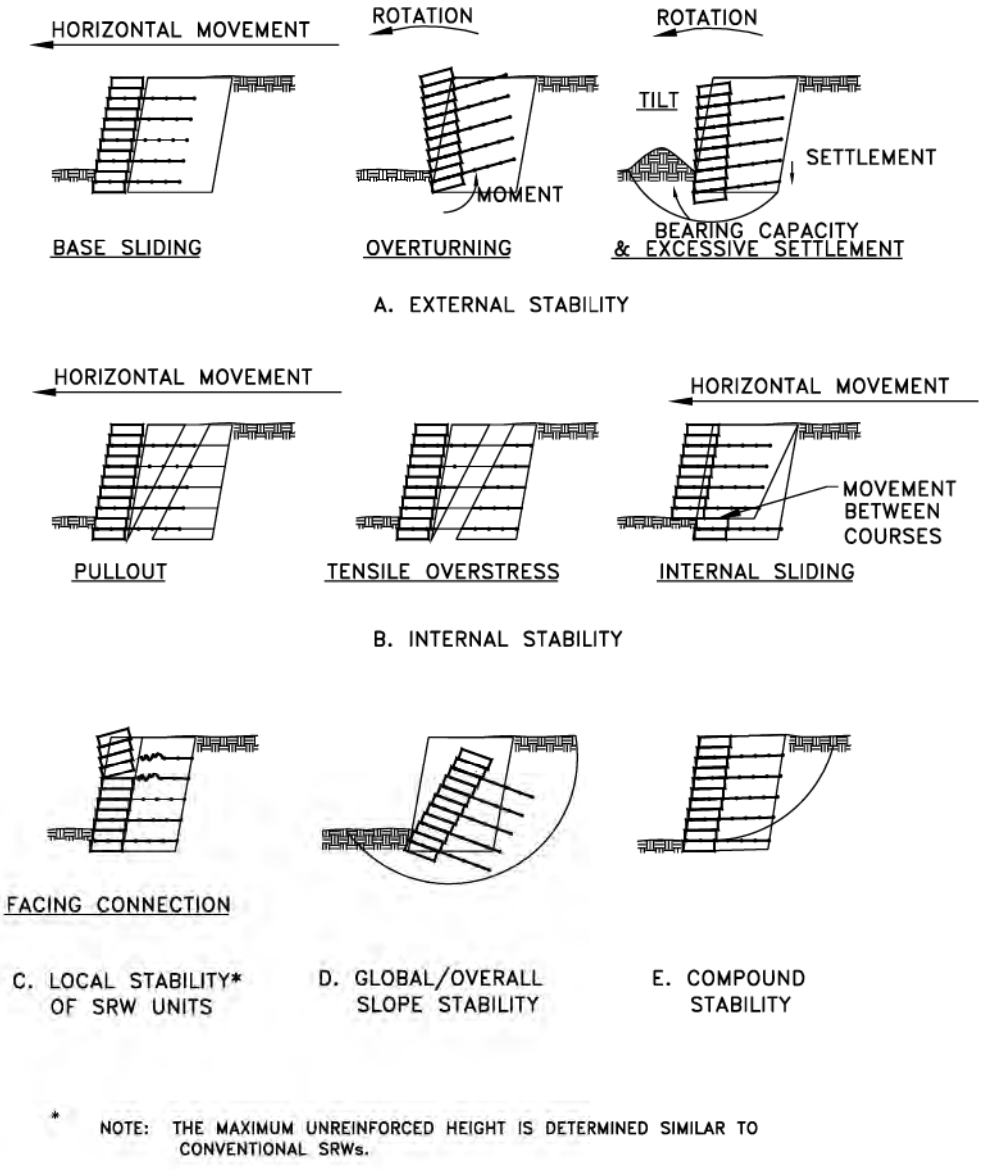

Figure 2. Failure modes for reinforced soil SRWs

Soil Properties

The previous editions of the DMSRW discuss the principal soil components associated with the analysis and design of SRW systems, indicating that representative soil properties must be assigned to each zone (i.e., reinforced (infill) soil, retained soil, foundation soils, gravel fill and aggregate leveling pad). Each soil zone material must be characterized by a peak friction angle (ϕ), cohesion term (c) and representative bulk unit weight defined as the moist unit weight per unit volume of sample (γ). However, the cohesion term for all representative soils with the exception of the foundation soils is ignored for design. This assumption simplifies calculations

and generally results in conservative designs. The Third Edition of the DMSRW greatly expands and enhances this discussion to include drained and undrained shear strengths and the specific shear strengths required to be used for specific design cases, specifically when clay soils are encountered at the site.

In particular, there may be SRW project sites where the water is present within a depth of 0.66H of the height of the wall below the leveling pad or the water table rises to, or is present above, the leveling pad on either a temporary or permanent basis. Under these conditions, the wall designer must design for cases where the soil conditions are either drained or undrained. This is especially important when saturated clay foundation soils, reinforced fills, or retained fills comprise the site soils (although the use of clay soils for reinforced fill is highly discouraged, especially if water is present). Under the appropriate conditions, the drained or undrained strength of the soil must be used to analyze sliding, bearing capacity, global stability, and compound stability.

Drained strength of the soil is the strength of the soil that results when the soil is loaded at a slow enough rate that pore pressures, induced by an applied load, are able to dissipate or drain. Pore pressures dissipate very quickly in free draining materials and very slowly in clay soils or other soils that are not free draining (P_{200} > 5 percent).

Undrained strength of the soil is the strength of the soil that occurs when the soil is loaded at a rate faster than the rate required to attain drained conditions and drained shear strength. Such conditions are referred to as undrained conditions. Undrained conditions are not encountered in free draining soils because pore pressures dissipate or drain immediately as a load is applied. In soils that are not free draining, the pore pressures cannot dissipate or drain at a rate fast enough to attain a drained condition.

There are three different shear strengths for saturated clay soils:

- Consolidated Drained shear strength (CD shear strength)
- Consolidated Undrained shear strength (CU shear strength)
- Unconsolidated Undrained shear strength (UU shear strength)

The *CD strength* of a saturated clay soil is obtained from a CD triaxial shear strength test in which the soil sample is consolidated under a confining pressure surrounding the soil that is similar in magnitude to that which the soil is expected to be subjected to in-situ. After the pore pressures in the soil generated by the applied confining pressure have dissipated, the soil sample is considered to be consolidated. The sample is then loaded axially, at a rate which allows the pore pressures generated by the applied axial load sufficient time to dissipate or drain, until the sample fails. As such, the CD test sample is consolidated prior to loading and sheared under drained conditions.

The *CU strength* of a saturated clay soil is obtained from a CU triaxial shear test in which the soil sample is first consolidated in the same manner as for the CD test. The sample is loaded axially to failure without allowing the pore pressures generated by the applied axial load to dissipate or drain. As such, the CU test sample is consolidated prior to loading and sheared under undrained conditions. The CU test may also be used to determine the CD strength of the

clay. Pore pressure measurements during the test are required in order to determine the drained shear strength.

The *UU strength* of a saturated clay soil is obtained from a UU triaxial shear test or from an unconfined compression test. In a UU test, a confining pressure is applied to the soil sample, as with a CD and CU test, but the pore pressures generated by the confining pressure are not allowed to dissipate or drain. The sample is immediately loaded axially to failure without allowing the pore pressures generated by the applied axial load to dissipate or drain, as for the CU test. As such, the UU test sample is unconsolidated prior to loading and sheared under undrained conditions. The unconfined compression test is a simple form of the UU test where the confining pressure is not applied to the sample and the sample is loaded axially as for the CU and UU tests.

Design Cases for the Failure Modes

Generally, total stress parameters are appropriate for the design of conventional gravity and reinforced SRW structures provided that porewater pressures are not present. However, when the groundwater table is within or in close proximity to the SRW system, effective stress parameters and effective shear strengths may be appropriate. Furthermore, three distinct design cases must be analyzed when saturated clays are present and specific shear strengths must be used for these design cases:

- End of Construction Case (EOC Case)
- Long Term Steady Seepage Case (LTSS Case)
- Rapid or Sudden Drawdown Case (RDD Case)

End of Construction Case. The EOC case represents undrained conditions in clay soils. Excess pore water pressure is present because the soil has not had time to drain since being loaded. Total stresses with UU soil shear strengths are used, along with the assumption that the soil has a friction angle equal to zero. An example of when this case would result is immediately after the construction of a SRW on a clay foundation soil. The SRW should be analyzed for the EOC case when analyzing sliding, bearing capacity, global stability, and compound stability.

Long Term Steady Seepage Case. The LTSS case results when a long time has passed since a SRW was constructed on a clay foundation or after a steady water level behind or in front of the a SRW has been maintained for a long time. Over this time period, the pore pressures generated in the clay foundation soil by constructing the SRW will have dissipated or drained, resulting in drained conditions. As such, effective stresses and CD shear strengths are used for this case. The SRW should be analyzed for the LTSS case when analyzing sliding, bearing capacity, global stability, and compound stability.

Rapid Drawdown Case. The RDD case is caused by the lowering of a water level adjacent to a SRW at a rate that is faster than the time required for the soil to drain significantly. The rapid or sudden drawdown is assumed to occur instantaneously for this design case, regardless of the actual rate of the lowering of the water level. As the water level drops, the stabilizing effect of the water is removed, increasing the shear stress acting on the soil, while the shear stresses are

being resisted by the undrained strengths of the soil (Duncan and Wright, 2005). For example, the water level in a storm water pond in front of a SRW may drop suddenly.

Alternatively, the water level in the pond may rise due to a significant runoff event and remain at a higher constant level for a length of time during which pore pressures dissipate or drain, followed by a rapid lowering of the new pond level to the normal water level in the pond. If the rapid drawdown occurs during or immediately after construction, total stresses and the undrained strengths used in the RDD analysis are the same as the undrained strengths used for the EOC case (UU strengths with a friction angle equal to zero). If the rapid drawdown occurs after the LTSS conditions develop, total stresses and the CU undrained shear strengths are used in the RDD analysis (Duncan and Wright 2005).

Minimum Required Factors of Safety

Selection of appropriate factors of safety should be based on the certainty with which design parameters and the consequences of failure are known. The Third Edition of the DMSRW includes a table, included herein as Table 1, with recommended minimum factors of safety for the external stability failure modes for reinforced SRWs (base sliding; overturning or eccentricity; bearing capacity; global stability; and, compound stability) based on several cases for each failure mode and the soil shear strength required to be used to analyze the failure mode for that case. Included in these recommended minimums are typical levels of uncertainty in wall geometry and imposed loadings; a separate portion of Table 1 addresses factors of safety with respect to the uncertainty of the accuracy of the design soil parameters.

Table 1: Recommended Minimum Factors of Safety: External Stability

Failure Mode		Shear Strength: All Soils	Minimum FS		
Base Sliding			Confidence		
			High	Med	Low
Case I	LTSS	CD	1.5	1.6	1.7
Case II	RDD	CU	1.0	1.1	1.2
Case III	EOC	UU	1.2	1.3	1.4
Overturning					
Case I	LTSS	CD	e/L < .167		
Case II	RDD	CU	e/L < .167		

Case III	EOC	UU	e/L < .167		
Bearing Capacity					
Case I	LTSS	CD	2.0	2.5	3.0
Case II	RDD	CU	1.6	2.1	2.3
Case III	EOC	UU	1.8	2.3	2.5
Global Stability					
Case I	LTSS	CD	1.3	1.4	1.5
Case II	RDD	CU	1.1	1.2	1.3
Case III	EOC	UU	1.2	1.3	1.4
Compound Stability					
Case I	LTSS	CD	1.3	1.4	1.5
Case II	RDD	CU	1.1	1.2	1.3
Case III	EOC	UU	1.2	1.3	1.4

Bearing Capacity Analysis

The bearing capacity discussion is modified in the Third Edition of the DMSRW to include bearing capacity analyses when a ground slope exists in front of the wall and when the groundwater table is at an elevation between the bottom of the footing and a depth equal to 0.66H below the bottom of the footing. The ultimate bearing capacity $\boldsymbol{Q_{ult}}$ is determined using Equation (1):

$$Q_{ult} = c_f\,N_c + 0.5\gamma_f\,B\,N_\gamma + \gamma_f\,H_{emb}\,N_q \;\ldots\ldots\ldots\ldots\ldots\ldots\ldots\ldots\ldots\ldots (1)$$

Bearing Capacity for Walls on Slopes

For walls on slopes additional bearing capacity factors for sloping ground in front of the wall, denoted g_c, g_q, and g_γ, are included in the bearing capacity equation (Bowles, 1982). Equation (1) is modified to the following form (Equation (2)):

$$Q_{ult} = c_f\,N_c g_c + 0.5\gamma_f\,B'_f\,N_\gamma g_q + \gamma_f\,H_{emb}\,N_{q\gamma} g_\gamma \;\ldots\ldots\ldots\ldots\ldots\ldots\ldots\ldots (2)$$

where: $g_c = 1 - \psi / 147^\circ$
$g_q = g_\gamma = (1 - 0.5 \tan \psi^\circ)^5$

For the EOC design case when the foundation soil is clay, $\varphi = 0$, Equation (1) is modified to the following form (Equation (3)):

$$Q_{ult} = 5.14\,s_u\,(1 - g_c') + q \ldots\ldots\ldots\ldots\ldots\ldots\ldots\ldots\ldots\ldots\ldots\ldots\ldots (3)$$

where: $g_c' = \psi / 147^\circ$, using $g_c' = 0.0$ for horizontal ground in front of the wall

Groundwater Effects on Bearing Capacity

A groundwater table beneath a SRW can decrease the bearing capacity of the foundation soil. Three possible groundwater conditions are possible. Ultimate bearing capacity varies for these three cases as discussed below.

Case 1: Groundwater table remains at a distance 0.66H below the base of the leveling pad elevation for the design life of the structure. Ultimate bearing capacity (Q_{ult}) when the groundwater is well below the leveling pad (e.g., greater than 0.66H below the toe of the wall) is determined using Equation (4):

$$Q_{ult} = c_f N_c + 0.5\,\gamma_f\, B'_f N_\gamma + \gamma_f H_{emb} N_q \quad \text{.....(4)}$$

where B'_f is the equivalent footing width due to eccentric footing loads and is calculated as $B'_f = B_f - 2e$ and γ_f = total unit weight of the foundation soil.

Case 2: Groundwater table rises to or remains just below the leveling pad elevation during the design life of the structure. Ultimate bearing capacity (Q_{ult}) when the groundwater table rises to or remains just below the leveling pad elevation during the design life of the structure is determined using Equation (5):

$$Q_{ult} = c_f N_c + 0.5\,\gamma_{f1}\, B'_f N_\gamma + \gamma_{f2} H_{emb} N_q \quad \text{.....(5)}$$

where:

γ_{f1} = buoyant or effective unit weight of soil

$\gamma_{f1} = \gamma_{sat} - \gamma_{water}$

γ_{sat} = saturated unit weight of soil

γ_{water} = unit weight of water

$\gamma_{f2} = \gamma_t$ = total unit weight of soil

If the groundwater is stable at an elevation between the leveling pad and a depth of 0.66H, an average unit weight should be used for γ_{f2}. This is a fourth case condition. Note that the cohesion (c_f) of the foundation soil may change as the groundwater table rises. Ground slope factors should be added to the appropriate bearing capacity terms.

Case 3: Permanent or intermittent groundwater is present in the retained soils above the leveling pad elevation. Ultimate bearing capacity (Q_{ult}) when permanent or intermittent groundwater is present in the retained soils above the leveling pad elevation is determined using Equation (6):

$$Q_{ult} = c_f N_c + 0.5\,\gamma_{f1}\, B'_f N_\gamma + \gamma_{f2} H_{emb} N_q \quad \text{.....(6)}$$

If the groundwater level is at the finished grade at the toe of the wall, both $\gamma f1$ and $\gamma f2$ are equal to γ. Note that the cohesion (cf) of the foundation soil may change as the groundwater table rises. Ground slope factors should be added to the appropriate bearing capacity terms.

REINFORCED FILL GRADATION RECOMMENDATIONS

The Third Edition of the DMSRW includes a recommended gradation for reinforced fill; this gradation is presented in Table 2. The reinforced backfill shall be free of debris and consist of

one of the following inorganic USCS soil types: GP, GW, GM, SW, SP, SM, meeting the following gradation as determined in accordance with ASTM D 422.

Table 2. Recommended Reinforced Fill Gradation

Sieve Size	Percent Passing
1 inch	100 - 75
No. 4	100 - 20
No. 40	0 - 60
No. 200	0 - 35

Special emphasis is place on the following qualifier statements:

- Cohesionless free-draining materials, which are materials having less than 5 percent passing the No. 200 sieve, are preferred, especially when the groundwater level is above the top of the leveling pad, unless proper internal drainage is installed behind and under the reinforced fill zone.
- Soils with low-plasticity (i.e., LL < 40, PI < 20) fines may be used provided the following four additional design criteria are implemented:
  - Proper internal drainage is installed.
  - Only soils with low to moderate frost heave potential are utilized.
  - The internal cohesive shear strength parameter c is conservatively ignored for stability analysis.
  - The final design is checked by a qualified geotechnical engineer to ensure that the use of cohesive soils does not result in unacceptable time-dependent movement of the SRW system.
- The maximum size should be limited to 1 inch for reinforced soil SRWs unless tests have been performed to evaluate potential strength reduction in the geosynthetic due to installation damage.
- The pH of the backfill material shall be between 3 and 9 when tested in accordance with ASTM G-51.

GRAVEL FILL GRADATIONS RECOMMENDATIONS

The Third Edition of the DMSRW includes a recommended gradation for reinforced fill; this gradation is presented in Table 3. Gravel fill shall be a clean crushed stone or granular fill meeting the following gradation as determined in accordance with ASTM D 422:

Table 3. Recommended Gravel Fill Gradation

Sieve Size	Percent Passing
1 inch	100
$^3/_4$ inch	75 - 100
No. 4	0 - 60
No. 40	0 - 50
No. 200	0 - 5

SURFACE AND SUBSURFACE WATER DRAINAGE DETAILS

The current version of the DMSRW incorporates the extensive drainage details provided in *Segmental Retaining Wall Drainage Manual*. This includes recommendations for drainage features when water is anticipated during the life of the structure.

RELATIONSHIP OF MANUAL CHANGES TO SRWALL SOFTWARE

The changes made to the previous versions of the DMSRW have not been incorporated into the current version of the SRWall software. The users of the SRWall software need to utilize manual computations in conjunction with the results obtained from SRWall to determine appropriate factors of safety. For example, the driving forces due to hydrostatic loads resulting from water in the retained fill need to be determined manually and added to the driving forces reported by SRWall for base sliding in order to determine an accurate factor of safety against base sliding that considers the impact of the hydrostatic loads.

COMPARISON TO AASHTO SRW DESIGN GUIDANCE

The changes made to the previous versions of the DMSRW should not impact the economics of the SRW systems used in private and commercial applications. There may be some concerns that the DMSRW is now more aligned with AASHTO (2002); the authors do not see that as a concern. The following paragraphs address the major comparisons between the NCMA and AASHTO (2002) for SRW design.

Minimum Reinforcement Length

The NCMA DMSRW requires a minimum required reinforcement length of 0.6L. AASHTO (2002) requires a minimum reinforcement length of 0.7L. Additionally, the definition of L varies between the two guides. The reinforcement length, L, includes the width of the SRW unit in NCMA DMSRW. AASHTO (2002) states that the reinforcement length, L, starts at the back face of the SRW unit. The DMSRW and AASHTO (2002) both require that all minimum external stability FS values be satisfied even if the reinforcement length is greater than 0.6L and 0.7L, respectively.

Uniform Reinforcement Length

The NCMA DMSRW allows for the use of non-uniform reinforcement lengths; the reinforcement length can vary along the height of the SRW. AASHTO (2002) generally (i.e., for non geometrically complex walls) requires the use of uniform reinforcement length along the height of the SRW.

Reinforced Fill Gradation

The NCMA DMSRW allows up to 35 percent of the reinforced fill to pass the No. 200 sieve; AASHTO (2002) allows only up to 15 percent of the reinforced fill to pass the No. 200 sieve. However, when water is present in the reinforced fill, the DMSRW suggests a maximum of 5 percent of the reinforced fill passing the No. 200 sieve.

Minimum Embedment Length of the Reinforcement

The NCMA DMSRW requires a minimum embedment length of 1 foot beyond the theoretical internal stability failure plane. AASHTO (2002) requires a minimum embedment length of 3 feet beyond the assumed internal stability failure plane. The DMSRW and AASHTO (2002) both require that all minimum internal stability FS values be satisfied even if the reinforcement length is greater than 1 foot or 3 feet, respectively.

SUMMARY AND CLOSURE

The third edition of the DMSRW combines the guidelines developed in the second edition of the DMSRW with the *Segmental Retaining Wall Drainage Manual* to create one comprehensive document for the static design of SRWs for conditions when either water is or is not present that is current with our state of knowledge of SRW design. As with any new technology, our knowledge increases with time and modification to the design is a natural outcome of the maturing of the technology. The changes that have been incorporated into the third edition of the DMSRW reflect the maturing of this technology.

REFERENCES

AASHTO (2002), *Standard Specifications for Highway Bridges, 17th Edition*, Washington, D.C
.

Bowles, Joseph E., (1983), *Foundation Analysis and Design, 3rd Edition*, McGraw-Hill Book Company.

Collin, J.G., Berg, R.R., and Meyers, M. (200x), *Design Manual for Segmental Retaining Walls*, Third Edition, National Concrete Masonry Association, Herndon, VA, (pending).

Collin, J.G. (1997) ed., *Design Manual for Segmental Retaining Walls*, Second Edition, National Concrete Masonry Association, Herndon, VA.

Collin, J.G., Berg, R.R., and Meyers, M. (2002), *Segmental Retaining Wall Drainage Manual,* National Concrete Masonry Association, Herndon, VA.

Duncan, J.M. and Wright, S.G. (2005), *Soil Strength and Slope Stability*, John Wiley & Sons, Inc.

NCMA (2002), Design Software for Segmental Retaining Walls, Version 3.22, Herndon, VA.

ACKNOWLEDGEMENTS

The authors would like to acknowledge the National Concrete Masonry Association for giving us the freedom to present the significant changes to the Design Manual for Segmental Retaining Walls at Geosynthetics 2007. We would also like to acknowledge the authors of the first edition of the design manual, Michael Simac, Richard Bathurst, Ryan Berg, and Steven Lothspeich and final the NCMA SRW Manual Task Group Members (Donal Armstrong, Mike Bernardi, Richard Bodie, Tim Bott, Robert Bowers, Michael Carroll, Lance Carter, Michael Dolby, Jan Jansson, Bruce Lacina, Steven Lothspeich, Keith Miller, Karen Nelson, Rodger Prunty, Cameron Roberson, Dean Sandri, Stephen Valero, Scott Vollmer, and Tom Zeisler) for providing guidance during the development of the third edition of the manual.

CONTACT:

Jim Collin
Consultant
The Collin Group, Ltd.
7445 Arlington Road
Bethesda, MD, 20814
Phone: 301-907-9501
Email: jim@thecollingroup.com

ENGINEERING PROPERTY EVALUATION OF GEOGRIDS IN REINFORCEMENT SYSTEM

Han-Yong Jeon, Division of Nano-Systems Engineering, INHA University

ABSTRACT

New improved bidirectional geogrids were made for the purpose of pavement reinforcement application. The main engineering properties of these bidirectional geogrids were tested and evaluated in accordance with the draft of GCI-PCP (Geosynthetic Certification Institute's - Product Certification Program) that assessed the manufacturing and quality systems of products evaluates manufactured products. Besides this, installation damage and creep behaviors were reviewed to confirm for the extension of application end-uses.

INTRODUCTION

New concept bidirectional geogrids were manufactured through combination of arrangement and coating of high tenacity polyester yarns. These new concept bidirectional geogrids have advantages of textile and membrane type geogrids for evaluation of application fields and long-term design allowable tensile strength from mechanical properties. For retaining wall and slope construction method, experimental construction and measurement were discussed and reanalyzed. We evaluated and verified more systematically the properties and applications and construction stability of these bidirectional geogrids. Firstly, requiring engineering properties and performance of bidirectional geogrids, we selected the most suitable industrial yarn and developed newly coating condition, especially, manufactured excellent engineering properties of bidirectional geogrids with continuous manufacturing process system. Secondly, direct shear test and pull-out test are adopted to estimate frictional behavior and long-term design allowable tensile strength of these bidirectional geogrids is estimated. Also, we examined installation damage and creep behaviors to review the extension of application end-uses. All the test methods of this study were done to certify with GCI-PCP of GSI and adopted the draft for bidirectional geogrids written by GSI (Geosynthetic Institute, Folsom, PA, USA).

Table 1. Standard specification for bidirectional geogrids in reinforcement applications (e.g., Pavements, Foundations, Bases)

Property	Test Method (ASTM or GRI)	Units	Class 3		Class 2		Class 1		Test Frequency
			MD	XMD	MD	XMD	MD	XMD	
Tensile Strength @ 1%	D6637	kN/m	2.5	4.5	3.5	4.0	4.0	5.0	MARV
Tensile Strength @ 2%	D6637	kN/m	4.0	6.5	5.0	7.5	8.0	9.0	MARV
Tensile Strength @ 5%	D6637	kN/m	8.0	13.0	10.0	16.0	17.0	19.0	MARV
Ultimate Tensile Strength	D6637	kN/m	11.0	17.0	16.0	26.0	25.0	29.0	MARV

Pullout Interaction Coef.	D6706	n/a	0.8	0.8	0.8	0.8	0.8	0.8	yearly
Direct Shear Friction	D5321	deg	30	30	30	30	30	30	yearly
Aperture Size	-	Mm	15-75	15-75	15-75	15-75	15-75	15-75	yearly
Torsional Rigidity	GG9	mm-kg/deg	15		30		60		yearly
Ultraviolet Stability	D4355	%ret. @500 hr	70	70	70	70	70	70	yearly

Notes:

Class Categories are approximately equivalent to that described in AASHTO M288 and more fully in GRI-GT13

MD – machine, or roll, direction

XMD – cross machine, or cross roll, direction

n/a – not applicable, i.e, dimensionless

2. EXPERIMENTAL

2.1 Sample Preparation

Table 2 shows the specifications of new concept bidirectional geogrids with manufacturing process. These bidirectional geogrids A and B were specially designed and manufactured to develop the junction and creep properties and to compensate for the disadvantages of textile and membrane drawn type geogrids. Also, these bidirectional geogrids, A and B are made of fiber-reinforced polymer strips on weaving technology and welded junctions. Firstly, high tenacity polyester filament yarns were supplied with the optimum numbers of reeling and then woven by specially designed technology. The schematic diagram and manufacturing process of these bidirectional geogrids was shown in Figure 1 and 2.

Table 2. Specifications of bidirectional geogrids

Bidirectional Geogrid	Manufacturing Process	Material	Aperture Size (mm)		Width (m)	Length (m)	Weight (g/m^2)
			MD	CD			
A	Welding	PET/PP	40	40	1.5	50	353.5
B	Welding	PET/PP	40	40	1.5	50	310.5

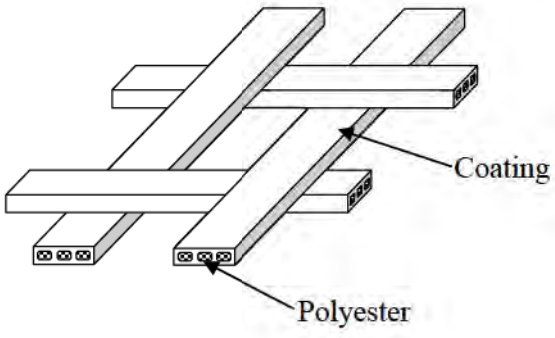

Figure 1. Schematic diagram of new concept bidirectional geogrid

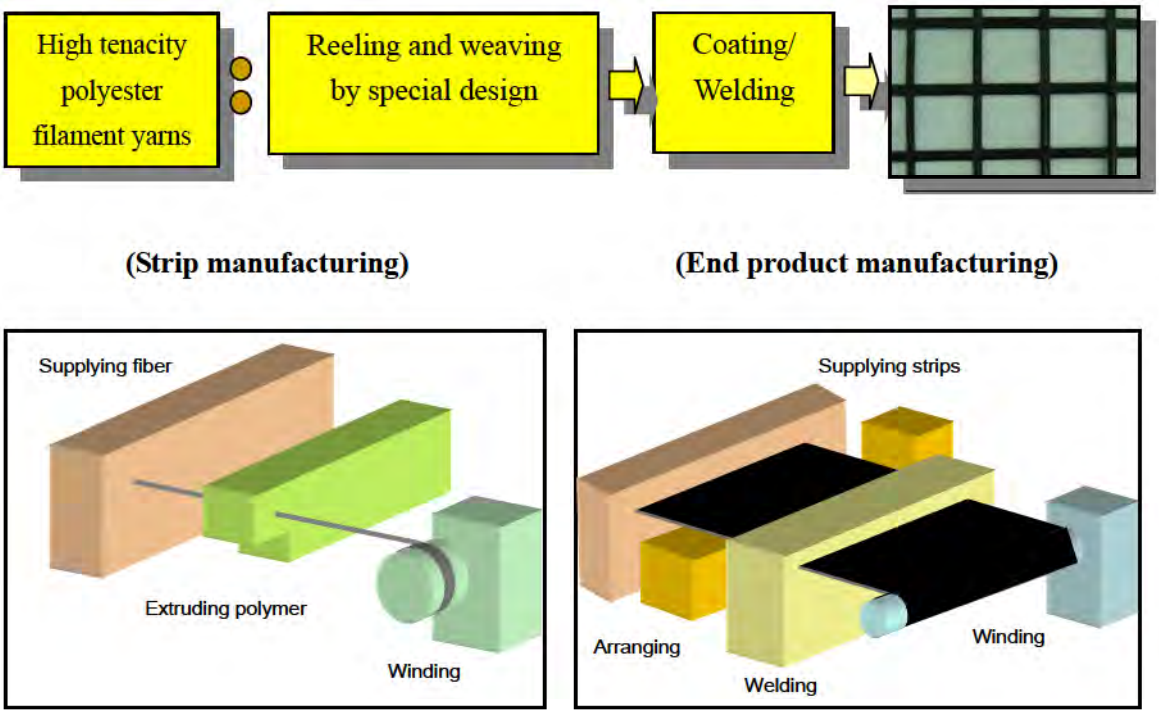

Figure 2. Manufacturing schematic diagram of bidirectional geogrids

3. RESULTS OF TESTING

3.1 Tensile Properties

The test was performed in general accordance with the ASTM D 6637-01: Standard Test Method for Determining Tensile Properties of Geogrids by the Single or Multi-Rib Tensile Method - Method B - Testing multiple geogrid ribs in tension on bidirectional geogrid A and B. The tensile test conducted with the number of ribs which constructed 200mm width and then converted to tensile strength per unit meter. Figure 3 and 4 show the tensile strength vs elongation curves of bidirectional geogrids A and B. From this, it is seen that these two bidirectional geogrids have the similar tensile properties in both MD and CMD. It is expected that this behavior is very useful for the application to the pavement related fields.

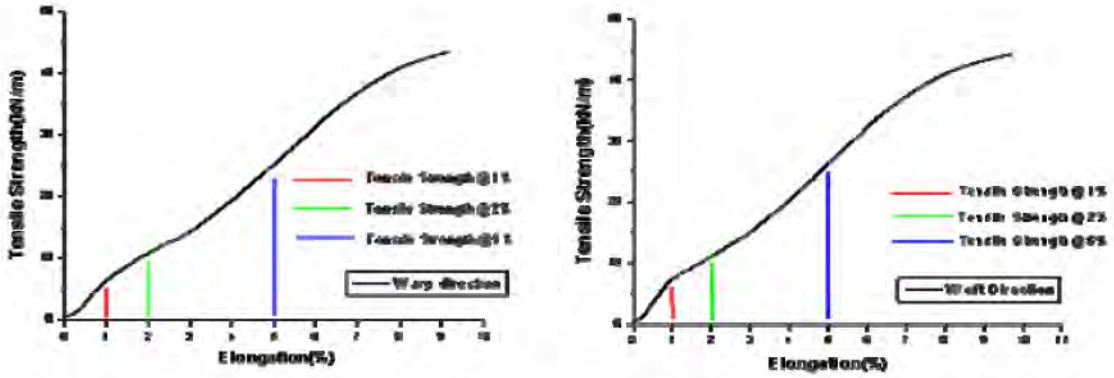

(a) MD (b) CMD

Figure 3. Tensile strength vs elongation curves of bidirectional geogrid A

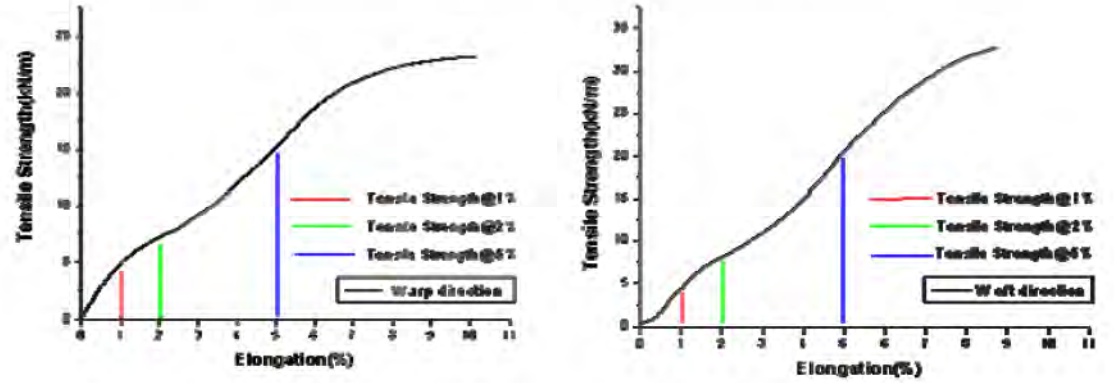

(a) MD (b) CMD

Figure 4. Tensile strength vs elongation curves of bidirectional geogrid B

3.2 Pull-out Interaction Coefficient

The test was performed in general accordance with the ASTM D 6706-01: Standard Test Method for Measuring Geosynthetic Pullout Resistance in Soil on bidirectional geogrid A and B. TRI/Environmental, Inc.'s (TRI's) large-scale pull-out box is a custom-made apparatus measuring, nominally, 762mm wide×610mm high×1.52m long. Soil is placed beneath and above the geosynthetic layer. Horizontal force is then applied to the geosynthetic and the force required to pull the geosynthetic out of the soil is recorded. Pullout resistance is obtained by dividing the maximum load attained by the test specimen width. Table 3 shows the pull-out properties of bidirectional geogrids. Interaction coefficient must be 0.8 and each product satisfied this requirement.

Table 3. Pull-out properties of bi-axial geogrids

Bidirectional Geogrid	A		B	
	MD	CD	MD	CD

Maximum Pull-out Force (kN/m)	23.8	21.5	14.30	19.03
Pull-out Interaction Coefficient (C_i)	1.49	1.35	0.90	1.19
Requirement Value	0.8			

3.3 Direct Shear Properties

The test was performed in general accordance with ASTM D 5321-02: Standard Test Method for Determining the Coefficient of Soil and Geosynthetic or Geosynthetic and Geosynthetic Friction by the Direct Shear Method on bidirectional geogrid A and B to soil for determining the angle of friction. The rate of shear was applied at a constant rate of horizontal displacement with 1mm/min and maximum shear displacement is 10.2cm. The applied normal stress in this test was 30, 50, 70kPa. The backfill soil was concrete sand as described in Table 4.

Table 4. Characteristic of concrete sand

Characteristics	Value
Maximum Dry Density (g/cm^3)	1.809
Dry Density at 95% Compact (g/cm^3)	1.719
Optimum Moisture Content (%)	10.9
Moisture Content at 95% Compact (%)	5.8
Soil Friction Angle (°)	38

The angle of friction was determined by slope of the plot from maximum shear stress versus applied normal stress. The friction angle between concrete sand and geogrids must be over 30°at certain stress. The friction angles of each product meet the requirement as in Table 5.

3.4 Aperture Size

The test was performed in general method using vernier calipers on each product. Aperture size should meet the range from 15mm to 75mm and aperture size of each products meet the requirement of specified class as shown in Table 6.

Table 5. Shear properties of bi-axial geogrids

Shear Property	Bidirectional Geogrid	MD			CMD		
Normal Stress (kPa)	A	30	50	70	30	50	70
	B	30	50	70	30	50	70
Maximum Shear Stress (kPa)	A	20.2	32.3	47.8	20.7	32.8	48.0
	B	20.9	33.3	49.4	20.7	34.1	48.5
Coefficient of Friction	A	0.690			0.6839		
	B	0.714			0.695		
Angle of Friction (˚)	A	34.6			34.4		

	B	35.5	34.8

Table 6. Aperture size of bidirectional geogrids

Bidirectional Geogrid	A		B	
	MD	CD	MD	CD
Aperture Size, mm	34.4	34.4	34.3	35.0

3.5 Torsional Rigidity

The test was performed in general accordance with GRI-GG9: Torsional Behavior of Bidirectional Geogrids When Subjected to In-Plane Rotation on bidirectional geogrid A and B. In this method, an unsupported square-frame loading specimen is fixed on its four sides in a horizontally oriented containment box. Its central node is then clamped by torque device that has the capability of applying moment to the geogrid structure and of simultaneously measuring the resulting rotation as shown in Figure 4. The modulus of the rotation versus moment curve is the desired value of geogrid torsional rigidity in units of mm-kg/deg. Torsional rigidity should meet the requirement of specified class and each products meet the requirement of specified class as shown in Table 7.

3.6 UV Stability

To determine the Ultra-violet resistance of geogrid, ASTM D 4355-02: Standard Test Method for Deterioration of Geotextiles by Exposure to Light, Moisture and Heat in a Xenon Arc Type Apparatus was used. The total exposure time is 500hours and the exposure cycles as follows: 102 min of light only (black panel temperature 65±3 , relative humidity 50±5%), followed 18 min of water spray and light. After exposure tensile strength were measured by ASTM D 6637 B method. Percent retention of tensile strength should meet over 70% at 500hrs UV exposure and each product meet the requirement of specified class as shown in Table 8.

Figure 4. Torsional rigidity test apparatus for bidirectional geogrids

Table 7. Aperture size of bidirectional geogrids

Bidirectional Geogrid	A	B

Torsional Rigidity, mm-kg/deg	33.1	27.4
Requirement Value	30	15

Table 8. Retention for tensile strength of bidirectional geogrids after UV testing

	Bidirectional Geogrid	As Received		After Weathering		Retention (%)	
		MD	CD	MD	CD	MD	CD
Tensile Strength, kN/m	A	43.5	42.4	44.1	43.1	101.3	101.6
	B	23.0	32.3	22.5	33.0	97.9	102.0
Requirement Value (%)	A					Over 70	
	B					Over 70	

3.7 Installation Damage

To review the extension of application end-uses, we examined installation damage and creep behaviors. Figure 5 shows the schematic diagram of real installation site. The strength retention of bidirectional geogrid A after installation was evaluated with filled material size in Figure 6. From this, it is seen that almost no strength change for bidirectional geogrids would be occurred by installation damage.

3.8 Creep Behaviors

To examine the long-term performance of bidirectional geogrid A, creep deformation behaviors were examined with additional creep load as shown in Figure 7 for 1,000 hours. However, it is recommended that the optimum and minimum test period of creep test is at least 10,000 hours. Therefore, this test is continuously on going now and Figure 8 shows the intermediate creep test result during 10,000 hours creep test. The result of this, it could be confirmed the creep limited strain of bidirectional geogrid A showed within 10%.

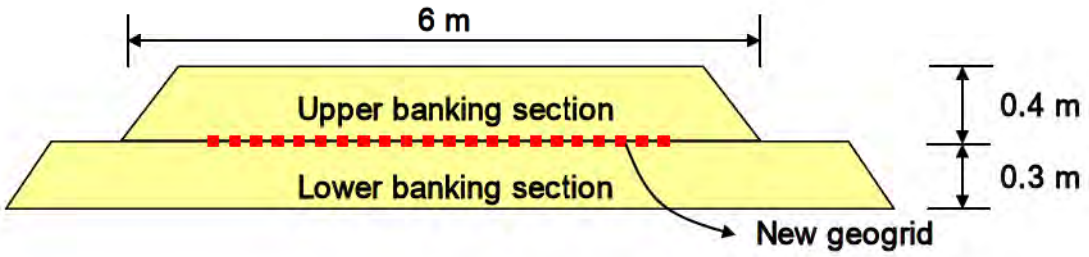

Figure 5. Schematic diagram of real installation site for bidirectional geogrid A

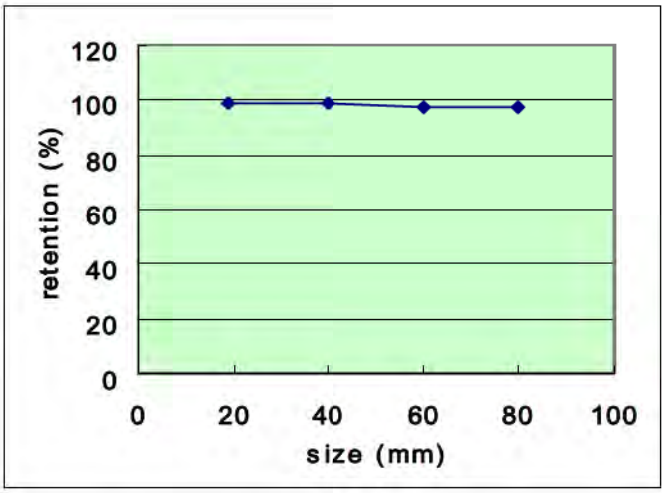

Figure 6. Torsional rigidity test apparatus for bidirectional geogrid A

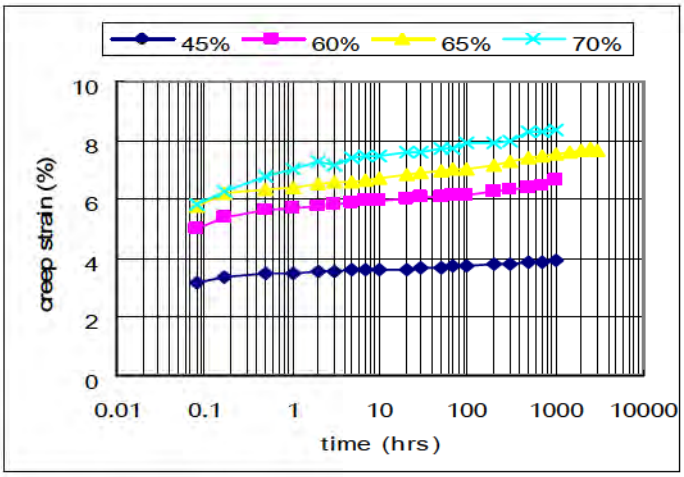

Figure 7. Creep behaviors for 1,000 hours of bidirectional geogrid A

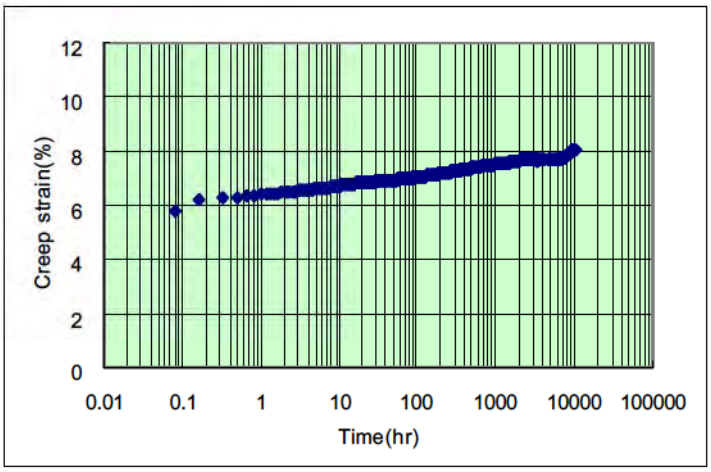

Figure 8. Creep behaviors for 10,000 hours of bidirectional geogrid A

4. CONCLUSION

Through the tests, we confirmed the evaluation value of each item was satisfied with the recommended and tolerance value ranges of GCI-PCP draft of bidirectional geogrids. New concept bidirectional geogrids A and B having good properties has been developed and is suited for pavement and any kind of soil reinforcement application.

REFERENCES

GRI (2005), GRI Test Methods GG, Drexel University, Philadelphia, USA.
GFR (2004), 2005 GFR Specifier's Guide, Industrial Fabrics Association International, Roseville, USA.
ASTM International (2005), Standard Test Methods on Geosynthetics, ASTM D35, Conshoken, USA.
R. M. Koerner (2005), Designing with Geosynthetics, 5th Edition, Prentice Hall, USA.

CONTACT:

Dr Han-Yong Jeon
Division of Nano-Systems Eng.
INHA University
253 Yonghyun-dong, Nam-gu
Incheon, KOREA 402-751
Phone: +82-32-860-7492
Email: hyjeon@inha.ac.kr

BEHAVIOR OF REINFORCED EMBANKMENTS ON SOFT RATE-SENSITIVE FOUNDATIONS

R. Kerry Rowe, GeoEngineering Centre at Queen's-RMCDepartment of Civil Engineering, Queen's University; C. Taechakumthorn, GeoEngineering Centre at Queen's-RMC, Department of Civil Engineering, Queen's University

ABSTRACT

The time-dependent behavior of reinforced embankments constructed on rate-sensitive clay is examined. The results indicated that the viscoplastic behavior of the rate-sensitive foundation soil can have a significant effect on the performance of the embankment, especially after the end of construction. The short-term failure height of the embankment is affected by viscoplastic behavior of soil and construction rate. The results also show that the effect of hydraulic conductivity and viscosity of soil are not significant during the construction period, however in the longer-term the differences are significant. For rate-sensitive soils, the role of reinforcement is especially significant after the end of construction since most of reinforcement strain is mobilized by foundation creep after the end of construction. The reinforcement is shown to have potential to both increase stability and decrease the long-term creep deformation.

KEYWORDS: elasto-viscoplastic; reinforced embankment; time-dependent behavior; finite element modeling.

INTRODUCTION

The behavior of reinforced embankments constructed on typical soft soils has been studied by many researchers using both field case histories (Rowe and Mylleville, 1996; Rowe et al., 1996; Hinchberger and Rowe, 1998 and Chai and Bergado, 1993) and the finite element method (Rowe and Mylleville, 1994; Hinchberger and Rowe, 2003 and Rowe and Li, 2005). However, the effect of the viscous behavior of rate-sensitive foundations on the short and long-term performance of reinforced embankments has only received limited attention as noted below.

The performance of a test embankment constructed over a soft rate-sensitive soil in Sackville, New Brunswick (Canada) has been reported (Rowe et al., 1995). A study by Rowe et al. (1996) showed that in order to accurately predict the response of this embankment it would be necessary to use a constitutive model that considered the viscous behavior of the foundation soil. In order to account for the rate-sensitive characteristic of this foundation soil, Rowe and Hinchberger (1998) used an elasto-viscoplastic constitutive model based on the elliptical cap yield surface (Chen and Mizuno, 1990) and Perzyna's overstress theory of viscoplasticity (Perzyna, 1963) and demonstrated that the proposed model could adequately described much of the measured behavior of the test embankment. Additional studies of the behavior of embankments on rate-sensitive soils have been reported by Rowe and Li (2002) and Li and Rowe (2002).

The objective of this paper is to perform a parametric study of the behavior of reinforced embankments on rate-sensitive soils. The short-term stability of the reinforced embankment will

be compared with the result from the conventional inviscous elasto-plastic model. The influence of factors such as the viscoplastic properties and hydraulic conductivity of soil, the stiffness of reinforcement, and rate of construction are examined with respect to the time-dependent responses of excess pore pressure, reinforcement strains, and deformations.

FINITE ELEMENT MODELLING OF REINFORCED EMBANKMENT

The finite element program AFENA (Carter and Balaam, 1990), previously modified by Rowe and Hinchberger (1998) to incorporate elasto-viscoplastic constitutive model, was adopted in this study. The results presented here were obtained for embankments with 2H:1V side slopes overlaying 15 m of soft rate-sensitive clay above the rigid and permeable sand layer. A typical mesh for a 5m high reinforced embankment (with a 28 m wide crest) is shown in Figure 1.

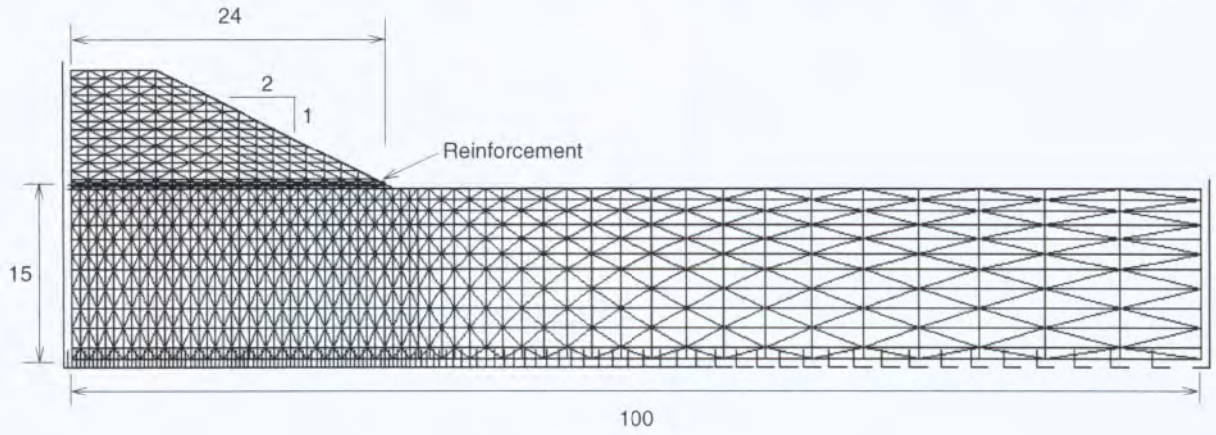

Figure 1. Finite Element Mesh Discretisation

Details of Mesh Discretisation

The finite element mesh included a total of 1847 elements with 3516 nodal points; consisting of six-noded linear strain triangle elements for the soil, two-noded nonlinear bar elements for the reinforcement, and elasto-plastic nodal joint elements (Rowe and Soderman, 1985) for the fill/reinforcement and fill/foundation interfaces.

The centerline of the embankment and far field boundary, located 100 m away from centerline, were taken to be smooth-rigid boundaries. The bottom boundary of the finite element mesh was assumed to be free draining and rough-rigid. The embankment construction was simulated by gradually turning on the gravity of the embankment in 0.75 m thick lifts at a rate corresponding to the construction rate of the embankment.

ELASTO-VISCOPLASTIC CONSTITUTIVE MODEL

Rowe and Hinchberger (1998) developed an elasto-viscoplastic soil model with fully coupled with Biot consolidation (Biot, 1941). This soil model formulation was based on Perzyna's theory of overstress viscoplasticity (Perzyna, 1963), an elliptical yield cap model (Chen and Mizuno,

1990), a Drucker-Prager failure envelope, and concepts drawn from the critical state framework (Roscoe and Schofield. 1963) as described by Rowe and Hinchberger (1998). The following is a brief summary of the model.

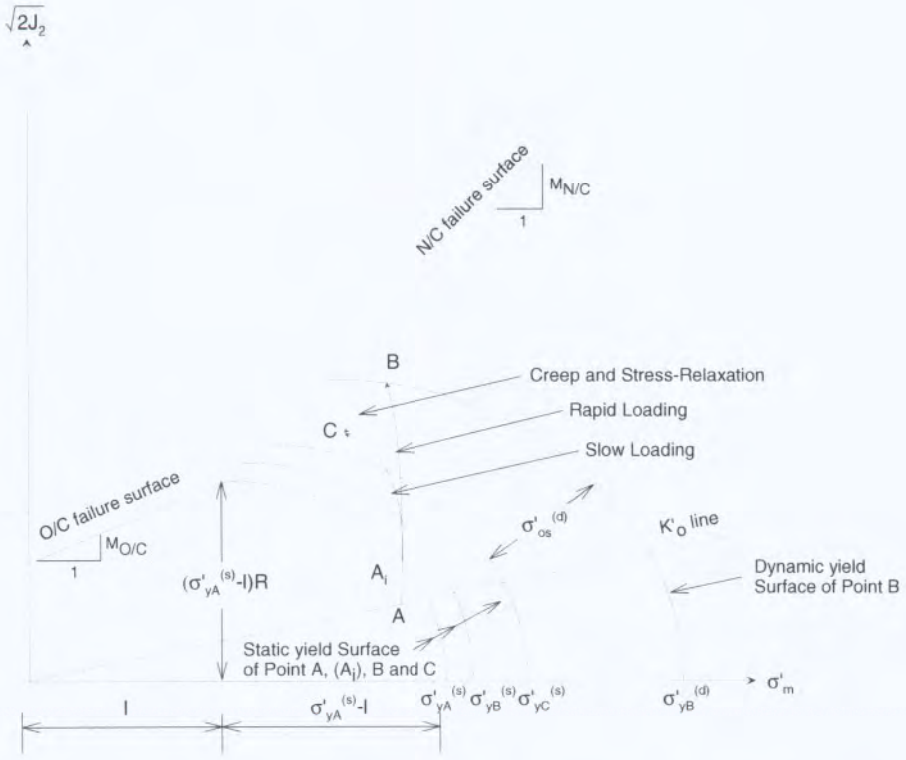

Figure 2. Elliptical Cap Model (Modified from Rowe and Hinchberger, 1998)

The yield surface of the elliptical cap model in $\sigma'_m - \sqrt{2J_2}$ stress space is shown in Figure 2. According to the Pernazy's overstress theory, the governing equation was expressed in terms of the strain rate tensor:

$$\dot{\varepsilon}_{ij} = \frac{\dot{S}_{ij}}{2G} + \frac{1}{3K}\dot{\sigma}_{ii} + \gamma^{vp}\langle\phi(F)\rangle\frac{\partial f}{\partial \sigma_{ij}} \qquad (1)$$

Where S_{ij} is deviatoric stress; G is shear modulus; σ_{ii} is sum of principle stresses; K is bulk modulus; γ^{vp} is the viscoplastic fluidity parameter and ø(F) is a flow function that can be expressed in term of overstress as:

$$\phi(F) = \left(\frac{\sigma'^{(s)}_{my} + \sigma'^{(d)}_{os}}{\sigma'^{(s)}_{my}}\right)^n - 1 \qquad (2)$$

where $\sigma'^{(d)}_{os}$ is overstress as defined in Figure 2; n is strain rate exponent and f is plastic potential function. The elastic bulk modulus K and shear modulus G are functions of mean effective stress as shown below:

$$K = \frac{1+e}{\kappa}\sigma'_m \quad (3)$$

$$G = \frac{3(1-2\nu')K}{2(1+\nu')} \quad (4)$$

where e is the void ratio; κ is the recompression index; σ'_m is mean effective stress and ν' is Poisson's ratio.

CONSTITUTIVE PARAMETERS

Foundation Soil Properties

The two soft rate-sensitive clays examined in this study are denoted as CR1 and CR2. Constitutive parameters used for soil CR1 are similar to the estimated soft soil foundation properties of the Sackville test embankment (Rowe and Hinchberger, 1998). Soil CR2 was assumed to have the same properties as soil CR1 except for the rate-sensitive parameters: the viscoplastic fluidity and strain rate exponent. The various parameters for CR1 and CR2 are listed in Table 1 and the current states of stress were obtained from the preconsolidation and initial vertical stress profiles (Figure 3) used by Rowe and Li (2002).

Table 1. Details of Foundation Soil Properties

Soil Parameter	Soil CR1	Soil CR2
Failure envelope, $M_{N/C}$ (ø')	0.96 (29°)	0.96 (29°)
Cohesion intercept, c_k (kPa)	0	0
Failure envelope, $M_{O/C}$	0.75	0.75
Aspect ratio, R	1.25	1.25
Compression index, λ	0.16	0.16
Recompression index, κ	0.034	0.034
Coefficient of at rest earth pressure, K_o'	0.75	0.75
Poisson's ratio, υ	0.3	0.3
Unit weight, γ (kN/m^3)	17	17
Initial void ratio, e_o	1.50	1.50
Viscoplastic fluidity, γ^{vp} (1/hour)	2.0 x 10^{-5}	1.0 x 10^{-7}
Strain rate exponent, n	20	30

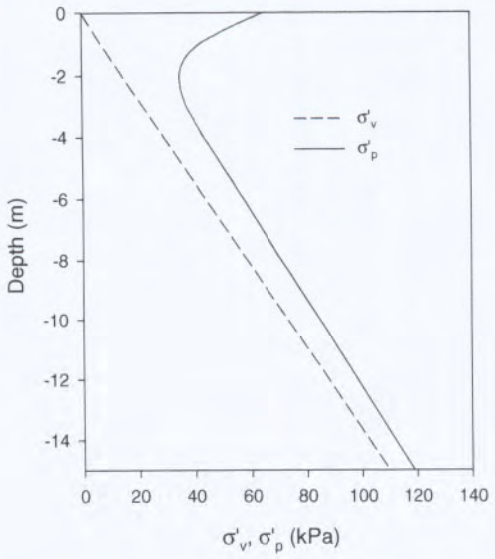

Figure 3. Preconsolidation Pressure and Initial Vertical Stress Profiles (based on Rowe and Li, 2002)

The hydraulic conductivity of soft clay was taken to be a function of void ratio as:

$$k_v = k_{vo} e^{\left(\frac{e-e_o}{C_k}\right)} \tag{5}$$

where k_{vo} is the reference hydraulic conductivity; e_o is the reference void ratio ($e_o = 1.5$) and C_k is hydraulic conductivity change index ($C_k = 0.2$).

In order to study the effect of hydraulic conductivity, the reference hydraulic conductivity, kvo, was varied between 2x10-9 and 4x10-10 m/s. The hydraulic conductivity was considered to be cross anisotropic with kh/kv = 4.

Embankment Fill Parameters and Construction Rates

The purely frictional granular soil is used to model the embankment fill. The assumed properties are friction angle ø' = 37o, dilation angle ψ = 6o and unit weight γ = 20 kN/m3. The non-linear elastic behaviour of the fill was modelled using Janbu's (1963) equation:

$$\frac{E}{P_a} = K\left(\frac{\sigma_3}{P_a}\right)^m \tag{6}$$

where E is the Young's modulus; P_a is the atmospheric pressure; σ_3 is the minor principle stress and K and m are material constants selected to be 300 and 0.5, respectively. The construction rates of two cases examined in this study were 2 m/month and 10 m/month.

Interface Parameters and Reinforcement Stiffness

Rigid-plastic joint elements (Rowe and Soderman, 1985) were used to model the fill/reinforcement and fill/foundation interface. The fill/reinforcement interface was assumed to frictional with ø' = 37o. The fill/foundation interfaces had the same shear strength as the foundation soil at ground surface. Reinforcement with tensile stiffness, J, of 0 (no reinforcement), 500, 1000, 2000, 4000 and 8000 kN/m was examined.

RESULTS AND DISCUSSIONS

Effect on Short Term Embankment Stability

The short term stability of the embankment was investigated by plotting the calculated variation in the net embankment height above the original ground surface with embankment fill thickness, defining the failure as the point where the net embankment height reached a maximum value (see Rowe and Soderman, 1985). Figure 4 shows that the rate-sensitivity of the clay can have a significant effect on the short term stability of the embankment.

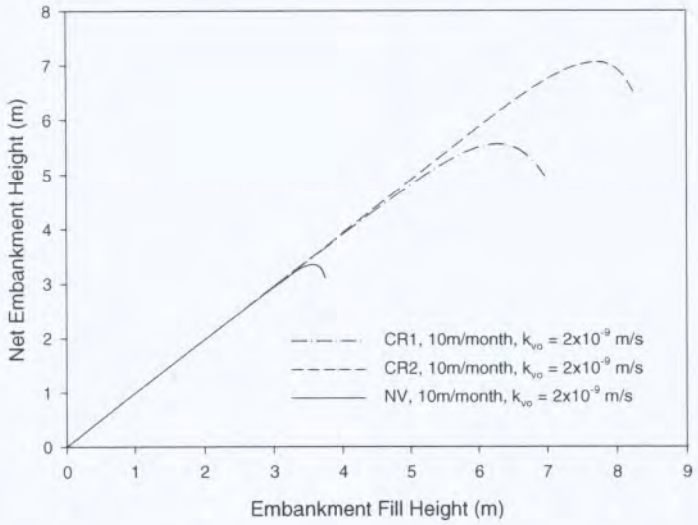

Figure 4. Effect of Rate-Sensitive Clay on Short Term Stability

The inviscous (NV) soil was modeled using elasto-plastic element with same elliptical cap model parameters and hydraulic conductivity as those of viscous soil foundation but the viscoplastic properties of soil were not taken into account. All embankments showed linear behaviour followed by nonlinear behaviour until reaching the failure heights of 3.35, 5.56, and 7.05 m for soils NV, CR1, and CR2 respectively. The results in Figure 4 also show that for soils having the same elasto-plastic properties, the more viscous soil (CR2) will exhibit higher undrained shear strength (Rowe and Hinchberger, 1998) and hence a greater short term failure height.

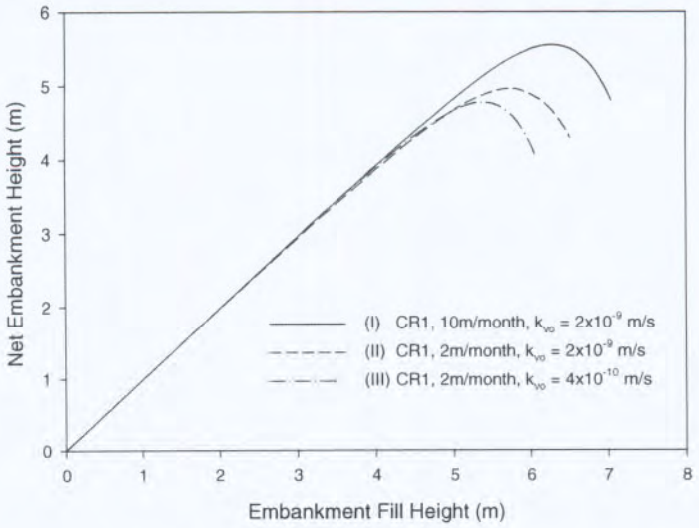

Figure 5. Effect of Hydraulic Conductivity and Construction Rate on Short Term Stability

The effect of hydraulic conductivity and construction rate on the short term stability of the embankment is presented in Figure 5. In case II (k=2x10-9 m/s) and III (k=4x10-10 m/s), the failure heights were 4.95 and 4.77 m, respectively. The higher hydraulic conductivity resulted in higher failure height because it allowed greater partial pore pressure dissipation to occur during construction. Cases I and II also show that construction rate can have a significant effect on the short term stability of the embankment. The failure height at a construction rate of 10 m/month (5.55 m) was 0.6m greater than at a rate of 2 m/month (4.95 m). This arises because the short-term strength of rate-sensitive clay is higher at a higher applied strain rate (Rowe and Hinchberger, 1998).

Effect on Reinforcement Strain

The construction of 5m high reinforced embankment with the reinforcement stiffness of 2000 kN/m was simulated to study the effects of hydraulic conductivity, construction rate and soil viscosity on the reinforcement strain as shown in Figure 6. For Cases I and II the two foundation soils have reference hydraulic conductivities, kvo, of 2x10-9 and 4x10-10 m/s respectively. During the construction period, the difference in reinforcement strain is not significant (at the end of construction the reinforcement strains were 2.4 % and 2.8 % respectively). The reinforcement strain subsequently increased to 4.2 % and 5.2 % at 3.75 months after the end of construction for kvo equal to 2x10-9 m/s and 4x10-10 m/s respectively. The strain for the case with the higher kvo was less than for the lower kvo because partial consolidation during construction reduced the amount of overstress in the soil and consequently reduced soil creep and the mobilized reinforcement strains.

Figure 6 also shows the effect of construction rate on the development of reinforcement strains. The reinforcement strains were 2.8 % at the end of construction and 5.2 % at 6.25 months for a rate of 2m/month (Case II). The corresponding values at 10 m/month (Case III) were 1.5 % and 5.5 %. Thus while the slower rate of construction resulted in larger reinforcement strains at the end of construction, due to consolidation and creep occurring during the longer construction

period, ultimately the slower construction rate gave smaller longer term strains due to less overstressing of the soil and hence less long term creep.

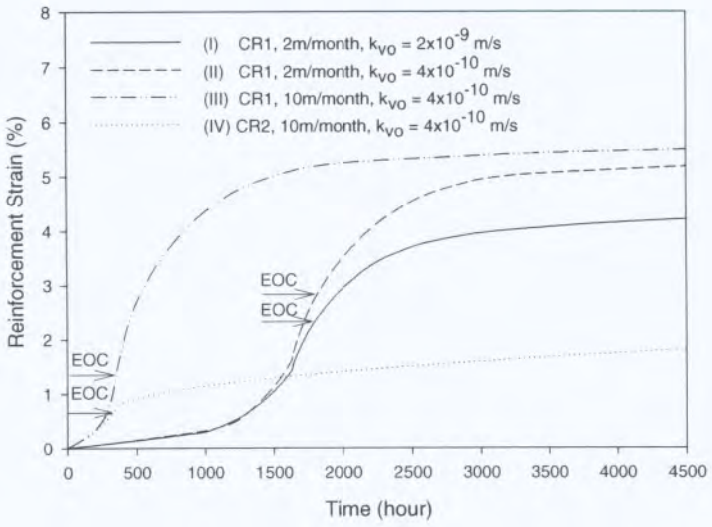

Figure 6. Effect of Construction Rate and Hydraulic Conductivity on Reinforcement Strain (*J = 2000 kN/m*)

The difference between Cases III and IV in Figure 6 shows the effect of soil viscosity on the reinforcement strain. Soil CR2, which has a much lower viscoplastic fluidity γvp, resulted in smaller reinforcement strains and a slower creep rate than was obtained for soil CR1 when loaded with the same thickness of fill.

Excess Pore Water Pressure Dissipation

The difference in hydraulic conductivity (2x10-9 and 4x10-10 m/s) had no significant effect on the pore pressures 4.4m below the centerline during construction (Figure 7) and the excess pore pressure increased almost linearly to 91.1 kPa at the end of construction for both Cases I and III. As might be expected, the higher hydraulic conductivity resulted in faster post construction pore pressure dissipation. The excess pore pressures calculated for soil CR2 (Case 2) were less than those for soil CR1 (Case 1). In both cases there was an increase in pore pressure following the end of construction (a common characteristic of rate-sensitive soils).

The effect of reinforcement stiffness on the development and dissipation of excess pore pressure 4.4 m under the crest of embankment is shown in Figure 8. The excess pore pressure increased linearly to 79 kPa at the end of construction and there was no significant effect of reinforcement stiffness during the construction period. After the end of construction, the excess pore pressures increased due to creep of the foundation. It is noted that the excess pore pressure decreased because of consolidation and increased because of creep of the foundation soil with the two processes occurring simultaneously (Rowe and Li, 2002). By providing greater confinement to the soil (reducing overstress) the stiffer reinforcement reduced the effects of creep induced pore water pressure and resulted in faster dissipation or pore pressure.

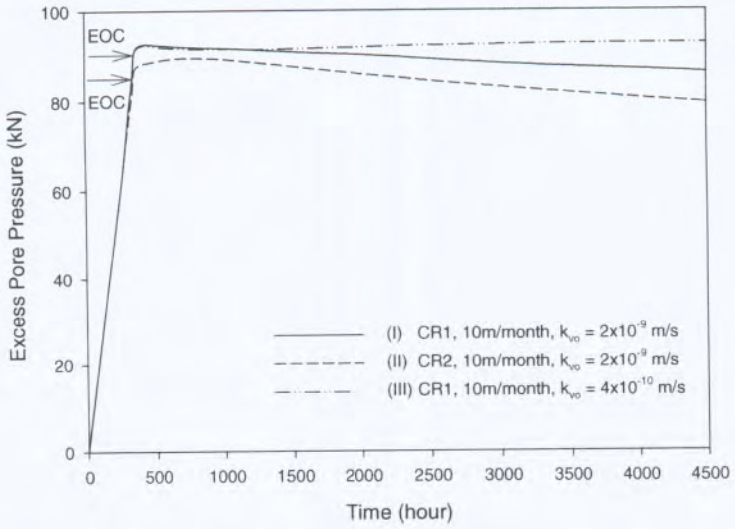

Figure 7. Effect of Viscosity and Hydraulic Conductivity on Excess Pore Pressure 4.4m below Ground Surface at the Centerline (*J = 2000 kN/m*)

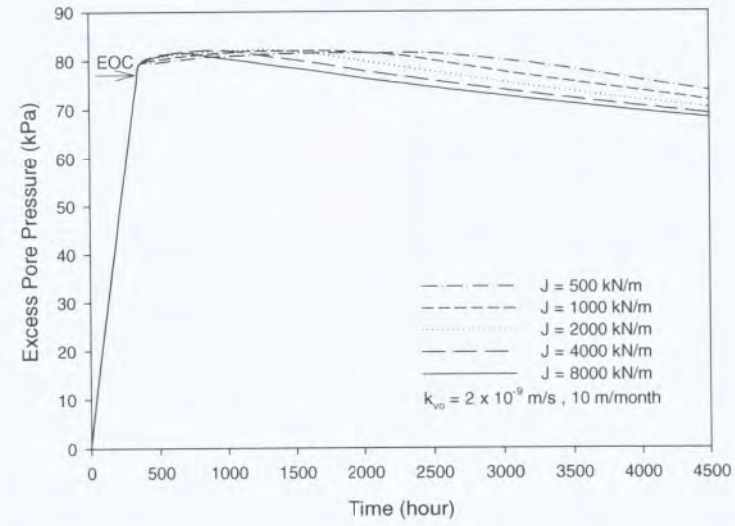

Figure 8. Excess Pore Water Pressure Dissipation 4.4m below Ground Surface at Embankment Crest

Differential Settlement and Lateral Deformation

Reinforcement can significantly reduce differential settlement, heave, and lateral deformations for embankments on rate-sensitive foundations. Figure 9 shows the profiles of points on the original ground surface for embankments with different reinforcement stiffnesses. For the unreinforced embankment (J = 0 kN/m), the differential settlement between center and crest of the embankment was 0.82 m while for the reinforced embankment this reduced to 0.25 and 0.06 m for reinforcement stiffnesses of 2000 and 8000 kN/m, respectively. The maximum calculated heaves were 1.57, 0.57, and 0.22 m for the reinforcement stiffness of 0, 2000, and 8000 kN/m, respectively.

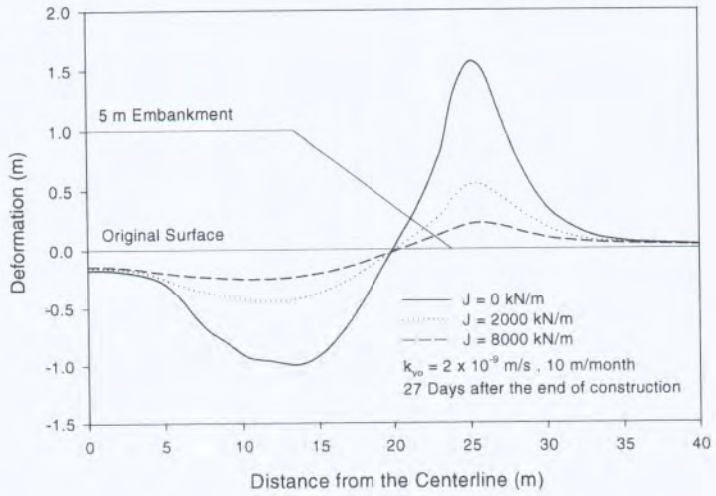

Figure 9. Effect of Reinforcement Stiffness on the Differential Settlement

Reinforcement also had a beneficial on lateral deformation (Figure 10). The maximum lateral deformations of soil reduced from 2.0 m, for the unreinforced case, to 0.7 and 0.3 m for reinforcement stiffness of 2000 and 8000 kN/m, respectively. The reinforcement stiffness also changes the failure mechanism. The stiffer reinforcement forces the failure surface into the deeper and stronger soil (since shear strength increase with depth). The depth of maximum lateral deformations increased from 1.0 to 1.5 and 2.0 m for the unreinforced case and reinforcement stiffnesses of 2000 kN/m, and 8000 kN/m, respectively.

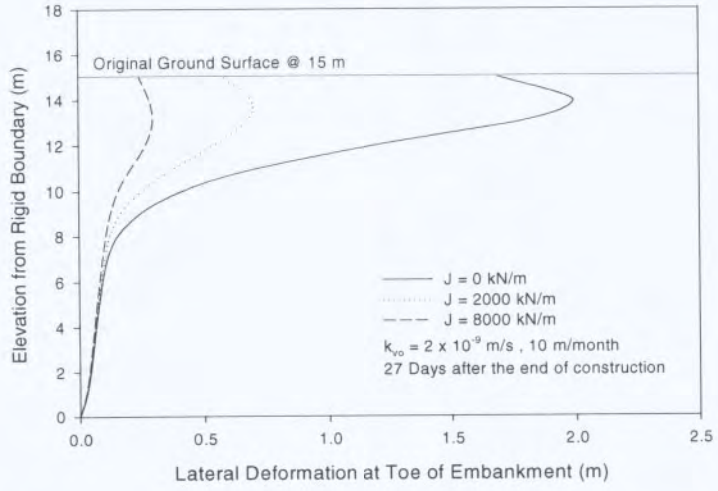

Figure 10. Effect of Reinforcement Stiffness on Lateral Deformations

SUMMARY AND CONCLUSIONS

The time-dependent behaviour of embankments constructed over rate-sensitive clay was investigated using a finite-element analysis. The viscoplastic properties of the foundation soil, hydraulic conductivity of the soil, reinforcement stiffness, and construction rate were examined. The results showed that the viscoplastic behaviour of the foundation soil can have a significant effect on the embankment performance, especially after the end of construction. The behaviour of reinforced embankment on the specific rate-sensitive clays modeled can be summarized as follows:

1. The short term stability was affected by viscoplastic characteristics of the soil, hydraulic conductivity, and rate of construction. The most viscous soil examined gave the highest short term failure height. The higher hydraulic conductivity allowed a higher degree of partial consolidation and resulted in a greater failure height. Finally for a viscous soil a higher construction rate gave higher strength and hence a higher short-term failure height.

2. The different hydraulic conductivity and soil viscoplasticity examined did not significantly affect the reinforcement strain during the construction period. However, they did have a significant effect on the long-term strains.

3. The excess pore water pressures continued to increase after the end of construction, reaching a maximum pressure at a short time after construction. This maximum excess pore pressure was not very sensitive to the soil reinforcement stiffness, although due to reduced overstress the pore pressures dissipated faster for the more highly reinforced embankment.

4. The differential settlement, heave, and lateral deformation were all substantially reduced by the use of basal reinforcement. The reinforcement also altered the failure mechanism by forcing the failure surface into deeper and stronger foundation soil.

ACKNOWLEDGEMENTS

The research reported in this paper was supported by the Natural Sciences and Engineering Research Council of Canada (NSERC). The authors are also very grateful to Dr. A.L. Li for his assistance.

REFFERENCES

Biot, M.A. 1941. General theory of three-dimensional consolidation. Journal of Applied Physics. 12, 155-164.

Britto, A.M., and Gunn, M.J. 1987. Critical state soil mechanics via finite elements. Ellis Horwood, Chichester, England.

Burland, J.B. 1990. On the compressibility and shear strength of natural clays. Géotechnique, 40(3): 329–378.

Carter, J.P. and Balaam, N.P. 1990. AFENA: A general finite element algorithm: users manual. School of Civil and Mining Engineering, University of Sydney, Australia.

Chai, J.C. and Bergado, D.T. 1993. Performance of reinforced embankment on Muar clay deposit, Soils and Foundations, 33 (4): 1-17.

Chen, W.F. and Mizuno, E. 1990. Nonlinear analysis in soil mechanics: theory and implementation. New York: Elsevier.

Hinchberger, S.D. 1996. The behaviour of reinforced and unreinforced embankment on rate sensitive clayey foundation. PhD thesis, University of Western Ontario, London, Canada.

Hinchberger, S.D. and Rowe, R.K. 2003. Geosynthetic reinforced embankments on soft clay foundations: predicting reinforcement strains at failure. Geotextiles and Geomembranes 21: 151-175.

Hinchberger, S.D., and Rowe, R.K. 1998. Modelling the ratesensitive characteristics of the Gloucester foundation soil. Canadian Geotechnical Journal, 35: 769–789.

Janbu, N. 1963. Soil compressibility as determined by oedometer and triaxial tests. Proceedings of the European Conference on Soil Mechanics and Foundation Engineering, Wiesbaden, Germany. 1:19-25.

Jewell, R.A. 1996. Soil reinforcement with geotextiles, CIRIA Special Publication 123. London: Thomas Telford

Li, A.L. 2000. Time dependent behaviour of reinforced embankments on soft foundations. Ph.D. thesis, The University of Western Ontario, London, Ont.

Li, A.L. and Rowe, R.K. 2002. Design considerations for embankments on rate sensitive soils. ASCE Journal of Geotechnical and Geoenvironmental Engineering, 128(11):885-897.

Perzyna, P. 1963. The constitutive equations for rate-sensitive plastic materials. Quarterly of Applied Mathematics, 20(4): 321-332.

Roscoe, K.H., and Schofield, A.N. 1963. Mechanical behaviour of an idealised "wet clay". Proceedings of the Second European Conference on Soil Mechanics. pp.47-54.

Rowe, R.K. and Hinchberger, S.D. 1998. The significant of rate effects in modeling the Sackville test embankment. Canadian Geotechnical Journal. 35, No.3, 500-516.

Rowe, R.K. and Li, A.L. 2002. Behaviour of reinforced embankment on soft rate-sensitive soil. Geotechnique. 52, No.1, 29-40

Rowe, R.K. and Soderman, K.L. 1985. An approximate method for estimating the stability for geotextiles reinforced embankments. Canadian Geotechnical Journal. 22, No.3, 392-398.

Rowe, R.K., and Li, A.L. 2005. Geosynthetic-reinforced embankments over soft foundations. Geosynthetics International, 12 No.1: 50-85.

Rowe, R.K., and Mylleville, L.J. 1994. Analysis and design of reinforced embankments on soft or weak foundation. "Soil structure interaction: Numerical analysis and modelling", (Ed.) J.W. Bull, E&FN Spon (Chapman & Hall), Chapter 7: 231-260.

Rowe, R.K., and Mylleville, L.J. 1996. A geogrid reinforced embankment on peat over organic silt: a case study. Canadian Geotechnical Journal, 33: 106-122.

Rowe, R.K., Gnanendran, C.T., Landva, A.O. and Valsangkar, A.J. 1995. Construction and performance of a full-scale geotextile reinforced test embankment, Sackville, New Brunswick. Canadian Geotechnical Journal. 32, No.3, 512-534.

Rowe, R.K., Gnanendran, C.T., Landva, A.O. and Valsangkar, A.J. 1996. Calculated and observed behaviour of reinforced embankment over soft compressible soil. Canadian Geotechnical Journal. 33, No.2, 324-338.

CONTACT:

Kerry Rowe
Professor
Vice-Principal (Research)
Queen's University
GeoEngineering Centre at Queen's-RMC
Department of Civil Engineering, Queen's University
Kingston, ONTARIO
CANADA, K7L 3N6
Phone: (613) 533-6933
Email: kerry@civil.queensu.ca

Study of Soil/PET Geogrid Shear Properties from Large Scale Direct Shear Tests

Chia Nan Liu, National Chi-Nan University; Y.H. Ho, Department of Civil Engineering, National Chi-Nan University; , T. C., Department of Civil Engineering, National Chi-Nan University

ABSTRACT

The results of a series of direct shear tests are presented in this paper. The direct shear tests are conducted to investigate the shear properties of the interface between PET geogrid and soils. During these tests, a large scale direct shear device is used. The shearing size of upper shear box is 45cm×45cm. Different setup of the lower shearing box including a larger box (45cm×60cm), box of the same size (45cm×45cm), and a steel plate, are used to investigate the appropriate set up. Three soils (sand, gravel, and clay) which are prepared to different unit weight are used in these tests. PET geogird of different tensile strengths of longitudinal and transverse direction, aperture size, and opening ratio are applied in tests. The test results are compared to study the important factors to the shear strength characteristics of soil/geogrid interface.

INTRODUCTION

Geosynthetics has been applied commonly in soil structures to provide functions such as reinforcement, drainage, infiltration and separation. For reinforced retaining wall, if the soil/geosynthetic interface strength is less than the shear strength of the soil, the interface indicates a plane of weakness that the direct shear mode failure tends to occur along the soil/geosynthetic interface. Besides, for the reinforced slope which place geosynthetic along slope, the inclusion of geosynthetic with higher interface shear strength between soils or other geosynthetic material indicates a reduce in the deformability of the cover soil and the tensile forces mobilized in the geomembrane, as well as a increase the inclination of the stable slope angle (Liu and Gilbert, 2003; Palmeira and Viana, 2003). Pullout test is usually conducted to estimate the resistance between soil and geosynthetic against pullout mechanism. Wang and Richwien (2002) proposed a model to estimate the pullout friction based on the shear properties of soil/geosynthetic interface and the basic material properties (friction angle, and dilation angle). Therefore, the understanding of geosynthetic/soil interface shear strength is essential to design and stability analysis of geosynthetic greinforced soil structures.

In general, the interactions between soil and geosynthetic mentioned on literatures include the following components: (1) friction between soil and geosynthetic; (2) friction between soil and soil which are trapped in the openings of geosynthetics; (3) passive earth pressure mobilized by the transverse ribs. Many researches show that the value of the friction of the interface between soil and geotextile are lower than the value of the internal friction angle of the soil (Cazzuffi et. al.,1993; Bakeer, 1998; Lee and Manjunath, 2000). For geomembrane and geotextiles, the shear resistance of soil/geosynthetic interface solely comes from the friction of geosynthetic surface against soil particles because soil particles are not trapped into the small openings of geosynhtetics. For geogrid, the frictional resistance composed of the soil to geosynthetic shear resistance and the soil to soil shear resistance within geogrid openings (Alfaro et. al. 1995). The

passive earth pressure between the geogrid and soils are identified and studied by researchers through conducting pull-out tests. The component is ambiguous when the direct shear tests are conducted and analyzed. For example, Lopez (2002) states that the contribution of the passive earth pressure induced by the bearing members of the geogrid is almost negligible for the direct shear interaction mechanism. However, Bergado et al. (1993) state the apertures of geogrid can provide bearing resistance when he conducted direct shear test and find the shear strength of Tensar (polymeric) geogrid/soil interface is greater than that of soil. It is of interest to test the shear strength of geogrid/soil interface for further study the interaction between geogrid and soil.

A lot of direct shear tests are conducted by considering factors such as type of geosynthetics, type of soil, size of testing device, and test procedures, on shear resistance of geosynthetic/soil interface. This study applies the similar approach to perform a series of direct shear tests on geogrid/soil interfaces and compares the test results.

TEST DEVICE

The size of shearing device can influence the direct shear test results. Generally, the boundary effect, and device friction, is more significant for a smaller shear box. The dimension of shear box, as regulated by ASTM D5321, with the minimum dimensions of 300 mm by 300 mm should be used in the direct shear test of geosynthetic/ soil interface. The similar regulation is denoted in Germany (DIN EN ISO 12957-1). In this study, a large scale direct shear device is used. The picture of the direct shear device is shown in Figure 1. The shearing area is 0.2025 m^2 (45cm×45cm). The shearing force in the horizontal direction is mobilized by an electric motor while the vertical loading is applied by a hydraulic jack between the rigid reaction frame and specimen. The capacities for both loading are 10 tons. Data collected during tests includes force and displacement in vertical and in horizontal directions which are measured using two load cells and two LVDT. The geosynthetic specimens are clamped on the lower shearing box (Figure 2).

TEST MATERIAL

Several soils including Ottawa sand, coarse gravel, finer gravel, and clay are used in the tests. The physical characteristics of each soil are listed in Table 1. The Ottawa sand are prepared into denser and looser conditions. Their relative densities (Dr) are controlled to 80 %, and 40 %, respectively. The clay is the fine material of laterite soil. The clay is compacted to 90% degree of compaction at the optimum water content (24.8 %). The total unit weight of the clay specimen is 17.07 kN/m^3. Six geosynthetics including one geotextile and five geogrid are used in this study. They are identified as GT, GG1, GG2, GG3, GG4, and GG5, respectively. The geogrid and geotextile are woven from polyester yarns and coated with PVC. The grid pattern of GG1, GG2, GG3, GG4 are similar while GG5 has a different grid pattern (Figure 3). They are products of the same manufacture. The geogrid and geotextile are commercial products while the PVE coating of geotextile is specially customized by the authors. The physical characteristics of these geosynthetics are listed in Table 2.

TEST SCHEME

A combination of large-scale direct shear tests was performed with the objective of estimating

the shear strength of soil/geogrid interfaces. These tests were conducted using normal stresses of 42, 92, and 187 kPa. The shear rate used for all the tests is 1 mm/min. The test was stopped when the shear displacement reaches about 65 mm, i.e., shear strain reached about 15%. The maximum shear strength during the shear process is recorded as the peak shear strength.

The set up of shearing device is not regulated by testing standards. Only the minimum size of shearing box is identified explicitly. The effects of different set up of shearing device on replicating the testing results have been investigated (Richards and Scott, 1985; Juran and Chen, 1988). Jewell (1996) also stated that the continuous geosynthetics such as geotextile and geomembrane can be tested with a solid block or soil in the lower part of the shear box, however geogrid must be tested by the device which both parts of the shear test device have to be filled with soil. In this study, three different set up of lower shearing box are used. The effect of different set up on the test results is evaluated by comparison with results obtained from shear test with different lower shear box. These set up include: the box with the same size (45cm×45cm) which is filled with the desired soil, the box with a larger size (45.5cm×58.4cm) filled with the desired soil, and the larger lower shear box filled with a solid block. These set up are symbolized as lower box (a), (b), and (c), respectively. The geogrid is placed on the top of lower shear box and clamped on one end of it. In this series, the PET geogrid GG3 is used in tests for it is the commercial product and it has the typical pattern.

The shear strength of soil/geogrid interface is compared with the shear strengths of soil/soil and soil/GT interfaces. The shear strength of soil/geogrid interface is investigated by using GG3. Five soils (dense sand, loose sand, coarser gravel, finer gravel, and clay) are used in this series of tests. The lower box (a) is used in this series of tests.

It is of interest to study the effect of longitudinal strength transverse strength, and opening ratio on the shear strength of soil/geogrid interface. In this series of test, five geogrids are used in tests. For the purpose of increasing data for analysis, GG1, GG2, and GG3 are transposed by 90° when they are placed on the lower shearing box, That is, they are sheared in the cross machine direction. These set up would change the longitudinal and transverse strength but keeps the same opening ratio. The transposed geogrids are named as GG1T, GG2, and GG3T. Besides, a fraction of longitudinal and transverse ribs of GG3 and GG4 are removed to change the opening ratio of geogrid. The laboratory trimmed geogrids are named as GG6, GG7, and GG8. The geometry and physical properties of these geogrids are also listed in Table2.

TEST RESULTS

The test results of soil/soil shear strength ($\tau_{soil/soil}$) for the soil material used in this study are listed in Table 3. The abbreviation symbol for each soil is also listed. These tests are performed using the large-scale direct shear testing device with lower shear box (a). In the test results described later in the paper, the shear strengths of these soils are used as baseline values. The results showed an apparent cohesion for soil/soil interface. This is due to nonlinearity of the relationship between the shear stress and the normal stress in the stress level used. Since it is non-linear, it is not reasonable to fit these data with Mohr-Coulomb failure criterion. The shear strengths of soil/geosynthetic interface ($\tau_{soil/geosynthetic}$) are normalized by the shear strength of soil/soil at the corresponding stress level. The normalized value is termed as an interface shear strength coefficient, α, similar to the "bond coefficient" by Bergado et al. (1993) or "interface

efficiency" by Tatlisoz et al. (1998). That is,

$$\alpha = (\tau_{soil/geosynthetic})/(\tau_{soil/soil})$$

The interface shear strength coefficients of soil/GG3 interfaces for different set up of lower shear box are shown in Figure 4. The presented on this figure is the average value of the three values for three normal stresses. It is observed that, among these set up, lower shear box (a) produces the greatest interface shear strength. However, the use of larger shear box produces lower shear strength. The difference in the measured shear strength between using different size of lower shear box has not been discussed. The reason for this difference is identified as follows. It is observed that soil particles are extruded out of shear box and heave up at the front edge of lower, larger shear box when the direct shear test proceeds (Figure 5). It indicates that some soil particles are not confined well enough. When the lower shear box is larger that some soils in it is not loaded by the normal loading applied through the upper shear box. This unloaded soil has a smaller strength thus it provides a smaller lateral confinement to the loaded soil (i.e., the soil which is sheared). Correspondingly, the measured shear strength is lower. The placement of steel plate on the lower shear box (lower shear box (c)) also produces lower shear box because the resistance mobilized within grid opening is the friction between soil and steel plate. Since the steel plate is smooth and there is no particle interlocking, the friction between soil and steel plate is smaller than the friction between soil and soil particles.

The interface shear strength coefficients of soil/Geotextile and soil/GG3 interfaces for different normal stress are shown in Figure 6. Most of the values of soil/GT for different soils are less than 1, except for the loose sand/GT case in which value is about 1. It means the shear strength of soil and geotextile interface is less than the shear strength of the soil. The GT/soil interface is the potential sliding surface when the direct shear mode is concerned. It is especially significant when geotextile is placed within clay for the value ranges between 0.6 and 0.8. It is observed that the values of soil/GG3 are greater than 1 for sand, and they are very close to 1 for gravel and for clay. The test results are similar to Bergado et al. (1993) that the shear strength of Tensar (polymeric) geogrid/soil interface is greater than that of soil. In general, the shear strength of soil/GG3 is larger than that of soil/GT by more than 15 % for dense sand, loose sand, and clay, while it is more than 5 % for gravel. It indicates that the apertures of geogrid can provide space for development of soil/soil resistance and interlocking. This could increase the shear strength of geogrid and soil interface.

The ratios of interface shear strength coefficients for different geogrid against soils are shown in Table 4, 5, and 6, respectively. This ratio indicates the comparison between shear strengths of two soil/geogrid interfaces of the same set up of shear device. They are calculated as the average

value of the three ratios of value of a soil/geogrid interface to that of another soil/geogrid interface under three different normal stresses. The standard deviation of the ratio is also presented.

The direct shear test results for GG1, GG2, and GG3 transposed by 90o are shown in Table 4. For the same geogrid but with different angle of displacement, they have the same opening ratio but different tensile strength in longitudinal and in transverse directions. The ratio of interface shear strength coefficient between them is helpful to identify the effect of rib strength on interface shear strength. These ratios are very close to 1.0 (range between 0.97 and 1.02), for both dense sand and loose sand cases. Considering the standard deviation (larger than 0.03) in these ratio, the difference in shear strength for geogrid placed in different direction is not significant. It indicates two possibilities: (1) neither the longitudinal nor the transverse strength has effect on interface shear strength; or, (2) both the longitudinal and the transverse strength have similar effect on interface shear strength. Mahmood et al. (2000) reported that the shear strength of geosynthetic/sand interface is not related to the tensile strength of the geosynthetic.

GG1 and GG2 have the same nominal transverse tensile strength (30kN/m) and similar opening ratio (65 % and 64 %, respectively) and grid pattern while GG2 has a greater longitudinal strength (100 versus 60 kN/m). The test results show that the shear strength of dense sand/GG2 interface is about 4 % higher than that of dense sand/GG1 interface while they are about the same when these geogrids are tested against loose sand (Table 5). It is noted that a similar test results are obtained for both set up (a) and set up (b) of lower shear box is used. Though set up (b) is not appropriate to estimate the shear strength of the geosynthetics with openings, it seems this set up is valid for comparing the test results for it induces the similar disturbing effect. GG2T has a greater transverse strength than GG1T. The test results show that the shear strength of loose sand/GG2T interface is about 3 % higher than that of loose sand/GG1T interface while they are about the same when these geogrids are tested against dense sand. The test results might indicate the geogrid with greater tensile strength has larger interface shear strength when it is placed against sand. However, this tendency is not significant and need more justification.

The effect of opening ratio on interface shear strength is also of interest. GG5 and GG3 have the same nominal longitudinal and transverse strength while GG3 has a smaller opening ratio (46 versus 55 %). The test results of these geogrid placed against sand show that there is not much difference between their interface shear strength (Table 5). Since the aperture pattern is significantly different and this series of test are performed using lower shear box (b) which will give a lower interface shear resistance, as illustrated in Figure 4, it is not appropriate to draw conclusion from this comparison. The direct shear test results of gravel against GG3, GG4, GG6,

GG7, and GG8 interface are presented in Table 6. This series of tests are conducted using lower box (a). These geogrids have the similar aperture pattern. It shows the gregrid with the lower longitudinal or transverse strength but with a larger opening ratio has the greater interface shear strength. Though the difference is not significant, the tendency is consistent for each case.

CONCLUSIONS

In this paper, series of large-scale direct shear tests are conducted on variety of geosynthetics and soil materials to evaluate the factors which affect the shear strength of soil.geosynthetic interfaces. The test results reveal that the set up of lower shearing box is important when geogrid is used in tests. A plane shear box is not appropriate because the soil/soil resistance is not developed by using this set up. A lower box which is larger than the loading area (usually the area of upper shear box) is also not appropriate because the soil outside the loading area is not well confined to provide lateral resistance. Both set up will produce lower shear strength. Geotextile placed within soil usually acts as a weak interface in terms of direct sliding. It can be observed that the interface coefficient for soil/geogrid is greater than soil/geotextile interface because the geogrid openings provide contributions. The contributions possibly include the soil to soil contact within the openings, the confinement of soil particles within the openings. The interface shear strength coefficients of sand/geogrid are greater than 1, it might indicate the interlocking of sand particles within grid aperture can increase the soil/geogrid interface shear strength. Though the tendency is not significant, the limit test results reveal that the geogrid with greater longitudinal strength, transverse strength and opening ratios, has larger interface shear strength.

Part of the test results and comparison are based on tests using larger lower shear box, which has been identified as not appropriate for the soil outside of the upper shear box is not confined and heaves during shearing. Though the limit comparison shown in Table 5 indicates that the different set up of lower shear box does not influence the ratio of interface shear strength coefficients significantly, more tests use the appropriate set up of lower box are currently under investigation by the authors to validate the analysis of this research.

REFERENCES

1. Alfaro, M. C., Miura, N., and Bergado, D. T., (1995), "Soil – Geogrid Reinforcement Interaction by Pullout and Direct Shear Tests", Geotechnical Testing Journal, Vol. 18, No.2, pp. 157-167.
2. Bakeer, R. M., Sayed, M., Cates, P. and Subramanian, R.(1998), "Pullout and shear test on geogrid reinforced lightweight aggregate," Geotextiles and Geomembranes, Vol.16, No. 2, Apr, p 119-133.
3. Bergado, D. T. , Chai, J. C., Abiera, H. O., Alfaro, M. C. and Balasubramaniam, A. S., (1993), "Interaction between cohesive-frictional soil and various grid reinforcements," Geotextiles and Geomembranes, Vol. 12, No. 4, pp. 327-349
4. Cazzuffi, D. , Picarelli, L., Ricciuti, A. and Rimold, P. (1993), "Laboratory investigations on the shear strength of geogrid reinforced soils," ASTM Special Technical Publication, No. 1190, p 119-137.
5. Jewell, R.A. (1996): Soil reinforcement with geotextiles. Thomas Telford, London.

6. Juran, I. and Chen, C. L., (1988), "Soil-Geotextile pull-out interaction properties: testing and interaction," Transportation Research Record 1188: Effects of Geosynthetics on Soil Properties and of Environment on Pavement Structures, Transportation Research Board, Washington, D. C., pp 37-47.
7. Lee, K.M. and Manjunath, V.R.(2000), "Soil-geotextile interface friction by direct shear test," Canadian Geotechnical Journal, Vol. 37, No. 1, Feb, 2000, p 238-252.
8. Liu, C. N., and Gilbert, R. B., (2003), Simplified method for estimating geosynthetic loads in landfill liner side slopes during filling, Geosynthetics Internatinoal, Vol. 10, No. 1, 24-33.
9. Lopes, M. L. (2002), "Soil–Geosynthetic Interaction", Geosynthetics and Their Applications, Shukla, S. K., editor. Thomas Telford Publishing, Thomas Telford Ltd, London.
10. Mahmood, A., Zakaria, N., Ahmad, F., 2000, "Studies on Geotextile / Soil Interface Shear Behavior", Electronic Journal of Geotechnical Engineering, Vol. 5
11. Palmeira, E. M., and Viana, H. N. L.,(2003), "Effectiveness of geogrids as inclusions in cover soils of slopes of waste disposal areas," Geotextiles and Geomembranes, Vol. 21, No. 5, p 317-337.
12. Richards, E. A. and Scott, J. D., (1985), "Soil geotextile frictional properties", Second Canadian Symposium on Geotextiles and Geomenbranes, Edmonton, pp. 13-24
13. Tatlisoz, N., Edil, T. B. and Benson, C. H. (1998), "Interaction between reinforcing geosynthetics and soil-tire chip mixtures." Journal of Geotechnical and Geoenvironmental Engineering, Vol. 124, No. 11, pp 1109-1119.
14. Wang, Z., and Richwien, W., (2002) "A Study of Soil – Reinforcement Interface Friction", Journal of Geotechnical and Geoenvironmental Engineering, Vol. 128, No.1, pp.92-94.

CONTACT:

Chia Nan-Liu

Associate Professor

National Chi-Nan University

Civil Engineering Department

National Chi-Nan University

1, University Road

Puli, Na 545

TAIWAN

Phone: 886-49-2910960-4958

Email: cnliu@ncnu.edu.tw

Table 1 Soil Characteristics

Property	Sand	Finer Gravel	Coarser Gravel	Clay
Specific gravity	2.64	2.70	2.71	2.54
D_{10} (mm)	0.25	2.6	5.3	0.01
D_{30} (mm)	0.30	2.9	6.2	0.05
D_{50} (mm)	0.36	3.2	7.4	0.07
D_{60} (mm)	0.38	3.6	7.9	0.095
Coefficient of uniformity	1.52	1.38	1.49	9.50
Coefficient of curvature	0.95	0.90	0.92	2.63
Liquid limit	-	-	-	53
Plastic limit	-	-	-	29
USCS symbol	SP	GP	GP	CH

Table 2-1 Geosynthetic Characteristics

Property	GT	GG1	GG2	GG3	GG4	GG5
Thickness (mm)	0.96	1.33	1.59	2.20	1.98	1.74
Length of Aperture (mm)	-	26.5	26.3	26.6	7.0	36.9
Width of Aperture (mm)	-	22.1	21.6	18.5	7.0	17.3
Width of longitudinal rib (mm)	-	6.6	6.9	10.1	2.5	15.0
Width of transverse rib (mm)	-	4.7	4.6	4.6	3.2	1.2
Opening ratio (%) (aperture area/m^2)/(total area/m^2)	-	65	64	55	49	46
Nominal Ultimate Tensile Strength longitudinal×transverse (kN/m)	100×50	60×30	100×30	200×40	100×100	200×40

Table 2-2 Geosynthetic Characteristics

Property	GG1T	GG2T	GG3T	GG6	GG7	GG8
Thickness (mm)	1.33	1.59	2.2	1.98	1.98	2.2
Length of Aperture (mm)	22.1	21.6	18.5	17.2	17.2	57.8
Width of Aperture (mm)	26.5	26.3	26.6	7	16.5	18.5
Width of longitudinal rib (mm)	4.7	4.6	4.6	2.5	2.5	10.1
Width of transverse rib (mm)	6.6	6.9	10.1	3.2	3.2	4.6
Opening ratio (%) (aperture area/m^2)/(total area/m^2)	65	64	55	61	72	60
Nominal Ultimate Tensile Strength longitudinal×transverse (kN/m)	30×60	30×100	40×200	100×50	50×50	200×20

Table 3 Soil/soil Direct Shear Test Results (use lower shear box (a))

Normal Stress (kPa)	Peak Shear Stress (kPa)				
	Dense Sand (DS)	Loose Sand (LS)	Coarser Gravel (CG)	Finer Gravel (FG)	Clay (CL)
42	33.4	28.8	64.1	50.3	56.9
92	64.7	50.8	115.3	95.6	110.5
187	118.91	105.7	201.9	182.6	197.5

Table 4 Ratio of interface shear strength coefficients for geogrids transposed by 90° (use lower shear box (b))

α ratio	GG1T/DS to GG1/DS	GG2T/DS to GG2/DS	GG3T/DS to GG3/DS	GG1T/LS to GG1/LS	GG2T/LS to GG2/LS	GG3T/LS to GG3/LS
mean	1.00	0.97	1.02	1.00	1.02	1.02
sdv	0.03	0.09	0.06	0.06	0.09	0.04

Table 5 Ratio of interface shear strength coefficients for different geosyntheitc/sand interfaces

α ratio	GG2/DS to GG1/DS	GG5/DS to GG3/DS	GG2T/DS to GG1T/DS	GG2/LS to GG1/LS	GG5/LS to GG3/LS	GG2T/LS to GG1T/LS
mean	1.04 (1.04)*	0.99	1.00	1.00 (1.01)*	1.02	1.03
sdv	0.08 (0.05)*	0.08	0.04	0.02 (0.06)*	0.07	0.04

*:indicate test results using shear box (a), the other test results using shear box (b)

Table 6 Ratio of interface shear strength coefficients for different geosyntheitc/gravel interfaces (use lower shear box (a))

ratio	GG7/CG to GG6/CG	GG6/CG to GG4/CG	GG8/CG to GG3/CG	GG7/FG to GG6/FG	GG6/FG to GG4/FG	GG8/FG to GG3/FG
mean	1.06	1.01	1.01	1.04	1.03	1.02
sdv	0.03	0.00	0.02	0.03	0.03	0.03

Figure 1. Large-scale direct shear apparatus

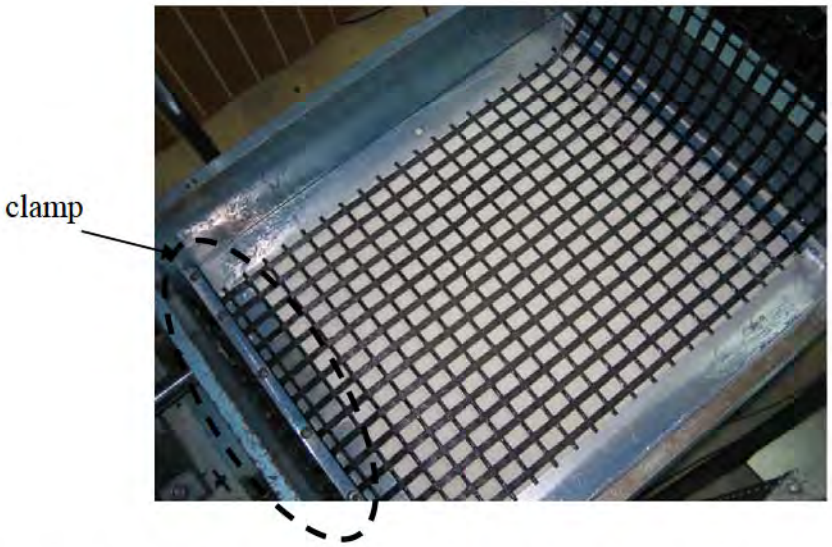

Figure 2. Geosynthetic specimens are clamped on the lower shearing box

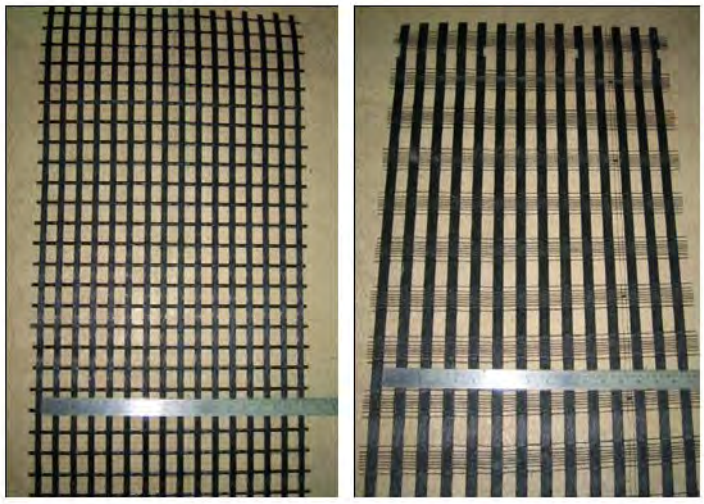

(a) GG3 □ □ □ □ □ (b) GG5

Figure 3. Geosynthetic specimens GG3 and GG5

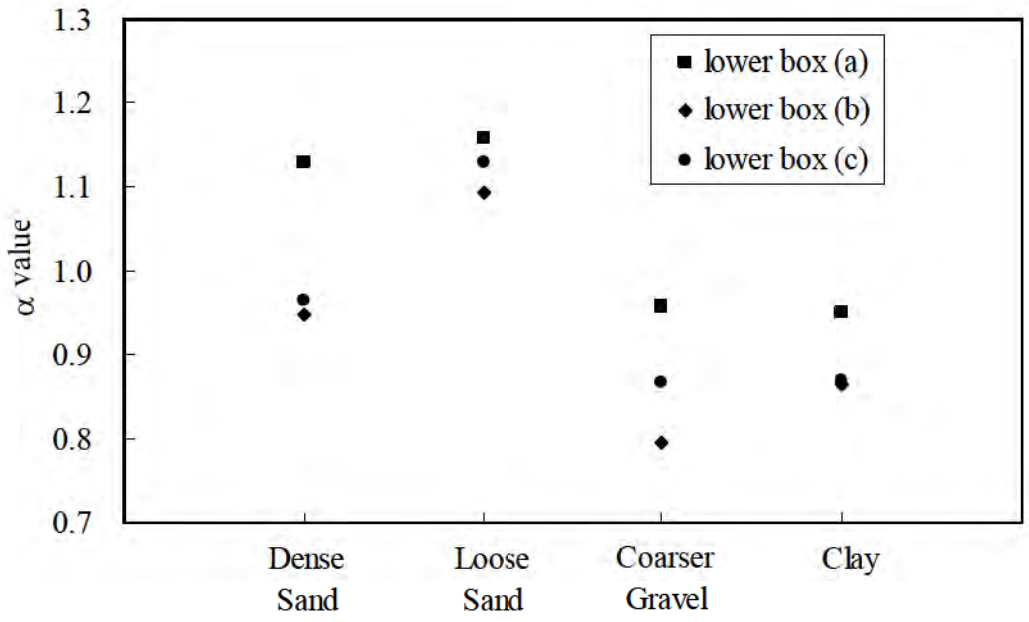

Figure 4. Interface shear strength coefficient of soil/GG3 interfaces for different set up of lower shear box

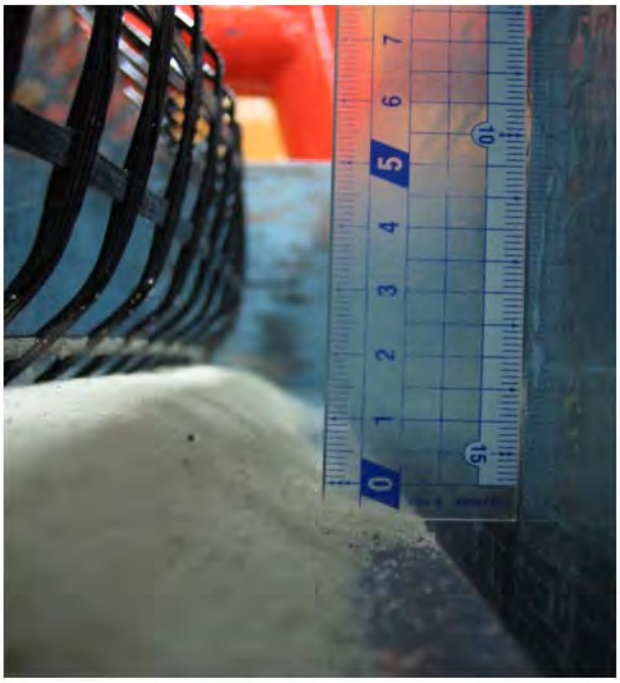

Figure 5. Soil particles are extruded out of shear box and heave up at the front edge of lower, larger shear box.

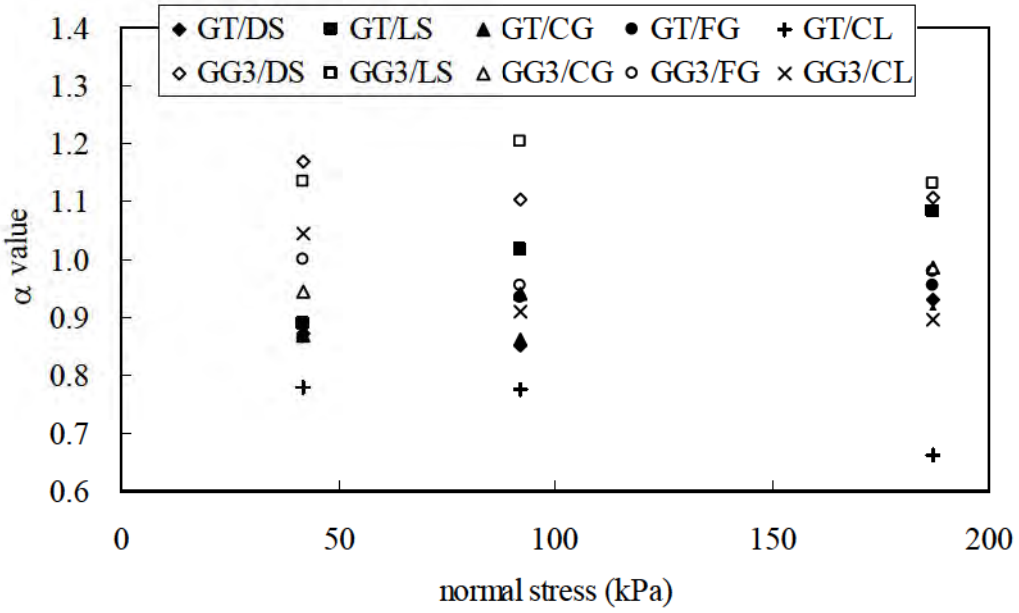

Figure 6. Interface shear strength coefficient of soil/Geotextile and soil/GG3 interfaces (use lower shear box (a)).

ANALYSIS OF GEOSYNTHETIC REINFORCED SOIL RETAINING WALLS USING COMPOSITE MATERIAL PROPERTIES

Wei F. Lee, Taiwan Construction Research Institute; Michael D. Harney, Shannon & Wilson Inc; Robert D. Holtz and Pedro ArduinoUniversity of Washington

ABSTRACT

This paper presents the theory of a composite material approach for the numerical analysis of geosynthetic reinforced soil (GRS) walls at working stresses. The methodology of interpreting laboratory test data using the approach is described, and to illustrate the approach, results of the numerical analysis of a GRS wall are presented. It is shown that the GRS composite approach is capable of explaining the behavior of GRS composites in different principal directions as well as and simplifying numerical analysis techniques for GRS walls.

INTRODUCTION

Probably the most common present design method for internal stability of GRS retaining walls is the tie-back wedge technique (Christopher and Holtz, 1985; Holtz et al., 1997). Because so few failures of GRS retaining walls have occurred, this method must be very conservative. Furthermore, because the method is based on limiting equilibrium conditions at the ultimate or failure stress state, in cannot in principle predict wall face deformations nor provide information on stresses in the reinforcement before failure. To improve performance prediction and design procedures for GRS walls, GRS walls must be analyzed under working stresses and this requires numerical methods.

However, numerical analyses of GRS walls are not simple because of the significant difference in geometry and engineering properties between the soil and geosynthetic reinforcement. For example, a very large aspect ratio element has to be built to model the geosynthetics and a large number of interfaces used to model the soil-geosynthetic interaction. Moreover, because a GRS element has different directional stress-strain behavior due to the presence of the reinforcement, different reinforcing mechanisms are assumed in different principal directions. In this context, the concept of homogenization, or composite material properties, offers a promising approach to simplify numerical analysis. Analytical models that use this concept represent the behavior of the reinforced soil composite as an equivalent homogeneous material.

In this paper, theory for analyzing GRS behavior using a composite material approach is described. Then the methodology for applying a composite approach to analysis of laboratory GRS test data will be presented. This approach is used to analyze behavior of the GRS composite under different working stresses. Finally, preliminary results of a case study utilizing GRS composite properties and numerical modeling to reproduce the instrumentation measurements from a 12.6 m high GRS retaining wall will be described.

This paper presents the basic theory of a composite material approach for analysis of geosynthetic reinforced soil, and investigates the feasibility of using the approach in numerical analysis of wall performance. Composite moduli of a GRS element are determined using

transversely isotropic model developed by Lee (2000) based on test results obtained from a plane strain geosynthetic-soil interaction device (Boyle, 1995). To verify the feasibility of the composite material approach, the performance of a high GRS retaining wall constructed at a major highway interchange the Rainier Avenue wall in Seattle, Washington, U.S.A. was back-analyzed. It is shown that the GRS composite approach is capable of both explaining the behavior of GRS composite in different principal directions, as well as offering simpler numerical analysis techniques.

TRANSVERSELY ISOTROPIC ELASTICITY MODEL FOR A GRS ELEMENT UNDER PLANE STRAIN LOADING

Figure 1 is a schematic diagram of a GRS element inside a reinforced soil wall. Note that in Fig. 1, the geosynthetic reinforcement is placed on a plane perpendicular to direction 1 and parallel to directions 2 and 3. The soil is reinforced in the horizontal directions by the tensile forces developed along the geosynthetic and then transmitted into the soil by friction. In the vertical direction, soil is also reinforced because additional resistance to gravitational force is provided by the horizontally placed reinforcement. Because the stress-strain behavior is different in the three principal directions, anisotropic orthotropic elasticity is used to characterize this behavior.

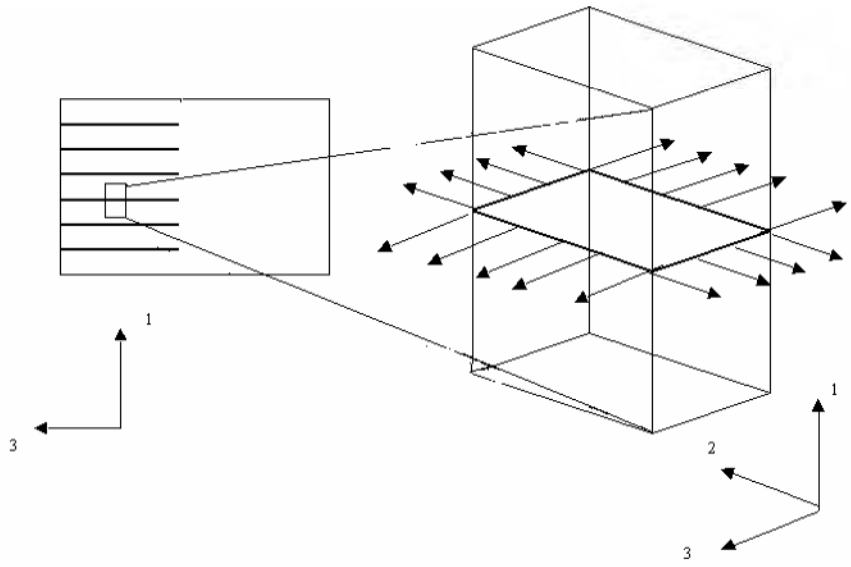

Figure 1. Geosynthetic Reinforced Soil Element.

Because this research concentrated on moduli in principal directions, only the normal stresses part of an orthotropic anisotropic elasticity matrix was used. In Eq.1, E1, E2, E3, ν32, ν23, ν13, ν12, ν21, and ν31 are the composite moduli and Poisson's ratios of the GRS element in the principal directions. To further simplify the problem, it was assumed that the geosynthetic has same in-soil stress-strain and strength properties in both the machine and cross machine directions. Based on this assumption, the same stress-strain behavior was assigned to directions

2 and 3. For the stress-strain behavior of a GRS element inside a retaining wall, plane strain loading conditions are appropriate; i.e., there is no strain in direction 2. Equations 1 to 3 then are the three equations representing the transversely isotropic elasticity model for a GRS element under plane strain loading conditions. Equation 1 can be simplified to transversely isotropic elasticity (Eq.2) by using the relations: E1 =Ev, E2 =E3 =Eh, ν32 = ν23 =νhh, ν31 = ν21 =νhv, and ν13 = ν12. =νvh. The composite moduli of the GRS element can then be determined using this model as long as adequate material test data is available.

$$\begin{bmatrix} \varepsilon_{11} \\ \varepsilon_{22} \\ \varepsilon_{33} \end{bmatrix} = \begin{bmatrix} \frac{1}{E_1} & \frac{-\nu_{21}}{E_2} & \frac{-\nu_{31}}{E_3} \\ \frac{-\nu_{21}}{E_1} & \frac{1}{E_2} & \frac{-\nu_{32}}{E_3} \\ \frac{-\nu_{31}}{E_1} & \frac{-\nu_{23}}{E_2} & \frac{1}{E_3} \end{bmatrix} \cdot \begin{bmatrix} \sigma_{11} \\ \sigma_{22} \\ \sigma_{33} \end{bmatrix} \tag{1}$$

$$\begin{bmatrix} \varepsilon_{11} \\ \varepsilon_{22} \\ \varepsilon_{33} \end{bmatrix} = \begin{bmatrix} \frac{1}{E_v} & \frac{-\nu_{hv}}{E_h} & \frac{-\nu_{hv}}{E_h} \\ \frac{-\nu_{vh}}{E_v} & \frac{1}{E_h} & \frac{-\nu_{hh}}{E_h} \\ \frac{-\nu_{vh}}{E_v} & \frac{-\nu_{hh}}{E_h} & \frac{1}{E_h} \end{bmatrix} \cdot \begin{bmatrix} \sigma_{11} \\ \sigma_{22} \\ \sigma_{33} \end{bmatrix} \tag{2}$$

Equations 3 to 5 are expanded from Eq.2 with plane strain loading conditions applied. These three equations therefore represent the transversely isotropic elasticity model for a GRS element under plane strain loading conditions. Composite moduli of the GRS element can be determined using this model with adequate material testing data, e.g., from the test results of the Unit Cell Device (UCD).

$$\nu_{hv} = \frac{\sigma_{22} - \nu_{hh}\sigma_{33}}{\sigma_{11}} \tag{3}$$

$$E_h = \frac{1}{\varepsilon_{33}} \cdot \left[B \cdot \sigma_{11} + (1 - C) \cdot \sigma_{33} \right] \tag{4}$$

$$E_v = \frac{E_h \cdot \sigma_{11}}{\varepsilon_{11} E_h + A\sigma_{11} - B\sigma_{33}} \tag{5}$$

where $A = \nu_{hv}^2$, $B = -\nu_{hv} - \nu_{hv}\nu_{hh}$, $C = \nu_{hh}^2$. Also $\nu_{vh} = \nu_{hv} E_v/E_h$.

INCREASED CONFINING PRESSURE CONCEPT AND EFFECTIVE SOIL CONFNING PRESSURE

Two hypotheses have been proposed to explain the fundamental mechanism by which reinforcing acts to improve the load-supporting capability of soil:

1. the reinforcing provides an apparent cohesion to the soil (Schlosser and Long, 1972), and
2. the effective confining pressure experienced by the soil increases due to tension which develops in the reinforcement when it is elongated (Yang and Singh, 1974).

Unit Cell Device tests by Boyle (1995) verified the Yang and Singh hypothesis: the tension developed in the reinforcement during straining increases the lateral pressure acting in the soil, thereby increasing the soil strength. Boyle (1995) was able to directly compute the effective lateral confining stress (effective soil confining pressure, or ESCP) in the UCD tests because the end area of the specimen was known and the load in the reinforcement was measured. Effective soil confining pressure is defined as:

$$ESCP = \sigma_{3C} + \frac{T}{B \cdot H} \qquad (6)$$

where:

ESCP = effective soil confining pressure (kPa),
σ_{3C} = lateral confining pressure acting on the soil-reinforcement composite (kPa),
T = tension in the reinforcement (kPa),
B = width of the composite (m),
H = height of the composite(m).

COMPOSITE GRS MODULI

In order to verify the analytical model developed above, test data obtained from the Unit Cell Device (UCD) were used to interpret composite moduli of GRS. The UCD was designed and fabricated in the University of Washington to test a GRS element under plane strain loading conditions. The UCD specimen models a GRS element shown in Fig. 1 with dimension of 100 mm in width and 200 mm in length and height (Boyle, 1995; Boyle and Holtz, 1994; Boyle et al., 1996). Both in-soil properties of geosynthetics and GRS composite properties are measured in the device. Therefore, terms σ_{11}, σ_{22}, σ_{33}, ε_{11}, and ε_{33} in Eqs. 1 to 3 can be obtained by reducing the UCD test data. However, there are still four unknowns (E_v, E_h, ν_{hh}, and ν_{hv}) remaining in these equations. Numerical analysis is performed to solve them. The steps of the numerical analysis are:

1. develop a spreadsheet to solve Eqs. 3 to 5,
2. insert a reasonable range of values for Poisson's ratio ν_{hh} into the spreadsheet, and
3. compute the composite moduli E_v and E_h using the spreadsheet.

UCD data interpretation--Twenty sets of UCD test data were used as input into the transversely isotropic elasticity model to obtain the composite GRS moduli. Four different types of geosynthetics at different confining pressures were tested. Table 1 lists names, material types, and 2% strain wide width tensile test moduli of geosynthetics used in the UCD tests. The effective confining pressures ranged from 10 kPa to 50 kPa. In this preliminarily investigation, stress and strain information were obtained from raw UCD test data when the lateral strain equaled an arbitrary 1%. To calculate the stress and strain information obtained from raw UCD test data, the lateral strain was sampled at 0.5%, 1%, 1.5%, and 2%. This stress and strain information were then reduced and applied to the transversely isotropic elasticity model to obtain the composite moduli of GRS reinforced by different geosynthetics at different effective soil confining pressures. The transversely isotropic elasticity model was also applied to soil-only tests to obtain the plane strain vertical and horizontal soil moduli. In this way, the reinforcing effect in both vertical and horizontal direction could be observed.

Table 1. Geosynthetic material used in UCD tests (Boyle, 1995).

Name	Material Type	2% M_{wwt} (kN/m)
GTF 200	Polypropylene	103
GTF 375	Polypropylene	204
GTF 500	Polypropylene	357
GTF 1225	Polyester	1126

2% M_{wwt} = secant moduli from wide width tensile test (ASTM 4595)at 2 % strain.

Composite GRS moduli--Figure 2 shows the horizontal composite moduli of GTF 200 material which were sampled at different lateral strain levels. As shown in the figure, the composite moduli are increased with effective soil confining pressure; and decreased as the lateral strain level increased.

Figures 3 and 4 show the horizontal and vertical composite moduli of both soil and GRS. The soil-only tests show that plane strain horizontal soil moduli are larger than vertical because the UCD specimens were prepared in a plane strain cell and compacted to the desired density during specimen preparation. As shown in Figs. 3 and 4, both vertical and horizontal GRS composite moduli increase as the effective soil confining pressure increases for each type of geosynthetic reinforcement. For different geosynthetics, one can see that the tendency that composite moduli increase as the in-isolation tensile moduli (2% M_{wwt}) of the geosynthetic reinforcements increase. In both the vertical and horizontal directions, GRS composite moduli are found to be larger than plane strain soil moduli. This shows that the geosynthetic contributes to the reinforcing function in the horizontal as well as in the vertical direction. Moreover, all the horizontal GRS composite moduli are found to be larger than all the vertical GRS moduli under the effective soil confining pressure range tested by Boyle (1995). This result confirms that the horizontal direction is the major reinforcing direction.

Figure 2 Horizontal composite moduli of GRS for GTF200 at different horizontal strain and with ν_{hh}=0.3.

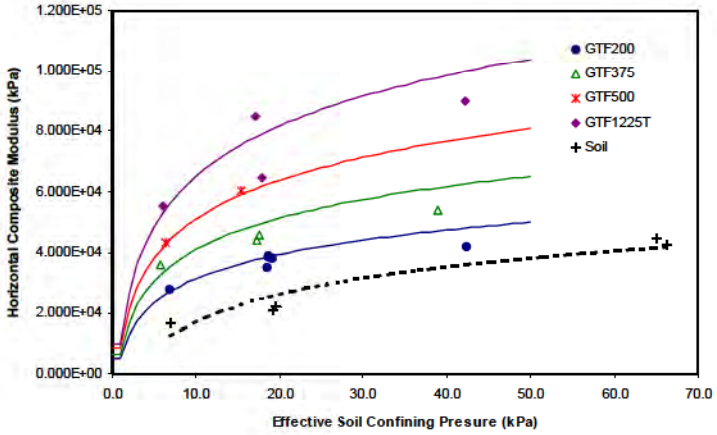

Figure 3 Horizontal composite moduli of GRS at 1.0% horizontal strain and with ν_{hh}=0.3.

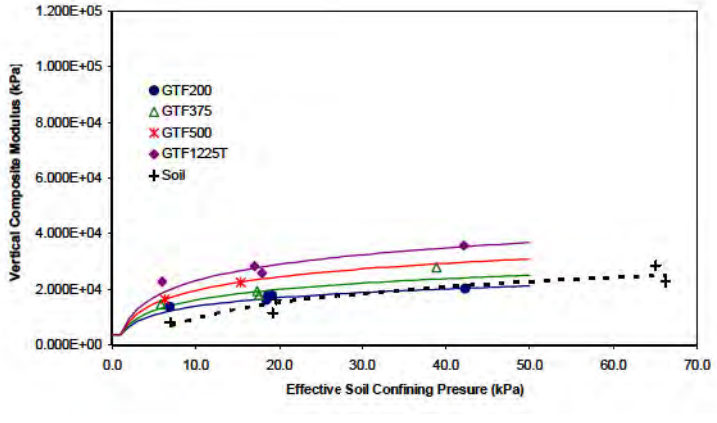

Figure 4 Vertical composite moduli of GRS at 1.0% horizontal strain and with ν_{hh}=0.3.

CASE STUDY

To verify the feasibility of the developed composite material approach, the performance of a rather high GRS retaining wall constructed at Rainier Avenue and Interstate 90 in Seattle, Washington, was back-analyzed. The Rainier Avenue wall was built in 1989 to a height of 12.6 m and supported a surcharge more than 5 m high. Its purpose was to retain a temporary preload fill for the foundation of a bridge abutment. Four different types of reinforcing geotextiles were used, and they were the same materials used in the UCD tests, except that the GTF 1000 was later replaced by GTF 1225T during construction. However, GTF 1000 and 1225T geotextiles are both multifilament woven polyesters and they have similar strength properties. The reinforcement geotextiles were placed in the Rainier Avenue wall at a uniform vertical spacing of 0.38 m in a classical wrapped-face construction. Table 2 lists the location and number of layers of each geosynthetic. The Rainier Avenue wall was fully instrumented to monitor its performance, and Figure 5 shows the instrumentation cross section of Rainier Avenue wall.

Table 2. Location and layers of geotextiles in Rainier Avenue wall.

Geotextile	Location from bottom of wall, (m)	Layers and layer numbers
GTF 1000	0 – 3	8 (1-8)
GTF 500	3 – 6	8 (9-16)
GTF 375	6 – 9	8 (17-24)
GTF 200	9 – 12	9 (25-33)

To simulate the performance of the Rainier Avenue wall, two numerical models, COMPA and COMPS, were developed using the computer program FLAC, a finite difference program (Itasca Consulting Group, 1993). Both COMPA and COMPS were composite property models consisting of anisotropic elastic material elements with these input properties: horizontal modulus, vertical modulus, and the horizontal-vertical plane shear modulus. Model COMPA simulated the Rainier Avenue wall performance at the end of construction, while model COMPS simulated the wall performance after applying the surcharge.

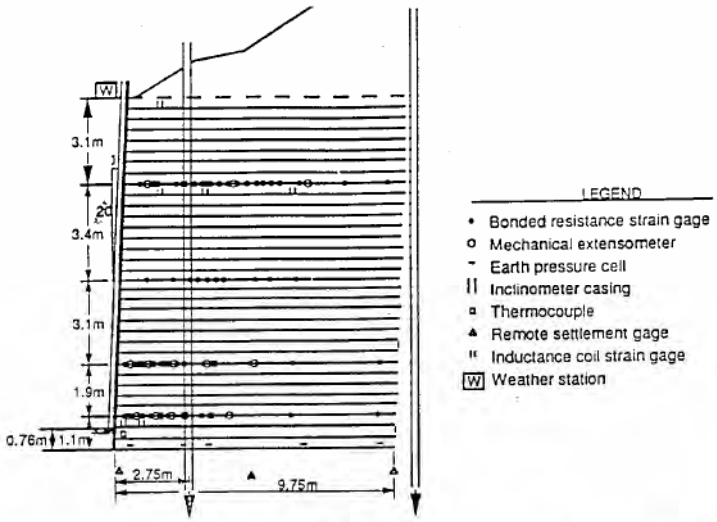

Figure 5 Instrumentation cross section of Rainier Avenue wall. (after Allen et al. 1992)

The GRS composite strength properties were used as the input properties for both models COMPA and COMPS. Eqs. 7 and 8 were also used to calculate the moduli numerically (from the curves shown in Figs. 2 and 3). Development of both equations are described in detail by Lee (2000)

$$M_{HC} = A \cdot \log \sigma_{ESCP} + B \tag{7}$$

$$M_{VC} = C \cdot \log \sigma_{ESCP} + D \tag{8}$$

where M_{HC} = horizontal GRS composite modulus (kPa),
M_{VC} = vertical GRS composite modulus (kPa), and
A, B, C, D = coefficients determined using UCD test data (Table3). Units of A and B are dimensionless; C and D have units of kPa.

Table 3. Coefficients A, B, C, and D of Eqs. (7) and (8) for GRS composite moduli at 1% horizontal strain and ν_{hh}=0.3.

Geosynthetic	A	B	C	D
GTF 200	10500	4000	4500	2500
GTF 375	12500	6000	5000	3000
GTF 500	16500	8000	6000	3500
GTF 1225T	22500	9000	8000	3700

Figure 6 shows the prediction of lateral deformation from numerical analysis at 3m behind the wall, along with the inclinometer measurements at the same location. Both models COMPA and COMPS show reasonable agreement with the inclinometer measurements, both at the end of construction and after surcharge was applied. As shown in Fig. 6, model COMPS tended to

underestimate the deflections at the upper portion of the wall, probably because the input properties of both models were sampled and reduced at 1% horizontal strain. Measurements of strain gages and extensometers (Table 4) indicated that the Rainier Avenue wall had horizontal strains close to 1% at the end of construction and larger than 1% after surcharge in the upper portion of the wall (Holtz et al., 1991; Allen et al., 1992). Model COMPA indicated that the wall had horizontal strains less than 1% below elevation 25.75 m and close to 1% above this elevation; model COMPS also indicated horizontal strains less than 1% below elevation 25 m and larger than 1% above this elevation.

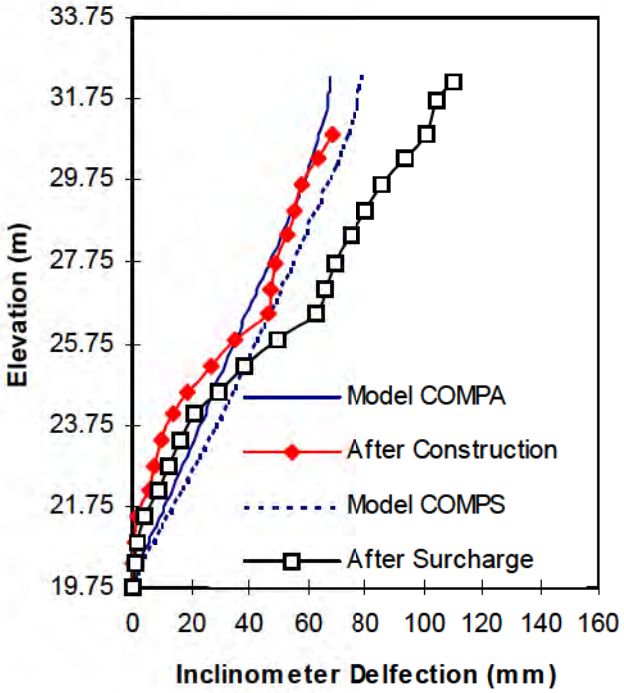

Figure 6. Results of Deflections of Models COMPA and COMPS at 3m behind Wall Face.

Table 4. Measurements of strain gages and extensometers inside the Rainier Avenue wall at locations 3m behind wall face (after Allen et al. 1992).

Elevations (m)	End of Construction		After Surcharge	
	SG (%)	ES (%)	SG (%)	ES (%)
21.27	0.25	--	0.31	--
23.17	0.4	0.45	0.6	0.6
26.21	0.9	--	1.2	--
29.63	0.8	--	1.4	--

SG = strain gage measurements
ES = extensometer measurements

CONCLUSIONS

1. The feasibility of analyzing GRS composite properties using the newly developed transversely isotropic elasticity model has been demonstrated.

2. Different composite moduli of GRS elements were found in different principal directions using the transversely isotropic elasticity model.
3. The assumption that different reinforcing mechanisms exists in different principal directions inside a GRS wall is verified.
4. This paper verifies that the GRS composite properties obtained from UCD test combined with an adequate numerical model is a feasible composite approach of modeling behavior of reinforced soil structures. The approach also simplifies numerical analyses of these structures.

ACKNOWLEDGEMENT

We thank the Washington State Department of Transportation for funding much of this research.

REFERENCES

Allen, T.M., Christopher, B.R., and Holtz, R.D., (1992), "Performance of a 12.6 m high geotextile wall in Seattle, Washington", *Geosynthetic-Reinforced Soil Retaining Walls*, Int. Symp. on Geosynthetic-Reinforced Soil Retaining Walls. Balkema Publ., pp. 81-100.

Boyle, S.R., (1995), "Deformation Prediction of Geosynthetic Reinforced Soil Retaining Walls", *PhD. Dissertation*, University of Washington, Seattle, U. S. 391p

Boyle, S.R., and Holtz, R.D., (1994), "Deformation Characteristics of Geosynthetic-Reinforced Soil", *5th International Conference on Geotextiles and Geomembranes and Related Products*, Singapore. Vol.1 pp. 361-364.

Boyle, S. R., Holtz, R. D., and Gallagher, M. (1996) "Influence of Strain Rate, Specimen Length, and Confinement on Measured Geotextile Strength Properties", *Geosynthetics International*, Vol. 3, No. 2, pp. 205-225.

Christopher, B.R., and Holtz, R.D. (1985), "Geotextile Engineering Manual", Report No. FHWA-TS-86/203, Federal Highway Administration, Washington, DC, U. S., March 1985, 1044p.

Christopher, B.R., Holtz, R.D., and Allen, T.M. (1990), "Instrumentation for a 12.6 m high geotextile-reinforced wall", *Performance of Reinforced Soil Structures*, British Geotechnical Society Conference, Glasgow, U. K. pp. 73-78.

Holtz, R.D., Allen, T.M., and Christopher, B.R., (1991), "Displacement of a 12.6 m high geotextile-reinforced wall", *Proc. Tenth European Conference on Soil Mechanics and Foundation Engineering*, Florence, France. pp. 725-728.

Holtz, R.D., Christopher, B.R., and Berg, R., (1997), *Geosynthetic Engineering*, BiTech, Inc, Vancourver, BC, Canada, 452 pp.

Itasca Consulting Group, (1993), "Fast Lagrangian Analysis of Continua Version 3.2", Itasca Consulting Group, Inc., Minneapolis, MN, U. S. Vol. I, II, III,

Lee, W. F. (2000), "Internal Stability Analyses of Geosynthetic Reinforced Retaining Walls", *PhD Dissertation*, University of Washington, Seattle, 380p.

Schlosser, F., and Long, N.T., (1972), "Recent Results in French Research on Reinforced Earth," *Journal of the Construction Division*, ASCE, Vol. 100, No. CO3, pp. 223-237.

Yang, Z., and Singh, A. (1974), "Strength and Deformation Characteristics of Reinforced Sand," *National Meeting on Water Resources Engineering*, ASCE, Los Angeles, Reprint 2189.

CONTACT:
Robert Holtz, PhD, PE
Professor of Engineering
University of Washington
Dept of Civil & Environmental Engineering
Box 352700
Seattle, WA
Phone: 206-543-7614
Email: holtz@u.washington.edu

Roads & Highways

Laboratory Test Studies of Concrete Slab over Triplanar Drainage Geocomposite

Jianjun Leng, Ph.D, PE, Tenax Corporation ; Aigen Zhao, Ph.D, PE, , Tenax Corporation; Roger H. L. Chen, Ph.D, Dept. of Civil and Environmental Engineering, West Virginia University; Joseph G. Sweet, Graduate Research Assistant, Dept. of Civil and Environmental Engineering, West Virginia University

ABSTRACT

As a pavement subsurface drainage alternative, triplanar drainage geocomposite has advantages over natural drainage materials in maintaining its flow capacity and compressive stiffness under the construction and service loads. This paper presents laboratory test studies of mechanical properties of concrete specimens over triplanar drainage geocomposite. Initial drying shrinkage within the normal concrete specimens has a greater rate than that of concrete specimens over geocomposite, and concrete cast on geocomposite has an average drying shrinkage of 9% less than that of concrete cast with a standard mold. The frictional study of concrete blocks cast over the geocomposite demonstrated that a strong bond exists between the geocomposite and concrete, so the governing friction behavior is that between the geocomposite and subgrade. The fatigue behaviors of concrete beams placed on top of geocomposite and soft subgrade were investigated.

BACKGROUND: PERMEABLE BASE PRACTICE OF CONCRETE PAVEMENTS

Concrete pavements have been widely used for highways, airports and streets. Concrete is by far the most rigid pavement material, which spreads wheel loads over large areas of the subgrade and yields small vertical deflections of pavements. However, concrete pavements are subject to cracking, due to traffic loads and environmental factors (changes of temperature and moisture). While contraction joints or reinforcing steel can be used to control cracking, it is also important to maintain uniform support and positive subsurface drainage in order for concrete pavements to perform throughout their service life. Critical concrete pavement distress, related to and accelerated by excess moisture and poor drainage conditions, includes pumping, faulting, and corner break (caused by erosion and loss of support beneath the corners or edges of concrete pavement slabs). Permeable base has been increasingly used to drain subsurface water away from the pavement system. Permeable base has much less fine particles than a typical dense graded base, with typical permeability from 3.5 × 10-3 m/sec (1,000 ft/day) to 3.5 × 10-2 m/sec (10,000 ft/day). Permeable base may be stabilized with Portland cement or asphalt to withstand construction traffic.

DRAINAGE GEOCOMPOSITE UNDER CONCRETE PAVEMENTS

An alternative for improving drainage of concrete pavements is to incorporate a triplanar geocomposite drainage layer under concrete pavement, which is tied into roadway edge drains as shown in Figure 1. This configuration directly removes the infiltration water entering the pavement system through cracks and joints before it enters the underlying subbase/subgrade. In addition, the geocomposite prevents fines of subbase or subgrade from pumping at the pavement cracks and joints by providing filtration and separation.

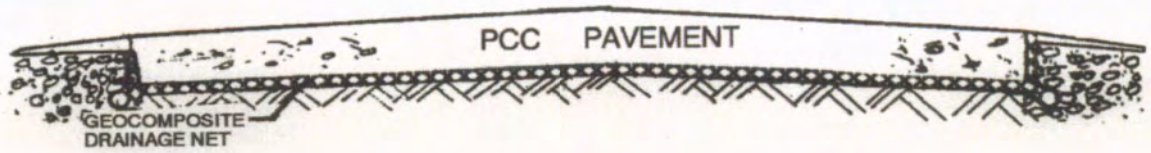

Figure 1
. Use of Geocomposite as Drainage underneath Concrete Pavement

A typical triplanar geocomposite placed under concrete pavement is hydraulically equivalent to 10 cm of open graded permeable base with hydraulic conductivity k = 2.4 × 10-2 m/sec (6,800 ft/day). Different from natural open-graded drainage materials, which usually have weak structural stability and are exposed to contamination by finer soils during or after construction, the triplanar geocomposite can maintain the voids and hydraulic performance under the construction loads and conditions.
A drainage coefficient Cd is included in AASHTO design method of rigid pavement (AASHTO, 1993). Table 1 provides the recommended values depending on the quality of drainage and the percent of time during the year of the pavement structure exposed to the moisture levels approaching saturation. 1. The configuration in Figure 1 allows the pavement to be designed using a higher drainage coefficient Cd. A side benefit of this configuration may be more uniform concrete hydration (research is ongoing to determine the extent of this benefit).

Table 1. Recommended values for drainage coefficient for rigid pavements (AASHTO, 1993).

Quality of Drainage	Percent of time pavement exposed to moisture levels approaching saturation			
	Less than 1%	1 to 5%	5 to 25%	More than 25%
Excellent	1.25-1.20	1.20-1.15	1.15-1.10	1.10
Good	1.20-1.15	1.15-1.10	1.10-1.00	1.00
Fair	1.15-1.10	1.10-1.00	1.00-0.90	0.90
Poor	1.10-1.05	1.00-0.90	0.90-0.80	0.80
Very Poor	1.00-0.90	0.90-0.80	0.80-0.70	0.70

Concrete pavement slabs will inevitably undergo cracking due to stresses induced by temperature fluctuations and drying shrinkage, and additional cracking may occur due to traffic loading. The cracking characteristics of concrete slab, in particular the sizes and spacing of the cracks, will determine the quality of performance and the life span of the concrete slabs. It is crucial to understand exactly how the use of a drainage geocomposite layer affects the cracking pattern and performance of concrete slabs. An experimental study of concrete pavement supported by triplanar geocomposite was conducted at West Virginia University, including concrete drying shrinkage and compressive strength, frictional resistance between concrete block and the underlying layers, geocomposite stiffness and modulus of subgrade reaction.

CONCRETE CURING AND DRYING SHRINKAGE

The presence of drainage geocomposite under the concrete slab helps the concrete slab to reach the commonly required water-vapor emission rate in a shorter period of time by providing additional porosity at the bottom. Shrinkage testing per ASTM C490 and water loss analysis were conducted on 27.8 cm × 7.6 cm × 7.6 cm (11-inch × 3-inch × 3-inch) concrete specimens with and without geocomposite.

The results of concrete specimens at two different w/c ratios (0.47 and 0.57) showed that concrete specimens cast on the geocomposite shrank less, as the concrete cures more rapidly in the initial stage leaving less water and causing less shrinkage. As seen in Figure 2, initial drying shrinkage within the normal specimens has a greater rate than that of the specimens cast on geocomposite. After a period of time, the drying shrinkages within both sets occurred at approximately the same rate. On average, concrete cast on the geocomposite has 9% less drying shrinkage than that of concrete cast with standard mold.

Figure 2. Shrinkage results of concrete samples (with 0.57 w/c ratios)

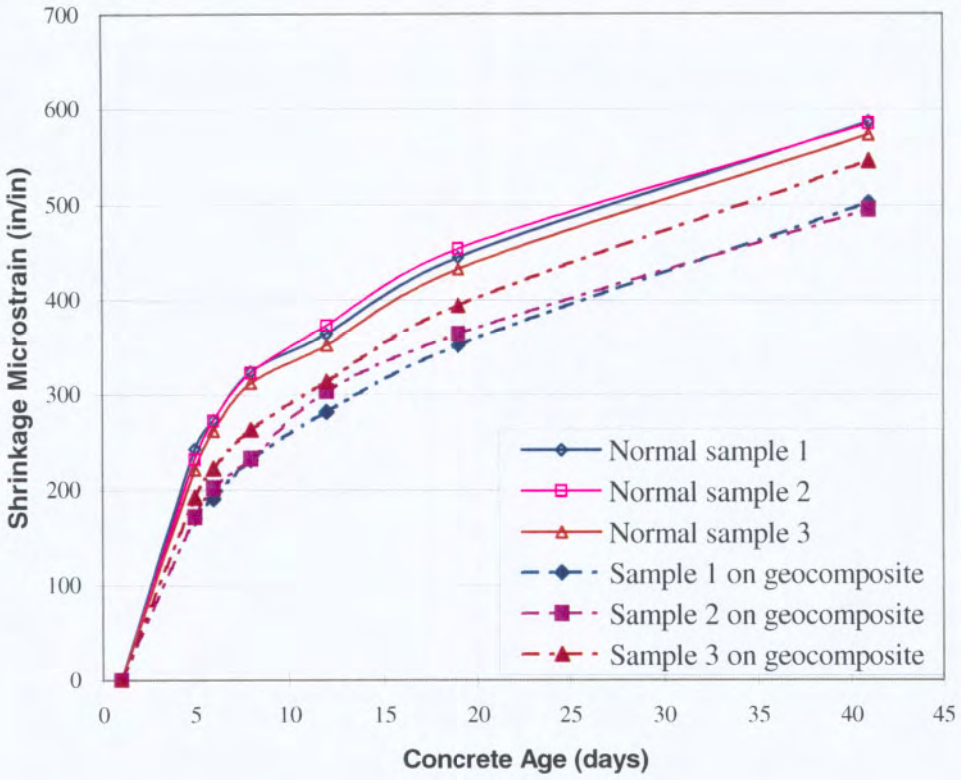

INTERFACE FRICTION BEHAVIOR

The frictional resistance provided by the underlying layer has a large influence on the cracking behavior of the pavement (Chen, et al, 2002). The friction behavior was investigated by push tests of concrete blocks (60-cm x 60-cm x 30-cm) cast on top of the geocomposite, as shown in

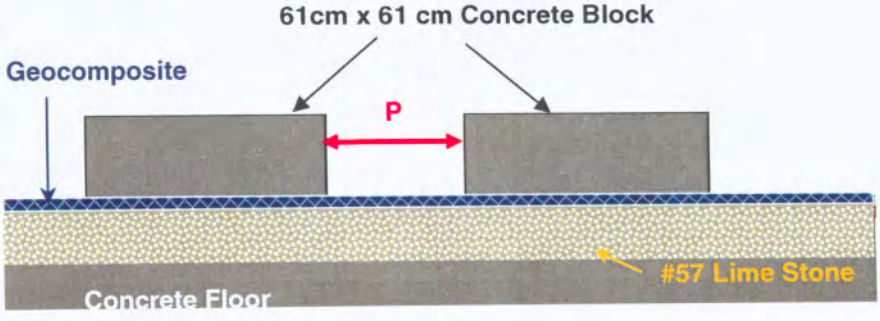

Figure 3, at different ages of concrete as well as different water cement ratios.

Figure 3. Schematic of push test setup

It was found that at even very early stages of concrete maturity, a strong bond is present between the geocomposite and concrete, where the governing friction behavior is the interface between the geocomposite and subgrade. No significant difference in the performance of the frictional resistance was observed when w/c ratio was varied from 0.47 to 0.57, as shown in Figure 4. A friction coefficient of about 0.68 was determined between the geocomposite and gravel subbase (#57 lime stone) in Figure 5.

The traditional subgrade drag method () is frequently used to determine the amount of shrinkage and temperature steel reinforcement as:

$$A_s = \frac{F L w}{2 f_s}$$

Where, As = cross section area of steel, F = coefficient of subgrade friction, L =slab length, w = weight of slab, fs = allowable working stress of reinforcement.

By applying the friction coefficient of 0.68, the introduction of geocomposite underneath concrete yields a reduced required amount of steel reinforcement against thermal expansion and shrinkage, compared to a typical friction coefficient of 1.5 for concrete floors on ground (Cook, 2004).

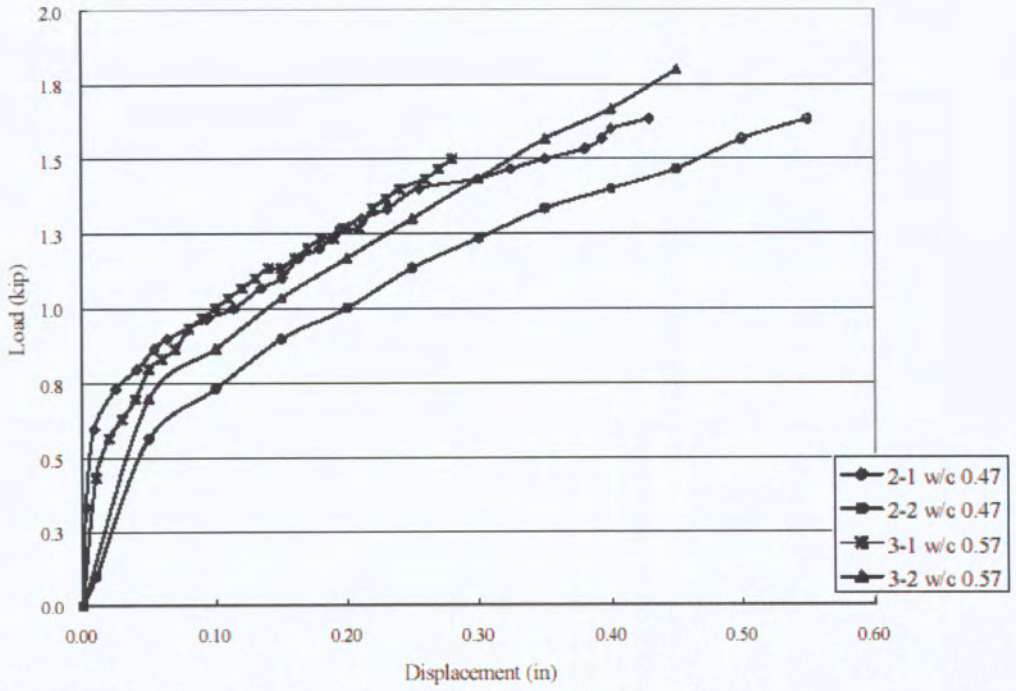

Figure 4. Push test results at two different w/c ratios

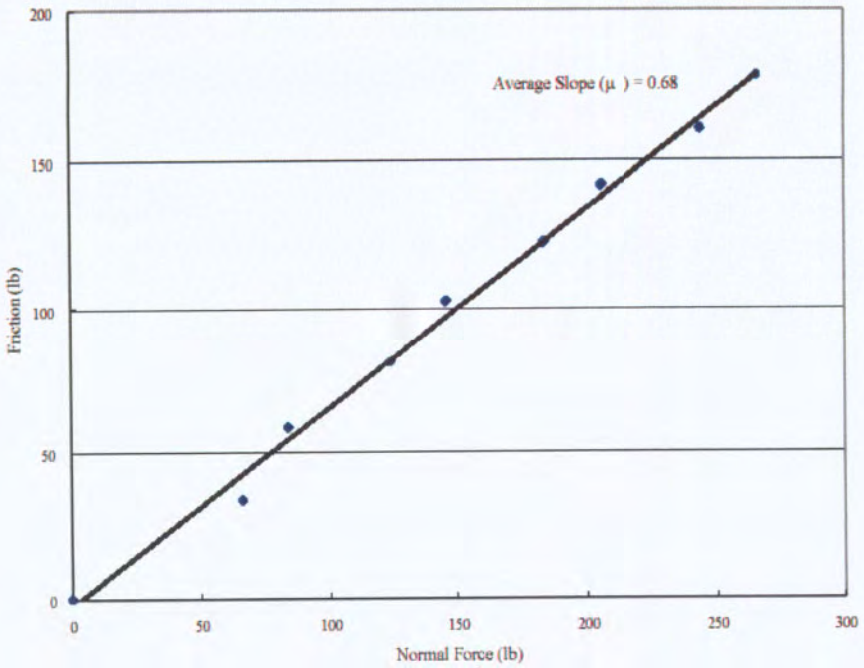

Figure 5. Interface friction resistance between geocomposite and gravel subbase

VERTICAL STRESSES UNDER PCC SLABS

In order to determine the approximate magnitude of stresses to which a geocomposite layer would be subjected when used in the field directly underneath a concrete pavement structure, a simplified Finite Element (FE) Analysis was done by Sweet and Chen (2005) on an un-doweled JPCP (jointed plain concrete pavement) section. The results of this FE analysis should give higher subbase stresses than stresses obtained from a doweled JPCP or a CRCP (continuously reinforced concrete pavement). The stress levels obtained would provide guidelines for the laboratory experiments done throughout this study.

The section had dimensions of 4.58 m (15 feet) in length, 3.66 m (12 feet) in lane width, and a depth of 0.20 m (8 inches). It was supported by a 3-layer system, comprised of a 0.15-m (6-inch) subbase course and a 0.46-m (18-inch) compacted subgrade; all underlying layers had dimensions of 6.40 m (21-foot) in length and 5.49 m (18-foot) in width. Solid brick elements were used to create the concrete slab, the subbase and the compacted subgrade, and the nodes at the bottom of the subgrade were assumed to be fixed. For simplicity, all materials were assumed to be linear-elastic, with the contact surfaces between the materials assumed to be bonded. The loading applied to the slab had the geometry of a typical dual-wheel, tandem truck axle. A load of 22.2 kN (5,000lbs) was applied to each wheel, totaling 177.9 kN (40,000lbs) for the axle. The contact area was reduced to a point load for each wheel, and the axle was placed as close to the corner of the slab as possible in order to obtain the highest localized stress values. Figure 6 shows the schematic of the modeled section. Figure 7 shows the cross-sectional view of the maximum principal stresses with concrete slab removed to expose the subbase. It can be seen that a typical stress for a sub-base for a non-dowelled JPCP can reach levels around 482 kPa (70 psi).

Subbases for dowelled JPCPs and CRCPs experience much smaller stress levels, since the shear transfer of these pavements distributes the axle load to multiple slabs and consequently over a larger area. ACPA (1995) describes these as being only about 20.7 kPa (3psi), while Childs and

Nussbaum (1962) cites the maximum subbase pressures due to a 40.0 kN (9,000lbs) load exerted on the corner of a 0.20-m (8-inch) concrete slab as about 124.1 kPa (18psi).

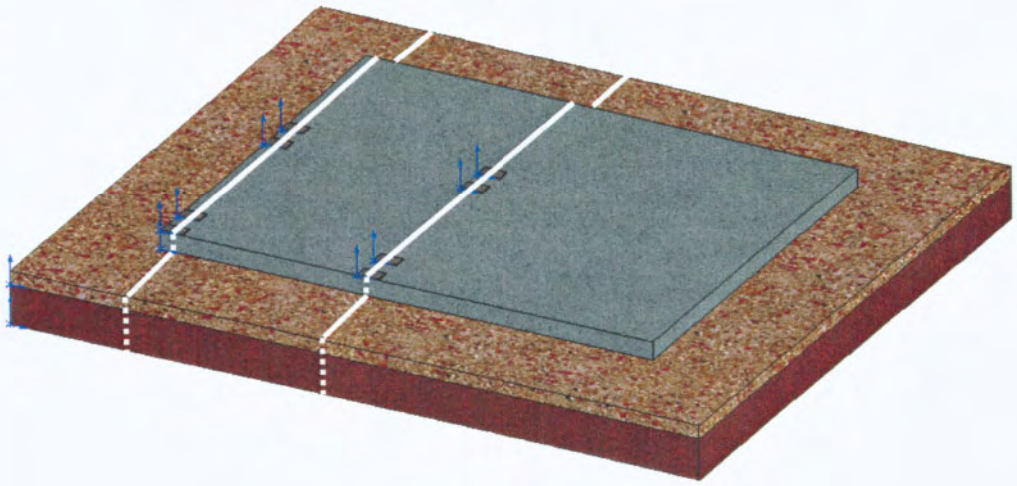

Figure 6. Schematic of FEM model

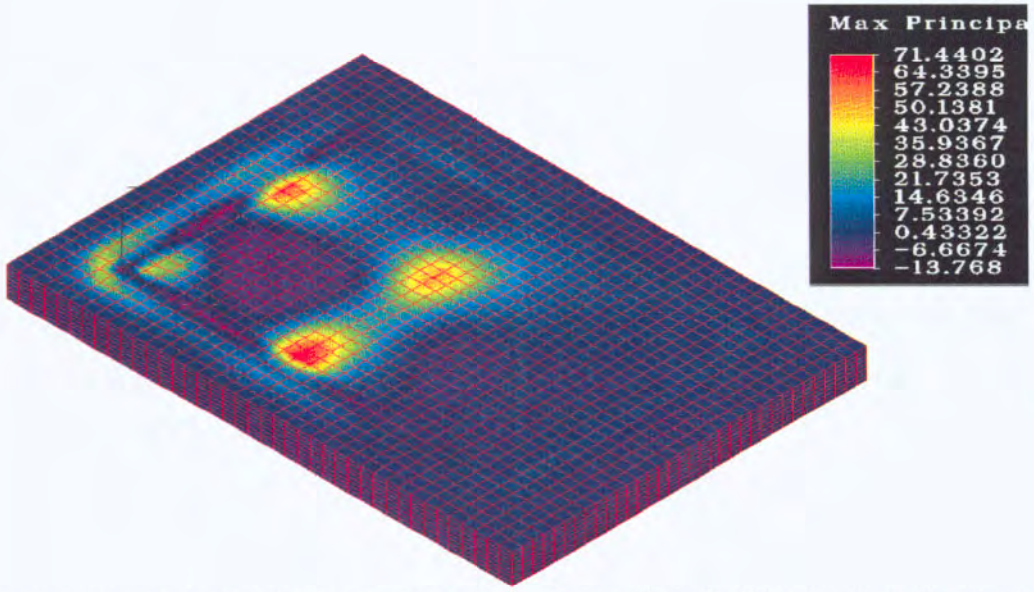

Figure 7. Maximum Principal Stresses obtained from the Finite Element Modeling with Slab Removed to Expose Subbase Surface.

Cyclic Fatigue Behaviors

As reported by Christopher and Zhao (2001), a larges-scale cyclic loading testing was previously conducted at the University of Illinois Advanced Transportation Research and Engineering Laboratory. The tested concrete beams were supported by the triplanar geocomposite overlying a clay subgrade and compared to results from a beam supported by the subgrade alone. The tests were performed at stress ratios (i.e., load versus ultimate beam strength) of 0.76 and 0.83. The test setup along with representative results at the higher stress level is shown in Figure 8. The test at the 0.83 stress ratio showed some improvement in fatigue life and the test at 0.76 stress ratios showed some reduction in fatigue life. Although the test results were inconclusive in relation to fatigue life, the results showed that the geocomposite improved post-cracking behavior of the beam at both stress levels. This improvement in beam performance was attributed to betterment in the uniformity of support under the beam after cracking and/or frictional improvement at the bottom of the beam, which reduced the post-cracking deflection.

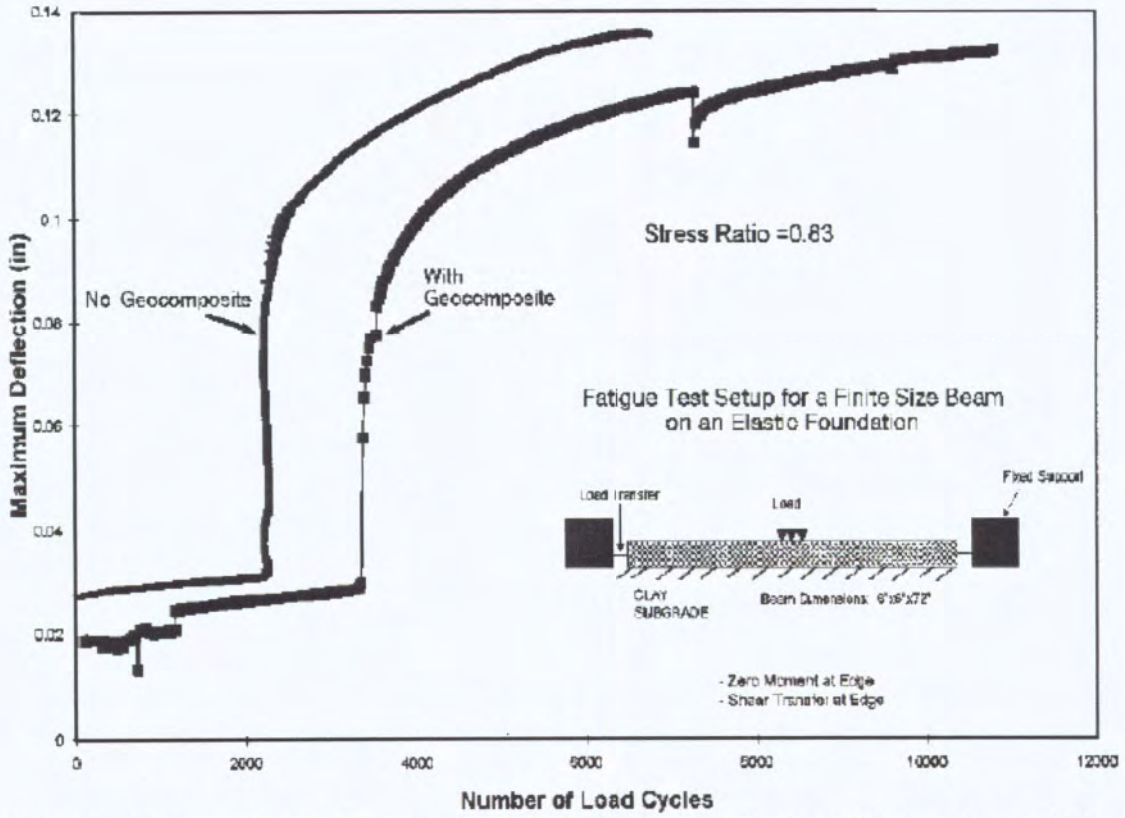

Figure 8. Fatigue Test of Concrete Beam on Clay Subgrade, from Christopher and Zhao (2001)

CONCLUSIONS

With superior hydraulic capacity and constructability, a triplanar drainage geocomposite shows great potentials as an alternative of the gravel drainage underneath concrete slabs. This study summarized a series of laboratory test studies on the mechanical properties of concrete specimens over the triplanar drainage geocomposite. Concrete specimens cast over the geocomposite show less drying shrinkage than that of concrete cast with a standard mold, and have about the same compressive strength. The frictional study of concrete blocks cast over the geocomposite demonstrated that a strong bond exists between the geocomposite and concrete, so

the governing friction behavior is that between the geocomposite and subgrade. The fatigue tests of concrete beams on a clay subgrade indicated that the presence of triplanar geocomposite improved post-cracking behavior of the concrete beams.

REFERENCES

American Association of State Highway and Transportation Officials (AASHTO), AASHTO Guide for Design of Pavement Structures, Washington, D.C., 1993.

American Concrete Pavement Association (ACPA), Subgrades and Subbases for Concrete Pavements Technical Bulletin TB011.02P. ACPA, Skokie, IL, 1995

Sweet, J. and Chen, H. L., "Vertical Stiffness Characterization of a TRIPLANAR GEOCOMPOSITE Drainage Layer for PCC Highway Pavement Design", Final Report (draft), submitted to Tenax Corporation, 2005.

Childs, L. D. and P. J. Nussbaum "Pressures at Foundation Soil Interfaces Under Loaded Concrete and Soil-Cement Highway Slabs," Proceedings of the American Society for Testing and Materials, Vol. 63, pp 1243-1263., 1962.

Christopher, B.R., Hayden, S.A., and Zhao, A., "Roadway Base and Subgrade Geocomposite Drainage Layers," Testing and Performance of Geosynthetics in Subsurface Drainage, ASTM STP 1390, J.S. Baldwin and L.D. Suits, Eds., American Society for Testing and Materials, West Conshohocken, PA., 1999.

Christopher, B. C. and Zhao, A., "Design Manual for Roadway Geocomposite Underdrain Systems", Tenax Corporation Document, Baltimore, MD., 2001.

Cook, J. B., "Frictional Resistance of Concrete on a Geocomposite Material", M. S. Thesis, West Virginia University, Morgantown, WV, 2004.

CONTACT:

Jianjun Leng, Ph.D, PE
Design Engineer
Tenax Corporation
4800 East Monument Street
Baltimore, MD, 21205
Phone: 410-522-7000
Email: jjleng@tenax.com

GEOTEXTILES FOR DUST CONTROL ON UNPAVED ROADS

Elisabeth A. Freeman, Burns & McDonnell; John J. Bowders (corresponding author), Civil & Environmental Engineering Department University of Missouri-Columbia

ABSTRACT

Dust can be a health concern because of its potential to contain respirable particles. Although numerous techniques are used in attempts to control dust generated from gravel roads, all have limitations and the search for more effective means of reducing dust levels continues. Geotextile separators offer the potential to reduce dust while providing enhanced driving characteristics and reduced maintenance of the roads. A field demonstration program was performed to quantitatively document the dust suppression effect of geotextile separators on unpaved, gravel-surfaced roads. The test site, located in Boone County, Missouri included two, 100-m geotextile test sections and a 100-m control section. Two nonwoven geotextiles (AASHTO Class 2), one a spunbonded and the other a needle-punched were used. Sampling events were taken to evaluate the effectiveness of the geotextiles for dust control. Initially, dust collected on the control section was 20 to 30% of the pre-geotextile dust levels. Over a six month period the dust levels in the control section increased and ranged from 80% to 230% of the pre-geotextile dust levels. Dust levels from the geotextile sections also increased. After six months in service, the control section contained 23 percent silt sized particles while the geotextile sections contained from 6 to 12 percent silt size particles. The US EPA's emissions factor calculation showed the geotextile section to reduce the dust emissions factor by 50 to 75 percent compared to that for the control section (58 Lbs/Vehicle Mile Traveled).

INTRODUCTION

Dust is a health concern because of its potential to contain respirable particles, particulate less than 10 microns in size (PM10). It can also be a safety issue and a nuisance for residents living in the vicinity of gravel roads (Figure 1). Numerous techniques (chlorides, resins, natural clays, asphalts, soybean oil, and others) are used in attempts to reduce the dust generated from gravel roads. All have limitations and the search for more effective means of reducing dust levels from gravel roads continues (Skorseth and Selim 2000).

Figure 1 - Gravel road test section located at the City of Columbia, Missouri landfill.

Anecdotal evidence suggests that dust from gravel roads is reduced for roads that incorporate a geotextile separator. Geotextile separators offer the potential to reduce dust while providing enhanced driving characteristics and reduced maintenance of roads. The later is well documented (Amoco Fibers 2000); however, the dust reduction function is not. The concept is that dust particulate originates from fines in the subgrade which migrate upward into the gravel surface over time. Vehicular traffic causes the fines in the gravel to be mobilized into the atmosphere. It is well recognized that geotextile separators limit the migration of fines into the overlying aggregate and also the intrusion of aggregate into the subgrade (Figure 2) (Holtz et al. 1997; Koerner 1998). Thus, adding a geotextile separator will reduce the amount of fines in the aggregate layer and therefore should decrease the dust generated from a gravel road.

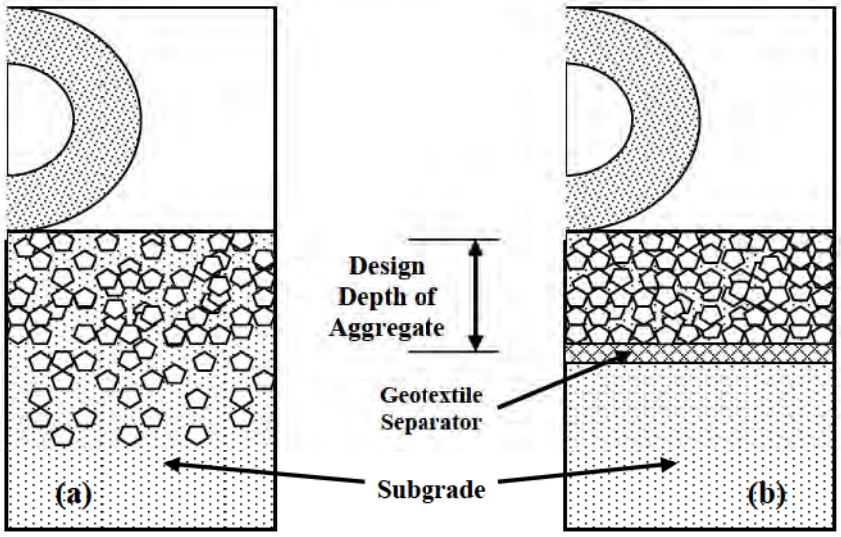

Figure 2 - Unpaved road (a) without and (b) with a geotextile separator.

The objective of the research was to quantify the effectiveness of geotextile separators in reducing the dust generated from gravel roads. In this paper, we review the results of the field demonstration program and focus on the effect that a geotextile separator can have on the calculated emissions including the annual assessment fee for air emissions.

FIELD DEMONSTRATION PROGRAM

A gravel road at the City of Columbia, Missouri landfill was used for the field demonstration. The general geographic area is located at the border between the glaciated high plains and the transition to the Ozark Plateau (Missouri State Highway Commission 1962; Unklesnay and Vineyard 1992). It is in the drainage basin of the Missouri river and is characterized as a humid climate with an annual average precipitation of 1200 mm. The surficial soils are primarily loess with some areas of glacial till (Young, Radatz and Marshall 2001). At the Columbia landfill site, very little loess remains at the roadway test section. The subgrade consists of crushed limestone that has intruded into the underlying glacial till. The upper 150 mm was firm to hard and was sampled for grain size analysis. Results showed the material to range from poorly graded gravel

(GP), poorly graded sand (SP), to well graded sand (SW) (Unified Soil Classification System, USCS) (Table 1).

A field monitoring program was implemented to determine the quantity and characteristics of dust generated at gravel road sites. The program consisted of using a system of dust collection pans (Freeman and Bowders 2007). The landfill road runs north-south and provides access to the administration building and the recycle center. It is typical for recycle bin rolloff trucks, two-axle cars and trucks, and other landfill maintenance vehicles to use the road. Vehicle types, number of passes per day and approximate weight of vehicles are given in Table 2. The roadway test section receives a total of about 140 passes per week from the combination of vehicles.

Table 1 - Grain size characteristics of the subgrade at the unbound road test section.

		Sample Number		
Property	**Opening Size (mm)**	**1**	**2**	**3**
Cu	---	173	31	19
Cc	---	0.7	0.7	1.3
Passing #10	2	34	42	47
Passing #40	0.4	21	25	20
Passing #200	0.07	5	4	4
USCS	---	GW	SP	SW
Max. Size (mm)	All material passed the 25 mm sieve and about 90% passed the 19 mm sieve.			

During the sampling periods, dust generation was made by driving a two-axle 2,100 kg pickup truck across the unbound roadway sections alternating between keeping the vehicle in the middle of the road and to the sides of the road. Traveling the length of the roadway in one direction was counted as one pass. Additional vehicles that traveled the road during testing were included in the number of passes. The vehicle was driven at an average speed of 32 to 34 kph, the posted speed for the road. The mass of dust per unit area was determined based on the surface area of the collection pans and mass of dust collected. A dust generation rate was calculated by dividing the mass per unit area by the number of vehicle passes used to generate the dust. All dust generation rates were normalized to 30 (one-way) passes of the vehicle.

Table 2 - Vehicle type and frequency on gravel road test section.

Vehicle Type	**Passes**		**Estimated Average Weight (kg)**
	Monday-Friday	**Saturday**	
Small Cars/Trucks	60	10	1,400

Roll-Off, Tandem Axle	4	0	25,000
Roll-Off, Single Axle	30	0	13,600
Mini Roll-Off, Tandem Axle	6	0	8,200
Split-Hopper, Tandem Axle	29	0	18,100

RESULTS OF GEOSYNTHETIC AND CONTROL SECTIONS

Two, 100-m long by roadway width geosynthetic test sections and a control section (new aggregate, no geotextile separator) were installed on September 29, 2005 at the landfill site. Non-woven, needle-punched (NW-NP) and non-woven, spunbonded (NW-SB) AASHTO Class 2 geotextiles were installed (Table 3). The top surface of the road consisting of old aggregate and fines was removed, the geotextiles were placed on the subgrade, and a new gravel layer was placed on the geotextiles and the control section. Clean aggregate (passing 25 mm sieve openings), the standard for gravel roads in this region, was provided from the local quarry. The subgrade classified as poorly graded gravel to well graded sand (Table 1), while the surface aggregate was classified as poorly graded gravel (USCS). An average thickness of 130 mm of aggregate was placed on the two geotextile sections and 70 mm on the control section.

The roadway was actively sampled for dust on four occasions. The initial dust sampling took place on October 5, 2005 which was one week after installation of the geotextiles. The remaining dust samplings occurred on January 19, February 14 and March 29, 2006. For each sampling date, dust generation was made by completing 30 passes (1 pass = one-way travel the length of the roadway) for each sampling and alternating between keeping the vehicle in the middle of the road and to the sides of the road. Additional vehicles that traveled the road during sampling events were included in the number of passes. The cumulative monthly precipitation, number of vehicle passes and sampling dates are presented in Figure 3.

The dust levels (g/m2/30 passes) measured during the sampling dates for the geotextile and control sections are presented in Figure 4. Sampling date number 1 (October 5, 2005) was just five days after installation of the geotextiles and control sections. There was no precipitation during this period and the roadway underwent approximately 140 routine vehicle passes as described in Table 1. The wind speed was 5 to 15 kph in a northeast direction and the relative humidity was 72 percent. On the upwind (west) side of the road dust levels were measured around 0.2 g/m2/30 passes and showed little variation between geotextile and control sections. The dust levels on the downwind (east) side of the road were slightly greater than those on the upwind side. The dust levels ranged from 0.11 to 0. 38 g/m2/30 passes.

Table 3 – Properties of the geotextiles used in the dust control demonstration.

		Nonwoven, Needle- Punched (NW-NP)	**Nonwoven, Spunbonded (NW-SB)**

Property	Test Method	Minimum Average Roll Value	Minimum Average Roll Value
Mass/Unit Area (g/m^2)	ASTM-D5261	200	140
Grab Tensile (kN)	ASTM-D4632	0.711	0.710
Grab Elongation (%)	ASTM-D4632	50	60
Mullen Burst (kPa)	ASTM-D3786	2135	
Puncture (kN)	ASTM-D4833	0.400	0.250
Trapezoidal Tear (kN)	ASTM-D4533	0.285	0.27
UV Resistance	ASTM-D4355	70 % at 500 hrs	70 % at 500 hrs
AOS[(1)] (mm)	ASTM-D4751	0.212	0.200
Permittivity (sec^{-1})	ASTM-D4491	1.1	0.5
Flow Rate ($L/min/m^2$)	ASTM-D4491	3340	2050

AOS = Apparent Opening Size

We found increased dust levels on sampling date number 2 (January 19, 2006). The roadway had undergone about 2210 passes of routine vehicles. There was approximately 50 mm of precipitation over the 30 days prior to dust sampling. The wind speed was 13 to 22 kph in a northeast direction and the relative humidity was 40 percent. Dust levels on the upwind side of the road ranged from 0.07 to 0.76 g/m2/30 passes with the control (no geotextile) showing about twice as much dust as the geotextile sections. The downwind monitoring showed two to three times as much dust as the upwind monitoring with the dust levels ranging from 0.62 to 1.96 g/m2/30 passes. The control showed slightly higher dust levels than the non-woven, needle-punched geotextile. The non-woven, spunbonded geotextile section showed the lowest dust generation.

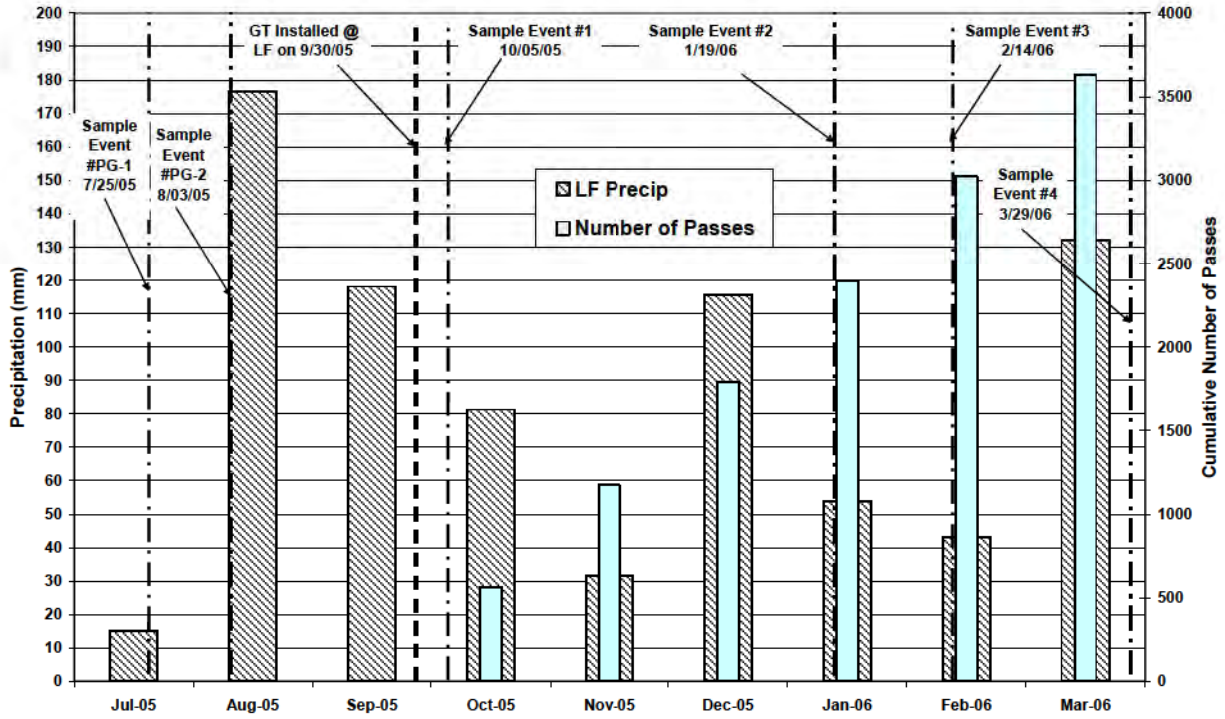

Figure 3 - Monthly precipitation, number of vehicle passes and dust sampling events.

Sampling date number 3 (February 14, 2006) showed dust levels similar to those measured during the second sampling date. About 40 mm of precipitation occurred between the second and third dust sampling dates, and the road had undergone about 2540 vehicle passes since installation of the test sections. Upwind dust levels ranged from 0.10 to 0.71 g/m2/30 passes while the downwind dust levels ranged from 0.77 to 2.81 g/m2/30 passes. The dust levels for the non-woven, needle-punched geotextile were higher and in some cases up to twice the level for the spunbonded geotextile and control sections. No explanation is available for this observation. The relative humidity was 37 percent, lowest of all the sampling dates and the winds were 11 to 23 kph in a northeast direction.

The 4th sampling date (29 March 2006) produced dust levels slightly lower than those measured in the second and third sampling dates. The dust levels on the upwind side of the road ranged from 0.02 to 0.15 g/m2/30 passes. On the downwind side of the road, dust levels ranged from 0.34 to 1.26 g/m2/30 passes. The geotextile sections showed dust levels similar to the control (no geotextile section). The wind speed was 8 to 13 kph and the relative humidity was 56 percent. The highest dust levels were recorded for the sampling date with the lowest relative humidity. Approximately 3630 vehicle passes were made on the roadway between the time of installation to the 4th sampling period.

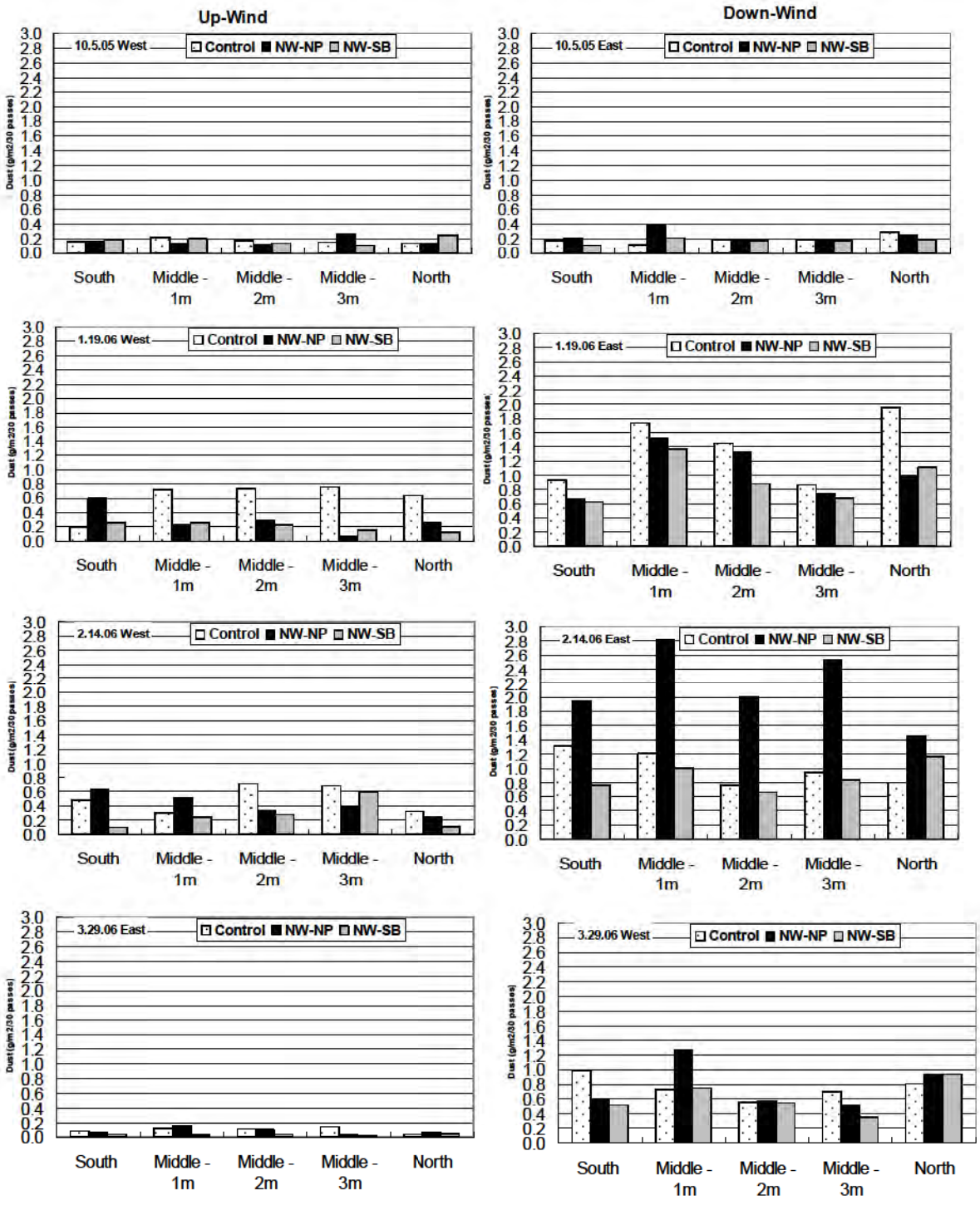

Figure 4 - Distribution of dust levels for gravel road control and geotextile test sections.

The dust rates were averaged for all collection pans at each test section for each sampling date and these are presented in Figure 5. The results indicate that the dust generation rate increased

over time. Recall the gravel layer was placed on September 29, 2005 so it was in place six months by the final sampling date (March 29, 2006). During this time the number of vehicle passes increased at a constant rate to reach a total of more than 3600 passes. The downwind results show that there were lower dust levels from the geotextile separator layers, with the exception of the non-woven, needle-punched geotextile on February 2006 sampling date, compared to the control (no geotextile section). The differences in dust generation levels are not great but there does appear to be some benefit to having the geotextiles in place.

An issue that presented itself at this site is the fact that the subgrade is competent and the unbound aggregate is relatively soft. A modified slake durability test (ASTM D4644) was performed on the aggregate and the resulting durability index was 80 percent indicating a soft, degradable aggregate (Freeman 2006). Although the geotextiles may be limiting the migration of fines from the subgrade into the unbound layer, fines generated from degradation of the aggregate may collect on top of the geotextile resulting in a source of dust particles

Samples of the surface aggregate were collected prior to placement of the test sections, at the time of placement of the new aggregate (September 29, 2005) and during the second third and fourth dust sampling dates. Sieve analyses were performed on each sample (ASTM D 422). The distributions showed that the aggregate is degrading over time (and under traffic). The percentage of fines increased indicating increasing particulate source in the roadway. The samples from the control (no geotextile) showed a higher accumulation of fines than those from above the geotextile separator.

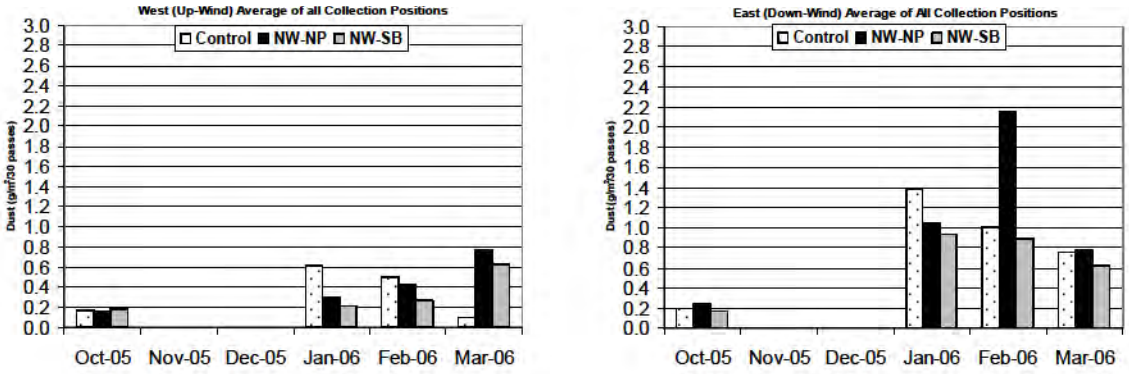

Figure 5 - Dust rates averaged for all collection pans presented for each test section during each sampling date.

The percentage of fines (particles passing 0.075 mm sieve) are shown versus time in Figure 6. At the time of placement, the aggregate contained about three percent fines. After four months in place (October through January), there was 6 to 12 percent fines in the aggregate placed above the geotextile and 23 percent fines in the unbound layer in the control section. The results were similar for the March sampling period which was six months after installation.

Clearly the percentage of fines in the unbound layer increased with time (time is a surrogate for number of vehicle passes). However, the increase in fines in the gravel layer above the geotextile separators was one-half that in the gravel layer in the control section. The indication here is that

the geotextile separators are acting to keep fines in the subgrade from migrating into the unbound layer. The geotextiles are reducing the fines in the gravel layer and ultimately the source for airborne particulate; however, the low quality aggregate used in the unbound layer readily degrades under traffic and provides significant fines above the geotexiles and ultimately a source for dust. It is also possible that in the Control section the aggregate "dug" into the subgrade resulting in increased particle-to-particle crushing campared to that on the geotextile sections.

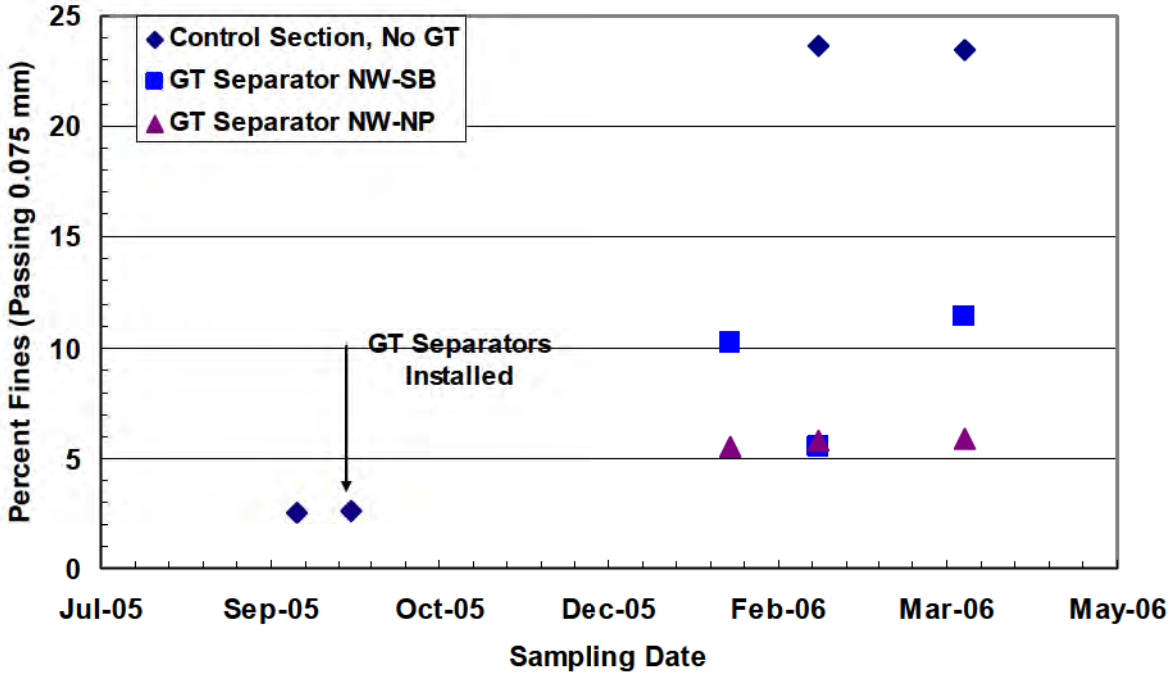

Figure 6 - Percentage of fines contained in the gravel layer versus time. Samples from the geotextile (GT) test sections were collected from the material overlying the geotextile.

REGULATORY EMISSIONS MONITORING PROGRAM

The Missouri Department of Natural Resources (MDNR, 2006) acting under the direction of the US Environmental Protection Agency (US EPA) requires facility owners, (in this case the City of Columbia) to perform and submit an annual Emission Inventory Questionnaire (EIQ). The EIQ is a self-reporting method for estimating particulate emissions from facilities including roads owned by the reporting entity. An annual fee is then assessed based on the quantities of emissions, particularly PM10, calculated and reported in the EIQ. The EIQ includes a procedure to estimate the amount of particulate generated from unpaved roads (US EPA 1998, 2006).

We used the EIS to calculate the estimated dust emissions (PM10) from the gravel road test section. The US EPA's default values were used in the calculation process and then compared to the resulting emissions using site specific measured input parameters. In addition, we used input

parameters from the test sections containing the geotextiles to evaluate the effect of the geotextiles on the resulting emissions factor.

An empirical expression for estimating the emissions from unpaved roads was developed by the US EPA (Equation 4-9 in US EPA 1998) and is given as Equation 1. Equation 1 has been modified according to US EPA (1998, 2006) protocol to calculate dust from gravel roads that is of the 10 µm (PM10) particle size. For our case a 200 m section of gravel road, the test section at the landfill, was used for estimation of the dust emissions.

$$E = k * \frac{\left(\frac{s}{12}\right)^a \left(\frac{W}{3}\right)^b \left(\frac{365 - p}{p}\right)}{\left(\frac{M}{0.2}\right)^c} \qquad \text{Equation 1}$$

where:

E = Emission Factor for particle size 10 µm (PM10) (Lbs/Vehicle Mile Traveled (VMT))
s = Surface Material Silt Content (%)
W = Mean Vehicle Weight (tons)
= (Unloaded Weight + Average Loaded Weight)/2
p = Number of Days with At Least 0.01 Inches of Precipitation per Year
M = Surface Material Moisture Content (%)
The empirical factors: k = 2.6; a = 0.8; b = 0.4 and c = 0.3 modify Equation 1 to be emission size specific for PM10.

To determine the emission factor for PM10, MDNR specifies default values for the silt content (s = 8.3%) and the moisture content of the surface material (M = 0.2%). The silt content is in the lower quarter of the range of values (1.8-35%) and the moisture content is at the low end of the range (0.03-13%) used to develop the empirical expression. Using the default values results in a conservative (high) estimate of the PM10 emissions factor and in the case of the facility owner, a higher than need be annual assessment fee. The calculated emission factor for the gravel road test section (200 m) was 50 Lbs/VMT and the annual assessment fee would be $1300.

TRADITIONAL DUST CONTROL METHODS

The US EPA and MDNR permit reductions in the calculated emissions factor for various dust control strategies that a facility owner applies to the gravel road. The MDNR (2006) provides "efficiency factors" for several dust control strategies. The efficiency factors are inversely proportional to reduction factors that are applied to the calculated annual assessment in cases where a control strategy has been used. Dust control strategies include: spraying water on the gravel road (undocumented or documented) and spraying a surfactant. The efficiency factors and associated cost reduction factors for various control methods are shown in Table 4. Presently, there is no efficiency factor for geotextiles used as dust suppression in gravel roads although we have listed them in the table.

Using water, regardless of whether or not it is documented, is a temporary dust control measure. During dry periods, gravel roads may need to be watered several times each day. Surfactants, while longer lasting than water, also must be periodically reapplied to maintain dust control. At

the demonstration test section, watering the gravel roads is the preferred dust control method; however, the watering program is undocumented, i.e., the roads are watered when someone thinks they are too dusty. This affords the facility owners a 50 percent reduction in their annual assessment fee. The unit cost for watering is estimated to be $5/m2/year. Manufactured surfactants (resins, organic fluids, magnesium chloride and emulsions), if applied typically twice per year provide the owner a reduction factor of 90 percent. The in place costs for surfactants range from $0.5/m2/year to $2.8/m2/year (Freeman 2006). In order to arrive at an idea of the impact and value of using a geotextile for dust suppression in gravel roads we must look at the impact the geotextile has on the input factors in the emissions calculation (Equ. 1).

Table 4 - Dust Control Method, Efficiency Factor and Annual Assessment Reduction Factor for 200 m Gravel Road at the City of Columbia Landfill.

Control Method	Efficiency Factor (%)	% of Untreated Cost
None	0	100
Water	50	50
Water Documented	>50	<50
Surfactant Spray	90	10
Geotextile	To be determined	To be determined

EFFECT OF GEOTEXTILE SEPARATORS ON CALCULATED EMISSIONS

The sole dust reduction function of the geotextile separator is to reduce and maintain a low percentage of silt-size particles in the gravel layer. The silt content (s) is the only parameter that the geotextile separator will impact in the emissions calculation (Equ. 1). The silt content (percent fines) for the control and geotextile test sections versus sampling date were shown in Figure 6. Initially the silt content was about three percent in the control and the geotextile layer. After six months, the silt content in the control was 23 percent and in the geotextile sections it ranged from 6 to 12 percent. The moisture content of the surface material averaged two percent for the control and the geotextile sections. The range of silt contents was applied in Equ. 1 for a two percent moisture content and the resulting emission factors (Lbs of PM10/VMT) are shown in Figure 7. At the time of placement of the new aggregate, the test and control sections contained the same amount of silt (about 3 percent) and the estimated emission factor was 10 Lbs/VMT. After 6 months in service, the control section had 23 percent silt resulting in an emissions factor of 58 Lbs/VMT. However, after 6 months of service, the geotextile sections showed a range of silt contents from 6 to 12 percent and corresponding emissions factor from 18 to 32 Lbs/VMT. Clearly, the geotextiles were successful at maintaining a lower silt content in the road and this resulted in a 50 to 75 percent reduction in the calculated emissions factor.

The 50 to 75 percent reduction in the emission factor might be an appropriate starting place for an efficiency factor for geotextile separators as presented in Table 4. The geotextiles performed better than water sprayed on the road but not quite as well as the surfactants. It must be noted that while water must be sprayed frequently and surfactant bi-annually, the geotextile is likely to have a lifetime of several years. In essence, the geotextile could provide low maintenance, long term dust control for the gravel road. The unit cost for the geotextile separator ranged from

$0.5/m^2$ to $0.8/m^2$. Assuming the geotextiles perform well for several years, the annual unit cost would be less and economically they would far out perform water and surfactants.

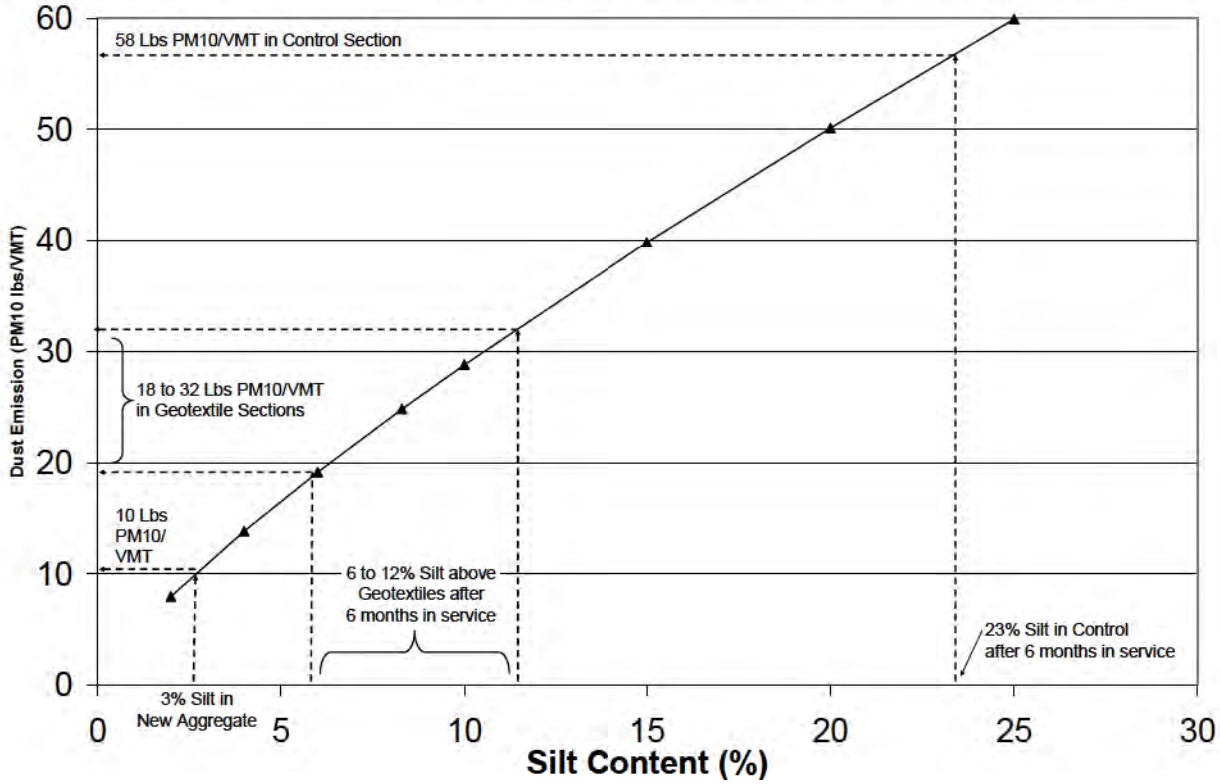

Figure 7 – Dust emissions factor versus silt content for the gravel road test section at the Columbia, Missouri landfill.

CONCLUSIONS

Dust from gravel roads can be problematic from health, safety, and general nuisance perspectives. Anecdotal evidence suggests that geotextile separators can reduce the amount of dust from gravel roads. Test sections including a two non-woven geotextile separators and a new aggregate-only layer were constructed and dust measurements were made over a six-month period, during which the road underwent more than 3600 vehicle passes. The following conclusions are based on observations made during the monitoring program:

- Dust levels were lowest immediately following the placement of new aggregate for the unbound layer.
- Dust levels increased with time (increased number of traffic passes).
- Initially the sections containing a geotextile separator produced slightly less dust than the control (no geotextile) section.
- After six months of service, dust levels from the geotextile and control sections were similar; however, the percentage of fines in the gravel layer above the geotextiles was about one-half the amount of fines in the control section.

Estimations of the dust emissions were made using the US EPA's methodology. The dust emission estimate for the control section (no geotextile) ranged from two to three times that for the road sections that incorporated a geotextile. The gravel used in this field demonstration is

known to be soft and easily degradable under traffic loading and thus provides a ready source for dust; however, even under these circumstances the geotextile showed evidence of dust suppression. The installed unit cost of the geotextile separator is competitive with other dust control techniques and in cases where the principal source of fines is from the subbase, and not from the surface aggregate, the geotextiles should provide even greater reduction in fines above the geotextile resulting in further reduction in the calculated emissions using the USEPA model.

ACKNOWLEDGEMENTS

The authors appreciate the assistance and collaboration of the many individuals and organizations working together to make this project possible. Mr. Mark L. Marienfeld, Propex Fabrics, initiated the project and provided valuable technical assistance. Mr. William Hawkins, BBA Nonwovens, provided valuable guidance and geosynthetic products. Gayla Neumeyer, City of Rocheport, and Cynthia Mitchell, Public Works, City of Columbia, kindly offered field sites. Dr. S.K. Loyolka of the Particulate Systems Research Center, University of Missouri, provided equipment and guidance for dust particle collection and analysis. The assistance of Wes Carmack, Jeffrey Bertel, Jianhua Li, Devi Tulasi, Joseph Chen and Young Kim all of the University of Missouri, has been invaluable.

Funding for this project was provided by the Geosynthetics Manufacturers Association (GMA). The authors greatly appreciate the continued support of the members of GMA.

REFERENCES

Amoco Fabrics and Fibers Company (2000) *Geotextile Enhanced Unpaved Roads Case History* No. 5, www.geotextile.com (Last accessed August 03, 2006).

Freeman, E (2006) "Geotextile Separators for Dust Suppression on Gravel Roads", *MS Thesis*, University of Missouri-Columbia, Department of Civil and Environmental Engrg, 137 pp.

Freeman EA and Bowders JJ (2007) "Geotextile Separators for Dust Suppression in Unbound (Gravel) Roads," *Proceedings* of the 9th International Conference on Low Volume Roads, Austin Texas, 24-27. in press.

Holtz RD, Christopher BR and Berg RR (1997) *Geosynthetic Engineering*, 1st Edition, BiTech Publishers Ltd., Richmond, British Columbia, Canada, 452pp.

Koerner RM (1998) *Designing with Geosynthetics*, 4th Edition, Prentice Hall, Englewood Cliffs, NJ, 761pp.

Missouri Department of Natural Resources (MDNR) (2006) *Emission Inventory Questionnaire*, http://www.dnr.mo.gov/forms/index.html#AirPollution#AirPollution, (last accessed 17 September 2006)

Missouri State Highway Commission (1962) *Geology and Soils Manual* 1962, Division of Materials.

Skorseth, K and Selim, AA (2000) *Gravel Roads Maintenance and Design Manual*, US Department of Transportation Federal Highway Administration, 104pp.

Unklesbay AG and Vineyard JD (1992) *Missouri Geology: Three Billion Years of Volcanoes, Seas, Sediments, and Erosion*, 1st Edition, Univ. of Missouri Press, Columbia, Missouri, 189pp.

U.S. Environmental Protection Agency (1998) *Emission Factor Documentation for AP-42 Section 13.2.2: Unpaved Roads Final Report*, EPA Purchase Order 7D-1554-NALX, MRI Project No. 4864, Research Triangle Park, NC, September.

US Environmental Protection Agency (US EPA) (2006) AP 42, Fifth Edition *Compilation of Air Pollutant Emission Factors, Volume 1: Stationary Point and Area Sources,* http://www.epa.gov/ttn/chief/ap42/index.html (last accessed 17 September 2006).
Young FJ, Radatz CA and Marshall CA (2001) *Soil Survey of Boone County Missouri*, USDA-NRCS, US Gov. Print. Office, Washington DC.

CONTACT:

Elisabeth A. Freeman
Geotechnical Engineer (Formerly, Graduate Research Assistant, Univ. of Missouri)
Burns & McDonnell
9400 Ward Pkwy
Kansas City, MO 64114
efreeman@burnsmcd.com

John J. Bowders (corresponding author)
Professor
Civil & Environmental Engineering Department
University of Missouri-Columbia
E2509 Lafferre Hall
Columbia, Missouri 65211
Phone: 573.882.8351
Fax: 573.882.4784
bowders@missouri.edu

Development of a Method to Test Geogrid Reinforcement of Base Materials in Flexible Pavements

Ayman Halim Abusaid, The University of Texas at Austin; Dr. Robert Gilbert, PhD, The University of Texas at Austin; C.Joel Sprague, PE, TRI Environmental, Inc.; John Allen, TRI Environmental, Inc.; Sam Allen, TRI Environmental Inc.

ABSTRACT

Full-scale road tests and large-scale laboratory tests have shown the benefit of inserting geogrids within or below the base layer of pavements. These performance tests are too expensive, time consuming and hence impractical to adopt as a part of a specification for geogrid reinforced pavements. On the other hand, common index properties of geogrids are not necessarily related to their performance in pavement systems. A bending stiffness index test described by Sprague *et al.* (2004) and Shields *et al.* (2005), developed to act as an indicator to the performance of geogrids in reinforcing the base material of pavements, was enhanced, analyzed and used to understand the basic mechanism of geogrid reinforcement.

An evaluation of the existing test procedure revealed significant variability in the test results. Consequently, the procedure was modified until repeatable and representative results were produced. Modifications to the test procedure included minimizing leaks in the test apparatus, improving the application of the confinement pressure, and replacing the static loading with a cyclic loading, which is more representative of vehicular loads applied on pavements.

The results of cyclic tests comparing the performance of geogrid-reinforced to unreinforced soil sections were related to the resilient modulus of pavements. An improvement of as much as 40 percent in the resilient modulus of the base layer of the pavement due to the insertion of a geogrid into the base was measured. Cyclic tests were used to investigate the mechanism by which a geogrid reinforces the base material of the pavement. It was shown that the development of tension in the geogrid is not necessary for reinforcement of the base material. Two basic mechanisms might be responsible for reinforcement: the interlocking between the geogrid and the soil and/or fiber reinforcement (localized tension) of the soil by the geogrid.

INTRODUCTION

Geogrid products are used to reinforce flexible pavements by inserting them within the base, within the subbase, at the base/subbase interface, or at the interface of the subbase with the subgrade. Berg *et al.* (2000) provided a summary of experimental work on the reinforcement of the base/subbase layers of flexible pavements up to the year 2000. The performance of the pavement sections reinforced with geogrids was evaluated by their corresponding Traffic Bearing Ratio (TBR) or Base Course Reduction (BCR). The summary provided by Berg *et al.* (2000) included results of twenty studies involving experimentations showing the benefit of using geogrids for reinforcing flexible pavements. TBR ranging from 0.8 to 670 and BCR ranging from 30 to more than 50 percent were reported. Miura *et al.* (1990) showed the general long term benefit of one layer of geogrid in a pavement to be comparable to that of a 10 cm base layer.

The two types of tests employed in experimentations on reinforced pavements were either tests with large-scale laboratory models of pavements or tests on field-scale pavement sections.

Although these tests are useful in showing the benefit of inserting geogrids in pavements, they are too expensive, time consuming and hence impractical to adopt as a part of a specification for geogrid reinforced pavements. On the other hand, common index properties of geogrids are not necessarily related to their performance in pavement systems. Hence, the general objective of this research was to develop a practical, representative, and relatively inexpensive test method that serves as an indicator to the performance of geogrids in the reinforcement of base material in pavements. The bending stiffness test, developed by both Sprague *et al* (2004) and Shields *et al* (2005), was to be enhanced and modeled for this purpose.

In laboratory and field tests, the benefit of geogrid reinforcement has been generally evaluated by its capacity to reduce rutting. The performance of the reinforced pavement sections was evaluated by their TBR and BCR, which are both related to rut depth. The effect of geogrid reinforcement on fatigue cracking of pavements was not generally addressed. The static loading process used in the bending stiffness test was to be replaced by cyclic loading which is more representative of traffic loads on pavements and which allows for the analysis of the effect of reinforcement on the fatigue cracking of the pavement section studied.

Different research studies disagree on the mechanism by which geogrids reinforce pavements. Bender and Barenberg (1978), Perkins (1999) and Berg *et al* (2000) suggest one of the mechanisms of reinforcement to be the transfer of the shear load stress from the base course to the geogrid that is put in tension which results in a decrease in the lateral strain and, hence, lower vertical permanent deformation. Cancelli *et al*. (1996) performed field tests showing reinforcement benefit for all the geogrid products tested, yet all the measured strains were less than 0.2 percent. The theory of tension developing in the geogrid as part of the reinforcing mechanism is debatable because such low strains are typically developed in flexible pavements.

Miura *et al*. (1990) investigated this theory using both laboratory and field tests on flexible pavements over a soft clay subgrade. The laboratory tests showed the tensile strength of the geogrid to be closely related to the performance of the reinforced pavement sections. The interlocking of the geogrid with the base layer material was also found to be a major part of the reinforcement. This was demonstrated by placing the geogrid in a slightly convex shape within the base layer. Compressive strains developed in the geogrid as the pavement was loaded and the geogrid still showed reinforcement benefit though it was not in tension. The field tests showed that placing the geogrid in tension was not attainable in the field. Therefore, Miura *et al*. (1990) suggested the interlocking effect to be the major source of reinforcement in flexible pavements. Giroud *el al* (1984) suggested that for unpaved roads with large deformations, only 10 percent of the reduction in thickness of the pavement was due to tension developing in the geogrid. The major reinforcement mechanism of the geogrid was thought to be subgrade confinement and load distribution resulting from the interlocking of the geogrid with the base layer material. Understanding the mechanism by which the geogrid reinforces the pavement is important in developing a method for the design of reinforced pavements. The final objective of this study was to use the bending stiffness test to investigate this mechanism.

TEST PROCEDURE

Sprague *et al*. (2004) developed a small-scale test procedure for investigating the interaction between base layer materials and geosynthetics inserted within the base layer for reinforcing the pavement. The purpose of the test, which was enhanced by Shields *et al.* (2005), was to create a practical and economical procedure to compare the reinforcement benefit of different

geosynthetic products and to isolate the interaction between the geosynthetics and the soil from the other variables of the different pavement system components.
The test section represented a 3.25-inch thick section of the base layer of a pavement system. The confining pressure of the overlying base material and asphalt concrete was characterized by a suction (vacuum) pressure applied inside the tested soil section. The traffic load on the surface of the pavement was represented by an inflation pressure applied on the bottom of the soil section. The inflation pressure resulted in the deflection of the soil section.
The test apparatus as shown in Figure 1 was a modified version of the multi-axial tension test for geomembranes (ASTM D 5617). The basic modification was the addition of 3.25-inch thick flange that contained the compacted soil section. Two geomembranes were placed on the top and the bottom of the soil section to provide an air tight medium where the required confinement (suction) pressure can be applied. O-rings were also inserted on both sides of the bottom geomembrane and under the top geomembrane to secure the air tightness of the soil section. A pneumatic "pogo-stick" was used for compacting the soil (two 3 inch lifts) prior to running the test.

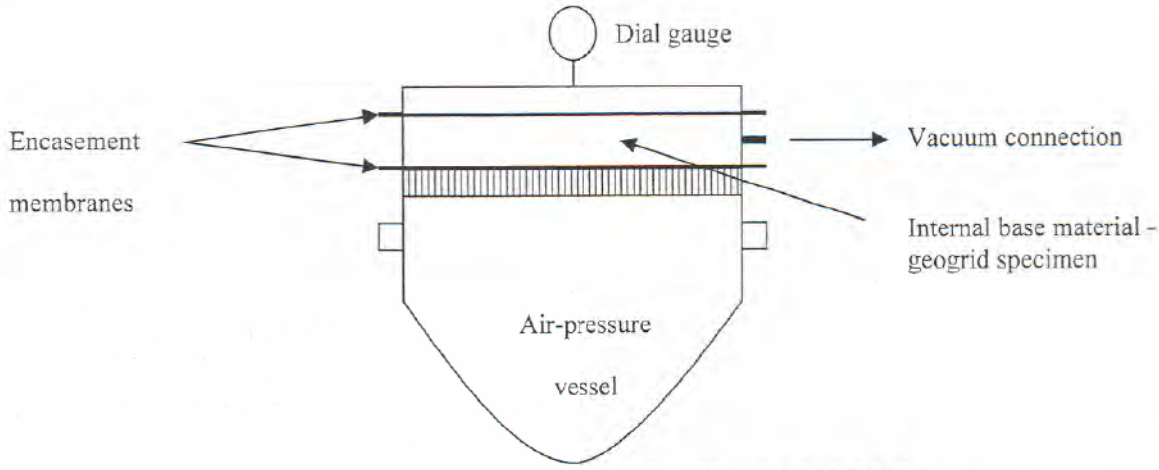

Figure 1 Schematic of the test apparatus (Shields *et al.* (2005)).

The dial gauge shown in Figure 1 is used to measure the center-point deflection of the soil section as it reacts to the inflation pressure. A quantity defined as the bending stiffness is used to evaluate the stiffness of the different tested soil sections. Specifically, bending stiffness is defined as the slope of the curve when the inflation pressure is plotted versus the resulting center-point deflection. The reinforcing benefit of different geogrid products was evaluated by comparing the bending stiffness of tests with a soil section only to that of tests with soil sections with the corresponding geogrid placed on top of the soil. A detailed description of the test method is presented in Shields (2004) and summarized in Shields *et al.* (2005).
The results of the tests reported by Shields *et al* (2005) showed a coefficient of variation, also known as c.o.v., up to 17 percent compared to a measured reinforcement benefit measured of 10 to 20 percent on average for most geogrids. Therefore, it was found necessary to improve the repeatability of the test results produced by the bending stiffness before the test is further enhanced, modeled, or analyzed.
The following modifications to the test procedure were found necessary:

1. The leaks detected in the system were found to be major sources of variability in the test results. Some leaks were controlled by replacing all the hoses and connections that were

used for either transmitting the inflation or the confinement pressures. A second type of leaks from pinhole punctures in the bottom geomembrane was prevented by placing a non woven needle-punched geotextile with a 35 mil thickness under the bottom geomembrane. The geotextile acted like a cushion that prevents the soil particles from puncturing the membrane during compaction.

2. The second modification of the bending stiffness test procedure was controlling the conditions of the soil used in the testing. Base aggregate with the same gradation (6 to 9 percent initial fines content) and compaction effort (360 blows per lift) were used for all the tested soil sections.
3. Another modification to the test procedure was the introduction of a five minute waiting period after the application of the confining pressure. This was accompanied by gentle tapping on the circumference of the soil flange. The waiting period and the tapping around the circumference allowed the confining pressure to be uniformly distributed along the soil section before starting the test. In the initial procedure, the test was started soon after applying the confining pressure, thus the stiffness was measured before uniform and complete confining pressure could be applied throughout the soil. The local variation in the actual value of the confining pressure applied throughout the soil and its difference between similar tests resulted in variability in their measured results.

The variability in the test results decreased after using these modifications. An example of the coefficients of variation of the measured inflation pressures required for a particular center-point deflection for different tests using both the existing and the new modified procedure is shown in Figure 2.

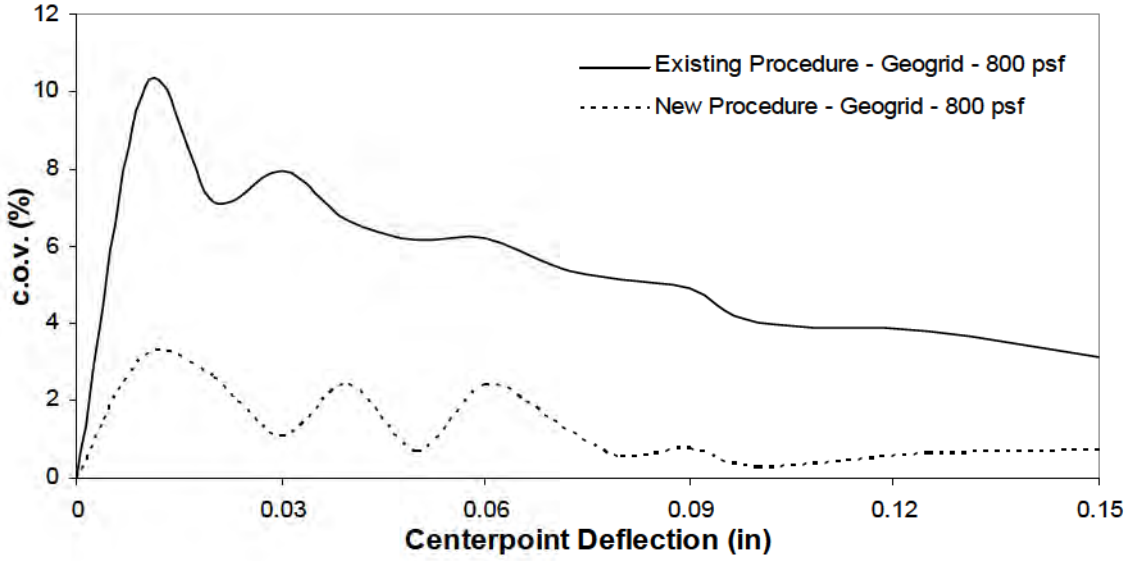

Figure 2 Comparison of the c.o.v. of the results of three tests (with geogrid on top of the soil and 800psf confining pressure) performed by the existing versus the new procedure.

CYCLIC LOADING

The mechanism of loading of the soil section in the bending stiffness test was modified to represent the actual conditions of flexible pavements. Pavements are subjected to traffic loads which are a cyclic type of load. The procedure as that specified for the static tests by Shields *et al.* (2005) with the modifications mentioned previously, was used in the cyclic tests except for a

different mechanism of inflation pressure application. Repeated cycles of pressure with the shape and values shown in Figure 3 were programmed to be applied on the soil section. Most cyclic tests on pavement materials, such as the resilient modulus test, use haversine shape loading with a cycle time of only one to a few seconds to represent traffic loads. In this research, only a minimum time interval of one minute could be used for any segment of the cycle. Also, all the segments of a cycle could only be programmed to be linear. Moreover fluctuation in the inflation when trying to reach the specified amount of pressure necessitated the addition of a horizontal segment of constant pressure for every target maximum or minimum pressure in the cycle.

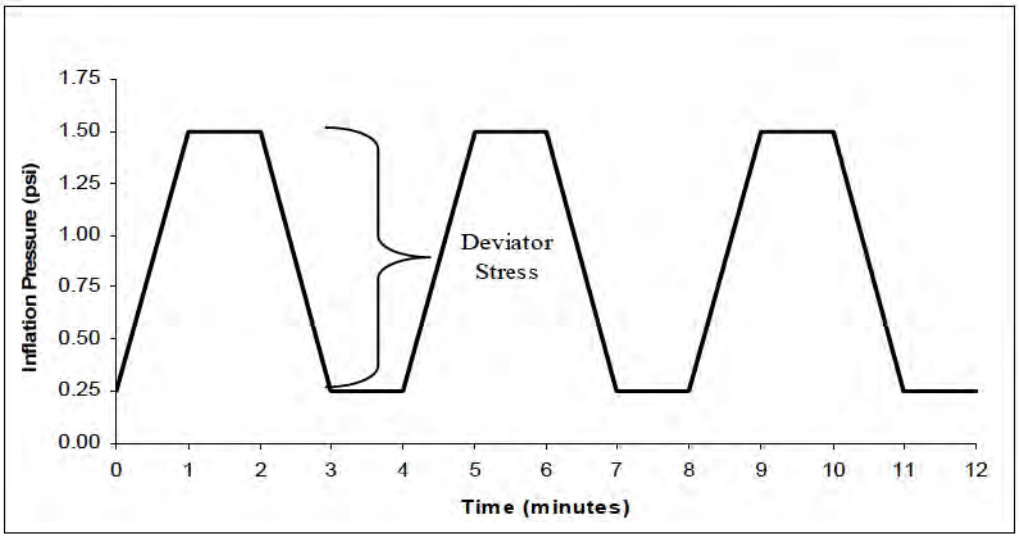

Figure 3 Designed inflation pressure cycles.

The pressure values used in the cycles were selected based on the properties of the particular soil used in the tests. The minimum pressure was selected such that the soil section would not be loaded negatively, yet a zero net pressure would be achieved. Therefore, this pressure had to be equivalent to the pressure applied by the weight of the soil section (0.25 psi) In a resilient modulus test (AASHTO T307), the load is applied on the soil specimen through a piston so a minimum stress equal to 10 percent of the applied maximum stress is used to maintain contact between the piston and the soil specimen. Contact in the bending stiffness test was provided by the steel flange supporting the soil specimen and the load was applied through air pressure so minimum stress was not required. The maximum pressure of 1.5 psi was chosen such that the resulting deformations in the soil section would be comparable to actual deformations in pavements. The number of cycles for which the test was run was selected based on two criteria: the practicality of the test and the predictability of the results. The time frame of the test had to be short enough to be practical as an index test, yet the soil properties measured by the test had to show a distinctive trend that could be projected on many additional cycles. Trial tests indicated that 60 cycles (4 hours) of inflation pressure application satisfied these two criteria.

As in the case of a static test, the quantities measured in a cyclic test were the applied inflation pressure and the corresponding center-point deflection of the soil section. The properties produced from these measurements and used to evaluate the different soil sections in cyclic tests were different than those produced in static tests. The deviator stress shown in Figure 3 is the difference between the maximum pressure and the minimum pressure at a specified time of the test. The resulting center deflection of the soil shown in Figure 4 can be divided into two types of

deformation: permanent and recoverable deformations. A property named the "Bending Stiffness" was derived from the deviator stress and the recoverable deformation (Equation 1).

$$B.S. = \frac{\text{Deviator Stress}}{\text{Recoverable Deformation}} \qquad (1)$$

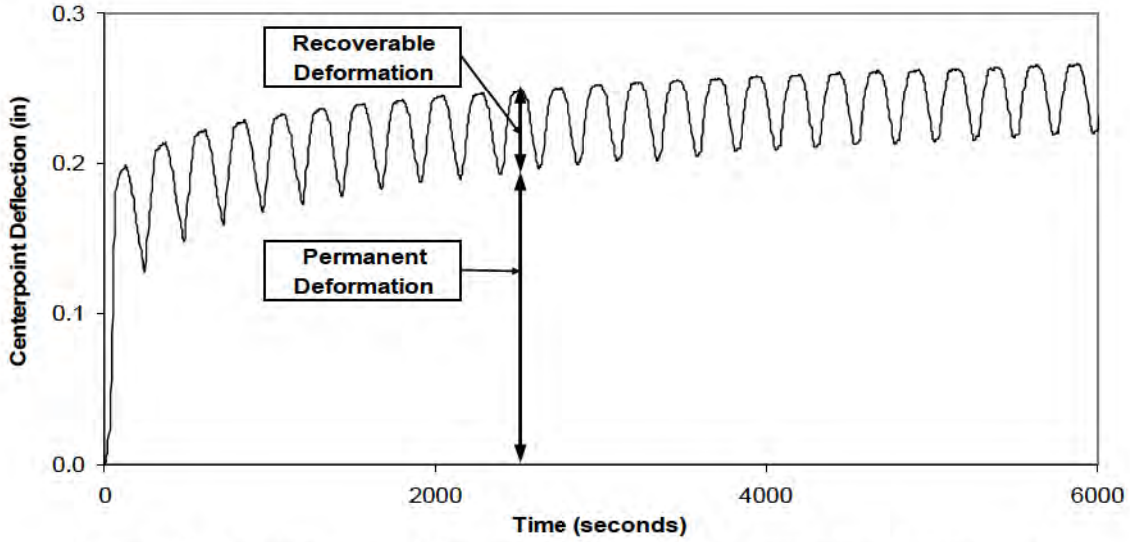

Figure 4 Two types of center deflection due to the inflation pressure can be measured.

A sketched definition of the bending stiffness on the plot of inflation pressure versus center deflection is shown in Figure 5a as the slope of the recoverable part of the curve. A bending stiffness is calculated for each cycle as shown by the detailed sketch in Figure 5. The bending stiffness was used to compare the performance of different soil sections under loading, where the bending stiffness for every cycle is plotted versus the number of cycles.

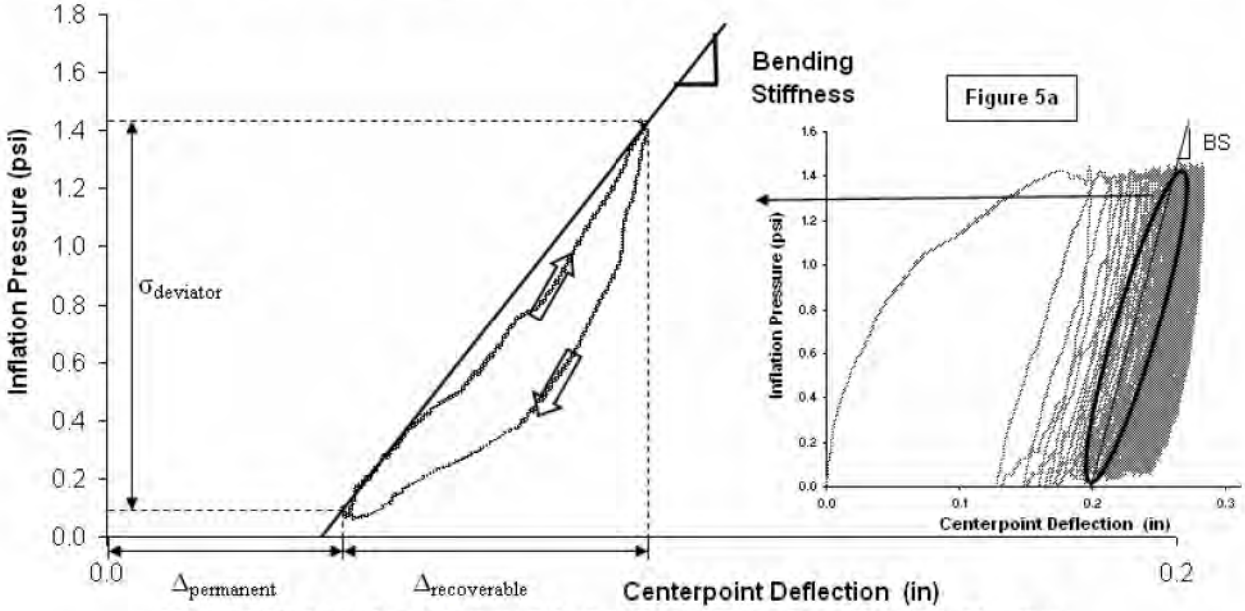

Figure 5 Method of calculation of the bending stiffness for each cycle of loading .

Test Results

A series of cyclic tests was performed on a base course with 7.0 percent initial fines content, compacted with 360 blows per lift, and tested under 100 psf confining pressure. A comparison of the results of these tests on different soil sections (reinforced vs. unreinforced) is shown in Figures 6 and 7. The mean results of the tests with the 95 percent confidence bounds are presented. The noticeable benefit of the addition of a BasX11 geogrid on top of the soil section is shown in Figure 6. The bending stiffness increased 42 percent on average throughout the cycles of loading between the unreinforced and the soil reinforced with BasX11. Similarly, as shown in Figure 7, when the BX1100 was placed on top of the soil section, the bending stiffness increased 24 percent on average throughout the test compared to the unreinforced soil section. It appears from the confidence bounds shown in Figures 6 and 7 that the variation in the results is tolerable in comparison to the measured reinforcement benefit.

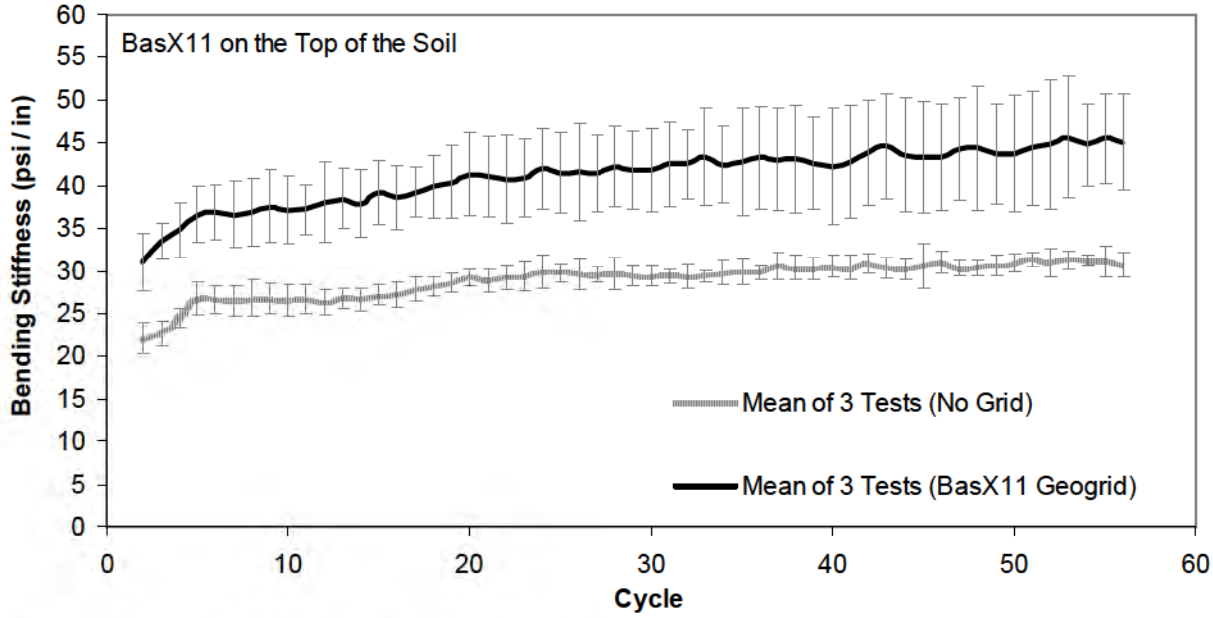

Figure 6 Comparison of the mean results of tests on Mirafi BasXgrid 11 reinforced and unreinforced soil sections with 95% confidence bounds.

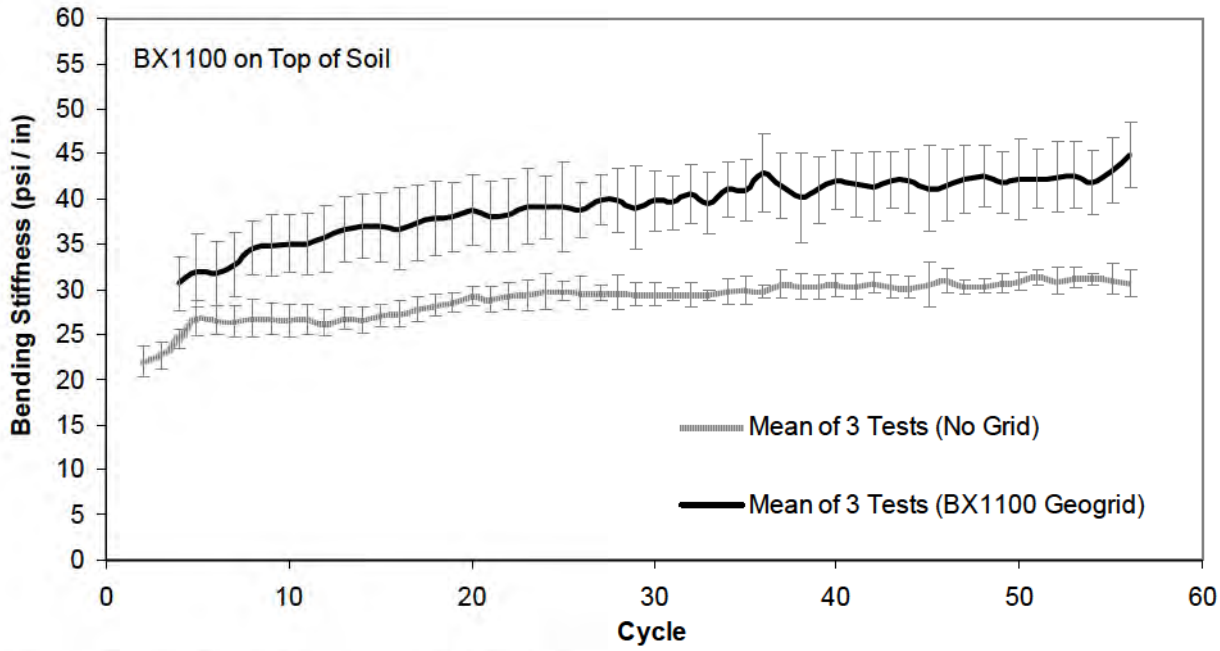

Figure 7 Comparison of the mean results of tests Tensar BX 1100 Geogrid reinforced and unreinforced soil sections with 95% confidence bounds.

Boundary Conditions and Relating Measurements to Pavements

It can be shown using design equations for pavements (AASHTO Guide for Design of Pavement Structures, 1993) that an increase in the resilient modulus of the base or subbase layer of the pavement leads to a significant reduction in the required thickness of the layer. The resilient modulus is a measure of the elastic property of the soil (AASHTO T307) so it is directly related to its elastic modulus. The bending stiffness of the soil section measured through the cyclic tests was approximately related to the elastic modulus. This simple relation was used to correlate the reinforcement benefit measured by this test to the resulting reinforcement benefit in pavements. The relation between the bending stiffness and the elastic modulus was produced by modeling the soil section as a structural element. This model was also useful in finding the effects of the test boundary conditions on the measured reinforcement benefit.

A schematic of a geogrid-reinforced soil section is shown in Figure 8. The soil section can be modeled as a reinforced beam with a thickness, H, a length, L, a distributed constant bottom load, w, and a resulting deformation, δ. The distributed load represents the inflation pressure applied on the soil section, while the deformation represents the center-point deflection measured in the test. The conditions at the edges of the test section were investigated to find the actual type of supporting mechanism available so as to model it properly. It was necessary to prove the absence of slipping at those edges so as to relate the test section to a structural element.

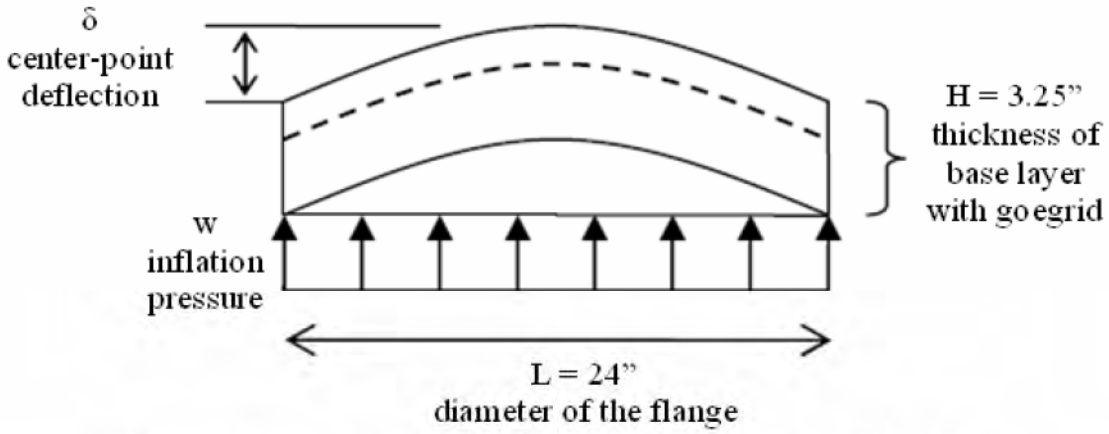

Figure 8 Schematic diagram of the soil section in the Bending Stiffness test.

As the inflation pressure is applied to the bottom geomembrane, the soil deforms in conjunction with the two membranes. But the geomembranes, anchored to the flange at the edges of the soil section, create a moment on the soil at the sides restricting it from deforming in that area. This resembles the support mechanism of a fixed-fixed beam. A test was performed to support this theory, where the soil section was subjected to a range of inflation pressures which were held constant until a steady deformation was recorded. Five different dial gages where installed at a distance of 0.25, 6, 12, 18, and 23.75 inches from the middle edge of the soil section. As expected, the soil section does not slip at the edges and it deflects similar to the fixed-fixed beam.

The bending stiffness of the soil section was measured as described by Equation 1. The deflection (δ) of a fixed-fixed beam can be related to the constant distributed load (w), the length of the beam (L), the moment of inertia of the beam (I), and its elastic modulus (E) through Equation 2. Therefore, the bending stiffness (BS) can be related to the elastic modulus of the soil section through Equations 3 and 4.

$$\delta = \frac{\omega L^4}{384EI} \tag{2}$$

$$BS = \frac{\omega}{\delta} = \frac{384EI}{5L^4} \tag{3}$$

$$BS = KE \text{, where } K = \frac{384I}{5L^4} \tag{4}$$

The measured increase in bending stiffness between the unreinforced and the geogrid-reinforced soil sections can be directly converted to the same increase in the soil's elastic modulus by using Equation 4. Equations 5 and 6 show that any change in the thickness or diameter of the soil section will not have any effect on the relationship between the increase in bending stiffness and the increase in the elastic modulus, as long as the boundary conditions have minimal effects on the measurements produced by the test.

$$\text{For } L' = aL \ \ (a < 1),\ BS = K'E \text{ where } K' < K \tag{5}$$

For $H' = aH \ \ (a > 1)$, $BS = K''E$ where $K'' > K$ (6)

Location of the Geogrid

A friction might be developing between the geogrid placed on the top of the soil section and the overlying geomembrane, which may be influencing the results of the test. The effect of the geogrid location on the results of the bending stiffness test was evaluated for two cases: the geogrid placed at the top and the geogrid placed at the middle of the soil section. A comparison between the results of two series of tests with BasX11 geogrid inserted at the top and at the bottom of the soil section is shown in Figure 9. A base aggrrgate with 7.0 percent initial fines content, compaction of 360 blows per lift, and a 100 psf confinement pressure were used in these tests. The bending stiffness resulting from cyclic tests with the geogrid placed on top of the soil was significantly higher than that resulting from placing the geogrid in the middle of the soil section (42 vs. 21 %). A possible reason for this observation could be friction developing between the geogrid and the top geomembrane, resulting in the higher bending stiffness.

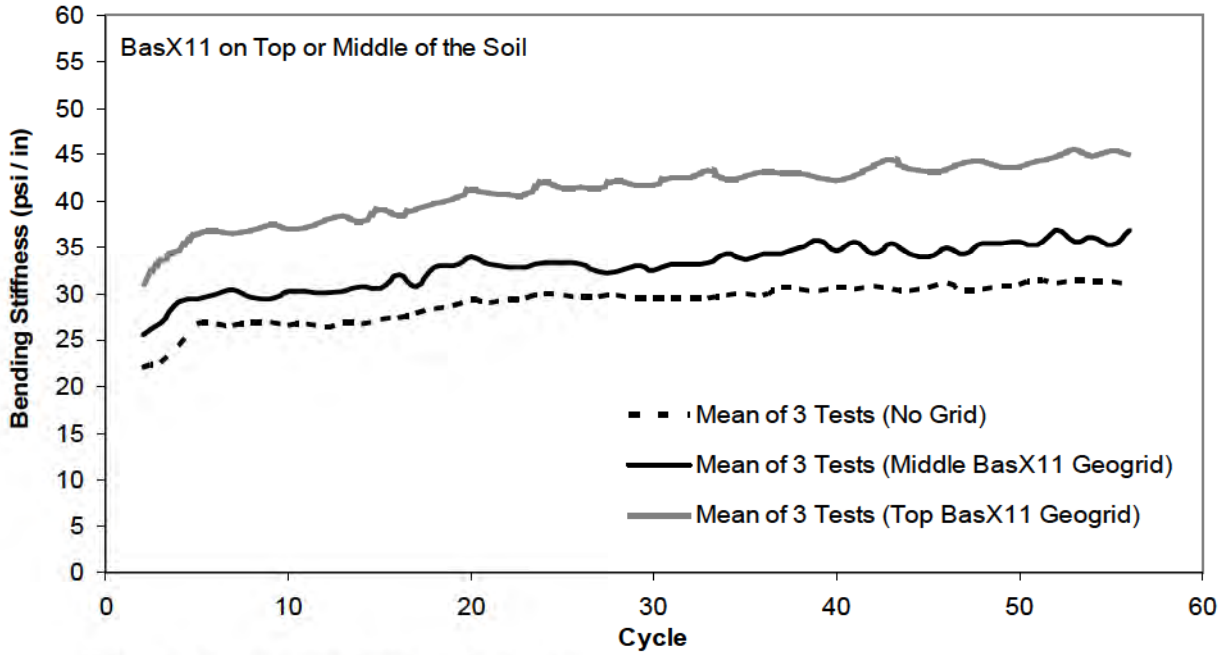

Figure 9 Comparison of results of cyclic tests with different geogrid locations within the soil.

Investigation of the Tension in the Geogrid

Bender and Barenberg (1978), Perkins (1999) and Berg *et al* (2000) suggest that the development of tension in the geogrid is one of the mechanism in which it reinforces the base layer of the pavement. On the other hand, Giroud *et al* (1984) and Miura *et al*. (1990) suggested the interlocking between the geogrid and the soil to be the major source of reinforcement in flexible pavements. A series of bending stiffness tests were performed to evaluate the major mechanisms of reinforcement captured by this test.

Three cyclic tests with 24-inch diameter BasX11 geogrid placed in the middle of each soil section were performed and the results obtained were compared with those obtained from tests

on three unreinforced sections of the same soil. By inserting the geogrid within the soil an average increase of 21 percent in the bending stiffness of the soil section was observed as compared to the unreinforced sections. Another series of three cyclic tests, with a 24-inch diameter BasX11 geogrid cut at 12-inch diameter and placed in the middle of each soil section, were performed under identical testing conditions and with the same soil. In this case, the introduction of the geogrid resulted in an average increase of 33 percent in the bending stiffness of the soil section. A schematic of the geogrid sections used in these two series of reinforced cyclic tests is shown in Figure 10. The average results of the two series of reinforced tests and the unreinforced tests are compared in Figure 11.

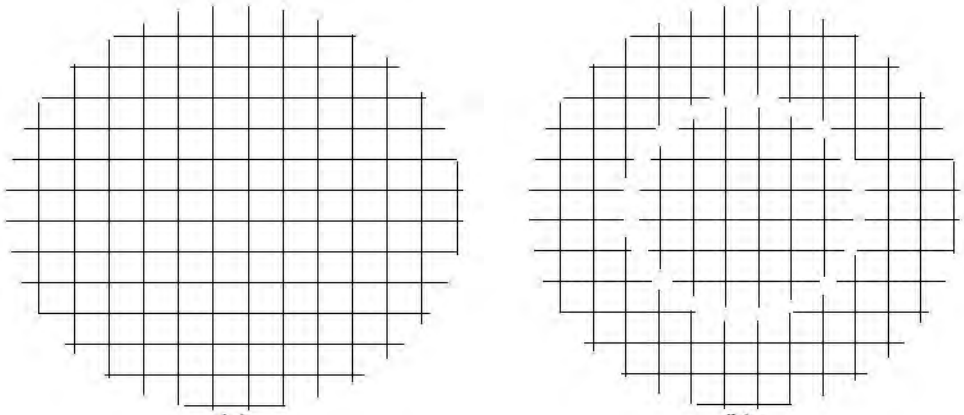

Figure 10 a) Continuous 24" diameter geogrid. b) 24" diameter geogrid cut at 12" diameter.

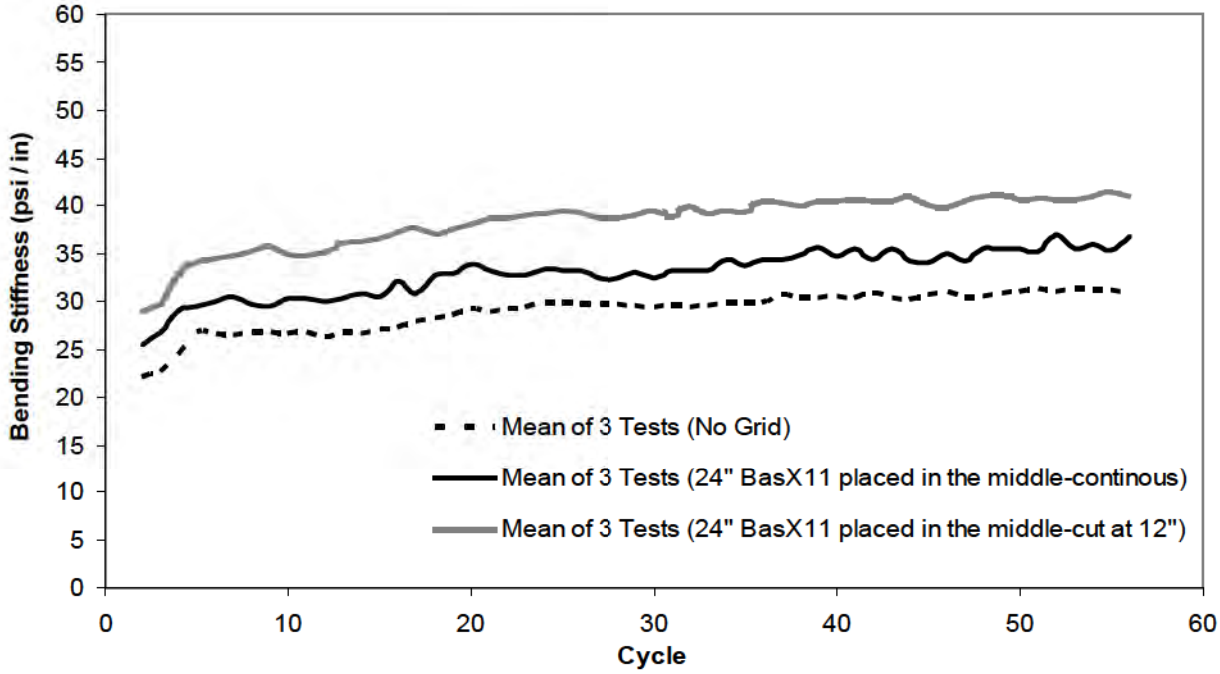

Figure 11 Mean results of continuous versus cut 24" geogrid reinforced tests.

The geogrid was cut at 12-inches diameter in the second series of reinforced tests to ensure that no tension develops throughout the geogrid. If the tensile strength of the geogrid was responsible for any of the reinforcement benefit found using a full continuous geogrid, then the tests with a cut geogrid inserted in the soil would have reported a reduced benefit, if any at all. Conversely, the results shown in Figure 11 report a higher reinforcement benefit with the insertion of the cut geogrids. The single case where tension might be responsible for the reinforcement benefit would be if, for both tests, the reinforcement was being generated by the inner fourth of the area, i.e. the 12-inch diameter geogrid. In order to investigate this scenario, another series of three cyclic tests with a 12-inch diameter BasX11 geogrid placed in the middle of each soil section was performed. The results shown in Figure 12 indicate that there was an insignificant amount of reinforcement benefit attained from inserting the 12-inch geogrid, with only an average increase of 5 percent in the bending stiffness of the soil section as compared to the same unreinforced soil. Note that when a geogrid with a quarter of the area of the full geogrid covering all the soil section was used, the reinforcement benefit was also reduced to around a quarter of the measured benefit.

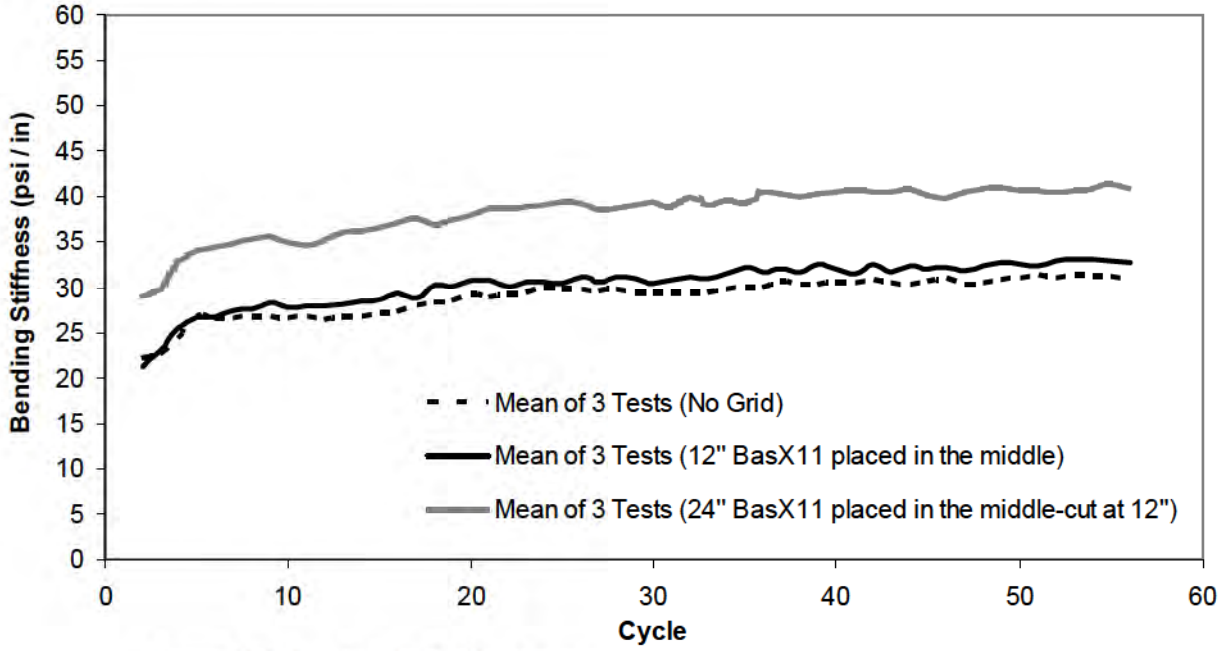

Figure 12 Mean results of 24"cut versus 12"continuous geogrid reinforced tests.

It is concluded that the whole 24-inch geogrid acts in reinforcing the soil section by increasing its bending stiffness. Moreover, the continuity of the geogrid is not integral for producing the same reinforcement benefit.

The geogrid may be acting as fiber reinforcement where it strengthens the soil at a micro-level (localized tension) rather than creating any large-scale effect. It was shown that a change in the area of soil over which the geogrid was inserted resulted in the same change in the reinforcement benefit of the geogrid. This is similar to what was shown by Zornberg (2002) for fiber-reinforced soils. Zornberg (2002) showed that the soil's shear strength increased by the same amount as the increase in its fiber content. Another possible mechanism of reinforcement is the interlocking effect between the geogrid and the soil which provides load distribution and more confinement of the soil as described by Giroud *el al* (1984) and Miura *et al* (1990).

CONCLUSION

The following were discovered in this research study:

1. The development of tension at a macro-scale in the geogrid is not necessary for reinforcing the base layer of a pavement. On the other hand, two mechanisms may be responsible for the reinforcement: the interlocking of the geogrid with the soil and/or fiber reinforcement of the soil by the geogrid (localized tension).
2. A cyclic mechanism for loading the soil section better represents the actual conditions of pavements. The bending stiffness of the soil section, which is the measurement resulting from the cyclic tests, was approximated to be directly proportional to the soil's elastic modulus.
3. The insertion of a geogrid into the soil section improves the elastic modulus of the soil by around 20 to 40 percent.
4. The interaction of the geogrid with the top geomembrane during the test increases the measured stiffness of the soil section which is not representative of actual pavements. Additionally, placing the geogrid on the top of the soil adds to the complexity of understanding and modeling the boundary conditions of this test. Therefore, inserting the geogrid inside the soil section is recommended for future bending stiffness tests.
5. The results of tests performed using the existing bending stiffness test procedure, as described by Shields *et al*. (2005), showed relatively high variability when compared to the reinforcement benefit of the geogrid. The results of the tests performed after the test procedure was modified showed less variability.
6. It was shown that leaks caused variability in the test results. The test apparatus was modified to minimize leaks in the system. It was concluded that instantly starting the test after the application of the confinement pressure possibly did not allow the complete and uniform spreading of the confinement pressure throughout the soil section. A new procedure for the application of the confinement pressure was developed. It included a five minute waiting period between the application of the confinement pressure and the start of the test. The waiting period was accompanied by gentle tapping around the flange containing the soil section. The new process was thought to allow uniform and complete spreading of the required confinement pressure before the inflation pressure is applied.

REFERENCES

AASHTO, 1993, *AASHTO Guide for Design of Pavement Structures*, Washington, DC.

AASHTO T307 "Standard Method of Test for Determining the Resilient Modulus of Soils and Aggregate Materials."

ASTM D 5617 "Standard Test Method for Multi-Axial Tension Test for Geosynthetics."

Bender, D.A. and Barenberg, E.J., 1978, "Design and Behavior of Soil-Fabric-Aggregate Systems," In *Transportation Research Record 671*, TRB, National Research Council, Washington, DC, pp. 64-75.

Berg R.R., Christopher, B.R. and Perkins, S.W., 2000, *Geosynthetic Reinforcement of the Aggregate Base Course of Flexible Pavement Structures, GMA White Paper II*, Geosynthetic Materials Association

Cancelli, A. And Montanelli, F., 1999, "In-Ground Test For Geosynthetic Reinforced Flexible Paved Roads," *Proceedings of the Conference Geosynthetics '99*, Boston, MA, USA, Vol. 2, pp. 863-878.
Cancelli, A., Montanelli, F., Rimoldi, P. and Zhao, A., 1996, "Full Scale Laboratory Testing on Geosynthetics Reinforced Paved Roads," Proceedings of the International Symposium on Earth Reinforcement, Fukuoka/Kyushu, Japan, November, Balkema, pp. 573-578.
Giroud, J.P., Ah-Line, C. and Bonaparte, R., 1984, "Design of Unpaved Roads and Trafficked Areas with Geogrids," *Polymer Grid Reinforcement*, Thomas Telford, London, UK, pp. 116-127.
.Hibbeler, R.C., Structural Analysis, 5th Edition, Prentice-Hall Inc., Upper Saddle River, NJ, 2002, 600 p.
Miura, N., Sakai, A., Taesiri, Y., Yamanouchi, T. and Yasuhara, K., 1990, "Polymer Grid Reinforced Pavement on Soft Clay Grounds," *Geotextiles and Geomembranes*, Elsevier Applied Science, Oxford, UK, Vol. 9, pp. 99-123.
Perkins, S.W., 1999, *Geosynthetic Reinforcement of Flexible Pavements: Laboratory Based Pavement Test Sections*, Federal Highway Administration Report FHWA/MT-99-001/8138, Montana Department of Transportation, 140 p.
Shields, M. Kent, Jr., 2004, "Bending Stiffness Index Test for Geogrid Reinforcement of Pavement Base Material," M.S. Thesis, Department of Civil Engineering, The University of Texas at Austin, 82 p.
Shields, M.K., Sprague, C.J., Gilbert, R.B., and Allen, S.R., 2005, "Bending Stiffness Index Test for Geogrid Reinforcement of Pavement Base," *Geotechnical Special Publications 130-142 & GRI-18*, Geo-Frontiers 2005, Austin.
Sprague, C. J., Lothspeich, S., Chuck, F., Goodrum, R., 2004, "Geogrid Reinforcement of Road Base Aggregate – Measuring the Confinement Benefit," *Proceedings*, Geo-Trans 2004 Conference, Los Angeles, pp. 996-1004.
Zornberg, J.G., 2002, "Discrete Framework for Limit Equilibrium Analysis of Fiber-Reinforced Soil," *Géotechnique*, Vol.52, No 8, pp. 593-604.

CONTACT:

Ayman Halim Abusaid
Geotechnical Engineer
Golder Associates Inc.
500 Century Plaza Drive, Suite 190
Houston, TX 77073
Phone: 281-821-6868
Email: aabusaid@golder.com

Testing

UNDERSTANDING AND MINIMIZING UNCERTAINTY IN GEOSYNTHETIC TESTING

R. Lacey, P.E., Geotechnics, Inc.

ABSTRACT

This paper describes a procedure for estimating the quality of laboratory test results in terms of test method precision and test result uncertainty. The technique can be used as a tool for resolving inter-laboratory discrepancies and enhancing the overall quality of test methods.

The sampling and testing strategies are governed by the spatially-linked variability characteristics typical of geosynthetics. Noticeable repeating patterns of the material properties as a function of location along the width and length of a roll of material dictate where the individual test specimens are obtained from the source and how they are grouped together to comprise a test sample. Then the necessary sample uniformity is generated without artificially homogenizing the geosynthetic under test. The resulting precision and uncertainty values will then be realistic and applicable to routine conformance test evaluations.

The measurement uncertainty assessment process is demonstrated with a geotextile source material and three test methods: mass per unit area, thickness and grab strength. The geotextile is sampled and tested in accordance with the test methods. Then the results are analyzed with rudimentary control chart statistics in order to calculate and monitor test method precision and uncertainty.

INTRODUCTION

Uncertainty in Geosynthetic Testing encompasses two controversial topics. One is the general uncertainty that we have when we compare a test result to results from another laboratory or to a specification value. The other is the uncertainty there is in the individual test methods themselves, that is, the uncertainty in the process that transforms the sample into a "number".

Since I just confused myself, I thought it would be appropriate to investigate this "Uncertainty" phenomenon with a Lab Man's approach. If Measurement Uncertainty is indeed a real attribute of test results, then all we need to do is run some tests. The Measurement Uncertainty should be right there in the data. We just have to extract it.

As it turns out, this extraction process is fairly simple: a typical geosynthetic sample is tested several times, while intelligently controlling the layout of the specimens and the conditions of the tests. The test results are plotted with standard deviation and means control charts to estimate precision and uncertainty.

The precision is the repeatability of the test method. It answers the question, "If I have a test result for a sample, what is the range of values that would result the test were performed again on the same sample?" The uncertainty, on the other hand, is the potential scatter of any individual test result, regardless of the result you might already have on the sample. The uncertainty was in the first test performed, and will be in the second and third tests, etc.

DEVELOPING THE SOURCE SAMPLE

The first step in the Measurement Uncertainty Assessment Process, or "MUAP, is the first step in any routine geosynthetic laboratory procedure; collect a sample of a geosynthetic that is typical of the test method under assessment. Our standards typically specify a one meter by roll width swatch of the material, which we refer to as the "Source sample". The actual sample may have to be somewhat longer than 1 meter in the machine direction in order to generate the preferred numbers of test results given the individual test specimen sizes. In this example, we are testing a nonwoven geotextile for Mass per Unit Area in accordance with ASTM D 5261, Thickness per D 5199, and Grab Strength per D 4632.

In order to calculate the precision of the test method, the Source sample is tested three consecutive times under repeatability conditions, that is, single operator, single apparatus in a single day. Each of these sets of three test results is referred to as a repeatability unit, or RU. The layout of the test specimens on the Source sample are shown on Figure 1. The tests for the repeatability units were performed on triplicates in the cross machine direction as shown, with Test Results 1, 2 and 3 taken from RU 1, Test Results 4, 5 and 6 from RU 2, etc.

Figure 1
TEST SPECIMEN LAYOUT

RU 1	1	2	3	1	2	3	1	2	3	1	2	3	1	2	3	1	2	3	1	2	3	1	2	3	1	2	3	1	2	3
RU 2	4	5	6	4	5	6	4	5	6	4	5	6	4	5	6	4	5	6	4	5	6	4	5	6	4	5	6	4	5	6
RU 3	7	8	9	7	8	9	7	8	9	7	8	9	7	8	9	7	8	9	7	8	9	7	8	9	7	8	9	7	8	9
RU 4	10	11	12	10	11	12	10	11	12	10	11	12	10	11	12	10	11	12	10	11	12	10	11	12	10	11	12	10	11	12

Mass per Unit Area

The mass measurements are tabulated in Figure M1 and plotted in Figure M2. A standard deviations control chart is constructed in M3, with the standard deviation of each RU plotted against the RU number. The average of the standard deviations, $\bar{s}$, is calculated (p units):

$\bar{s} = \sum s / p = 0.049$

The upper control limit is:

$UCLs = B4 * \bar{s} = 2.568 * 0.049 = 0.125$

The standard deviations chart does not indicate anything remarkable about the within-unit variations. An estimate of the repeatability standard deviation, or within-lab test method precision, is computed from the average s as:

$sr = \bar{s} / c4 = 0.049 / 0.8862 = 0.055$

Figure M1
MASS TEST RESULTS

	A	B	C	D	E	F	G	H	I	J	AVE	RU MEAN	S.D.
	12.27	13.55	11.73	12.43	13.11	12.51	12.82	12.38	12.43	12.53	12.58		
RU1	12.33	13.45	12.23	12.56	12.62	12.82	12.13	12.17	12.81	12.59	12.57	12.60	0.049
	12.60	12.97	12.62	12.35	12.42	12.39	12.71	12.41	13.06	13.05	12.66		
	13.56	13.35	11.95	12.54	11.99	12.98	12.41	12.44	12.14	13.48	12.68		
RU2	13.49	13.16	12.23	12.30	12.08	13.07	12.54	12.35	12.50	13.83	12.76	12.73	0.038
	13.36	12.61	12.81	12.33	12.28	12.67	12.99	12.53	13.11	~~14.57~~	12.74		
	13.68	13.17	12.58	13.04	12.56	13.34	12.68	12.18	11.85	12.23	12.73		
RU3	13.09	12.77	12.84	12.86	13.26	12.98	12.66	11.64	12.38	12.11	12.66	12.72	0.050
	13.36	12.41	13.17	13.15	12.79	12.66	13.01	11.98	12.07	12.96	12.76		
	12.96	13.00	12.69	13.38	12.13	12.65	12.58	12.36	12.78	12.86	12.74		
RU4	12.73	12.92	12.47	12.96	12.81	12.56	12.15	12.05	12.39	13.45	12.65	12.67	0.057
	14.30	12.70	13.05	12.76	12.33	11.92	12.74	12.31	12.49	13.40	12.63		

AVERAGE: 12.68 0.049

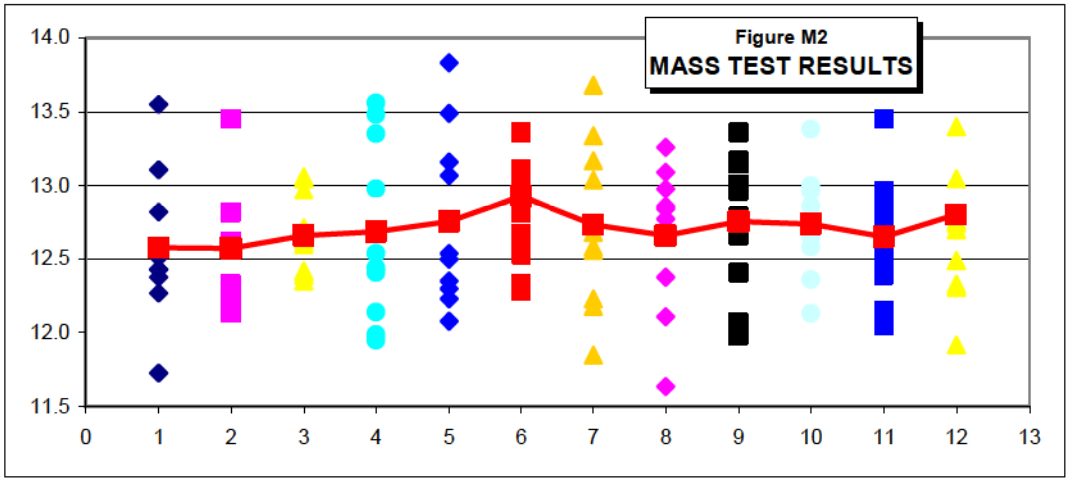

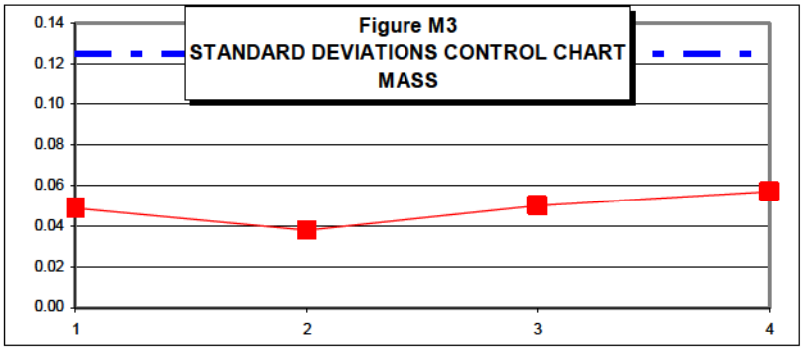

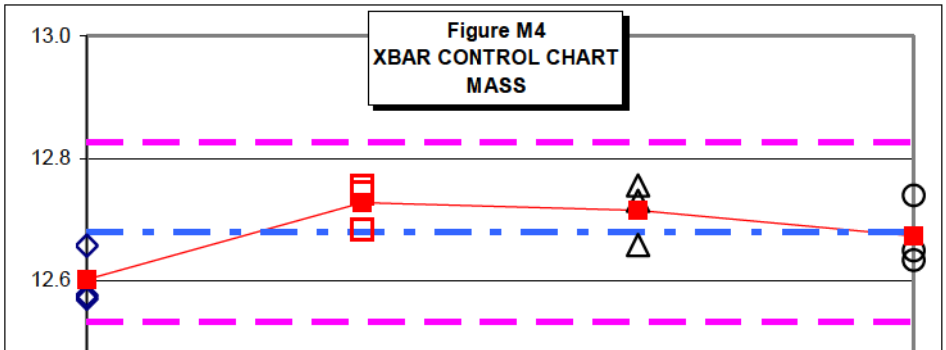

The averages between repeatability units are examined next. First, the grand average of the four units is calculated, which is 12.68. The 3-sigma control limits then are:

UCL = 12.68 + 3 * 0.049 = 12.78
LCL = 12.68 - 3 * 0.049 = 12.58

The uncertainty standard deviation is estimated with the standard deviation of the RU averages, that is, the standard deviation of the means control chart, which is 0.057.

Summary of Mass per Unit Area Variability

Condition	Stdev	%CV
Test Method Repeatability	0.055	0.44%
Test Result Uncertainty	0.057	0.45%

Thickness Test Results

The thickness measurements are tabulated in Figure T1 and plotted in Figure T2. The standard deviations control chart is constructed in T3. The average of the RU standard deviations, $\bar{s}$, is:

$\bar{s} = \sum s / p = 1.09$

The upper control limit for the standard deviation chart is:

UCLs = B4 * $\bar{s}$ = 2.568 * 1.09 = 2.79

Again, the standard deviations chart does not merit further investigation at this point in time. An estimate of the repeatability standard deviation, is computed from the average of the RU standard deviations, s as:

sr = $\bar{s}$ / c4 = 1.09 / 0.8862 = 1.39

The grand average of the four units is 195.7. The 3-sigma control limits are:

UCL = 12.68 + 3 * 195.7 = 199.4
LCL = 12.68 - 3 * 195.7 = 192.0

The uncertainty standard deviation is the standard deviation of the RU averages, or 1.83.

Figure T1
THICKNESS TEST RESULTS

	A	B	C	D	E	F	G	H	I	J	AVE	RU MEAN	S.D.
	179.0	203.5	191.0	200.0	195.0	185.5	197.0	191.0	198.0	190.5	193.05		
RU1	189.0	194.5	197.0	196.0	195.5	194.5	186.0	185.0	**203.5**	198.0	193.90	193.52	0.431
	191.0	198.5	197.0	192.5	189.0	191.5	207.0	187.5	197.0	185.0	193.60		
	206.5	203.5	199.0	196.0	186.5	197.5	190.5	202.0	193.5	204.5	197.95		
RU2	207.5	203.0	191.0	188.5	186.0	198.0	209.0	190.0	183.5	198.0	195.45	197.18	1.504
	207.5	205.0	202.0	188.0	186.5	189.5	207.0	189.5	195.5	211.0	198.15		
	201.5	213.0	206.0	202.0	188.5	203.5	198.0	198.5	189.0	176.0	197.60		
RU3	179.5	199.0	182.0	199.0	201.0	201.0	195.5	**218.0**	204.0	196.0	197.50	197.20	0.608
	214.0	194.0	205.5	204.5	190.5	188.0	203.5	194.5	181.5	189.0	196.50		
	199.0	204.5	201.0	195.0	181.5	192.5	191.5	200.0	201.5	198.5	196.50		
RU4	194.5	195.5	191.0	204.5	184.0	185.0	188.0	182.5	199.5	204.5	192.90	194.76	1.803
	230.0	198.0	192.0	198.0	181.5	182.5	208.5	194.5	195.5	203.5	194.89		

AVERAGE: 195.67 1.087

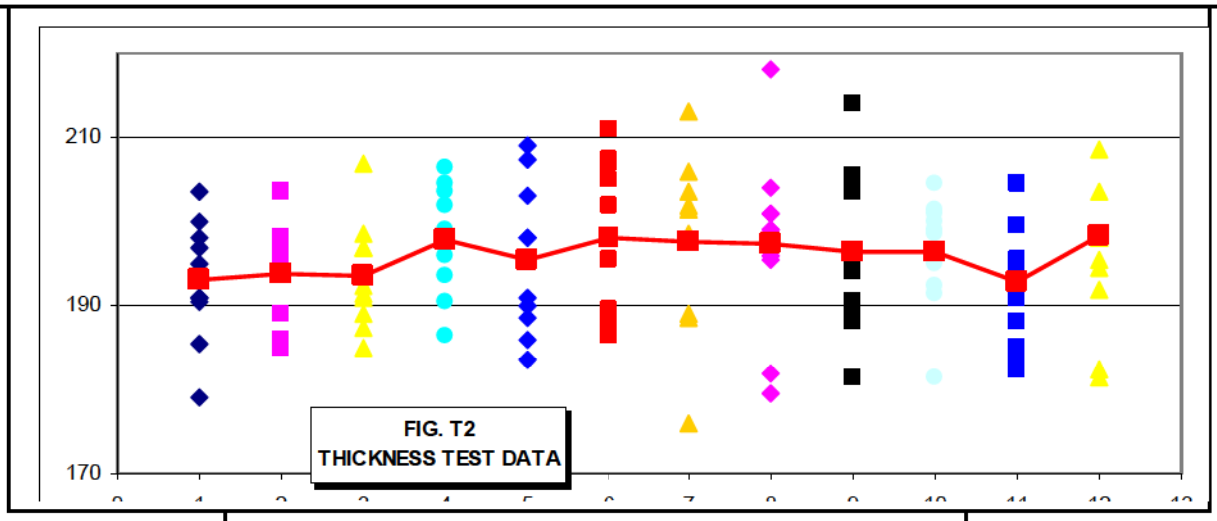

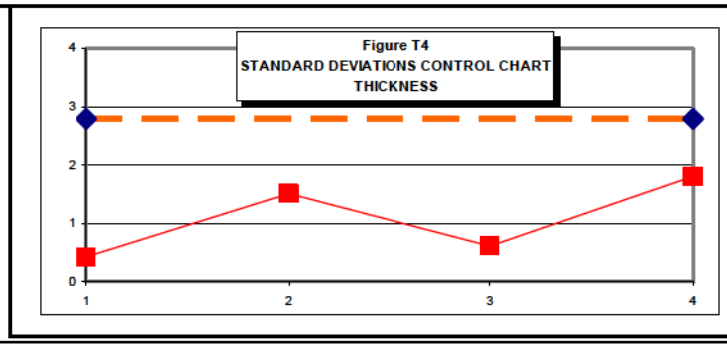

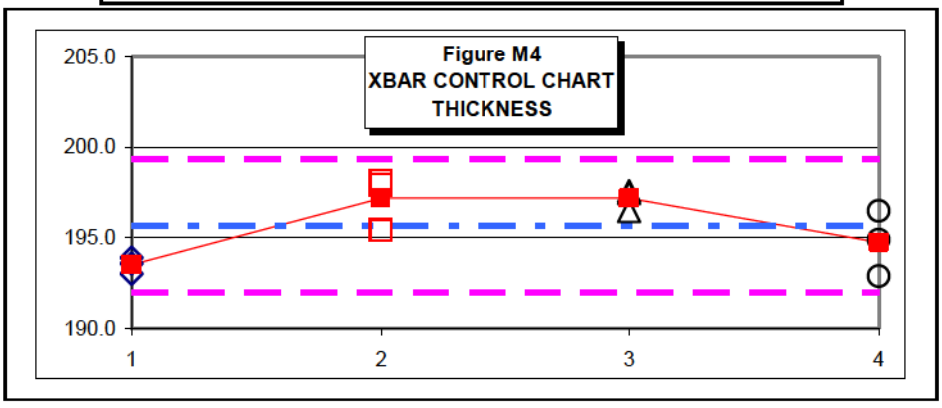

SUMMARY OF THICKNESS TEST METHOD VARIABILITY

Condition	Stdev	%CV
Test Method Repeatability	1.39	0.71%
Test Result Uncertainty	1.83	0.94%

Incidentally, the test method repeatability of 0.71% compares well with the precision statement published in ASTM D 5199, where the lowest repeatability listed of the four materials included in the inter-laboratory study is 3 %.

Grab Strength Test Results

The test data for grab strength is shown in Figures G1 and G2. The standard deviation control chart is presented in Figure G3, and the means control chart in Figure G4.

The repeatability standard deviation for the grab strength results is:

$sr = \bar{s} / c4 = 8.2 / 0.8862 = 9.2$

The grand average of the units is 405.7. The 3-sigma control limits are:

UCL = 405.7 + 3 * 9.2 = 433.3
LCL = 405.7 - 3 * 9.2 = 378.0

The uncertainty standard deviation for grab strength test results is 5.6.

The individual test result plot as well as the standard deviations control chart show that there might be some change developing in the source sample at RU4. If we are continuing to take samples in the machine direction from the source roll, we should watch for this trend to continue.

Summary of Grab Strength Test Method Variability

Condition	Stdev	%CV
Test Method Repeatability	9.2	2.3 %
Test Result Uncertainty	5.6	1.4 %

Figure G1

GRAB STRENGTH

	A	B	C	D	E	F	G	H	I	J	AVE	RU MEAN	S.D.
	420.7	453.8	392.5	403.4	418.7	401.5	430.8	401.8	379.9	423.5	412.66		
RU1	423.4	437.4	397.1	368.3	429.8	441.7	388.1	388.8	**404.8**	432.7	411.21	411.66	0.864
	406.2	449.6	410.4	388.4	390.5	414.3	400.0	383.4	412.9	455.5	411.12		
	459.8	423.6	366.8	379.0	401.0	424.2	378.5	371.1	372.5	455.1	403.16		
RU2	420.6	378.6	355.9	380.0	376.5	413.5	415.7	368.9	415.3	426.3	395.13	404.08	9.449
	457.7	393.4	380.2	355.9	371.1	400.1	444.9	369.8	442.1	**524.4**	413.96		
	459.8	425.2	381.6	384.6	380.4	443.6	427.5	366.0	369.5	420.1	405.83		
RU3	450.9	427.7	383.2	404.4	449.7	413.4	378.4	**355.9**	388.3	399.9	405.18	408.22	4.714
	469.7	366.5	366.2	400.9	410.1	408.3	422.2	415.5	403.1	474.0	413.65		
	446.7	417.8	412.6	433.4	413.4	421.2	392.4	358.4	408.2	454.6	415.87		
RU4	430.9	365.8	360.9	365.7	377.9	392.7	336.5	350.3	403.8	421.3	380.58	398.66	17.661
	462.0	386.0	353.4	399.0	368.3	382.8	381.6	404.3	440.0	480.3	399.52		

AVERAGE: 405.66 8.172

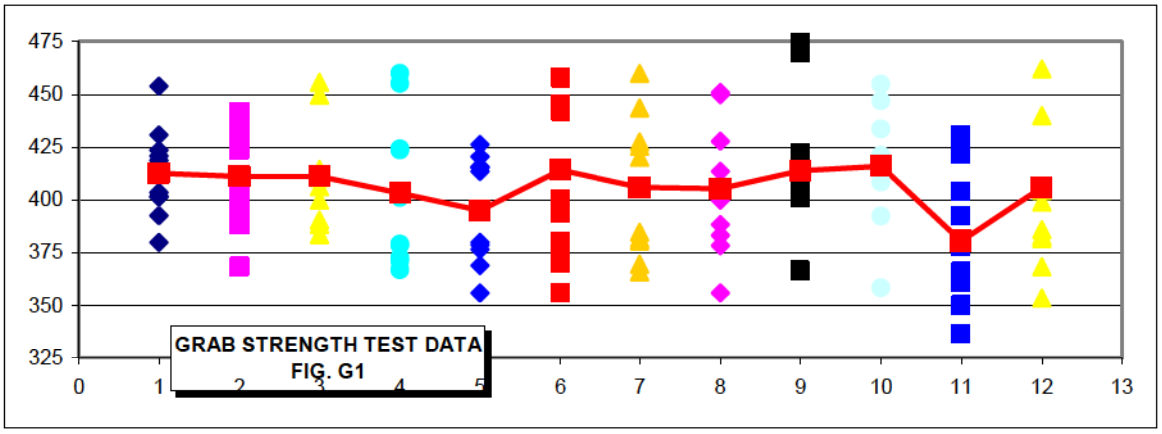

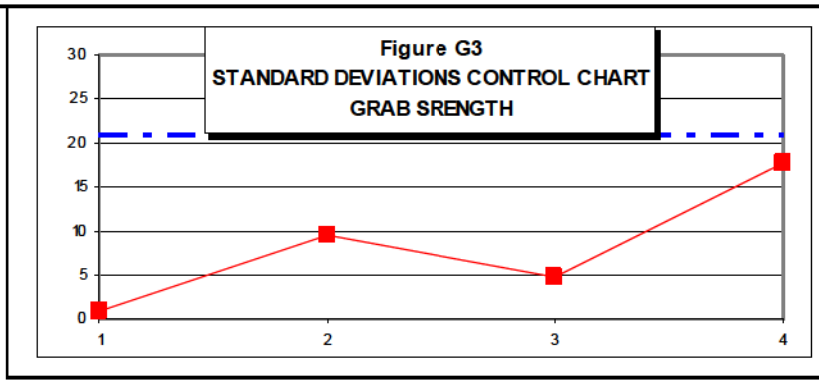

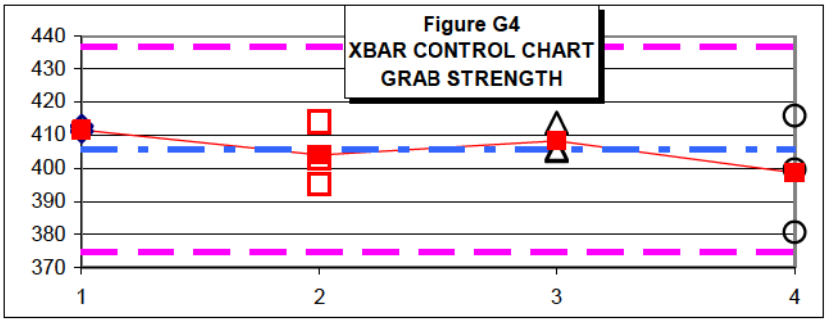

REDUCING MEASUREMENT UNCERTAINTY

All of the uncertainty estimates have been confined to "repeatability" conditions. In order to estimate the total uncertainty for the test method in this laboratory, the various influence factors such as operators, apparatus, reagents, environmental conditions, etc. must be varied while performing the RU tests. The total uncertainty would then represent the range of test results that could have been generated on the sample submitted given the normal day-to-day random variations and options in the laboratory system.

Influence factors may cause increases or decreases, or "shifts", in the test results, without affecting their variance. These shifts are referred to as "systematic effects". The influence factors also may cause changes in the variability of the test results. These are referred to as "random effects". Our experience is that the most dominant factors are systematic and cause discrete shifts in the data. An example of a systematic factor would be using excessive grip pressure while performing grab strength tests. This shifts the mean value of the data down due to premature grip-edge ruptures. On the other hand, too low of a grip pressure allows the stronger test specimens to slip in the grips, then gather and snag on the edges of the grips, while the weaker ones behave normally, causing an increase in the overall variance of the data.

Improvements in the quality of the results within a lab will depend on the sensitivity of the individual test method, on the experience and expertise of the personnel, and their proficiency with the measurement uncertainty assessment process.

REPRODCIBILITY, SHIFT AND DRIFT

In order to determine the variability of test results between laboratories, the MUAP is merely extended in scope. One lab is the designated "Baseline Laboratory, or BL". The BL distributes consecutive roll width Repeatability Units of the Source sample to the participating laboratories. The Baseline Laboratory retains several bracketing RU samples that span all of the samples distributed.

Then with each lab following the MUAP procedure for repeatability conditions, the between lab reproducibility of the test method as well as the between laboratory uncertainty can be estimated. The interstitial BL results are plotted vs the machine direction to identify possible "drift" of the Source properties across the samples distributed.

The magnitude of discrete "shifts' of the data between the labs, accounting for any identified material property drift, can then be quantified relative to the Baseline Lab as the "reference". The test method uncertainty of a particular Lab X in the Interlaboratory study would be their uncertainty plus their specific "shift with sign" relative to the BL Lab. This information would be invaluable for resolving Interlaboratory discrepancy issues and would ultimately minimize uncertainty in geosynthetic test results.

CONCLUSION

The measurement uncertainty assessment process is a procedure for calculating test result uncertainty with a single typical geosynthetic sample source. While the statistics are elementary, the effectiveness of the process will depend heavily on the sampling strategy. The key is to preserve the "roll width" natural variations in the individual test determinations, while monitoring the test result drifts in the machine direction due to source material changes. Two immediate applications of this technique include product conformance testing and interlaboratory dispute resolution.

REFERENCES

Subcommittee E11.20 June 2006 "Standard Practice for Estimating the Uncertainty of a Test Method Using Control Chart Techniques", Work Item WK3561. (Note: This is not an ASTM standard; it is under consideration within an ASTM technical committee but has not received all approvals required to become an ASTM standard.)

Ullman, Neil 1997 "Statistics in Standards and Standards Development, Getting to Precision and Bias Course Notes", PCN #36-023033-00.

ASTM Committee E-11 on Quality and Statistics 1991 "Manual on Presentation of Data and Control Chart Analysis", Sixth Edition.

ASTM D 4632-91 2006 "Standard Test Method for Grab Breaking Load and Elongation of Geotextiles", Annual Book of ASTM Standards, Volume 4.13.

ASTM D 5199-01 2006 "Standard Test Method for Determining the Nominal Thickness of Geosynthetics", Annual Book of ASTM Standards, Volume 4.13.

ASTM D 5261-92 2006 "Standard Test Method for Measuring Mass per Unit Area of Geotextiles", Annual Book of ASTM Standards, Volume 4.13.

KEYWORDS

Geosynthetics, Measurement Uncertainty, Precision, Repeatability, Reproducibility, Laboratory Testing, Control Charts

CONTACT:

Rich Lacey
Geotechnics
Phone: 412-823-7600
Email: RLACEY@GEOTECHNICS.NET

GEOTEXTILE FILTERS IN CYCLIC FLOW: TEST RESULTS AND DESIGN CRITERIA

R. Jonathan Fannin, Univ. Of British Columbia, Department of Civil Engineering, A. Srikongrsi, Univ. Of British Columbia, Department of Civil Engineering

ABSTRACT

In contrast to unidirectional seepage flow in routine filter applications, where there is a longstanding body of knowledge on use of geotextiles that is based on considerable field experience and many laboratory studies, the issue of bidirectional, reversing or cyclic flow is one for which our current understanding is very much limited. In this paper, a comparison is made of each laboratory test device, together with a review of the major findings reported from each program of testing. Implications of the laboratory tests are then considered for use of empirical design rules in engineering practice.

INTRODUCTION

In the current state-of-practice, it is reasonable to observe that the behavior of geotextile filters in earthworks subject to unidirectional flow of groundwater seepage through soils is well-understood and, consequently, the companion design criteria may be used with confidence. The confidence is predicated on a thorough understanding of the physical processes that govern compatibility. The design criteria are wholly empirical and, importantly, assume the soils are internally stable (Palmeira and Fannin, 2002).

In contrast to unidirectional seepage flow in routine filter applications, where there is a longstanding body of knowledge on use of geotextiles that is based on considerable field experience and many laboratory studies, the issue of bidirectional, reversing or cyclic flow is one for which our current understanding is very much limited (Fannin, 2006). This may be attributed to several factors, including the uncommon occurrence of reversing flow in routine engineering works, and corresponding lack of good documented field experience, coupled with a paucity of laboratory studies that address the specifics of such flow regimes. Yet considerable challenges exist in the confident provision of filters for protection of civil infrastructure in estuarine and coastal environments, where a subtle distinction can be made between slow reversing flow, such as that of tidal environments, and the relatively faster reversing flow that occurs in the presence of wave action.

Several laboratory studies have examined the nature of soil-geotextile compatibility in cyclic flow (Cazzaffi et al., 1999; Chew et al., 2000; Hameiri, 2000; Fannin and Pishe, 2001; Hawley, 2001; Hameiri and Fannin, 2002). In this paper, a comparison is made of each laboratory test device, together with a review of the major findings reported from each program of testing. Implications of the laboratory tests are then considered for use of empirical design rules in engineering practice.

2. LABORATORY TEST DEVICES

Three separate programs of laboratory testing are examined using devices that were designed and commissioned in Italy, Singapore and Canada. In the absence of a standardized test method, it is reasonable to make a general comparison between each of the studies, but inappropriate to draw detailed comparative conclusions. Nonetheless, findings from these studies prove highly instructive for design practice.

In imposing cyclic flow on a soil-geotextile interface, a test device may be designed to operate using one of two basic principles, namely that of flow-control or that of head-control. The studies conducted in Italy and Singapore were undertaken using similar, but identical, test devices based on flow-control. In contrast the study conducted in Canada was undertaken using a test device based on head-control (see Table 1). All three studies imposed a cyclic flow regime perpendicular to the interface. Details of the size, configuration and operation of each permeameter device are described separately below.

Table 1 Comparison of permeameter test device

Specification detail	**Italy**	**Singapore (NUS)**	**Canada (UBC)**
Reference Standard	None	None	Modified ASTM GR test device
Internal diameter of permeameter (mm)	300	315	100
Length of closest port from geotextile (mm)	100	45	8
Applied confining stress (kPa)	0 - 150	110	0, 25
Operating system	Flow control	Flow control	Head control
Water supply	2-way automatic flow pump	2-way automatic flow pump	3-Constant head tanks
Hydraulic gradient	1 - 15	15	4
Wave period (s)	2 to 20	2 to 15	5 to 50
Washout collection	Yes	Yes	Yes
Cover layer	Available	Available	Not Available
Permeameter wall	Flexible	Rigid	Rigid

2.2 Unsteady flow permeameter (Italy)

Cazzuffi et al. (1999) sought to evaluate the retention capacity of a geotextile in cyclic flow, giving particular emphasis to the influence of confining stress on the hydraulic gradient at which the system response changes from stable to unstable. In so doing, they recognized the combined role of hydraulic and mechanical loading on development of a stable arching network at the interface.

Permeameter: The test device is illustrated schematically in Fig. 1. It comprises a flow device, a permeameter in which the test specimen is reconstituted, and a tank for collection of soil passing

through the geotextile. The permeameter itself is a rigid-walled cylinder of 300 mm diameter that incorporates a flexible section at the location of the base soil against which the geotextile rests. It enables deformation with the soil (and virtually no side friction), hence very little shear stress is mobilized. Therefore it is assumed the base soil transfers the full magnitude of the applied vertical stress to the soil-geotextile interface. The cylinder is made of steel, so the soil specimen cannot be observed during testing.

Collector Trough: A pressurized water tank or base chamber connects the flow pump to the permeameter cell. It functions as a collector trough for soil particles that pass through the geotextile. The bottom of the tank is a cone shape, enabling the particles to settle above a port through which they can be removed for analysis.

Axial Loading System: Vertical stress is applied to the top of the reconstituted soil specimen by means of an axial loading system. The system reacts against a loading frame that is integral to the permeameter cell. Test results are reported for a working range of applied stress to 150 kPa.

Top and Bottom Boundaries: The geotextile is placed on top of a layer of cobbles that are hand-placed on a grid at the basal outlet of the permeamater. This layer is intended to replicate the type of cover system used in field applications. After filling the permeameter with de-aired water, the overlying base soil is reconstituted using one of several methods chosen in order to avoid its segregation during the process of reconstitution.

Hydraulic Control System: The test apparatus is based on flow control, using an automatic pump with interchangeable cylinder of varying capacity. It is capable of simulating a range of wave periods between 2 s and 20 s.

Instrumentations and Measurements: Pressure transducers are inserted into the test specimen at three locations (see Fig. 1). The measurements yield a value of head relative to a datum or equilibrium condition. They enable calculation of the average hydraulic gradient between gauge locations 1 and 2, across a gauge length of approximately 150 mm which captures the soil-geotextile interface, and between locations 2 and 3, which are separated by a distance of 186 mm within the base soil only. These values are reported as the interface gradient, i_{int} and reference gradient, i_{ref}, respectively. A ratio of the two values yields a quantitative measure of the system compatibility given by:

$$R = i_{int} / i_{ref} \quad (1)$$

The ratio of values is directly comparable to the gradient ratio that is measured and reported in the standardized ASTM Gradient Ratio test (ASTM D5101), where the latter is defined over considerably shorter gauge lengths (see eqn. 2, below).

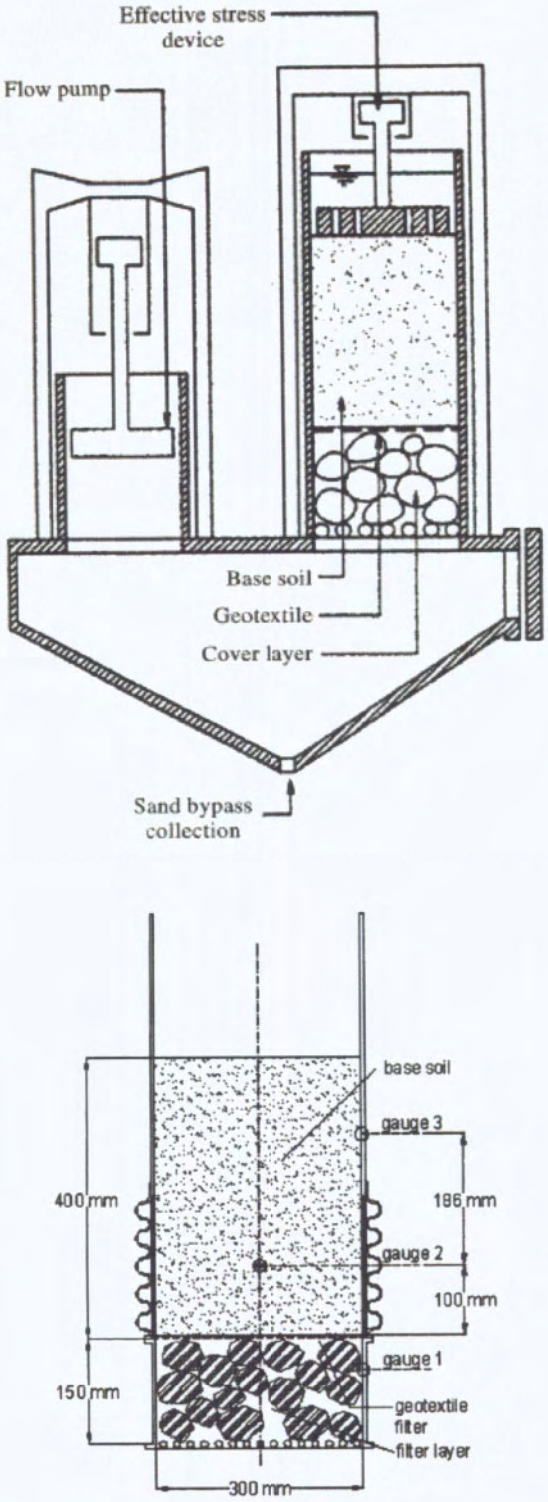

Figure 1. Unsteady flow permeameter: (a) system configuration and (b) permeameter cell (after Cazzuffi et al., 1999)

2.2 Bi-directional flow apparatus (Singapore)

The apparatus developed by Chew et al. (2000), at the National University of Singapore, shares many similarities with that developed by Cadzuffi et al. (1999) and on which it is modeled. It too operates on a principle of flow-control and comprises three basic units, namely a permeameter chamber in which the test specimen locates, a cyclic wave generator, and a water reservoir that acts to collect soil particles that washout during the test (Fig. 2).

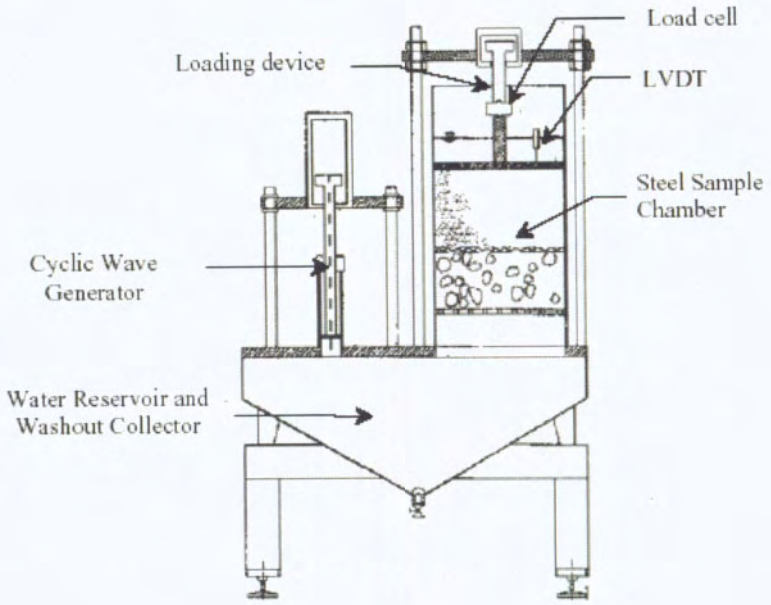

(a)

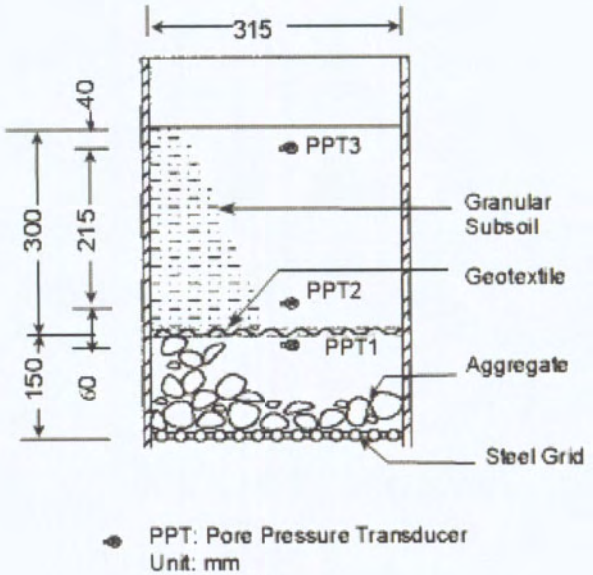

(b)

Figure 2. Bi-directional flow apparatus: (a) system configuration (b) permeameter cell (after Chew et al., 2000).

Permeameter: In contrast to the Italian device, this permeameter has a fully rigid wall. The internal diameter is slightly larger at 315 mm. Once again, it comprises a supporting steel grid, an aggregate layer simulating the protective stone layer, the geotextile, and the stone layer to be protected.

Collector Trough: Like the Italian device, a lower water reservoir serves also to collect particles that pass through the geotextile.

Axial Loading System: Electro-pneumatic control of a loading cylinder enables application of a vertical stress to the top of the test specimen, by means of a piston and top cap. Results are reported for an applied stress of 110 kPa.

Top and Bottom Boundaries: As noted earlier, the configuration of the boundaries is very similar to that of the Italian device on which its design is based. In the absence of a flexible section being incorporated in the wall of the permeameter, the inside wall of the permeameter was covered in a layer of grease to reduce the effect of sidewall friction.

Hydraulic Control System: The test apparatus is based on flow control, using an automatic two-way wave generator. It allows for imposition of a wave period in the range 2 s to 15 s.

Instrumentations and Measurements: Although the response to cyclic flow was once again quantified with reference to measurement of water head at three locations within the permeameter, the relative position of the port locations varies from that in the Italian device. More specifically, the 60 mm spacing between PPT1 and PPT2 yields a shorter gauge length across the soil-geotextile interface, and the 215 mm spacing between PPT2 and PPT3 results in a longer gauge length in the base soil.

2.3 Gradient Ratio test device (Canada)

A cyclic gradient ratio (CGR) test device was developed at the University of British Columbia (Hameiri, 2000; Hameiri and Fannin, 2000) from experienced gained in modifying the ASTM gradient ratio test device (Fannin et al., 1996) to more precisely characterize changes in water head distribution in base soil immediately adjacent to the geotextile. The device comprises a permeameter, collector trough, axial loading system, and hydraulic control system (see Fig. 3).

Permeameter: The rigid-wall permeameter is made of Plexiglas to permit observations of the soil sample during testing. These visual observations have proved valuable for an interpretation of test behavior, especially for clogging of the geotextile. The permeameter accommodates a cylindrical soil sample of diameter and length approximately 100 mm. Four ports located on the wall of the permeameter (Port numbers 2, 3, 5, and 6), together with an additional port located above and below the sample (Port numbers 1 and 7), are used to define the distribution of water head. The position of port 2, 3, 5 and 6 are located at 101 mm, 75 mm, 25 mm and 8 mm above the geotextile (see Fig. 4).

The gradient ratio value is defined by the ratio of the hydraulic gradient in the soil-geotextile composite (i_{sg}) to that in the soil (i_s), where with reference to Ports 3, 5, and 7:

$$GR_{ASTM} = i_{sg}/i_s = i_{57}/i_{35} \quad (2)$$

and a modified value based on an additional port number 6, can be expressed as:

$$GR_{MOD} = i_{sg}/i_s = i_{67}/i_{35} \quad (3)$$

The geotextile specimen seats on a stainless steel wire mesh, with 2.4-mm-square openings, which rests on a base plate that is 11 mm thick, with 1.9-mm holes on a 2.8-mm center-to-center spacing. This provides for unimpeded flow through the geotextile.

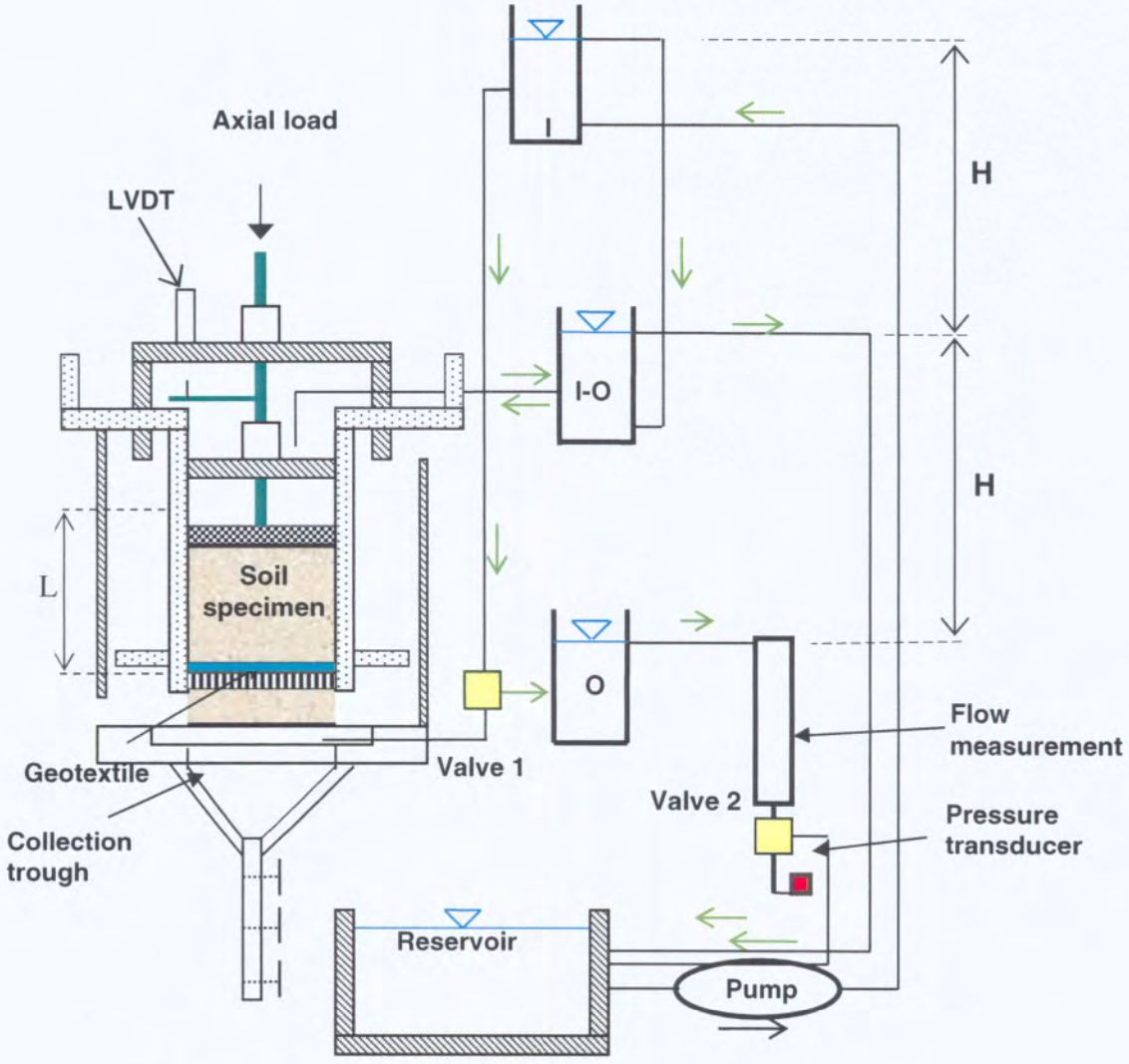

Figure 3. Cyclic gradient ratio device (after Hameiri, 2000).

Collector Trough: A conical trough mounts below the permeameter and connects to a flexible silicon tube. Particles from the sample that pass through the geotextile specimen are collected in this trough, and settle in the hose. A series of discrete samples may be collected during sample preparation and testing by clamping the hose at various intervals.

Upon termination of the test, the tube is removed and the samples extracted for particle size analysis. The analyses were made using an X-ray particle size analyzer. It operates on the principal of sedimentation. A sample of mass greater than 2g, which corresponds to a mass/unit area greater than 250 g/m^2 passing through the geotextile, is sufficient for purposes of analysis.

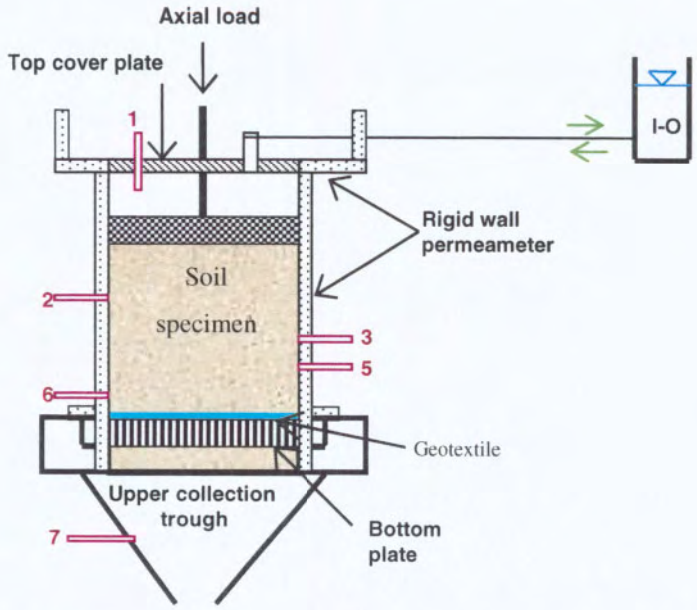

Figure 4. Configuration of the permeameter cell (after Hawley, 2001).

Axial Loading System: Vertical stress is applied pneumatically to the top of the sample. The load is transmitted to a loading plate through a piston (see Fig.3). Results are reported here for tests performed at a relatively low confining stress of 25 kPa, and for zero confining stress.

Top and Bottom Boundaries: Geotextile is placed above and below the soil sample. The lower geotextile, which is the test specimen under examination, seats on a wire mesh which in turn is supported by a bottom plate having 5 mm holes perforated with a triangular spacing of 3mm. Two geotextile specimens are incorporated within the top loading plate, to protect against upward soil migration during reversing flows. The permeameter is sealed by a top plate on which port 1 is located.

Hydraulic Control System: The principle of operation is that of head control, by means of three constant head tanks (see Fig.3), termed the inflow (I) tank, the inflow outflow (I-O) tank, and the outflow (O) tank. These tanks are supplied with de-aired water from a reservoir, by a peristaltic pump. Overflow discharge from the I tank is routed to the I-O tank, and then returned to the reservoir. Overflow from the O tank is routed to an outflow measurement tank, described below. Unidirectional, downward seepage through the permeameter occurs with flow from the I-O tank to the O tank. Reversing seepage occurs with a downward component under this arrangement, and an upward component with flow from the I to the I-O tank. A switching operation invokes the reversal of flow, whereby a computer-controlled solenoid valve (Valve 1) is set either to receive flow from the inlet tank or direct flow to the outlet tank. For a given sample length (L), the imposed hydraulic gradient is controlled by the equidistant spacing (H) of the three tanks.

Instrumentations and Measurements: Filtration compatibility is evaluated with reference to the distribution of water head across the interface of the soil sample and geotextile specimen. The variation in water head between each port (h12, h23, h35, h56, and h67) is measured with differential pressure transducers. These transducers are well-suited to the measurement of transient pore water pressures in comparison to manometers. Flow rate is calculated using the volumetric discharge from the outflow (O) tank, which monitors both unidirectional flow and the downward component of reversing flow. Discharge is recorded using a total pressure transducer mounted below the outflow measurement tank (M). The tank is emptied periodically under the control of a solenoid valve (Valve 2). Additionally, the sample length is monitored with an LVDT, and the applied normal stress is deduced from measurement of the axial load.

3. FINDINGS OF THE INTERNATIONAL STUDIES

Each of the three international initiatives sought to examine factors influencing compatibility of the soil-geotextile filtration zone. A common feature of each device is the imposition of cyclic flow in a direction perpendicular to the plane of the geotextile, and the evaluation of the system response with reference to a ratio of hydraulic gradient and with reference to the mass of soil passing through the geotextile. Cohesionless soils were examined in the respective programs of testing (see Fig. 5). Results are reported here for those six gradations, which range from a sand with some silt through to a gravelly sand.

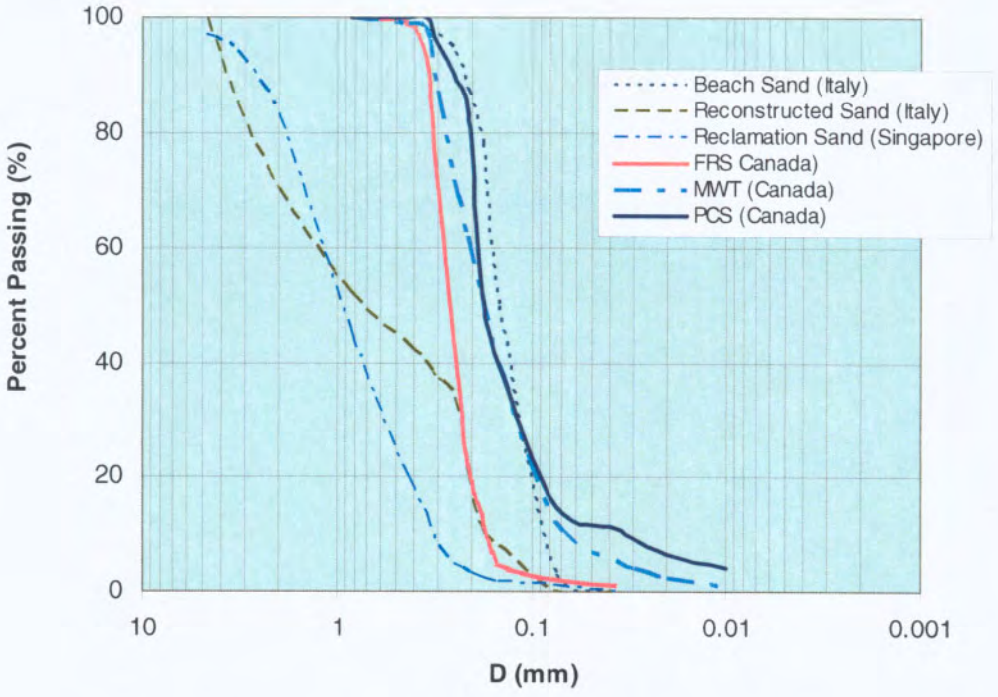

Figure 5. Range of soil gradation tested in cyclic flow.

Subtle differences exist in the focus of each experimental study. The Italian work had a focus on the relation between hydraulic gradient and stress on the onset of instability, whereas the Singapore work had a focus on the period of cyclic loading and its implications for design. The work in Canada sought to verify empirical design criteria, for given conditions of imposed

hydraulic gradient and confining stress. These subtle differences are reflected in the corresponding test programs and materials (see Table 2).

Table 2. Summary of the test programs.

Item		Italy	Singapore	Canada (UBC)
Soil		Beach sand; Reconstituted sand	Reclamation sand	River sand; Mine waste tailings
Sample size (mm)	Dia.	300	315	100
	Length	400	300	100
Geotextile opening size (mm)	AOS		0.10 (NW)	0.21 (NW), 0.21-0.6 (W)
	FOS			0.10-0.29 (NW)
	Other	O_{95}= 0.16 (NW) & 0.44 (W) (Italian Std. CNR 144)	OSA = 0.47 (W) (E DIN 60 500)	
Soil placement		Pluviation (uniformly graded soils); Aerial deposition (well graded soils)	Pluviation	Water pluviation (uniformly graded soils); Slurry deposition (well graded soils)
Performance index		R; Mass. of washout	R_i; Mass of washout	Gradient Ratio; Mass of washout

Note: R = Ratio of interface gradient to in-soil gradient (see Eq.1)
R_i = Rate of change of gradient in a wave period $\approx 2\Delta i/T$
where Δi = change of hydraulic gradient, T = wave period

3.1 Influence of effective stress

Combinations of two soils and two geotextiles were tested using hydraulic gradients ranging to from 1 to 15 (periods ranging from 5 s to 20 s) and effective stresses ranging from 0 to 150 kPa. Measured values of soil passing in tests with the uniformly graded beach sand and the woven geotextile with O_{95} = 0.44 mm, after 1500 cycles, are summarized in Fig. 6. The quantity of soil passing with this combination of test materials was noted to be strongly dependent on the applied gradient and, in particular, the effective stress on the soil-geotextile interface. More significantly, Cazzufi et al. (1999) observe that when "the effective stress increases over the 100 kPa value, the filter becomes stable, regardless of the applied gradient". In contrast, the same uniform sand tested in combination with the needle-punched nonwoven of smaller O_{95} = 0.16 mm, exhibited an almost negligible loss of particles to washout.

These and other results led to the postulation of a conceptual model for soil retention, and therefore interface stability, as a function of normal effective stress and cyclic gradients (see Fig. 7). The conceptual model applies to combinations of soil and geotextile for which the characteristic opening size of the geotextile (O_{95}) exceeds the maximum grain size of the soil (D_{100}), yielding an interface that is not "soil tight"

Given this influence of effective stress, it was suggested that acceptance criteria for compatibility be based on the quantity of soil passing (g/m^2) during the test, and on a limit value to the ratio value R of hydraulic gradient. The latter value provides an indirect measure of the reduction of soil hydraulic conductivity adjacent to the geotextile. Further laboratory testing, and monitoring of field test sites, were deemed necessary to establish specific values for design practice.

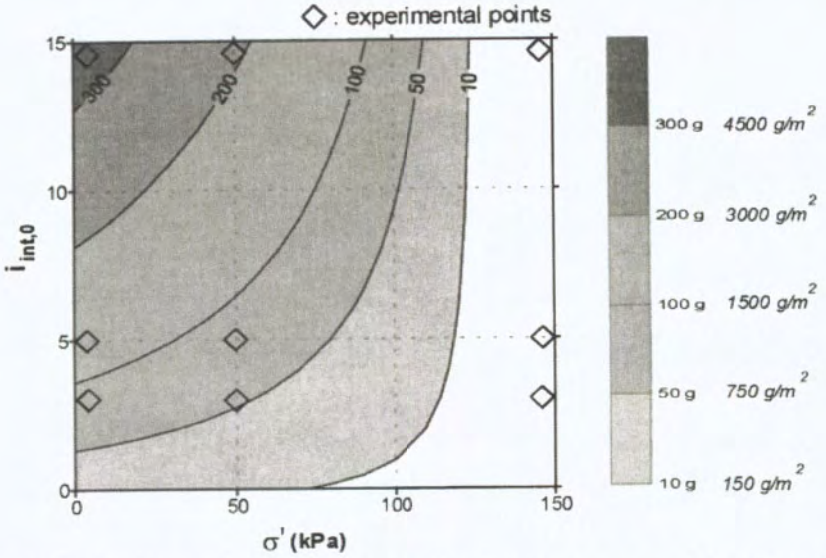

Figure 6. Variation of soil passing: uniform sand and woven geotextile (after Cazzuffi et al., 1999).

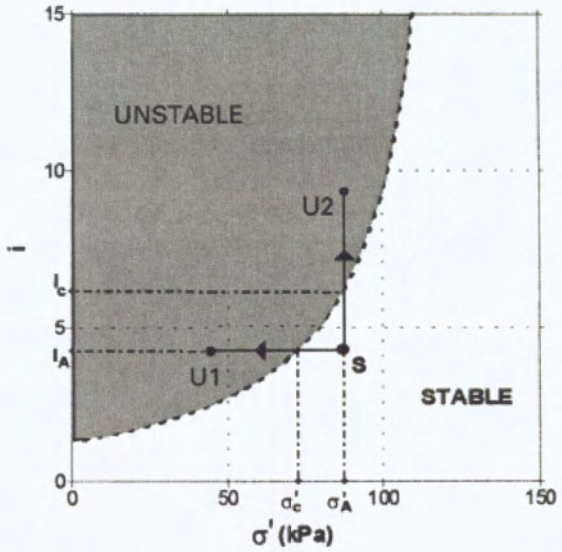

Figure 7. Conceptual model for evaluation of stability of soil-geotextile interface (after Cazzuffi et al., 1999)

3.2 Influence of wave period

Combinations of one uniformly graded gravelly sand and two geotextiles (see Table 2) were tested at periods ranging from 2 s to 15 s, for a constant applied effective stress of 110 kPa. The

nonwoven geotextile exhibited a characteristic opening size slightly smaller than that of the Italian study, and the woven geotextile a value slightly larger than the comparable geotextile in the Italian study. For both geotextiles, the opening size was considerably smaller than the D_{85} of the soil, and therefore it was expected that the combinations should exhibit a stable interface. Indeed Chew et al. (2000) note that for the combination tested, $O_{95} < D_{50}$, implying satisfaction of the Leuttich et al. (1992) criterion for dynamic flow conditions. The variation in soil passing with imposed period of cyclic flow, for each geotextile, is illustrated in Fig. 8 after a total of 2000 cycles. Chew et al. (2000) observe that inspection of the figure suggests the loss is similar for both geotextiles at long wave periods (> 10 s), but at short periods (2 s) the woven geotextile experiences a relatively greater loss.

Analysis of the results led to the conclusion that the quantity and grain size distribution of soil washing through the geotextile are "functions of not only the wave magnitude (based on the wave period and the number of cycles), but also the type and characteristic opening size of the geotextile". Further the rate of change of hydraulic gradient, R_i, was found a useful parameter for performance evaluation of soil-geotextile compatibility. The R_i values are approximately equal to $2\Delta_i/T$, where Δ_i is a change in magnitude of hydraulic gradient within a wave period (T). More specifically, the utility of pore pressure measurements close to the soil geotextile interface was given explicit recognition.

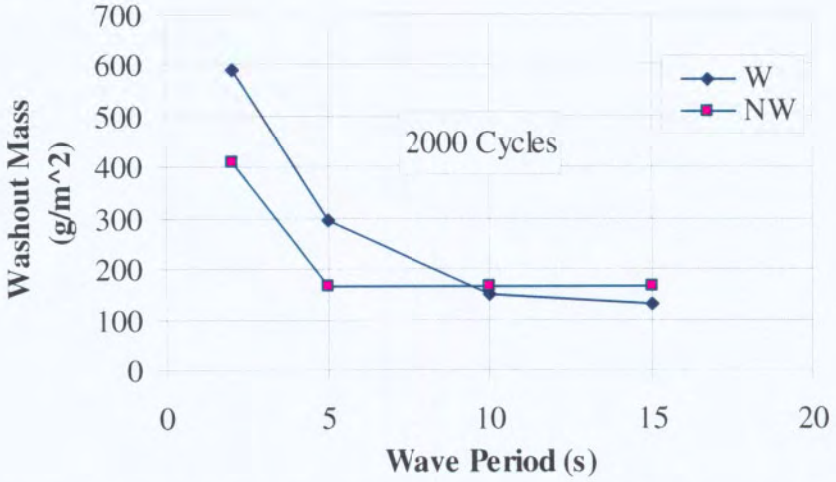

Figure 8. Effect of wave period on soil loss (redrawn after Chew et al., 2000).

3.3 Criteria for soil retention

The focus of the research program at the University of British Columbia was primarily to evaluate design criteria for dynamic flow conditions. A series of multistage cyclic flows tests, on specimens of reconstituted glass beads, was used to commission the laboratory test device (Hameiri, 2000). The utility of a modified value of gradient ratio was demonstrated, based on measurement of the hydraulic gradient across a gauge length of only 6 mm across the base soil and geotextile. The rationale for this relatively short gauge length is that any change in the fabric and structure of the interface is most evident in this relatively thin zone. Additionally, a threshold value of 2500 g/m^2 for the mass of soil passing through the geotextile (after Lafleur et al, 1989) was examined and found reasonable.

Hawley (2001) extended the scope of that work by conducting a series of tests on two natural soils, a Fraser River sand and Port Coquitlam sand, and a mine waste tailings deposit. The Fraser River sand (FRS) is a naturally occurring river deposit comprising subangular to subrounded fine sand with little silt: The grain size distribution is uniform with a coefficient of uniformity (C_u) of 1.8 and a D_{85} of 0.330 mm (see Fig. 5). The Mine Waste Tailings material (MWT) is an angular to subangular deposit with a C_u of 3.3 and a D_{85} of 0.290 mm. The Port Coquitlam silty sand (PCS), also a river-deposited material, comprises a subrounded silty sand having a C_u of 5.8 and a relatively small D_{85} of 0.215 mm. Two of the soils, MWT and PCS, were identified as being potentially problematic from a filtration standpoint based on local engineering experience.

Combinations of the three soils were tested against seven geotextiles, for which material properties are reported in Table 3. The two nonwoven geotextiles have the same opening size of 0.212 mm, and the woven geotextiles exhibit a range from 0.212 mm to 0.6 mm. Tests were conducted at average hydraulic gradients ranging to from 2 to 4. Test variables examined were (i) the flow regime (unidirectional or cyclic), (ii) the imposed normal stress (0 or 25 kPa), and (iii) the period of cyclic flow reversal (50 s or 10 s). A summary of the multistage test sequence followed in testing is given in Table 4.

Table 3. Physical properties of the geotextiles (after Hawley, 2001).

Geotextile (code)	Type	Mass / Unit Area	AOS (ASTM D4751)	Permittivity (ASTM D4491)	Permeability
	NW/W	(g/m^2)	(mm)	(sec^{-1})	(cm/s)
140	NW	287	0.212	1.310	0.290
160	NW	185	0.212	1.192	0.134
700	W	218	0.212	0.511	0.021
500	W	225	0.300	0.769	0.049
404	W	282	0.425	0.881	0.080
402	W	304	0.425	2.003	0.194
570	W	453	0.600	0.366	0.061

Table 4. Modified multistage test sequence (after Hawley, 2001).

Stage	UNI1	CYC1	UNI2	CYC2	UNI3	CYC3	UNI4
Normal Stress (kPa)	0	25	25	25	25	0	0
Wave Period (s)	0	50	0	10	0	10	0

Measured values of soil passing in the first stage (CYC1: 1152 cycles over 16 h) and third stage (CYC3: 260 cycles over 43.3 min) of testing are reported in Fig. 9, as a relation between soil loss and the ratio of characteristic opening size of the geotextile to grain size of the base soil (AOS/D_{85}). The general trend is one of increasing loss with value of AOS/D_{85}. The relation appears sensitive to opening size of the geotextile, given a typical loss between 1 and 60 g/m^2 at $AOS/D_{85} = 1$ and a loss between 100 and 1000 g/m^2 at $AOS/D_{85} = 2$, during the first stage of cyclic loading performed at a confining stress of 25 kPa. None of these results exceed the limit of

2500 g/m^2 advocated by Lafleur et al. (1989). However the more aggressive loading of the third stage, during which the normal stress was reduced from 25 kPa to zero and the period reduced from 50 s to 10 s, produced a greater loss of soil and values in excess of 2500 g/m^2. The generalized nature of this response, namely increased loss at reduced confining stress and wave period, appears consistent with the observations of Cazzuffi et al. (1999) and Chew et al. (2000).

Holtz et al. (1997) proposed an acceptance criterion for soil retention of $AOS/D_{85} \leq 0.5$, for conditions of dynamic, pulsating or reversing flow. By inspection of the laboratory test data of Fig. 9, it appears this criterion would be consistent with a soil loss that is acceptably low.

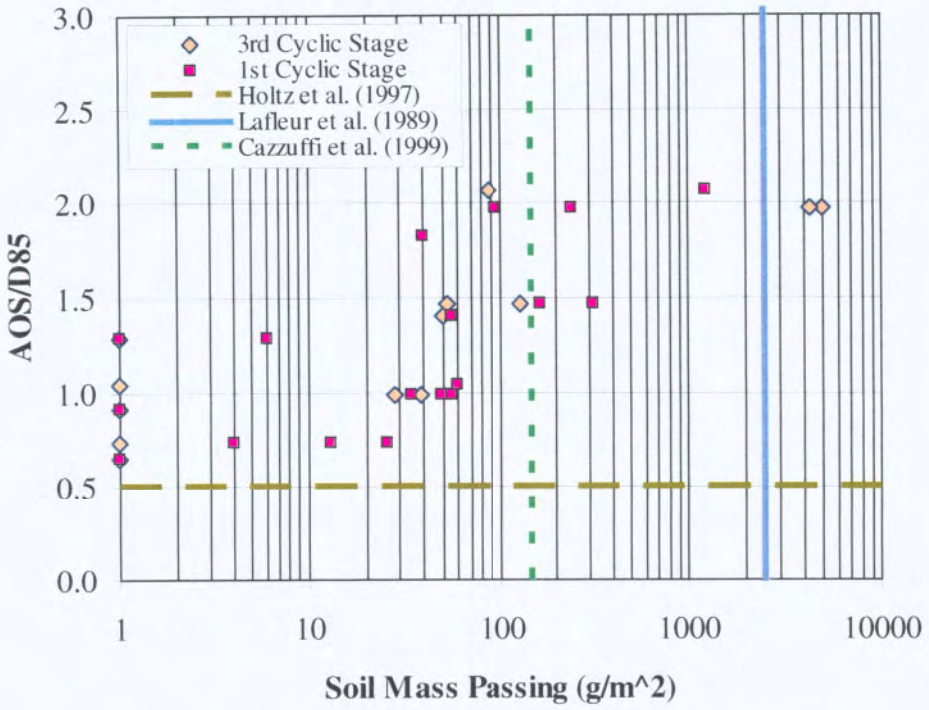

Figure 9. Relation between soil mass passing and AOS/D_{85}

SUMMARY REMARKS

Comparison of the three international studies yields insights that are relevant both to laboratory testing intended to evaluate soil-geotextile compatibility in cyclic flow, and also to empirical design criteria for soil retention in engineering practice. In laboratory testing, the two criteria commonly used to evaluate compatibility are that of mass of soil passing through a unit area of the geotextile and that of the ratio of hydraulic gradient across the soil-geotextile interface to the soil alone. Notwithstanding the relatively short duration of laboratory tests, relative to the service life of shoreline protection works, the mass of soil passing is observed to increase as the period of wave loading is reduced, and also to increase as the confining stress is reduced. The finding has implications for protection works where the wave period may be less than 10 s and the confining stress is anticipated to be very low.

The laboratory data are supportive of the Holtz et al. (1997) criterion for soil retention of AOS ≤ 0.5 D_{85}. However, it must be recognized that shoreline protection works often encounter soils that are predominately fine sand. Yet there are few geotextiles with an AOS smaller than 0.05 to 0.075 mm. Accordingly, the rule would eliminate use of a geotextile in soils with a D_{85} less than 0.1 to 0.15 mm, which represents many problematic soils. This may be unnecessarily punitive, and further research is urgently needed to address this issue of undue conservatism.

REFERENCES

Cazzuffi, D.A., Mazzucato, A., Moraci, N., & Tondello, M. (1999). A new test apparatus for the study of geotextiles behaviour as filters in unsteady flow conditions: relevance and use, Geotextiles and Geomembranes, Elsevier, England, Vol. 17, No. 5-6, pp. 313 - 329.

Chew, S.H., Zhao, Z.K., Karunaratne, G.P., Tan, S.A, Delmas, Ph., and Loke, K.H. (2000). Revetment Geotextile Filter Subjected to Cyclic Wave Loading, Advances in Transportation and Geoenvironmental Systems Using Geosynthetics, Proceedings of Sessions of Geo-Denver 2000, August 5-8, Denver, CO, pp. 162 – 175.

Fannin, R.J. (2006). Chapter 6: Filtration, in Geosynthetics (Ed. R.W. Sarsby), published by Woodhead Publishing, Cambridge, U.K., pp. 127-147 (in press).

Fannin, R.J. and Pishe, R. (2001). Testing and specifications for geotextile filters in cyclic flow applications, Proceedings, Geosynthetics 2001, February 12-14, Portland, OR, pp. 423-435.

Fannin, R.J., Vaid, Y.P., Palmeira, E.M. and Shi, Y.C. (1996). A Modified Gradient Ratio Device, Recent Developments in Geotextile Filters and Prefabricated Drainage Geocomposites, ASTM STP 1281, S.K Bhatia and L.D. Suits, Eds., ASTM, Philadelphia, pp. 100 – 112.

Hameiri, A. (2000). Soil Geotextile Filtration Behavior Under Dynamic Conditions of Vibration and Cyclic Flow. PhD Thesis, University of British Columbia, Vancouver.

Hameiri, A. and Fannin, R.J. (2002). A Cyclic Gradient Ratio test Device. ASTM Geotechnical Testing Journal, Vol. 39, No.2, pp.266-276

Hawley, R. (2001). Filtration Performance of Geotextiles in Cyclic Flow Conditions. MASc Thesis, University of British Columbia, Vancouver.

Holtz, R.D, Christopher, B.R., and Berg, R.R. (1997). Geosynthetic Engineering, BiTech Publishers, Richmond, BC, pp.29-68.

Lafleur J., Mlynarek J., and Rollin A. L. (1989). Filtration of Broadly Graded Cohesionless Soils, Journal of Geotechnical Engineering, ASCE, Vol. 115, No. 12, pp. 1747-1768.

Luettich, S.M., Giroud, J.P., and Bachus, R.C. (1992). Geotextile Filter Design Guide, Geotextiles and Geomembranes, Elsevier, England, No. 11, pp. 355 - 370.

Palmeria, E.M. and Fannin, R.J. (2002). Soil-geotextile compatibility in filtration, Proceedings, 7th International Conference on Geosynthetics, Nice, France, September 22-27, 2001, pp. 853-872.

Mannsbart, G. and Christopher, B.R. (1997). Long-Term Performance of Nonwoven Geotextile Filters in Five Coastal and Bank Protection Projects, Geotextiles and Geomembranes, Elsevier, England, No. 15, pp. 207 – 221.

CONTACT:
Dr. Jonathan Fannin, PE
Professor of Civil Engineering
University of British Columbia
6250 Applied Science Way
Vancouver, BC
CANADA
Phone: 604 822 3557
Email: jonathan.fannin@ubc.ca

Mechanistic Response Measurements of Geogrid Reinforced Flexible Pavements to Vehicular Loading

I.L. Al-Qadi[1], E. Tutumluer[2], S. Dessouky[3] and J. Kwon[4]

[1] Founder Professor of Engineering, Ph (217) 265-0427, E-mail: alqadi@uiuc.edu
[2] Associate Professor, Ph (217) 333-8637, E-mail: tutumlue@uiuc.edu
[3] Research Scientist, Ph (217) 893-0406, E-mail: dsamer@uiuc.edu
[4] Research Assistant, Ph (217) 333-6973, E-mail: jaykwon@uiuc.edu

Department of Civil and Environmental Engineering, University of Illinois at Urbana-Champaign, 205 N. Mathews, Urbana, Illinois 61801, FAX (217) 333-1924.

ABSTRACT

Current ongoing research at the University of Illinois has focused on the development of a mechanistic model to analyze geogrid base-reinforced pavements. To validate the recently developed mechanistic response model as well as to develop pavement distress models for typical low-volume roads, a total of nine flexible pavement sections were constructed and tested at the University of Illinois Advanced Transportation Research and Engineering Laboratory (ATREL). The variables considered in this full-scale testing study were: (1) type and stiffness of geogrid reinforcement; (2) pavement layer thicknesses; and (3) location of the geogrid within the aggregate base. The sections were heavily instrumented with load-associated instrumentation such as pressure cells, linear variable displacement transducers (LVDTs), and strain gauges. Environmental conditions were also monitored throughout the test using thermocouples, time domain reflectometry (TDR) probes, and piezometers. The subgrade California Bearing Ratio (CBR) was maintained below 4% throughout all tested sections. The test sections were loaded utilizing the University of Illinois Advanced Transportation Loading ASsembly (ATLAS). Response testing was conducted by applying three load levels, 26.7, 35.6, and 44.5 kN at two trafficking speeds, 8 and 16 km/h. Then, the 44.5-kN loading was applied at 8 km/h until the pavement sections failed (with 25mm-wide ruts in the wheel paths). Preliminary analyses of the pavement sections indicated that the geogrid reinforcement reduced lateral movement in the aggregate base layer, especially in the direction of traffic, when compared to unreinforced sections. Lower vertical deflections were also measured on top of the subgrade in the reinforced sections.

INTRODUCTION

The effectiveness of geogrid reinforcement appears to be more pronounced when used in roads designed for low to moderate traffic volumes, especially when the pavement structure consists of a thin hot-mix asphalt (HMA) layer on top of a granular base/subbase layer constructed on weak subgrade. Although significant testing has been conducted in the laboratory and theoretical models have been developed, limited information to quantify the performance of geogrid-reinforced pavement systems exists (Al-Qadi, 2002; Al-Qadi and Bhutta, 1999; Brandon *et al*., 1996; Perkins and Cortez, 2004). Because of the complexity of layered pavement systems and applied loading

conditions, it was difficult to reliably identify the effectiveness of geogrid when incorporated in in flexible pavement systems. Hence in the past, mainly performance-based tests had been conducted to evaluate the structural contribution of geogrid.

One reliable method of quantifying the effectiveness of geogrids in pavements is by testing full-scale pavement sections with embedded instruments and measuring the pavement's response to loading. Accelerated load testing is a middle solution between real, in-the-field pavement measurements and simple laboratory tests, compressing many years of road deterioration into a few months, if not weeks, of testing. In accelerated load testing, pavement instrumentation has become an important tool in monitoring in-situ pavement material performance and quantitatively measuring pavement system response under different vehicular and environmental loading conditions. In-situ measurements of these parameters allow for the development of accurate performance models and the calibration of mechanistic pavement design approaches.

Full-scale accelerated pavement testing was initiated recently to validate and calibrate geogrid base reinforcement mechanistic response models, such as the one recently presented by Kwon et al. (2005), as well as to develop transfer functions (or distress models) to predict the rutting and fatigue performances of geogrid-reinforced pavements. Nine instrumented full-scale flexible pavement test sections were designed and constructed to evaluate and quantify the effectiveness of using geogrids in flexible pavements. The subgrade California Bearing Ratio (CBR) was maintained below 4%. The nine sections were divided into three categories based on the total thicknesses of the pavement layered structures. Test sections were instrumented for measuring pavement response to axle and environmental loading.

This paper presents preliminary results of the ongoing full-scale test section study. The focus will be on the measured responses and performances of the three pavement sections in the thinnest cell. Each section has only 76mm HMA underlain by 203mm unbound aggregate base layers. The constructed pavement test sections included two sections having different types of geogrids and one unreinforced control section. Measured responses to vehicular loading are presented together with the failed layer profiles of the pavement sections to quantify the effectiveness of geogrid reinforcement in low volume pavements.

TEST SECTION LAYOUT

Three pavement cells, each 3.65m wide and divided into a total of nine instrumented flexible pavement test sections, were constructed at the University of Illinois Advanced Transportation Research and Engineering Laboratory (ATREL) facility. Table 1 provides the layout of the test sections with the locations and geogrid types used. The geogrid properties used in the full-scale test sections are listed in Table 2. The test sections differed in granular base layer thicknesses (203, 305, and 457mm) and HMA layer thicknesses (76 and 127mm). They were loaded utilizing the University of Illinois Advanced Transportation Loading ASsembly (ATLAS), which has a traffic length of 25m. The length of each cell, which includes three pavement sections, is less than 25m. This allows testing under the same loading and environmental conditions. Transition sections were located between the test sections to ensure that when pavement geometry changed, propagation of pavement distresses from neighboring test sections was minimized.

Table 1 Pavement Test Section Geometry

Pavement test cell no.	Section No.	Base thickness (mm)	HMA thickness (mm)	Length (m)	Geogrid type and location
A	A-1	203	76	6.1	GG1 @ Subgrade-base interface
	A-2			6.1	GG2 @ Subgrade-base interface
	A-3			6.1	Control
B/C	B-1	305	76	6.1	Control
	B-2			7.6	GG2 @ Subgrade-base interface
	C-1		127	7.6	Control
D	D-1	457	76	6.1	GG2 @ 153mm from top base
	D-2			6.1	GG2 @ Subgrade-base interface & GG2 @ 153mm from top base
	D-3			6.1	Control

Table 2 Properties of Geogrid Products Used in the Full-Scale Test Sections

Properties	**Test method**	**Units**	**GG1**		**GG2**	
Geometry			**MD** *	**TD** *	**MD**	**TD**
Aperture size	Calipered	mm	25	33	25	33
Rib thickness	Calipered	mm	1.07	0.76	1.78	1.14
Load capacity			**MD**	**TD**	**MD**	**TD**
Initial modulus	ASTM D6637-01	kN/m	250	400	400	650
Tensile strength at 2% strain	ASTM D6637-01	kN/m	4.1	6.6	6.0	9.0
Tensile strength at 5% strain	ASTM D6637-01	kN/m	8.5	13.4	11.8	19.6
Ultimate tensile strength	ASTM D6637-01	kN/m	850	1,300	1,315	1,975

*Note: *. MD = Machine Direction (along roll length), TD = Cross-Machine Direction (across roll width)*

The subgrade soil was in general classified as ML, CL, or a combination of ML and CL using the dual classification in accordance with the Unified Soil Classification System. The soil specific gravity is 2.72. Atterberg limit tests (ASTM D 4318) were

conducted and indicated that the subgrade soils had an average liquid limit (LL) of 21, an average plasticity limit (PL) of 16, and an average plasticity index (PI) of 5.

INSTRUMENTATION AND DATA ACQUISITION SYSTEM

Instrumentation

Instruments used in this experimental study can be divided into two categories: those used to measure environmental effects (temperature and moisture) and the ones used to monitor loading effects (stress, strain, deflection, and pore-water pressure). A total of 173 instruments were placed during the construction. Load-associated instruments were installed at the centerline to measure response underneath the wheel loading path, and environmental instruments were installed at a 0.9m offset from the centerline of the 3.65m one-lane section (Al-Qadi *et al.*, 2004). Instrument wires were protected with mastic geosynthetics. All instrument wires were collected from the three sections of each cell and extended to the data acquisition systems. One hundred percent instrumentation survivability was achieved after construction. Table 3 presents a summary of the sensor types used in each pavement test section.

Table 3 Summary of Test Section Field Instrumentation

Test section	SG[1]	PC[2]	TDR[3]	TC[4]	LVDT[5]	PZ[6]	Total
A1	1	2	2	NA	4	NA	9
A2	2	2	NA	16	4	NA	24
A3	1	2	2	NA	4	NA	9
B1	1	2	NA	NA	5	NA	8
B2	2	2	2	20	5	NA	31
C1	1	2	2	22	5	NA	32
D1	1	2	NA	NA	6	NA	9
D2	2	2	2	24	8	1	39
D3	1	2	NA	NA	8	1	12
Total	12	18	10	82	49	2	**173**

[1] SG: Dynatest strain gauge; [2] PC: Pressure cell; [3] TDR: Time domain reflectometry;
[4] TC: Thermocouple; [5] LVDT: Linear variable displacement transducers; [6] PZ: Piezometer

Data Acquisition System

An in-house custom data acquisition system was developed to monitor the pavement response using the National Instruments Labview data acquisition software. The system consisted of five modules based on the instrument types to collect static and dynamic response data for different loading and environmental conditions. Static measurements reflected the environmental effects and dynamic measurements reflected response to axle wheel loading. Time intervals for collecting static data were 15min for temperature and 30min for moisture (Loulizi *et al.,* 2002; Diefenderfer, *et al.* 2000).

ACCELERATED LOADING FACILITY AND EXPERIMENTAL PROGRAM

A typical overloaded truck with a dual-wheel axle configuration (44.5kN per half axle) moving at 8km/hr was used to apply loading to the pavement test sections. During response testing, the pavement test sections were loaded both at the centerline and three additional offset locations (153, 305, and 457mm). Traffic loading was applied only at the centerline of the test section.

Response testing was first conducted at three wheel loads (26.7, 35.6, and 44.5kN) at two speeds, 8 and 16km/hr. To evaluate pavement responses under various tire pressures, 551, 689, and 758kPa were used to study the effects at each of the three wheel loads trafficked at the two speeds.

Traffic testing was conducted next at 8km/hr using the 44.5kN tire load and 689kPa tire pressure. Pavement rut profiles were measured periodically for each test section using a straight edge. A leveled, 4.3m long straight steel beam was placed across the test sections at six to eight locations in the longitudinal direction. Profiles were surveyed every 1.2m in the longitudinal direction. A digital caliper was used to measure the profiles of the pavement surface with respect to the leveled steel beam. At each surveyed location, 21 measurements were taken across the transverse direction. An average rut depth of 25mm was considered an indication of pavement failure. Visual inspections were also made regularly to monitor crack evolution and propagation.

"A" TEST SECTIONS RESULTS

Temperature profiles of all pavement layers and moisture contents of the subgrade locations were continuously monitored from the beginning of test section construction to the end of the test program. The TDR readings showed that the moisture contents in the subgrade were somewhat constant indicating a stable subgrade during the course of both response and performance testing. Figure 1 shows the volumetric moisture contents monitored by two TDR probes in the A-sections maintained at an average of 51% of volumetric moisture content (18.75% gravimetric). This value, which is the same as the constructed subgrade moisture content, indicates that the low as-built CBR was maintained during the course of testing. The moisture stability during testing is because of the transverse and edge drain system installed during the pavement construction.

Trafficking test results starting from 500 passes are shown in Figures 3 through 5. Pavement temperature profiles measured in the fall of 2005 using thermocouples placed in each layer showed that the HMA surface layer was the most sensitive to temperature changes (see Figure 2). To compare measured responses for the same test parameters, all responses were shifted to a reference temperature of 25°C (77°F) (Diefenderfer *et al.*, 2006; Al-Qadi *et al.*, 2002). A temperature correction factor calculated as the ratio of response at reference temperature to response at testing temperature was then multiplied by the measured responses. Figure 3 shows measured responses at various temperatures shifted to the responses at reference temperature for this correction.

As shown in Figure 4, load-associated responses beyond 3,000 passes became quite unpredictable in the weak A-sections. Visual inspection of surface distresses, rutting, and cracking indicated that the control section (A-3) had subgrade shear failure at around 3,000 passes. After 3,000 passes, the control section shows a relative rapid increase in the tensile strain at the bottom of the HMA layer, compared to the reinforced sections (see Figure 4). Reinforced section A-2 reached the limit of the strain gauge at

2,000 passes. The deflection in the subgrade also showed the same trend as the strain at the bottom of the HMA layer.

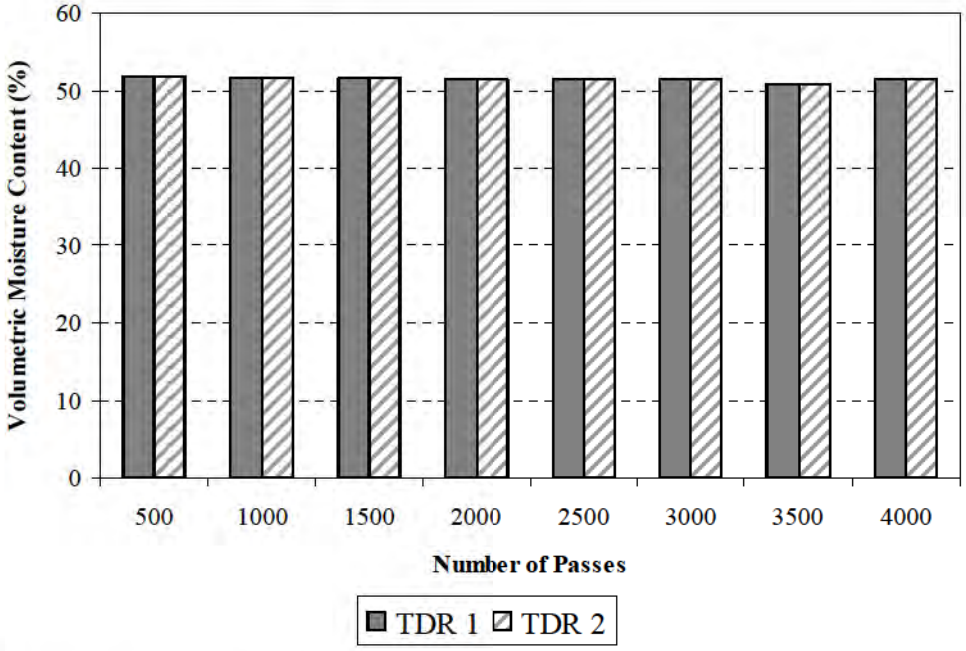

Figure 1 Volumetric moisture contents of the A-Section subgrades during trafficking.

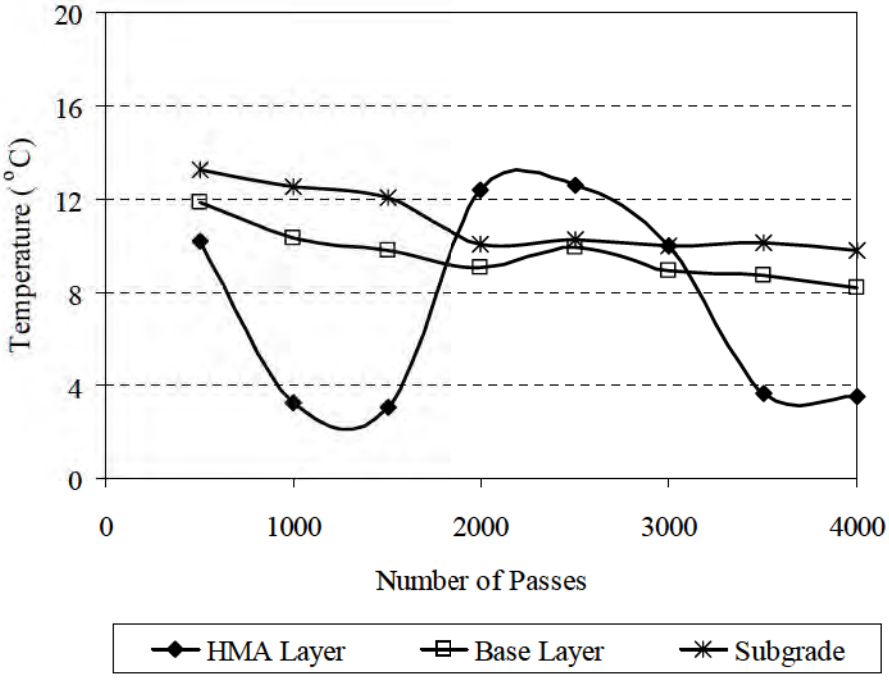

Figure 2 Temperature variations in A-2 section pavement layers during trafficking.

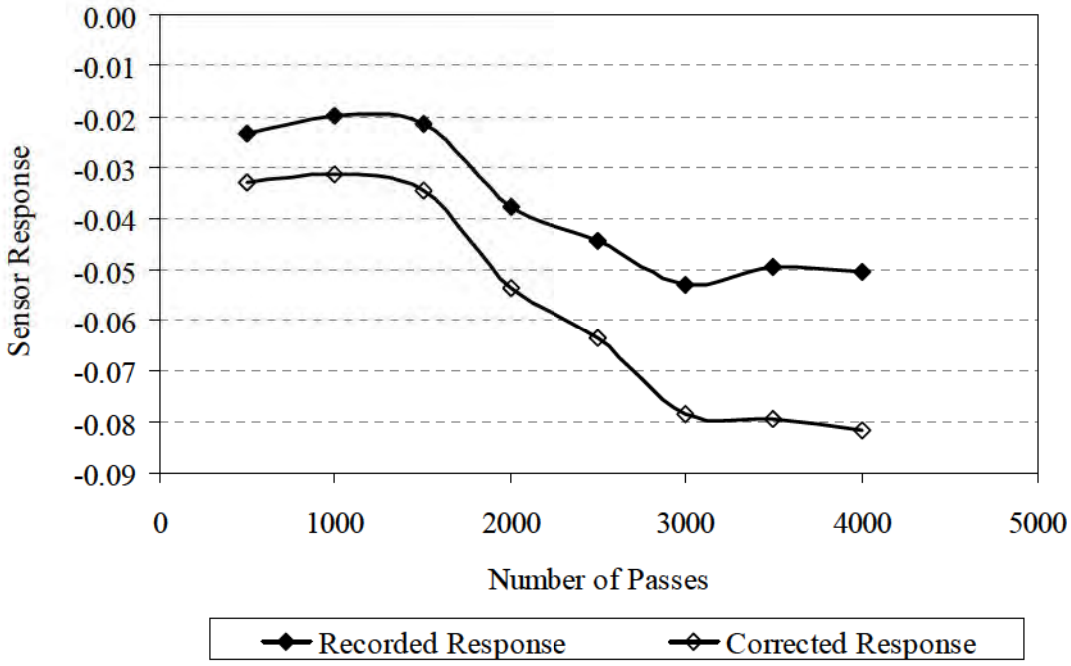

Figure 3 Response correction examples for various HMA temperatures.

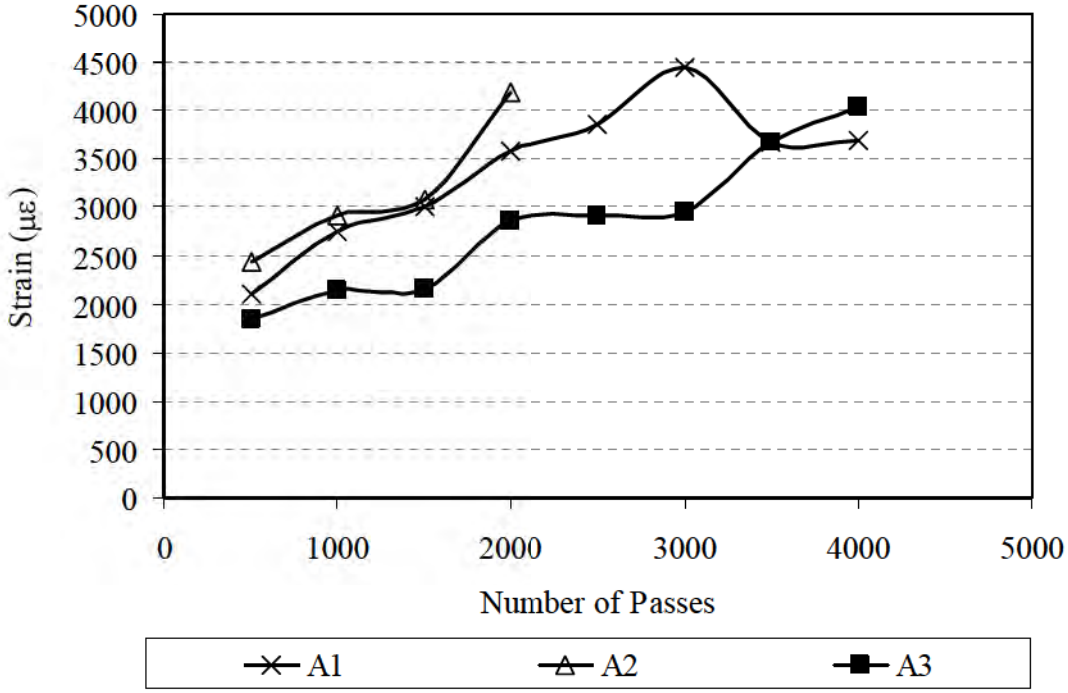

Figure 4 Critical pavement responses collected during trafficking at the bottom of the HMA layer.

Figures 5a and 5b show lateral resilient displacements measured at the bottom of base layers during trafficking for the A-sections. Aggregate lateral movement was

evident in the two horizontal directions, transversely and longitudinally. However, it was notable that lateral movement in the direction of traffic was greatest when geogrid was absent. In addition, Figure 6 clearly shows that in the A-3 control section, the greater the lateral movements in the aggregate base, the larger the surface rut accumulations. Figure 6 also shows the as-constructed CBR profile, which is almost constant. After 3,000 passes, there was severe longitudinal cracking at 150 to 200mm from the edge of the loading wheel in the control section due to the high stresses at this location (Al-Qadi *et al.,* 2002). These results also indicated that the control section had failed in subgrade shear, which clearly affected the behavior of the A-2 reinforced section adjacent to it (see Figure 6). That was visually confirmed after a trench was made in A-sections to observe the pavement cross-section profile after the completion of testing.

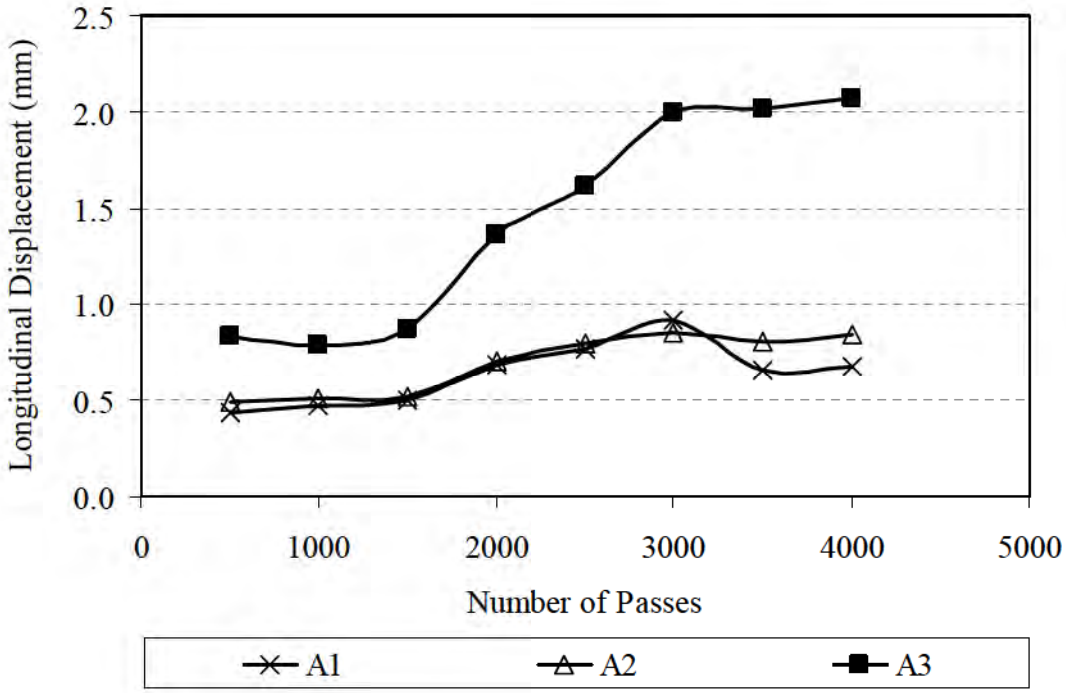

(a) Longitudinal displacement at bottom of base layer

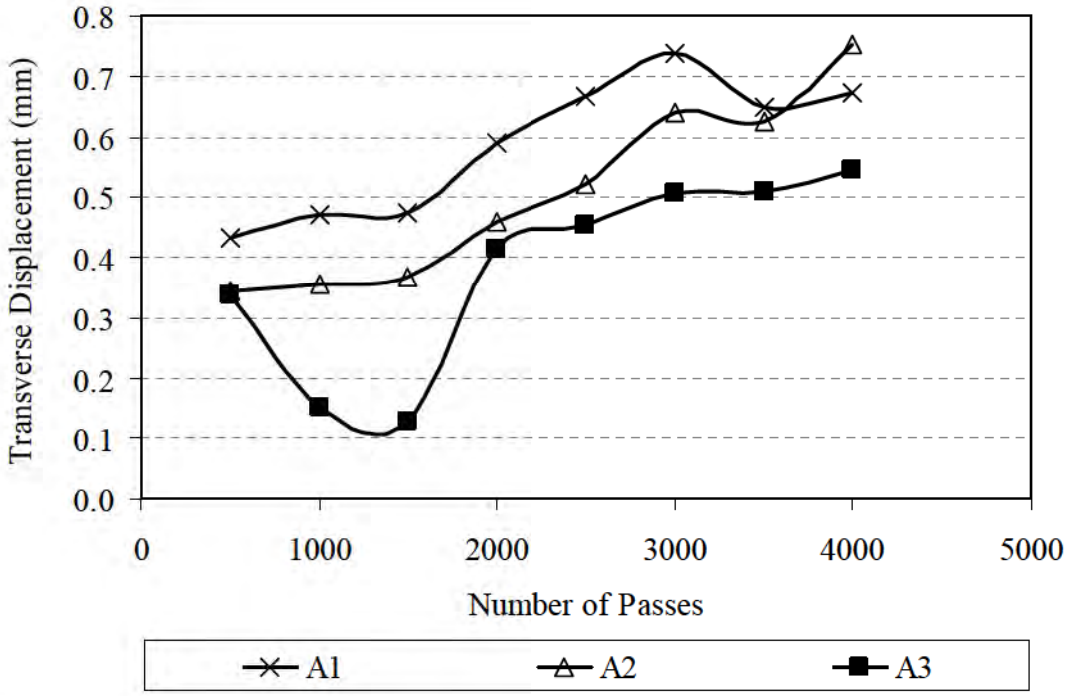

(b) Transverse displacement at bottom of base layer

Figure 5 Horizontal resilient displacements at bottom of base layer, measured during trafficking: (a) longitudinally, and (b) transversely.

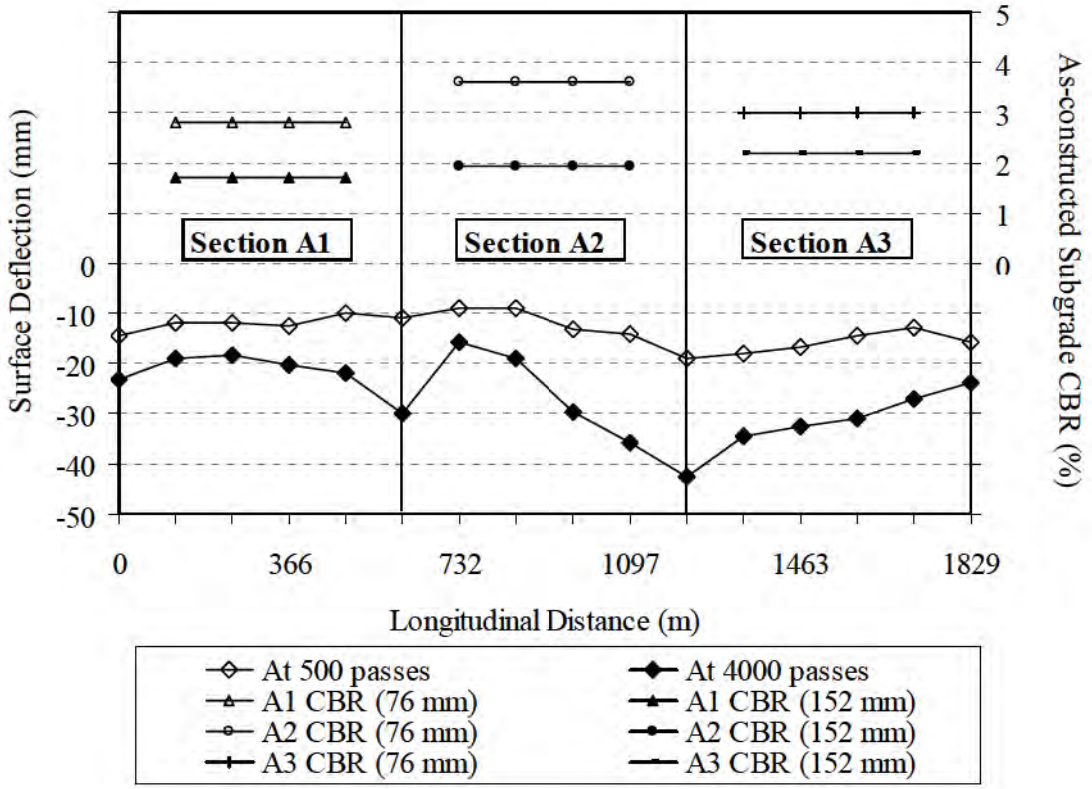

Figure 6 Surface rut profiles along the centerline of the "A" pavement sections.

Pavement trenches were later excavated to further examine test section performances. Rut profile data obtained from open trench measurements clearly indicate that all test sections reached shear failure (see Figure 7). However, subgrade shear failure was most pronounced in the control section and to a lesser degree in the other two reinforced sections. Observations of the pavement trenches revealed intermixing of unbound aggregates and fine-grained subgrade soils in the A sections; it was more pronounced in the control section, however.

Figure 8 shows the accumulation of surface ruts with number of passes in the A-sections, measured at two surface locations in each test section. The A-3 control sections had the deepest ruts accumulated from the beginning until the end of the trafficking test. Considerable rutting also took place in the reinforced A-2 section due to its proximity to the A-3 location, see Figure 8 for A2_2 (clearly shown in Figure 6 by the surface rut profiles measured after 4500 passes).

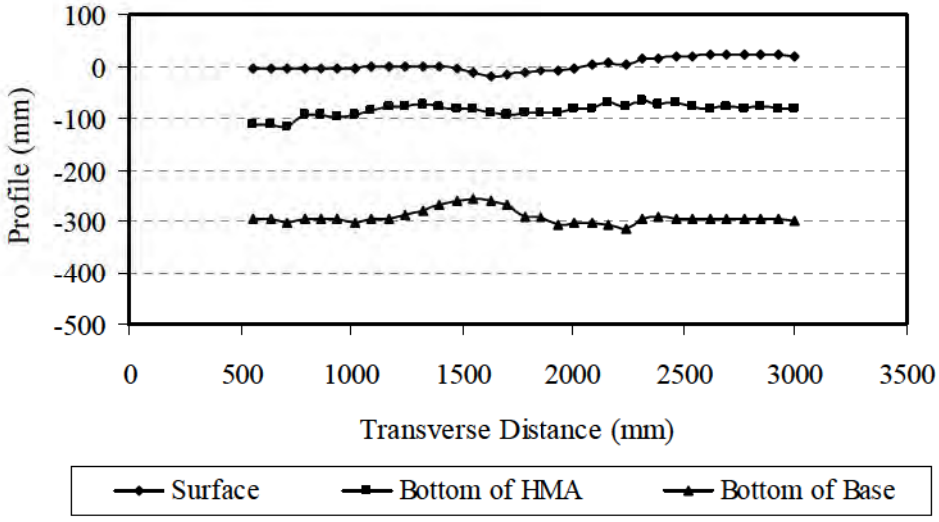

(a) Profile data of section A-1

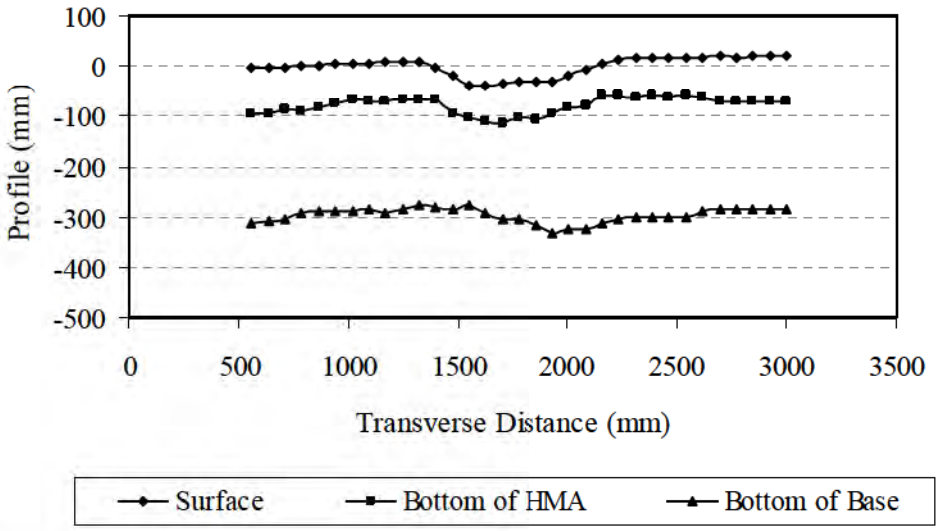

(b) Profile data of section A-2

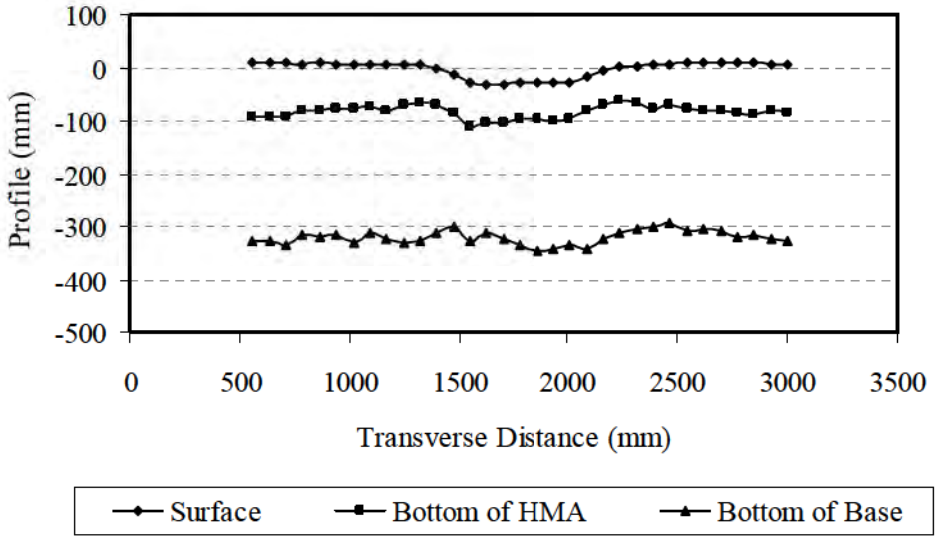

(c) Profile data of section A-3

Figure 7 Rut profiles of trenches excavated from pavement sections A-1, A-2, and A-3.

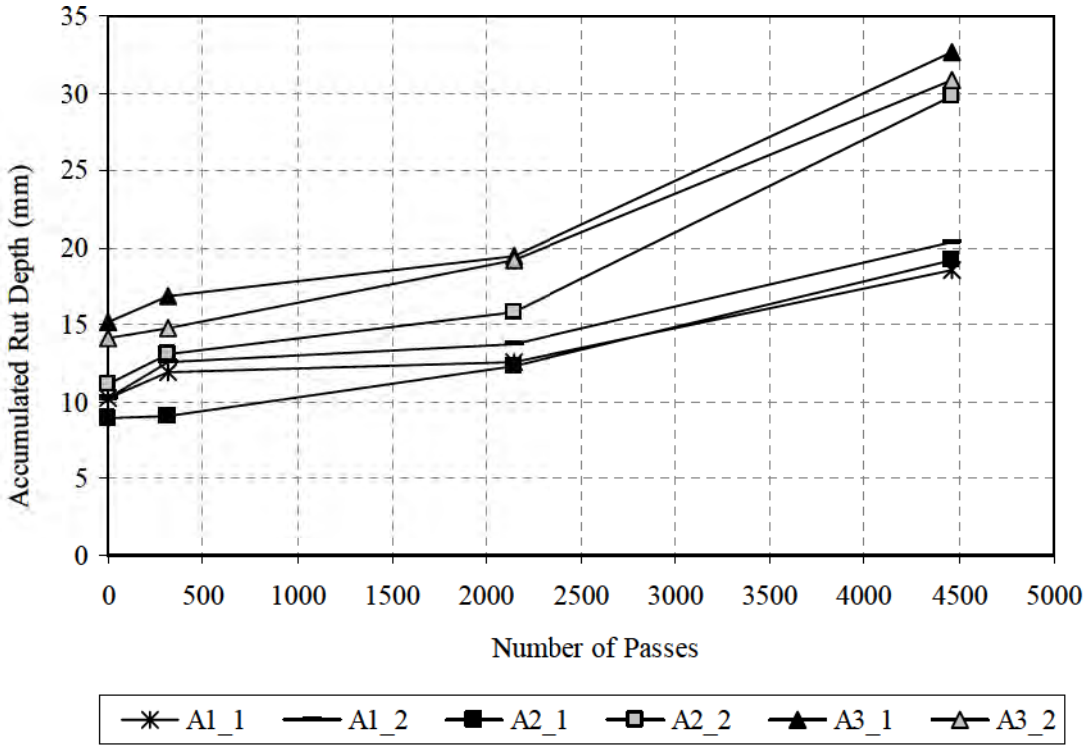

Figure 8 Accumulation of rut depths in the A-sections after various number of passes.

SUMMARY

Nine pavement test sections were recently built at the University of Illinois Advanced Transportation and Research and Engineering Laboratory (ATREL) facility to evaluate the effectiveness of flexible pavements reinforced with geogrid granular base. The test sections were extensively instrumented with pressure cells, linear variable pressure transducers (LVDTs), and strain gauges to measure pavement response to vehicular loading. The instrumentation also included thermocouples and time domain reflectometry (TDR) probes to capture effect of environmental changes and piezometers to measure pore-water pressure. Both response and performance testing were conducted using ATLAS, the mobile accelerated loading system.

Preliminary results are presented here for three pavement test sections, all constructed of 76mm hot-mix asphalt and 203mm aggregate base over a weak subgrade. Two sections had different types of biaxial geogrids placed at the base-subgrade interface; the third section was constructed with no reinforcement as the control. The subgrade conditions were similar in all sections, the California Bearing Ratio (CBR) values maintained at less than 4% with no variation in the moisture content throughout the response and trafficking tests. Pavement response to vehicular loading showed that the control section had the clear greater lateral movement in the aggregate base layer, especially in the direction of traffic, compared to the reinforced sections. This could also accelerated the observed shear failure in the subgrade and resulted in a higher rate of surface rutting. Trenches excavated to reveal the pavement layer profiles confirmed that all pavement failed in subgrade shear although at different number of loading cycles.

ACKNOWLEDGMENTS

This study was sponsored by Tensar Earth Technologies, Inc. The assistance of J. Baek, P-J Yoo, E. Fini, J. Meister, M. Elseifi, B. Harkanwal, J. Anochie-Boateng, C. Montgomery, K. Jiang, and Z. Leng during pavement construction and instrumentation is greatly appreciated. The contents of this paper reflect the views of the authors, who are responsible for the facts and the accuracy of the data presented herein. This paper does not constitute a standard, specification, or regulation.

REFERENCES

Al-Qadi, I.L., Loulizi, A., Janajreh, I., and T.E. Freeman. "Pavement Response to Dual Tires and New Wide-Base Tires at Same Tire Pressure," *Transportation Research Record No. 1816, Journal of the Transportation Research Board*, National Research Council, Washington D.C., 2002, pp. 125-136.

Al-Qadi, I. L. "The Proper Use of Geosynthetics in Flexible Pavements," 7th International Conference on Geosynthetics, Ph. Delmas and P. G. Grous, Eds., Nice, France, September 22-27, 2002, pp. 913-916.

Brandon, T. L., I. L. Al-Qadi, B. A. Lacina, and S. A. Bhutta. "Construction and Instrumentation of Geosynthetically Stabilized Secondary Road Test Sections," Transportation Research Record, No. 1534, Transportation Research Board of the National Academies, December 1996, pp. 50-57.

Al-Qadi, I. L. and S. A. Bhutta. "Designing Low Volume Roads with Geosynthetics," Transportation Research Record, No. 1652, Vol. 2, Transportation Research Board of the National Academies, 1999, pp. 206-216.

Al-Qadi, I. L., A. Loulizi, M. A. Elseifi, and S. Lahouar. "The Virginia Smart Road: The Impact of Pavement Instrumentation on Understanding Pavement Performance," *The Journal of the APPT*, Vol. 73, 2004, pp. 427-466.

Diefenderfer, B. K., I. L. Al-Qadi, and A. Loulizi. "Laboratory Calibration and Field Verification of Soil Moisture Content Using Two Types of Time-Domain Reflectometry Probes," *Journal of the Transportation Research Record, No. 1699*, Transportation Research Board of the National Academies, 2000, pp.142-150.

Loulizi, A., I. L. Al-Qadi, S. Lahouar, and T. E. Freeman. "Data Collection and Management of the Instrumented Smart Road Flexible Pavement Sections," *Journal of the Transportation Research Record, No. 1769*, Transportation Research Board of the National Academies, 2002, pp. 142-151.

Diefenderfer, B. K., I. L. Al-Qadi, and S. D. Diefenderfer. "Model to Predict Pavement Temperature Profile: Development and Validation," ASCE, *Journal of Transportation Engineering*, Vol. 132, No. 2, 2006, pp.162-167.

Kwon, J., Tutumluer, E., and M. Kim. "Development of A Mechanistic Model for Geogrid Reinforced Flexible Pavements," *Geosynthetics International*, Vol. 12, No. 6, 2005, pp. 310-320.

Perkins, S., and E. Cortez. "Evaluation of Base-Reinforced Pavements Using a Heavy Vehicle Simulator," Compendium of Papers CD-ROM, 83rd Annual Meeting of the Transportation Research Board, National Research Council, Washington D.C., 2004.

Soil Improvements & Foundations

REDUCING THE SEISMIC EARTH PRESSURES ON RETAINING WALLS BY EPS GEOFOAM BUFFERS - NUMERICAL PARAMETRIC ANALYSES

G. A. Athanasopoulos, Professor, Dept of Civil Engineering, University of Patras;
C. P. Nikolopoulou, Civil Engineer, MSc, Patras; V. C. Xenaki, Civil Engineer, MSc, PhD, Edafomichaniki, SA;V. D. Stathopoulou, Civil Engineer, MSc, Patras,

ABSTRACT

Results of numerical analyses (using the FEM) are presented for determining the response of earth retaining walls, seismically isolated by EPS geofoam buffers, to harmonic base excitation. In the first part of the investigation the dynamic properties of EPS were evaluated by a laboratory testing program (resonant column tests, bender element tests, cyclic and monotonic triaxial tests with local strain measuring transducers) on specimens of varying densities under isotropic confinement ranging from 0% to 60% of the compressive strength of the material. By combining the results of all tests empirical relations (and graphs) were developed providing values of Poisson's ratio, static and dynamic moduli of deformation and damping ratio as a function of EPS density (12 to 30kg/m3), strain amplitude (10-6 to 10-1) and isotropic confining pressure (0 to 100kPa). In the second part of the study (involving the numerical analyses) the isolation efficiency, Ar, of the buffer (i.e. the percent reduction of the seismic thrust increment compared to the case without isolation) was examined as a function of buffer shape, density and thickness, of wall flexibility and height and of intensity and frequency of base motion. The reliability of the method of analysis was first checked and verified by analyzing a reported case of physical model shaking table tests. Then, based on the results of the parametric analyses, a two-step tentative design procedure was proposed for EPS geofoam seismically isolated soil retaining structures.

INTRODUCTION

Earth retaining structures constitute an important component of many civil engineering works. These structures may be of a number of types (e.g. reinforced concrete retaining walls -gravity or cantilevered-, bridge abutments or basement walls) and they are designed to safely resist the lateral pressures exerted by earth masses, Figure 1. In earthquake prone areas an earth retaining structure must be designed to be able to withstand the seismic earth pressures in addition to the static ones. It is known that in the case of strong ground motion the combined (i.e. static plus dynamic) earth pressures may be more than two times higher, compared to the static pressures. Poor design in such cases may lead into serious damage or even collapse of the retaining structure, with catastrophic consequences to important infrastructure works. On the other hand, the appropriate design against the increased lateral -static plus dynamic-

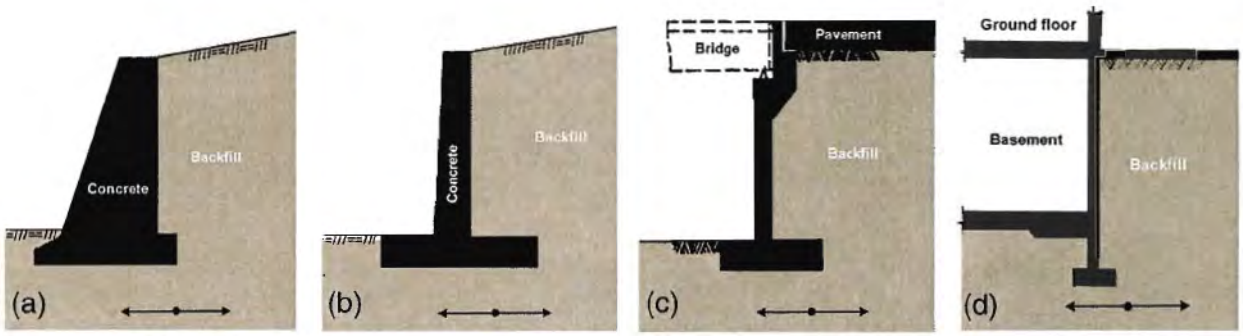

Figure 1 Common types of earth retaining structures

loading results in a significant increase in the construction cost. For this reason a method for the seismic earth pressure reduction (or isolation) would be particularly welcome by the civil engineering profession and construction industry (for both new and existing structures).

In the last decade a new method for the isolation of retaining structures against lateral seismic earth pressures has been proposed and is currently the subject of intensive research (Horvath, 1995; Inglis et al., 1996; Pelekis et al. 2000; Hazarika, 2001; Hazarika et al., 2001; Hazarika and Okuzono, 2004; Hazarika, 2005). In this method a layer of EPS geofoam (playing the role of a compressible inclusion) is placed between the back face of the wall and the backfill material, Figure 2. During earthquake loading the backfill seismic pressures are first applied to the EPS layer. This layer acts as a buffer (due to its greater compressibility) absorbing the major part of the thrust and transfering only a portion of it to the retaining structure. It should be mentioned that the method of seismic isolation described above has evolved as an extension of the use of EPS compressible inclusions for reducing the static earth pressures acting on retaining walls. The static isolation of earth retaining structures by a compressible inclusion was first examined by Partos and Kazaniwsky(1987). In subsequent years the subject was studied by several investigators by using experimental and analytical techniques (McGown et al., 1988; Horvath, 1991; Karpurapu and Bathurst, 1992; Horvath, 1997; Tsukamoto et al., 2001; Tsukamoto et al., 2002; Horvath, 2004) and a design methodology has already been developed which may be used in practical applications (Horvath, 2004).

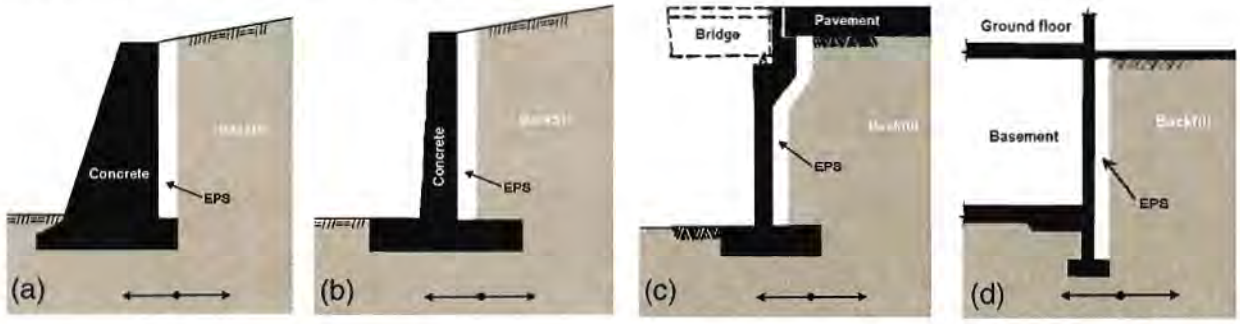

Figure 2 Isolation against the seismic lateral thrust on earth retaining structures by an EPS geofoam compressible inclusion

The subject of the present study is 1) the systematic investigation of the effectiveness of an EPS geofoam compressible inclusion as a seismic isolator against lateral earthquake earth pressures, and 2) the development of a pertinent design methodology.

PROGRAM OF INVESTIGATION

A systematic approach to the study of the effectiveness of EPS geofoam as a seismic buffer would require the investigation of a) the dynamic behavior of EPS as well as of the interface behavior between EPS and backfill material (Athanasopoulos et al., 1999; Xenaki and Athanasopoulos, 2001) and b) the response of seismically isolated walls under varying seismic base excitations (Pelekis et al.,2000). Accordingly, in the present study two main directions of research were followed: 1) an experimental (laboratory) evaluation of the dynamic properties (moduli and damping ratios) of EPS (Xenaki, 2005) and 2) performance of a number of parametric response analyses of reinforced concrete retaining walls seismically isolated by EPS geofoam compressible inclusions (Stathopoulou, 2005; Nikolopoulou, 2006).

1. Experimental study

The dynamic properties of EPS geofoam (elastic moduli, damping ratios and Poisson ratio) in the present study were evaluated by conducting four types of tests (Xenaki, 2005):

a. Monotonic (uniaxial and triaxial) tests
The tests were conducted in a GDS monotonic/cyclic triaxial testing system with a loading rate ranging from 1%/min to 2.5%/min, Figure 3. The confining pressure in these tests was varied from 0 to 60% of the EPS compressive strength. It was found that in this range of loading the rate of volumetric creep of the material becomes negligibly small after 15 min to 30 min following the load application. In these tests the

Figure 3 (a) The triaxial (cyclic/monotonic) loading system used in the laboratory program, (b) the local strain measuring transducers used in the triaxial tests on EPS specimens

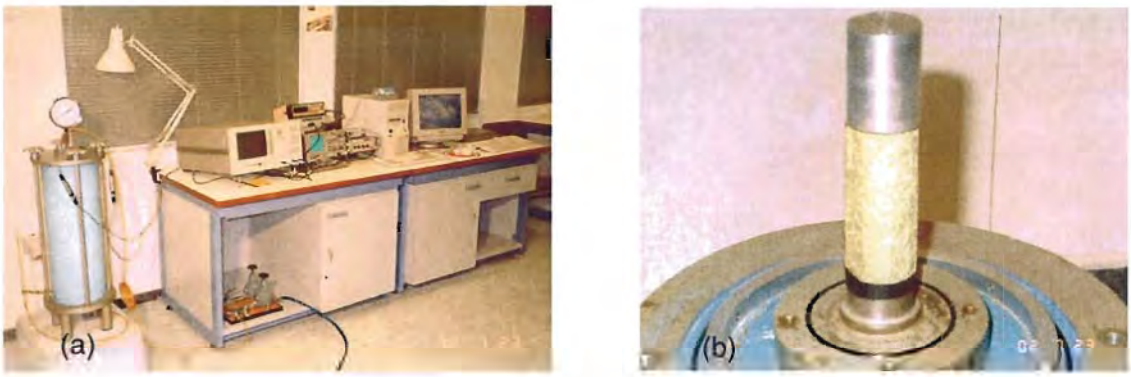

Figure 4 (a) The resonant column system used in the laboratory program, (b) cylindrical EPS specimen mounted to the pedestal of the resonant column device

maximum compressive strain was equal to 10%. Also, the reliable measurement of very small material strains was accomplished by using "Hall effect" type local-strain transducers, attached to the mid-height area of the test specimens (Clayton and Khatrush, 1989; Clayton et al., 1989).

b. Cyclic triaxial tests

These tests were conducted in the GDS testing system mentioned above, under controlled stress conditions and varying confining pressures and amplitudes of loading. The frequency of harmonic axial loading was approximately equal to 1%/min. Local strain measuring transducers were also used in these tests.

c. Resonant column tests (torsional)

These tests were conducted, in a "fixed-free" resonant column device, designed and fabricated by the senior author, Figure 4. The shear strains in these tests ranged from 10-6 to 10-3 whereas the loading frequency ranged from 35Hz to 70Hz (producing loading rates approximately equal to 6%/min). Due to the significant volumetric contraction of the EPS specimens under even small values of confining stress, (which resulted in a contact between magnet and coils) the resonant column testing was conducted on unconfined only specimens.

d. Bender element tests

Figure 5 The bender-extender system used in the laboratory program (a) the pedestal of the device with the insert element, (b) EPS specimen mounted in the testing system

These tests were conducted in a GDS bender-extender element testing system with wave frequencies ranging from 6.5kHz to 10kHz and amplitude of vibration less than 10-6, Figure 5. In these tests the loading rate was approximately equal to 200%/min.
All specimens used in the experimental study were cylindrical with a height to diameter ratio equal to 2 and they were formed from EPS blocks having densities from 12kg/m3 to 30kg/m3. The final trimming of the specimens was accomplished by a sand paper, instead of a hot wire, to avoid any thermal disturbance of the surface of the specimens.

2. Numerical Analyses

The effectiveness of an EPS compressible inclusion as a seismic isolator in soil retaining structures was investigated in the present study, by performing numerical seismic response analyses. The response of vertical walls with horizontal backfill, under horizontal harmonic excitation of varying intensity and frequency was analysed. The dynamic analyses were conducted by the finite element code PLAXIS assuming non-linear material behavior for the backfill and the EPS material. Conventional walls, as well as walls seismically isolated with an EPS compressible inclusion, were analyzed.
In Figure 6a, the G/G0 vs. γc curves used in the numerical analyses for the backfill material (average curve for sandy soils based on: Vucetic and Dobry, 1991; Stokoe et al., 2004; Hardin and Kalinski, 2005; Zhang et al., 2005) and the EPS compressible inclusion (Xenaki 2005), are shown. The two curves shown in Figure 6a, indicate that the behavior of EPS material remains approximately linear for strains almost two orders of magnitude greater compared to those of the backfill material.
In Figure 6b, an example of the finite element mesh used in the numerical analyses is shown, with a length ten times greater than the height of the wall. In these analyses the wall was modeled as a vertical elastic beam with finite rigidity. This beam was connected to a rigid base through a rotational spring (the results of the present study were obtained for the case of a rigid connection). Veletsos and Younan (1997)

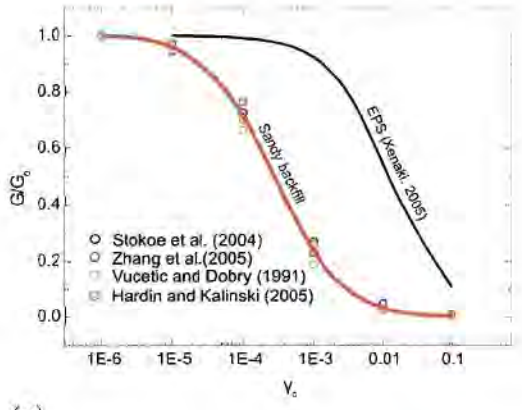

(a)

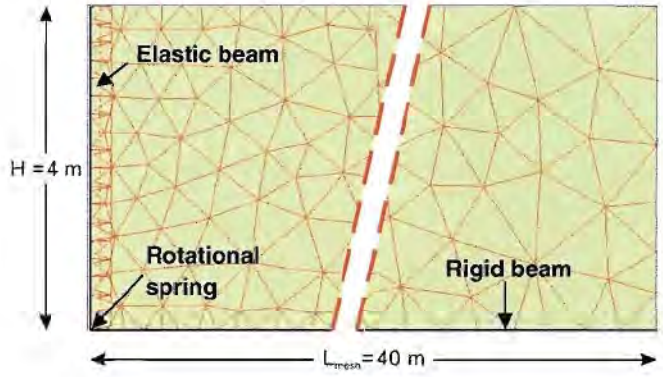

(b)

Figure 6 Finite element analyses (a) G/G0-γc used in the analyses, (b) example of a finite element mesh

have shown that elastic models of soil retaining systems provide reliable estimates of soil thrust when the flexibility of the wall is taken into account. The frequency of the base harmonic motion ranged from 0.5Hz to 20Hz

The effectiveness of seismic isolation in the present study is quantified by the isolation efficiency, Ar, defined as the ratio (in percent) of seismic thrust reduction (due to isolation) to the earthquake thrust without isolation. Many parametric analyses were conducted to investigate the effect of the following parameters on the isolation efficiency: (a) shape, mean thickness and density of the compressible inclusion, (b) flexibility and height of the wall and (c) intensity and predominant frequency of the ground motion.

RESULTS

In this section the results are presented of the two parts of the present study i.e. of the experimental evaluation of EPS mechanical behavior and of the seismic response analyses of the reinforced concrete retaining walls.

A. Mechanical Behavior of EPS

The results of laboratory testing indicate that for stains less than 10-4 (0.01%) (small strains) the mechanical behavior of EPS geofoam is linear (i.e. independent of strain magnitude), whereas for strains ranging from 10-4 to 10-3 the behavior is approximately linear (i.e. the deviation from the linear behavior is less than 10%). For strains greater than 10-3 (0.1%) (large strains) the behavior is non-linear and the dependence of dynamic properties on strain should be taken into account.

For low-amplitude vibrations the experimental results indicate that the values of elastic moduli (Go, Eo) of EPS increase with increasing density of material, ρ, and decrease with increasing mean confining pressure, σ3. The low-amplitude value of Poisson ratio, vo, depends mainly on confining pressure and decreases with increasing values of σ3 (taking values from 0.30 to -0.05). Based on the experimental results, the following empirical equations are proposed for estimating the values of Go (in MPa) and vo as a function of material density, ρ :

$$G_{0(\sigma_3=0)} = 0.32\rho - 1.4 \quad (1)$$

$$v_{0(\sigma_3=0)} = 0.22 + 0.0033\rho \quad (2)$$

where ρ=EPS geofoam density (kg/m3)

The experimental results of the present study also indicate that as the mean confining pressure applied to the material is increased, the values of G0 and v0 are reduced. The following empirical equations can be used to take into account the effect of σ3:

$$\frac{G_{o(\sigma_3)}}{G_{o(\sigma_{3=0})}} = 1.02 + 0.599\frac{\sigma_3}{\sigma_{c10}} - 1.41\left(\frac{\sigma_3}{\sigma_{c10}}\right)^2 \quad (3)$$

$$v_{0(\sigma_3)} = 0.25 - 0.33\frac{\sigma_3}{\sigma_{c10}} \quad (4)$$

where σc10=EPS compressive strength (kPa), σ3=confining stress (kPa)

According to the experimental results of this study the value of σc10 (in kPa) may be estimated from the following empirical equations:

$$\sigma_{c10} = 7.68\rho - 48.3 \quad (5)$$

$$\frac{\sigma_{c10(\sigma_3)}}{\sigma_{c10(\sigma_{3=0})}} = 1.0 - 0.84\frac{\sigma_3}{\sigma_{c10}} \quad (6)$$

where ρ=EPS geofoam density (kg/m3)

The experimental results also indicate that the low-amplitude damping ratio, D0, of EPS (for both the hydrostatic and deviatoric components of loading) takes low values and does not depend on material density. The value of D0 increases somewhat with confining pressure and a mean value of D0=1.70% is suggested for all low-amplitude vibration applications.

For high-amplitude vibrations the dynamic properties of EPS geofoam, in addition to material density and confining pressure, depend also on strain amplitude. More specifically, for increasing values of strain the elastic moduli decrease, the damping ratio increases whereas the Poisson ratio decreases markedly and may take negative values. A very interesting finding is that the EPS modulus of elasticity, E, in the range of intermediate to large strains (10-4 to 10-2) also depends on the type of loading (monotonic vs. cyclic). More specifically, as shown in the diagrams of Figure 7a and Figure 7b, in the above mentioned strain range, the moduli obtained from cyclic loading are approximately 20% higher compared to the values from monotonic (i.e. static) loading. This behavior shows a remarkable similarity to the behavior of soils (Lo Presti et al., 1997; Pradhan and Ueno, 1998)

The modulus degradation curve of EPS geofoam was found to depend –although not significantly –on the material density, confining pressure and type of loading. As a first approximation these effects may be neglected and a unique relation (Eq.7) is proposed for practical applications (depicted as an equivalent G/G0-γc curve in Fig. 6a) :

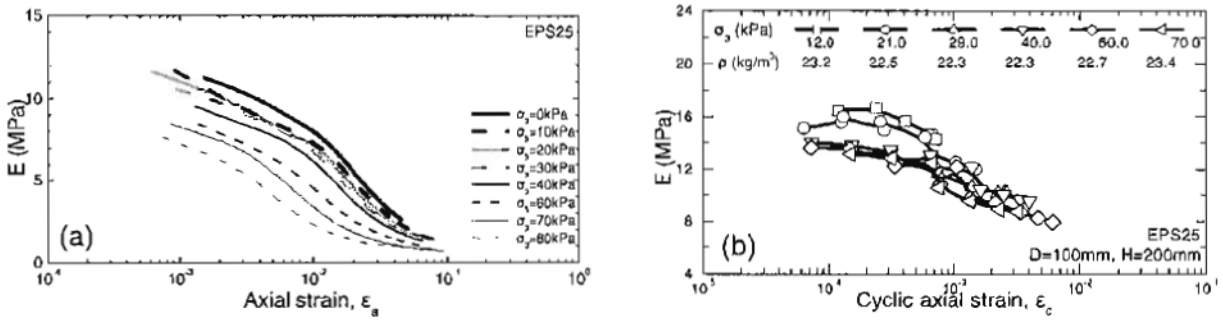

Figure 7 EPS geofoam modulus of elasticity as a function of strain and confining pressure, (a) from monotonic triaxial tests, (b) from cyclic triaxial tests

$$\frac{E}{E_o} = \frac{1}{1+\frac{\varepsilon_c}{0.01}} \qquad (7)$$

Values of Poisson's ratio, v, -estimated from the measured axial and radial deformations of specimens- were obtained mainly from the monotonic triaxial tests, assuming an equivalent-linear material behavior. It was found that the value of v decreases with increasing confining pressure and axial strain whereas it is insensitive to the value of EPS density. The test results are summarized in the diagrams of Figure 8, which indicate that for large strains and high confining pressures Poisson's ratio may take negative values (up to -0.30). This indicates that under such conditions, the EPS behaves as an "auxetic" material (Stavroulakis, 2004). Values of EPS Poisson's ratio for practical applications may be obtained from the diagrams of Figure 8 by linear interpolation between the limit values of σ3 shown in the graphs.
Finally, according to the test results, the damping ratio value of EPS is increased for large strains and furthermore it increases with increasing confining pressure and decreasing material density. However, the most important effect seems to be associated with the type of loading, with damping ratio values for compressive loading being about 4 times the corresponding values for shear loading. For practical applications involving large strains it is suggested to use the values of D≈3% and D≈14% for the deviatoric and hydrostatic component of loading, respectively.

B. Effectiveness of EPS Seismic Buffers

The reliability of the numerical method of analysis used in this part of the investigation was first checked by analyzing a published case of shaking table test on a

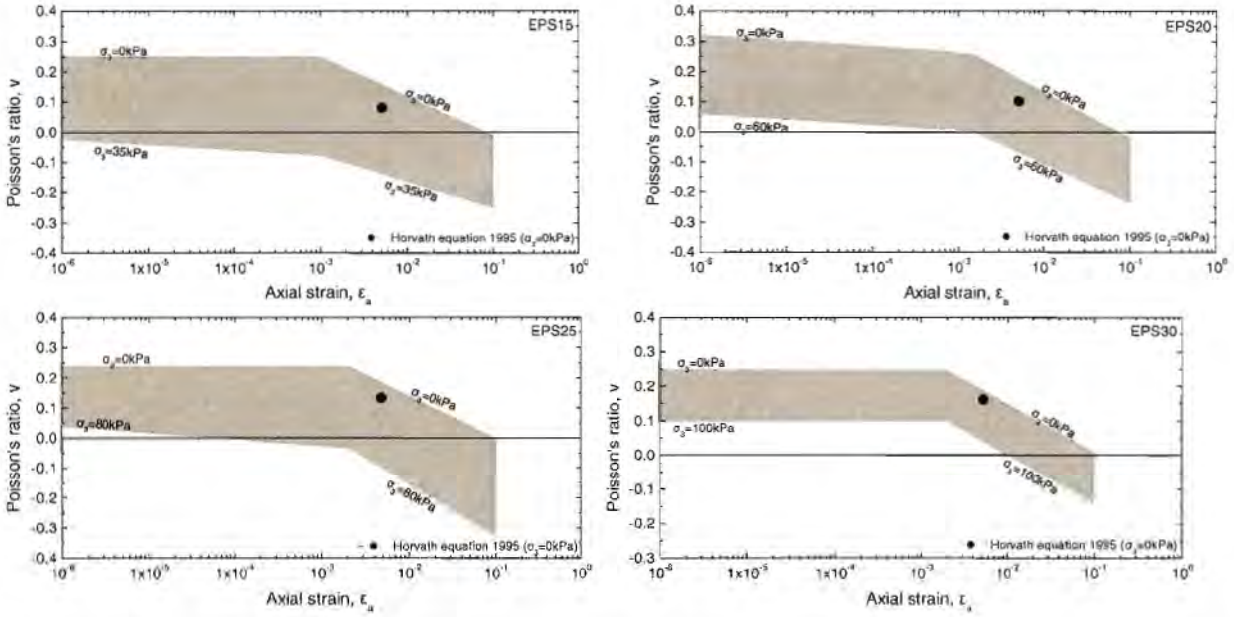

Figure 8 Poison's ratio of EPS geofoam as a function of strain, confining pressure and material density

small scale physical model of a retaining wall (Zarnani and Bathurst, 2005, Zarnani et al., 2005). In the diagrams of Figure 9, the results of a comparison are shown between the measured values of active seismic thrust on the wall vs. the estimated values obtained by using the code PLAXIS. The comparisons are shown for the case of non-isolated wall as well as for two cases of seismic isolation using EPS12 and EPS16. In all cases the agreement between measured and estimated response is satisfactory. The diagrams also include results estimated by using the code FLAC, which are also in general agreement with the experimental values.
Having obtained confidence with the modeling capability of the PLAXIS code, a series of parametric analyses were conducted to investigate the effect of several parameters on the effectiveness of EPS compressible inclusion as a seismic isolator. The results of these analyses are briefly discussed in the following sections.

a. Method of Analysis

A number of comparisons between the results of linear vs. non-linear finite element analyses showed that a non-linear analysis describes better the behavior of the system (wall-EPS buffer-backfill). Based also on the fact that the measured response of the physical model test, described in the previous section, was best modeled by implementing the non-linear behavior of EPS and soil material (Figure 9), it was decided to assume non-linear behavior of materials in all subsequent analyses.

b. Shape of Compressible Inclusion

A number of seismic response analyses were conducted for walls having a height of 4.0m and four different shapes of EPS buffer: orthogonal, (i.e. constant thickness with depth) and triangular (with maximum thickness at top, bottom and mid-height of wall), Figure 10. In all cases the area of the cross-section of the compressible inclusion (and therefore its mean thickness) was the same. The results of analyses indicated that the maximum values of isolation efficiency, Ar were obtained for shapes (a) and (b) with the shape (b) being slightly superior to shape (a). By considering the

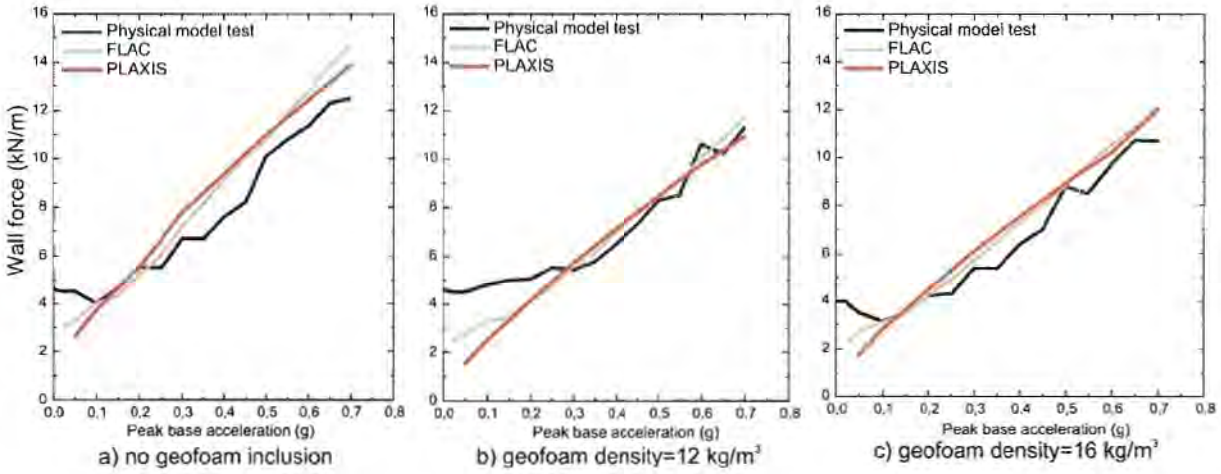

Figure 9 Measured vs. calculated response of a physical model of retaining wall in a shaking table test

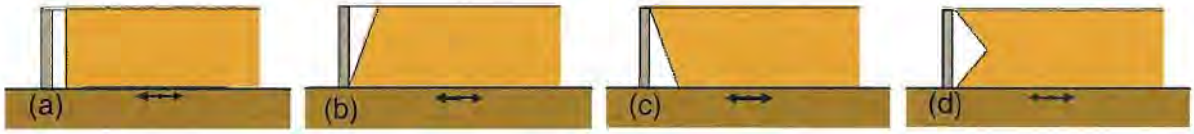

Figure 10 Different shapes of a compressible inclusion behind an earth retaining wall examined in the present study

convenience of installing a constant thickness inclusion behind the wall it was decided to favor the orthogonal shape of inclusion, which was used in all subsequent analyses and it is recommended for practical applications (Stathopoulou, 2005). In subsequent sections the thickness of the compressible inclusion is normalized with respect to the wall height and denoted by tr (%).

c. Flexibility of Wall

The results of many parametric analyses showed that the isolation efficiency of EPS compressible inclusion increases with increasing wall flexibility. It was found that the differentiation of response between perfectly rigid walls and walls with common flexibility was less than 16 %. For this reason most of the results presented herein were obtained for rigid walls and are considered to be applicable to most common reinforced concrete walls.

d. Density and Thickness of Compressible Inclusion

Most of the analyses were conducted for walls with a height of 4.0m, with EPS buffers having density 15, 20 and 25kg/m3 and normalized thickness, tr, ranging from 5% to 40%. Typical results are presented in the diagrams of Figure 11, indicating that isolation efficiencies as great as 90% can be realized for shaking intensities ranging from 0.1g to 0.5g. Careful observation of the above diagrams, however, reveals that the realization of Ar values greater than 50% requires a significant increase of the thickness of the EPS inclusion (up to 40% of the wall height). Based on the above observation it was decided to consider the isolation efficiency of 50% as the preferable value for the

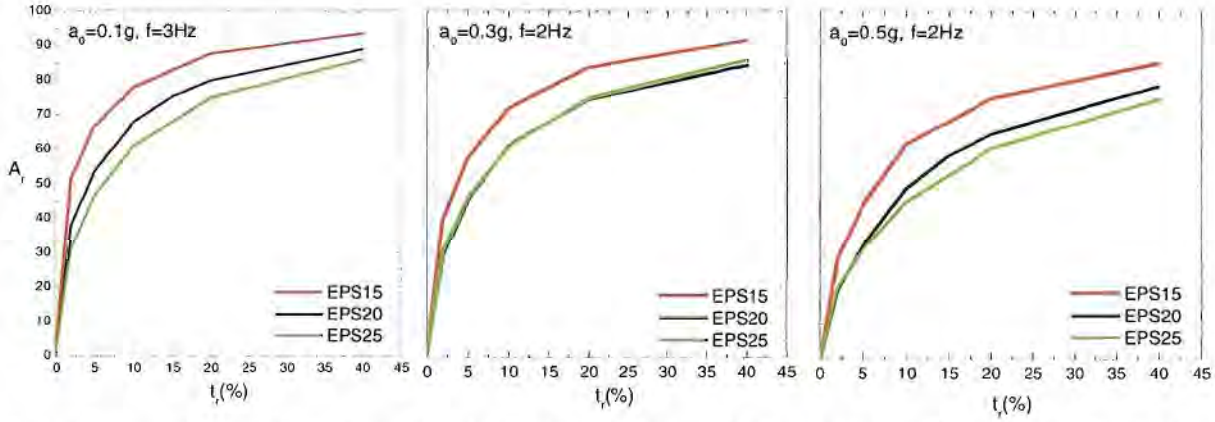

Figure 11 Seismic isolation efficiency of a compressible inclusion as a function of thickness, material density and intensity of motion

estimation of the required thickness of inclusion. Further observation of Figure 11, also reveals that the isolation efficiency increases with decreasing EPS density; this effect is not significant, however, and in practical applications a balance between the desired higher isolation efficiency and the undesired backfill deformations may be established by using an EPS density equal to ρ=20kg/m3.

e. Wall Height and Intensity of Base Motion

A number of non-linear analyses were conducted for different wall heights and intensities of base motion varying from 0.1g to 0.5g. It was found that the isolation efficiency of the EPS buffer decreases for increasing wall height especially for strong ground motions. The diagrams of Figure 12 depict this type of behavior by comparing the responses of two walls with heights equal to 4.0m and 8.0m. Thus, when selecting the value of thickness tr, corresponding to isolation efficiency of Ar=50%, the effects of base motion and wall height should be taken into account. The diagram of Figure13 (a), is based on the results of the present study and may be used for selecting the appropriate value of thickness, tr, of an EPS 20 compressible inclusion for rigid walls of varying heights under different base motion intensities.

f. Frequency of Base Excitation

The results of a number of analyses have shown that the isolation efficiency of an EPS compressible inclusion is dramatically reduced for excitation frequencies in the vicinity of the fundamental frequency, f1, of the wall-backfill system, Figure 13 (b), especially in the case of rigid walls. An approximate value of f1 may be obtained from the relationship f1 = VS/4H where H = the wall height, and VS= shear wave velocity of backfill material. Based on the available results it is concluded that the seismic isolation system remains fully effective only when the predominant frequency of base motion is less than 0.3f1 or greater than 2f1.

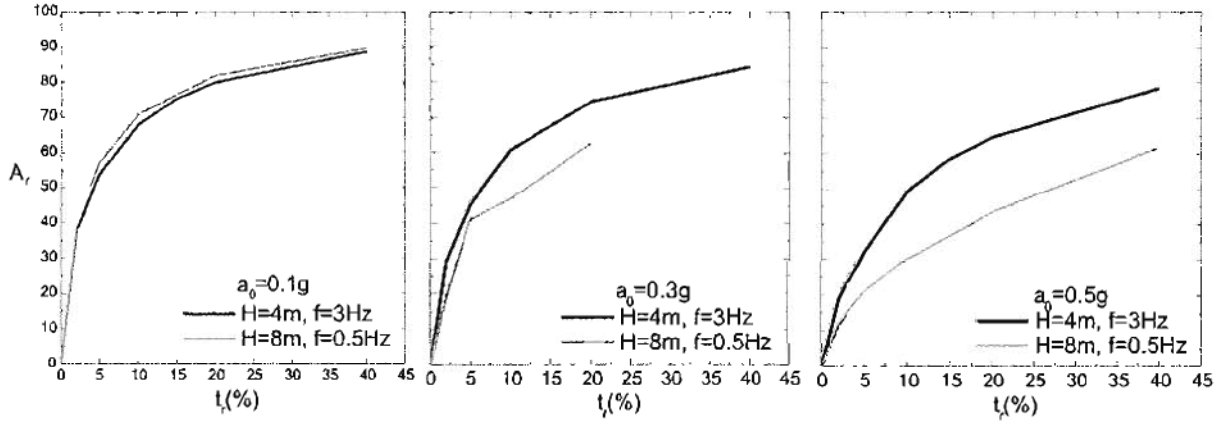

Figure 12 Effect of wall height and intensity of base motion on the seismic isolation efficiency of an EPS 20 compressible inclusion

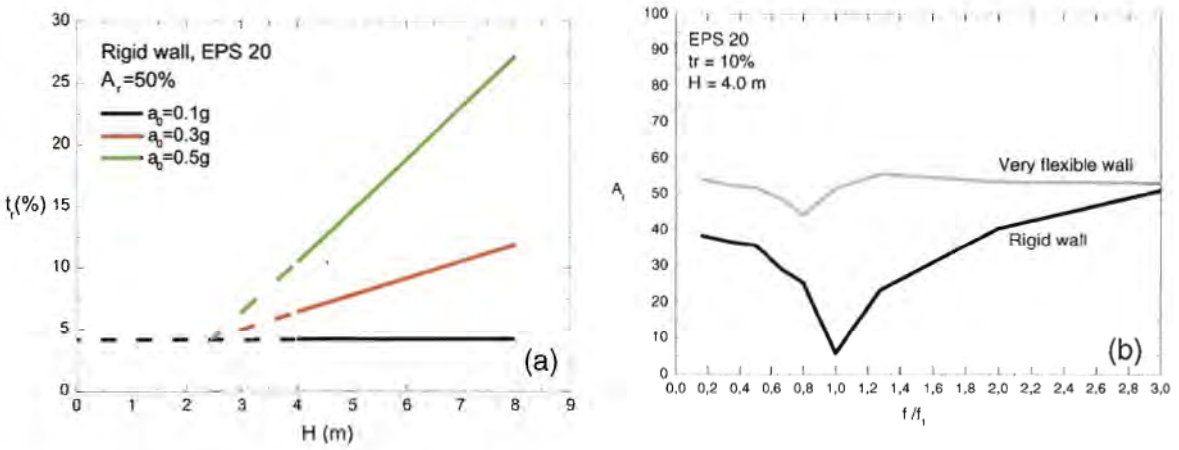

Figure 13 (a) Effect of wall height and intensity of base motion on the thickness of an EPS 20 compressible inclusion for Ar=50%,
(b) Effect of normalized excitation frequency on the seismic isolation efficiency of an EPS compressible inclusion, for rigid and very flexible walls

g. Height of Application of the Seismic Component of Thrust

According to the results of the analyses of the present study the height of application of the seismic component of the lateral thrust is not affected by the presence of an EPS compressible inclusion.

h. Compressible Material vs. Light-weight Material

An interesting question regarding the seismic isolation efficiency of the EPS geofoam is whether this efficiency is due to its very low unit weight or to its high compressibility, compared to the soil materials. To obtain an answer on this issue a number of analyses were conducted, for a wall having a height of 4.0m. In these analyses the wall is seismically isolated with an inclusion having a thickness of tr=5%. The magnitude of the seismic component of the thrust was estimated for three cases: (a) for a non-isolated wall, (b) for an isolation inclusion having a density equal to actual EPS density and stiffness equal to the stiffness of the backfill material and (c) for an isolation inclusion having a density equal to the density of the backfill and a very low stiffness, compared to the stiffness of the soil. The results of the analyses indicate that for both weak and strong ground motion the isolation efficiency of EPS is derived almost entirely from its low stiffness rather than from its low unit weight (Nikolopoulou, 2006).

PROPOSED DESIGN METHODOLOGY

Based on the results of the tests and analyses presented in the previous sections the following two-step design methodology is proposed for reinforced concrete retaining walls seismically isolated by EPS geofoam compressible inclusions:

1. Proportion the structure by considering a seismic component of thrust equal to 50% of the value that would be used for a non-isolated wall,

2. Estimate the required thickness of the EPS 20 compressible inclusion as a function of wall height and intensity of base motion, based on the diagrams developed in the present study.

Preliminary comparative cost analyses have shown that by applying the above methodology, a cost reduction of 50% or more, can be realized. Also, further analyses are underway to compare the required thickness of compressible inclusion for the cases of static and seismic isolation. The results of such a comparison will allow the development of a unified design methodology for both static and seismic isolation of earth retaining structures.

CONCLUSIONS

The static and dynamic properties of EPS geofoam (strength, moduli, damping and void ratio) depend mainly on density, mean confining pressure and amplitude of deformation. Empirical relations are proposed for estimating values of these properties. The relations are useful not only for the compressible inclusion application but for other applications as well.
The effectiveness of an EPS geofoam seismic buffer depends on material density and thickness, wall height and flexibility and intensity and frequency of base motion. The proposed tentative design methodology is based on the concept of 50% reduction of the seismic component of lateral thrust by using a material with density of 20kg/m3.
An advantage of the above method of seismic isolation is its potential to be used in seismic retrofit and rehabilitation of existing structures.

ACKNOWLEDGMENT

Part of the present study was supported by a research grant from the Research Committee of the University of Patras. This financial assistance is gratefully acknowledged.

REFERENCES

Athanasopoulos, G.A., Pelekis, P.C. and Xenaki, V.C., 1999, "Dynamic Properties of EPS Geofoam: An Experimental Investigation", Geosynthetics International, Vol.6, No. 3, pp.171-194

Clayton, C. R. I. and Khatrush, S. A., 1986, "A New Device for Measuring Local Axial Strains on Triaxial Specimens", Technical Note, Géotechnique, Vol. 36, No. 4, pp. 593-597

Clayton, C. R. I., Khatrush, S. A., Bica, A. V. D. and Siddique, A., 1989, "The Use of Hall Effect Semiconductors in Geotechnical Instrumentation", Geotechnical Testing Journal, GTJODJ, March 1989, Vol. 12, No. 1, pp. 69-76

Hardin, B.O. and Kalinski, M.E., 2005, "Estimating the Shear Modulus of Gravelly Soils", Journal of Geotechnical and Geoenvironmental Engineering, ASCE, July 2005, pp.867-875

Hazarika, H., 2001, "Mitigation of Seismic Hazard on Retaining Structures – A Numerical Experiment", Proceedings of the Eleventh (2001) International Offshore and Polar Engineering

Conference, Stavanger, Norway, June 17-22, 2001, International Society of Offshore and Polar Engineers, pp. 459-464
Hazarika, H., Nakazawa, J., Matsuzawa, H. and Negussey, D., 2001, "On The Seismic Earth Pressure Reduction Against Retaining Structures Using Lightweight Geofoam Fill", Proceedings of Fourth International Conference on Recent Advances in Geotechnical Earthquake Engineering and Soil Dynamics in Honor of Professor W.D. Liam Finn, 2001, San Diego, California, March 2001
Hazarika, H. and Okuzono, S., 2004, ''Modeling the Behavior of a Hybrid Interactive System Involving Soil, Structure and EPS Geofoam'', Soils and Foundations, Japanese Geotechnical Society, October 2004, Vol. 44, No. 5, pp. 149-162
Hazarika, H., 2005, "A Soil-Structure Interaction Model With Multiple Participating Components", Proceedings of the Eleventh International Conference on Computer Methods and Advances in Geomechanics, 2005, Torino, Italy, June 2005, G. Barla, M. Barla Eds., Prediction Analysis and Design in Geomechanical Applications, Vol. 3, pp. 659-666
Horvath, J. S., 1991, "Using Geosynthetics to Reduce Earth Loads on Rigid Retaining Structures", Proceedings of Geosynthetics '91 Conference, Atlanta, USA, 1991
Horvath, J. S., 1995, "Geofoam Geosynthetic", Horvath Engineering, P.C. Scarsdale, N.Y. U.S.A, 217p.
Horvath, J. S., 1997, "The Compressible Inclusion Function of EPS Geofoam", Geotextiles and Geomembranes, Vol.15, pp. 77-120
Horvath, J. S., 2004, "Geofoam Compressible Inclusions: The New Frontier in Earth Retaining Structures", Geotechnical Engineering for Transportation Projects, Proceedings of Geo-Trans 2004, ASCE Geotechnical Special Publication No. 126, July 27-31, 2004, Los Angeles, California, M. K. Yegian and E. Kavazanjian Eds., Vol. 2, pp. 1925-1934
Inglis, D., Macleod, G., Naesgaard, E. and Zergoun, M., 1996, ''Basement Wall with Seismic Earth Pressure and Novel Expanded Polystyrene Foam Buffer Layer'', Proceedings of 10th Annual Symposium of the Vancouver Geotechnical Society, Vancouver, B.C., 18p.
Karpurapu, R. and Bathurst, R. J., 1992, "Numerical Investigation of Controlled Yielding of Soil-Retaining Wall Structures", Geotextiles and Geomembranes, Vol.11, No. 2, pp. 115-131
Lo Presti, D.C.F., Jamiokolwski, M., Pallara, O., Cavallaro, A. And Pedroni, S.(1997), "Shear Modulus and Damping og Soils", Geotechnique 47, No 3, 603-617
McGown, A., Andrawes, K. Z. and Murray, R. T., 1988, "Controlled Yielding of the Lateral Boundaries of Soil Retaining Structures", In Proceedings of the ASCE Symposium on Geosynthetics for Soil Improvement,1988, ed. R.D. Holtz, Nashville, TN, USA, pp. 193-211
Nikolopoulou, C. P., 2006 "Seismic Isolation of Earth Retaining Structures Using EPS Geofoam Compressible Inclusion – Effect of Non-Linear Material Behavior", Master 's Thesis, Department of Civil Engineering, University of Patras, September 2005 (in Greek)
Partos, A. M. and Kazaniwsky, P. M., 1987, "Geoboard Reduces Lateral Earth Pressures", In Proceedings of Geosynthetics '87, New Orleans, USA, February 1987
Pelekis, P. C., Xenaki, V. C. and Athanasopoulos, G. A., 2000, "Use of EPS Geofoam for Seismic Isolation of Earth Retaining Structures: Results of a FEM Study", Proceedings of the 2nd European Geosynthetics Conference, EuroGeo 2000, Bologna, Italy, October 2000, A. Cancelli, D. Cazzuffi and C. Soccodato Eds., Vol. 2, pp. 843-846
PLAXIS, "A Finite Element Code for Soil and Rock Analyses", R. B. J. Brinkgreve, Professional Version 8.1, 2002, Balkema, Lisse

Pradhan, T.B,S.,and Ueno, Y. (1998), "Cyclic Deformation Characteristics of Clay Under Different Consolidation Histories", in Pre-failure Deformation Behavior of Geomaterials, R.J Jardine, M.C.R. Davies, D.W. Hight, A.K.C. Smith, S.E. Stallebrass, Eds, ICE, Thomas Telford, 1998, Great Britain, pp.329-335

Stathopoulou, V. D., 2005, "Seismic Isolation of Earth Retaining Structures Using EPS Geofoam –Numerical Parametric Analyses", Master 's Thesis, Department of Civil Engineering, University of Patras, July 2005 (in Greek)

Stavroulakis, G. E., 2004, ''Auxetic Behaviour: Appearance and Engineering Applications'', Invited Presentation, Workshop on Auxetics and Related Systems, Organized by Krzysztof W. Wojciechowski, June 27-30 2004, Poznan, Poland, Special Issue of Physica Status Solidi (b), Wiley InterScience

Stokoe, K.H., Darendeli, M.B., Menq, F.-Y. and Choi, W.K., 2004, "Comparison of the Linear and Nonlinear Dynamic Properties of Gravels, Sands, Silts and Clays", Proceedings of The 11th International Conference on Soil Dynamics & Earthquake Engineering, Proceedings of The 3rd International Conference on Earthquake Geotechnical Engineering, University of California, Berkeley, USA, 7th-9th January 2004, ed. D. Doolin, A. Kammerer, T. Nogami, R.B. Seed, I. Towhata., pp. 628-638

Tsukamoto, Y., Ishihara, K., Nakazawa H., Kon, H., Masuo, T. and Hara, K., 2001, "Combined Reinforcement by Means of EPS Blocks and Geogrids for Retaining Wall Structures", Landmarks in Earth Reinforcement, Proceedings of International Symposium on Earth Reinforcement, Ochiai, Otani, Yasufuku and Omine Eds., Swets & Zeitlinger 2001, pp. 483-487

Tsukamoto, Y., Ishihara, K., Kon, H. and Masuo, T., 2002, "Use of Compressible Expanded Polystyrene Blocks and Geogrids for Retaining Wall Structures", Soils and Foundations, Japanese Geotechnical Society, Vol. 42, No. 4, August 2002, pp. 2

Veletsos A. S. and Younan A. H., 1997, "Dynamic Response of Cantilever Retaining Walls", Journal of Geotechnical and Geoenvironmental Engineering, Vol. 123, No. 2, February 1997, pp.161-172

Vucetic, M. and Dobry, R., 1991, ''Effect of Soil Plasticity on Cyclic Response'', Journal of Geotechnical Engineering, Vol. 117, No. 1, pp. 89-108

Xenaki, V.C. and Athanasopoulos, G.A. ,2001, "Experimental Investigation of the Interaction Mechanism at the EPS Geofoam – Sand Interface by Direct Shear Testing", Geosynthetics International, Vol.8, No. 6, pp.471-499

Xenaki, V. C., 2005, "Experimental Investigation of the Mechanical Behavior of EPS Geofoam Under static and Dynamic/Cyclic Loading", Doctoral Thesis, Department of Civil Engineering, University of Patras, March 2005 (in Greek)

Zarnani, S. and, Bathurst, R. J., 2005, "Numerical Investigation of Geofoam Seismic Buffers Using FLAC", In Proceedings of the North American Geosynthetics Society (NAGS)/GRI19 Conference, 2005, Las Vegas, NV, USA, December 2005

Zarnani, S. and, Bathurst, R. J., 2005, "Experimentall Investigation of Geofoam Seismic Buffers Using A Shaking Table", In Proceedings of the North American Geosynthetics Society (NAGS)/GRI19 Conference, 2005, Las Vegas, NV, USA, December 2005

Zhang, J., Andrus, R.D. and Hsein Juang, C., 2005, "Normalized Shear Modulus and Material Damping Ratio Relationships", Journal of Geotechnical and Geoenvironmental Engineering, ASCE, April 2005, pp.453-464

CONTACT:
G.A. Athanasopoulos
University of Patras
Department of Civil Engineering
Patras, GREECE
Phone: 30 2610 996543
Email: gaa@upatras.gr

Performance of Electrically Conductive Vertical (Wick) Drains in the Treatment of Soft Clay

Lee E.C., Emas Kiara Marketing Sdn. Bhd., Malaysia;Neoh C.A., Direcrtor, E-Geo Consultant Sdn. Bhd., Malaysia; Douglas R.S.,Managing Director, Kiaratex Exports Pte. Ltd., Singapore

ABSTRACT

Electro-osmotic treatment of soft clays and the use of Prefabricated Vertical Drains (PVD) with surcharge load have been well documented and proven to accelerate the consolidation of soft clay. The coupling of these two technologies has given rise to a fairly new concept of soft ground improvement using EVD or Electro-Osmotic Vertical Drain. This new technology has been driven by the successful manufacture of drainage electrodes in the identical form of PVD, hence enabling very competitive installation method, which has for long been a barrier to electro-osmotic ground improvement. The main difference between EVD and PVD is that EVD achieves a very much faster rate of treatment.

Two field applications of the electro-osmotic ground treatment technology using EVD have been carried out in Malaysia. This paper describes the field implementation and the effectiveness of the treatment. Marked increase in the undrained shear strength of the soft clay has been observed. Further analysis showed that the improved foundation soil could support a higher embankment load than the traditional PVD ground treatment under similar conditions.

1. INTRODUCTION

Innovative applications of geosynthetics in ground treatment of soft clay have been progressed by incorporating the electro-osmotic phenomena with the traditional functions of geosynthetic materials. This entails the development of a new range of geosynthetic materials that are electrically conductive. These electrically conductive geosynthetics can be applied in accelerating the consolidation of soft clay. This innovative product takes advantage of effectiveness and simplicity of Prefabricated Vertical Drains (PVD) to provide vertical drainage and incorporating electrical conductivity along core to facilitate electric current flow into the soil, enabling electro-osmotic (EO) ground treatment process. These special materials are referred to as the Electro-Osmotic Vertical Drains (EVD) in this paper.

EO is a process where flow of water between the soil particles is induced under an applied electrical potential. EO based soil improvement is suitable for fine-grained soils (clay) which possess a net surface negative charge. It would have equal charges of cations and anions to maintain electrical neutrality of the clay soil (Mitchell, 1993). Under an applied electrical potential, cations are attracted towards the anode while anions are attracted towards the cathode. As ions move, they drag along water of hydration and the surrounding free water by viscous force. This will induce a flow of pore water towards the cathode. Hence, this will initiate the dewatering and strengthening of clay.

Field applications of EVD recently at two road projects have shown promising results. The comparative influence of EO ground treatment approach and the conventional PVD consolidation approach; especially with regards to increase in undrained shear strength, is the main objective of this study.

2. BENEFITS TO THE END USER

These electro-osmotic vertical drains (EVD) will enhance the improvement of the shear strength and hence reduce the compressibility of the soft clay. A distinct benefit to the end user is the significantly shortened period of treatment to achieve the required shear strength. Typical treatment periods of 3 to 4 months using PVD can now be shortened to about 1 month with the use of EVD.

Furthermore, with EVD system, the need for significant surcharge material is negated.

3. GENERAL PRINCIPLES OF APPLICATION

EVD applies the principle of electro-osmosis in combination with prefabricated vertical drains to improve the engineering properties of soft clay and, in the process, accelerate the consolidation and strengthening of soft clay.

Amongst the many processes occurring during EO treatment is the reduction of pore water in the soil. This reduction in soil moisture indirectly improves the shear strength and compressibility characteristic of the soil. This type of soil improvement is potentially more effective in reducing the water content that conventional PVD which relies on hydraulic gradient created by external loading.

In electro-osmotic ground treatment, the hydraulic conductivity or flow of water under an electric gradient potential is a function of the coefficient of electro-osmotic permeability, k_e (m^2/sV), the electric potential gradient, i_e (V/m), and the cross-sectional area of flow, A (m^2). The relationship is similar to Darcy's Law and may be written as:

$$Q_A = k_e \, i_e \, A$$

where Q_A is the discharge capacity (m^3/s)

4. FIELD APPLICATION LOCATION NO. 1

The project site is located in Dengkil near the Kuala Lumpur International Airport (KLIA), Malaysia.. The project is part of a road project and the application of EVD is essentially to improve the foundation soils of an approach embankment to a bridge structure, with embankment heights of about 2.5m.

The site is underlain by soft to very soft alluvial silty clay of up to 10m thickness. Beneath the soft silty clay lies medium dense silty sand. Some decayed wood was encountered at various depths. Ground water table was encountered at approximately 1m below existing ground level (EGL). The initial properties of the soil are as shown in Table 1 below:

Table 1: Initial Soil Properties

~~Liquid Limit (%)~~	Plastic Limit (%)	Plasticity Index (%)	**Moisture Content (%)**
154	**79**	**75**	**132**

The pre-treatment undisturbed shear strength as measured by geonor vane shear apparatus (push-in) ranged from 8.8 kPa at 1m below EGL to 18.5 kPa at 9m below existing ground level. An exceptionally high shear strength of 23 kPa was recorded at a depth of 7m; this was thought to be due to presence of fibrous and decayed wood material. Figure 1 shows the variations of undisturbed shear strength with depth.

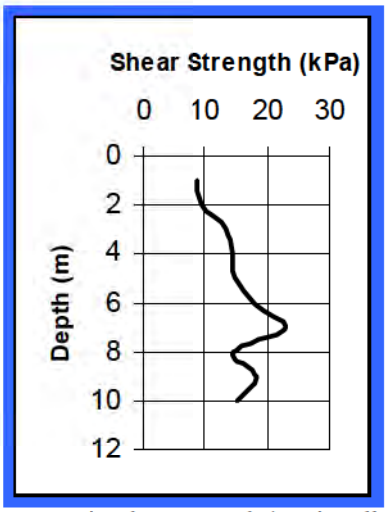

Figure 1: In-situ shear strength (Pre-installation)

4.1 Field Setup

A plot size measuring 20m x 20m was installed with EVD with a rectangular spacing of 1.5m. A total of 198 points were installed in 14 rows, as illustrated in the sketch shown in Figure 2.

A 0.5m thick sand drainage blanket was provided to enable the discharge of ground water to the ditches on the edges. The electrodes at the top of each EVD were connected to an electric power generator supplying DC current. The electric current was applied for 14 days on a 12 hour cycle with intermittent reversals in the polarity of the current.

Upon completion of the charging, the embankment fill was placed to a height of 2.5m. Figure 2 shows a layout of the test plot.

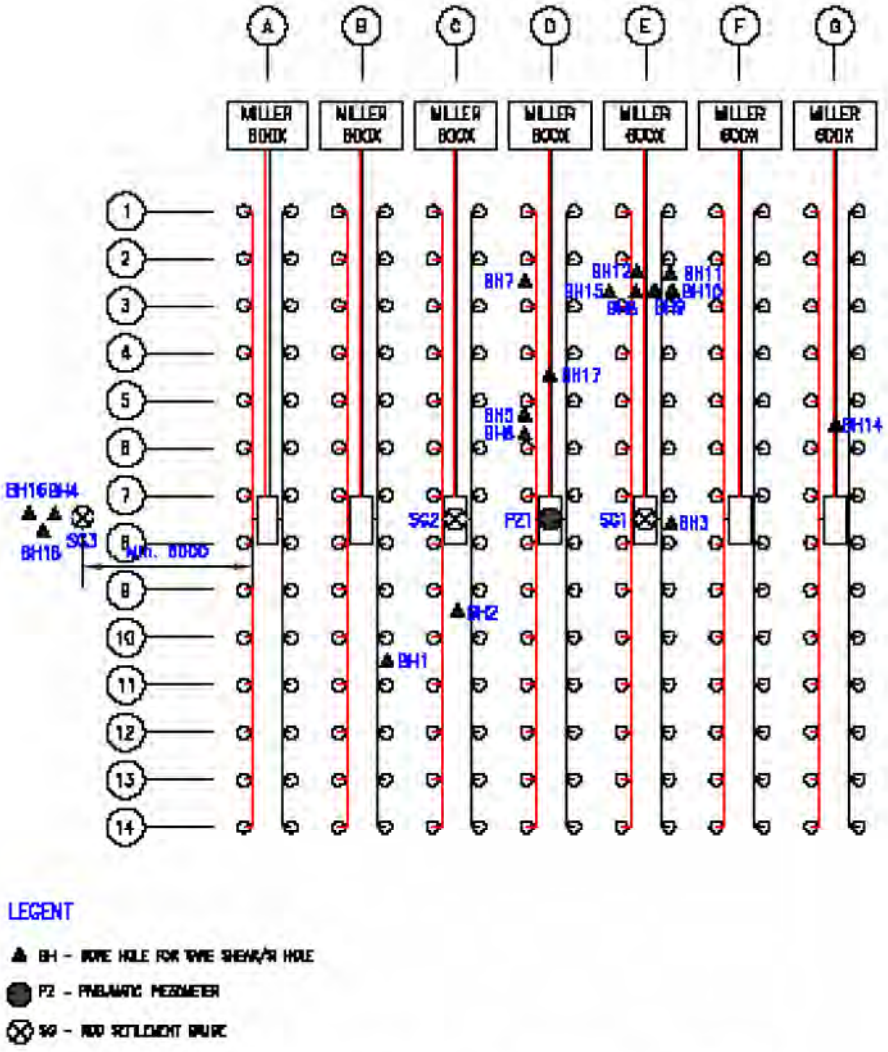

Figure 2: Layout of Charging Pattern, Instrumentation and Testing

The shear strength improvement was closely monitored on a regular basis following the commencement of charging. This was carried out using the penetration field vane (geonor vane) at 1m depth intervals.

4.2 Test Results and Discussion

The most distinct observation of the behavior of the EVD during charging was the constant discharge of ground water through the cathodes. This was accompanied with gas bubbles being discharged as well. This started to occurr about twenty minutes after commencement of charging. It indicated that the electrodes was successfully transferring the electrical charge to the soft ground and the EO treatment as indicated in Section 2.3 above was observed. Figure 3 shows the setup at the site, and Figure 4 shows the discharge of water through the EVD.

There was some slight depression in the area immediately surrounding the anodes. This indicated that consolidation of the soft soil was occurring surrounding the anode, as discussed in Section 2 above.

Figure 3: Setup at site


Figure 4: Discharge of ground water at EVD

Figure 5 below shows the increases in undrained shear strength as measured in the vane shear tests. As indicated in the figure, initially there are increases in shear strength, particularly within the top 5m. This increase became more distinct at 72 days, which show a significant increase in the undrained shear strength. This increase may be attributed to the electro-osmosis treatment of the soil as well as the PVD effect of the EVD during the placement of the embankment load. The percentage of shear strength increase exceeded 100% of the initial values.

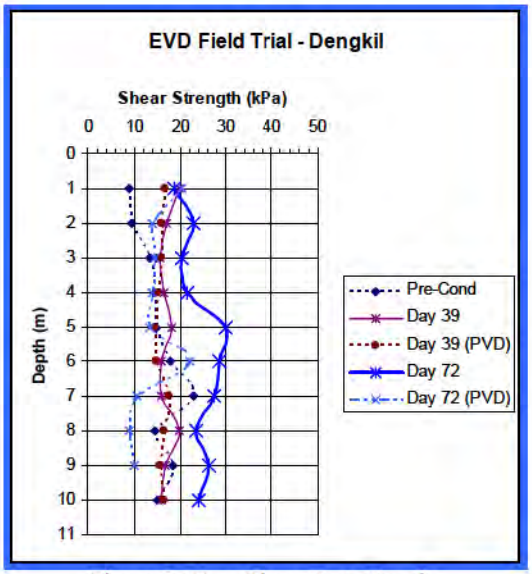

Figure 5: Vane Shear Tests Results

5. FIELD APPLICATION NO. 2

An upgrade of an access road to an oil terminal in Kuching, Sarawak, Malaysia required widening of the road from an existing road width of 8m to a new road width of 16m, constituting a 4-lane single carriageway. This required the widening of 4m on either wide of the existing carriageway. The proposed road structure consists of 1m high embankment fill with approximately 0.5m thick pavement structure. The treatment area measures approximately 560m x 4m on each side of the existing road.

The ground condition at the site consists of very soft to soft organic silty clay up to 15m depth. The ground water table exists at near surface levels. Because of the proximity of the site to the coastline, tidal water variations were observed. To prevent ingress of incoming tidal waters into the site, a bund was built along the external boundaries of the treatment.

The initial site investigation program included field tests such as the vane shear tests. Based on these tests, the undisturbed shear strength of the untreated soil ranges from 5 kPa at the surface to 16 kPa at 9m depth. Site preparation works included placement of a 1m thick granular fill above the soft soils. This served both as a drainage blanket as well as a working platform.

Due to budget constraints, it was decided to improve the soft soil up to a depth of about 6m with EVD. The spacing of the EVD is 1.4m x 1.0m. A total of 3 rows of EVD were installed on both sides of the road widening. Figures 6 and 7 below show the layout of the EVD installed at the site.

Figure 6: View of EVD installed


Figure 7: View of EVD with cables attached

The entire section was sub-divided into 8 sub-plots and the electrification period for the entire area took 2 weeks, based on a 20 hour working day. Polarity reversals were carried out daily. During the electrification period, discharge of ground water was observed at the cathode, as shown in Figures 8 and 9 below.

Figure 8: Discharge of groundwater from Cathode

Figure 9: Discharge of groundwater from Cathode

Field vane shear tests were carried out a week after completion of the electrification works for the entire treatment area. Figure 10 below shows the results of the shear strength profile. The results show that there is a significant increase in the shear strength profile of the treated soils. Figure 10 below shows the shear strength measurements before and after treatment. The lines shown are computed regressions. It is clearly evident that significant improvement has been achieved. On the average, shear strength was increased from 9.15 kPa to 31.1 kPa.

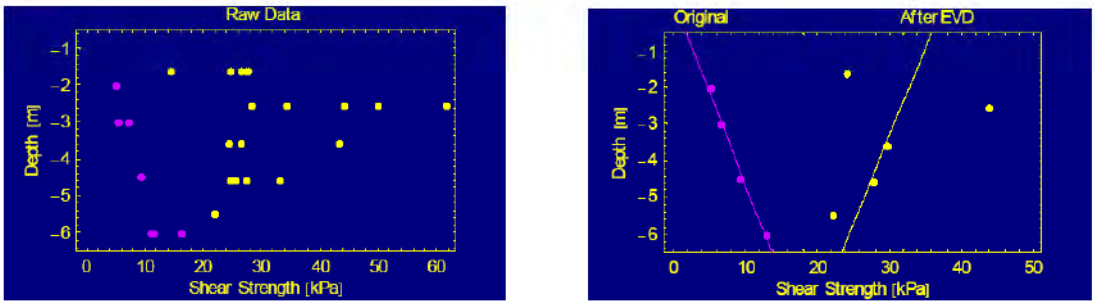

Figure 10: Results of shear strength measurements [raw data and averaged data]

6. CONCLUSION

Two field applications of the EVD have shown significant increases of shear strength within a short period of time. The increased shear strength permits construction of higher embankment heights as compared to conventional PVD ground treatment. This system of ground improvement has proved effective in increasing the shear strength of the soft soils within a short period.

7. REFERENCES

Karunaratne G.P., Jong H.K. & Chew S.H. (2002), "New Electrically Conductive Geosynthetics for Soft Clay Consolidation", proceedings of the 7th International Conference on Geosynthetics, NICE, pp. 277-284

Lee, E.C. (2005), "A Case Study of Electro-Osmotic Ground Treatment of Soft Clay in Dengkil, Selangor", proceedings of Octoberforum, Institution of Engineers, Malaysia, October 2005.

Lo K.Y., Inculet I.I. & Ho K.S. (1991), "Electro-osmotic Strengthening of Soft Sensitive Clays", Canadian Geotechnical Journal, Vol. 28, PP. 62-73.

Mitchell, J.K. (1993). Fundamentals of Soil Behavior, 2nd Edition, John Wiley & Sons, New York.

CONTACT:
Eng Choy Lee
Emas Kiara Marketing Sdn. Bhd.
Suite E-16-D1, Block E, Wisma Sunrise, Plaza Mont Kiara
No. 3, Jalan Kiara, 50480 Kuala Lumpur
Kuala Lumpur
Malaysia
Phone: 603-27813388
Email: engchoy.lee@emaskiara.com

NAGS Student Paper Competition

Development of a low altitude aerial photogrammetry technique to quantify geomembrane wrinkles

M. J. Chappel, Graduate Student, GeoEngineering Centre at Queen's-RMC Queen's University; R. W. I. Brachman, Assistant Professor, GeoEngineering Centre at Queen's-RMC Queen's University;W. A. Take, Assistant Professor, GeoEngineering Centre at Queen's-RMC Queen's University; R. K. Rowe, Vice Principal (Research) and Professor, GeoEngineering Centre at Queen's-RMC Queen's University

ABSTRACT

A low altitude air photo system has been developed to quantify the geometry of geomembrane (GM) wrinkles at a large scale. Wrinkles which are caused mostly by solar heating and expansion are of particular interest for high-density polyethylene (HDPE) geomembranes. It is important to improve wrinkle quantification because wrinkles may lead to greater leakage through the geomembrane if a hole is at or near a wrinkle. Wrinkles also result in greater local tensile strains in the geomembrane.

A low altitude aerial photogrammetry technique to quantify geomembrane wrinkles is presented. The system consists of a Digital Single Lens Reflex (DSLR) camera, with remote infrared shutter control mounted on a tethered helium blimp. This system allows the operator to obtain clear, accurate near-vertical air photos.

The wrinkle geometry is analyzed from the low altitude air photos using the digital image processing capabilities and custom functions in Matlab. This allows the user to geometrically correct images; stitch images of parts of a site together into a single image; and select and quantify wrinkle geometry from the image of the site. Preliminary results on the length, connectivity and frequency of wrinkles are presented.

INTRODUCTION

Calculations commonly used to estimate leakage through composite liners typically assume that there is intimate contact between the geomembrane and the compacted clay liner or the geosynthetic clay liner beneath it. This contact restricts the horizontal flow of leachate between the two barriers in a low transmissivity interface zone. Wrinkles (also referred to as waves) substantially increase the potential leakage though a hole in the geomembrane when it coincided with a wrinkle (Rowe, 2005). They also increase the tensile strains in the geomembrane when covered and buried beneath waste (Gudina and Brachman, 2006). The wrinkles in high-density-polyethylene (HDPE) geomembranes predominantly form due to material expansion by heating from the sun.

Rowe et al. (2004) reported the distribution of wrinkles on the base of one particular landfill cell during construction. These wrinkles were randomly distributed with no discernable patterns, thus making it challenging to quantify their length and spacing. Wrinkles developed at, and

parallel to, the geomembrane seams as well at locations both perpendicular and inclined to the seams. The longest wrinkle was at least 17 m and may have extended the entire length of the cell (≈40 m). The shortest wrinkle was roughly 1 m long and the minimum spacing between wrinkles was about 0.5 m. The wrinkles inclined to the seams appeared to be connected to the long wrinkles at each seam. Such a distribution of wrinkles would provide an extensive preferential pathway for liquid migration beneath the geomembrane if there were any holes in the geomembrane at any point on the interconnected wrinkles.

Pelte et al. (1994) reported field observations of wrinkles for 1.5 mm thick black HDPE geomembrane overlying clay in a 30 m by 30 m cell in a landfill in France. They observed that major wrinkles occurred parallel to the length of the geomembrane roll at the location of seams, and also perpendicular to the seam direction. They reported large wrinkles between 0.05 to 0.1 m high and 0.2 to 0.3 m wide, and had a spacing of 4 to 5 m and appeared to extend across a significant width of the cell. They also noticed small wrinkles (less than 0.05 m high and 0.2 m wide) occurred perpendicular to the seams.

Touze-Foltz et al. (2001) quantified wrinkles in a 2 mm thick HDPE geomembrane over compacted clay using a photogrammetric technique. Wrinkle heights varied between 0.05 and 0.13 m, wrinkle widths between 0.1 and 0.8 m, spacing between wrinkles from 0.3 and 1.6 m, while the length of wrinkles was less than 4 m with most wrinkles 1-2 m long. The size of installation was only 7.5 m by 7.5 m, and consequently most likely limited the length of wrinkle that could form. However, the technique of Touze-Foltz et al. (2001) represents a very useful way of quantifying wrinkles at larger sites.

The objective of this paper is to present the details of the development of a low altitude air photogrammetry system to quantify the geometry of geomembrane (GM) wrinkles at a large scale. Details of the equipment used for obtaining the photos, the method of acquiring the photos, digital wrinkle analysis and the photo calibration are presented. Preliminary results from a large geomembrane installation are presented.

LOW ALTITUDE AERIAL PHOTOGRAPHY EQUIPMENT

The system consists of a Digital Single Lens Reflex (DSLR) camera with remote infrared shutter control, attached to a tethered helium blimp (Figures 1 and 2). A Canon 5D DSLR camera is used for this application. It has a 13.3 megapixel complementary metal oxide semiconductor (CMOS) that measures 35.8 mm by 23.9 mm. The high density of pixels allows a greater resolution than cameras with a lower pixel count. The area of the CMOS is very close to the format of a film 35 mm SLR camera, which permits the use of the full focal length of a lens, unlike most DSLR cameras.

The blimp stability is a function of both the blimp size and wind speed. The blimp is 6.4 m long by 2.1 m diameter, which optimizes platform stability and ease of handling on the ground. The wind speed at ground level is greater and less predictable because there are many localized currents due to uneven ground surface and differential heating. At an elevation of about 60 m, the wind speed is more constant. Thus a flying elevation of approximately 60 m is used in this

study for the best possible stability. The blimp can lift 4.8 kg, and requires a 15 kg anchor. Since the blimp is streamlined and has tailfins, it will always orient itself into the wind. This prevents the blimp from becoming a large kite, and reduces the lifting or dragging the anchor in high winds; higher winds result in more side-to- side movements, as well as a decrease in altitude as the blimp blows downwind. Increased camera motion must be accommodated by a higher shutter speed although this reduces the resolution of the image.

Figure 1 Photograph showing blimp equipped with a digital camera used to obtain images of geomembrane wrinkles.

LOW ALTITUDE AERIAL PHOTOGRAMMETRY TECHNIQUE

This blimp and camera system allows the operator to take clear, accurate near-vertical air photos by optimizing the following variables: altitude of the camera, focal length of the lens, resolution of the image, field of view (or ground coverage), and number of images required to capture the site.

The altitude of the camera is controlled by the length of the blimp tether. The control over the altitude of the camera using this method should be considered nominal, as the true height of the blimp, and therefore the camera, is ultimately controlled by the wind speed and direction. The wind direction affects the direction of the blimp, because the blimp will always point into the wind, and a greater wind speed will push the blimp downwind, and decrease the altitude. If the blimp moves in the air with gusts of wind, then the angle of the camera with respect to the

ground will also change. The choice of nominal camera altitude is particularly important as the scale, S, of a captured photo is determined by the ratio of the focal length, f, of the camera lens to the altitude, A, of the camera. In the present study, the focal length of the camera is 0.050m and the nominal camera elevation is 60m, leading to a scale factor of 0.050/60, or 1:1200.

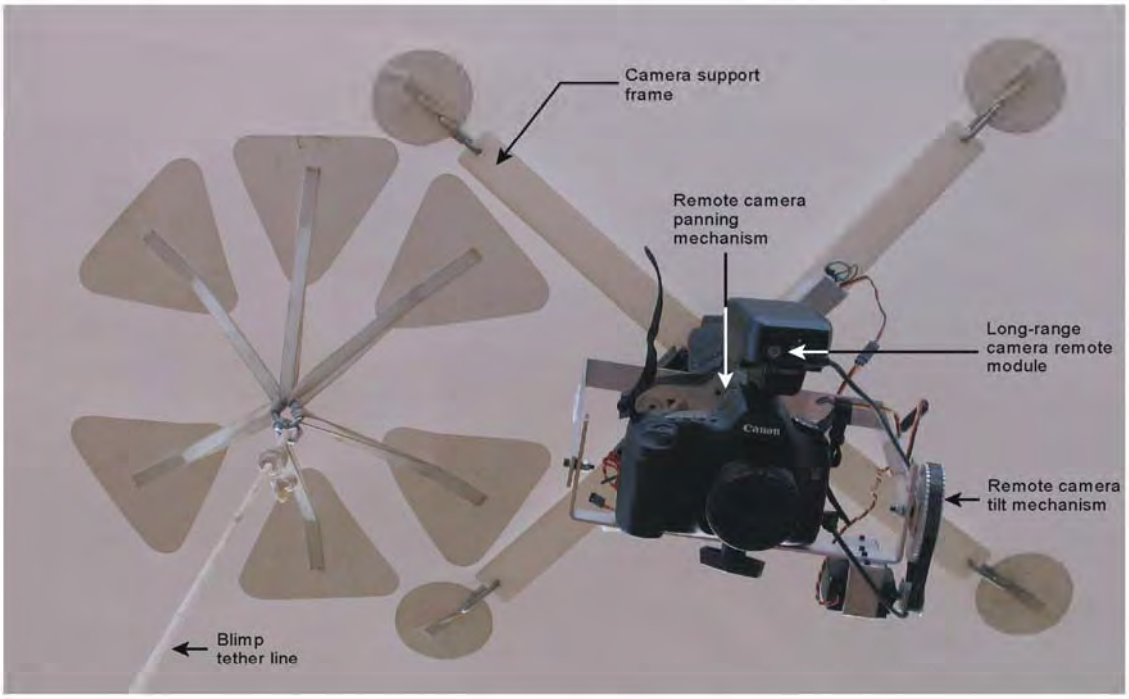

Figure 2 Photograph showing digital camera mounted to the underside of the blimp.

At a given blimp altitude, changing the focal length of the lens allows the user to change the object-space resolution and the ground coverage (i.e. field of view) of the photo. The object-space resolution describes the effective size in real-world units (i.e. mm) of a single pixel. This resolution can be calculated by considering a simple pin-hole camera model in which:

$$ground\ \mathrm{cov}erage(m) = \frac{altitude(m) \times CMOSsensorwidth(mm)}{focallength(mm)}$$

Thus, for the same camera orientation the object-space resolution of the images will be the ground coverage / number of pixels in the CMOS sensor. Whereas a shorter focal length will take wider angle photos and enable greater land coverage, this will be at the expense of the object-space resolution of the image and increased lens distortion. The resolution and image quality of the photo is very important, because the system must have sufficient resolution to define wrinkles of a few centimetres in height at a camera elevation of 60 m. For image collection, a 50 mm lens is the optimal size to maximize land coverage per photo (19.1m x 28.6m) while still maintaining the precision needed to detect small wrinkles. The 50 mm lens at 60 m above the ground results in a theoretical resolution of 1 pixel = 5 mm on the ground. This can commonly be achieved in the field under good conditions. Photos for analysis are taken as

close as possible to vertical. This minimises the image transformation errors when correcting the projection of the image.

During data collection, there is a theoretical minimum number of photos required to cover the entire field site. In practice, since the photo content and quality are initially unknown, with an unknown camera location, hundreds of photos must be taken to choose the best set of images required to produce a single image of the entire GM.

XY PLANE WRINGLE GEOMETRY ANALYSIS

The black GM reflects enough light that the wrinkles are easily delineated by the contrast difference between the wrinkle reflecting the sunlight and the flat black of the non-reflecting flat portions. The wrinkles are linear white features on the black geomembrane (Figure 3).

The wrinkle geometry is determined by manipulating and analyzing the low altitude air photos with the image processing features and custom functions developed with Matlab. For this analysis, a single large image of the GM area is created from a selection of photos that cover the entire area to allow the analysis of the full area.

The wrinkles are subsequently located and quantified. The user digitally selects the wrinkles and the continuity of the linear features. The vectors created are located by a Matlab function which determines the geometric wrinkle properties of interest: length, connectivity and frequency, as well as the hydraulic connectivity.

Figure 3 Air photo of geomembrane installation. 1.5 mm smooth HDPE; Camera elevation 65 m; Latitude 43°16′ N; Air temperature 28°C; 1:20 pm Aug 18 2006

CALIBRATION OF IMAGES

Calibration is achieved by using the surveyed control points (CPs) as known points in the photos of the GM. This allows the photos to be geometrically corrected and stitched together to create one large image of the entire GM with a known scale. The scale chosen is one pixel represents 10 mm on the ground, which is a lower resolution than the original photo with one pixel representing 5 mm on the ground. This reduces the file size of the large image, and simplifies further measurements and quantification.

To develop an image of the entire GM area, a grid of labelled CPs every 10 m were drawn and labelled on the geomembrane. The spacing of 10 m ensures that there will always be many CPs in each picture. Each CP is marked on the GM by an "X" and is labelled with a grid coordinate. These ground control points are surveyed using a total station, and are visible in the photos. By connecting the grid locations of the CPs to the markings in the photos, the user can determine the orientation and scale of the objects in the photo in real world units. This also allows the user to further quantify the images.

Geometrically corrected images are created from the original photographs, using the known locations of the CPs. The individual images are then digitally stitched together to create one large image of the site, once again by utilizing the actual surveyed location of the CPs.

In a vertical air photo, there is geometric distortion due to three dimensional objects being projected on a two dimensional plane. This distortion results in a change in scale between the centre of the photo and the edges. In a geometrically corrected image, this distortion is eliminated by determining the three dimensional coordinates of objects of several points in each photo. This correction is completed by the user manually choosing the points on the digital photo and inputting relative coordinates into a custom Matlab function.

After photos have been geometrically corrected, the grid of CPs can be used to stitch all of the geometrically corrected images of the field site. This creates one large image with a scale of 1 pixel represents 1 cm.

PRELIMINARY RESULTS

The air photo shown in Figure 3 was obtained during installation of a 1.5 mm thick, smooth HDPE geomembrane. The site was at a latitude 43°16′ N and the image was captured at 4:09 pm on August 17, when the air temperature was 24°C. The camera was at an elevation of 60 m.

Wrinkles parallel, perpendicular and inclined to the geomembrane panels are visible in Figure 3. There were at least 76 wrinkle features identified over the 1172 m^2 area capture in this image. If extrapolated, this represents nearly 650 wrinkles per hectare. The minimum wrinkle length was 0.5 m, maximum wrinkle length was 29 m. Sixty-eight percent of the wrinkles had lengths

between 1-5 m, while 9% has lengths between 20-30 m. At many locations, it appears that adjacent wrinkles may be interconnected as they intersect and join each other and thus the length of hydraulically connected wrinkles is much greater than the maximum wrinkle length.

SUMMARY

High resolution, digital images have been successfully used to capture wrinkle formation in geomembrane liners. Following photogrammetric principles, the altitude of the camera platform (in this case, a 6.4 m long blimp), the camera lens, the land coverage, and the resolution of the photos have been optimized to yield images of sufficient quality to define the spatial orientation of wrinkles over large areas. The wrinkles are analyzed using the image processing toolbox in Matlab, as well as custom functions. The photos are calibrated and connected together to create one large image of a GM installation. Work is currently ongoing to gather and analyse wrinkle image data from different field installations to better quantify the process of wrinkle formation in geomembrane liners.

ACKNOWLEDGEMENTS

This study was financed by the Natural Sciences and Engineering Research Council of Canada (NSERC). The authors are grateful to their industrial partners, Solmax International, Terrafix Geosynthetics Inc, Ontario Ministry of Environment, Gartner Lee Ltd, AMEC Earth and Environmental, Golder Associates Ltd., and CTT group.

Corresponding author: R.W.I. Brachman; brachman@civil.queensu.ca; Phone: (613) 533-3096

REFERENCES

Gudina, S. and Brachman, R.W.I. 2006. Physical Response of Geomembrane Wrinkles Overlying Compacted Clay, Journal of Geotechnical and Geoenvironmental Engineering, **132**(10): 1346-1353.

Pelte, T., Pierson, P. and Gourc, J.P.(1994) Thermal analysis of geomembranes exposed to solar radiation, Geosynthetics International, 1(1): 21-44.

Rowe, R.K. (2005) "Long-Term Performance of Contaminant Barrier Systems", 45th Rankine Lecture, Geotechnique, **55** (9): 631-678.

Rowe, R.K., Quigley, R.M., Brachman, R.W.I., and Booker, J.R. 2004. Barrier Systems for Waste Disposal Facilities, Taylor & Francis / Spon, London, U.K., 579 p.

Touze-Foltz, N., Schmittbuhl, J., and Memier, M. (2001) Geometric and spatial parameters of geomembrane wrinkles on large scale model tests, in Proceedings of Geosynthetics 2001, Portland, USA, pp. 715-728.

CONTACT:
Melissa Chappel
GeoEngineering Centre at Queen's-RMC
Civil Engineering, Queen's University
Kingston, Ontario
CANADA
Phone: 613-533-6000 ext. 77142
Email: chappel@civil.queensu.ca

ASSESSMENT OF GEOTEXTILE FILAMENT PROPERTIES AND SIZE VARIATIONS DURING INTERFACE SHEARING

Duhwan Kim, and J. David Frost, Georgia Institute of Technology

ABSTRACT

The shear induced micro-mechanical interaction of geotextile filaments and geomembrane surface texture elements have been quantified using needle punched nonwoven geotextiles in combination with a coextruded HDPE geomembrane. The tensile properties of single filaments from three geotextiles were determined using an advanced optical experimental setup. The change in filament diameter was monitored at different tensile strain levels, using a helium neon gas reflectometer. A sample preparation method of epoxy resin impregnation followed by optical image analysis was applied to allow the sensitive geotextile microstructure at different stages of interface shear loading to be observed. The variations in filament size distributions were quantitatively evaluated under various boundary conditions. The filaments at strain levels corresponding to peak shear resistance showed the largest change in diameter and indicated that 50 % of the filaments were smaller than 27 μm at a normal stress of 100 kPa. In contrast, for compressed but unsheared specimens under the same normal stress, the corresponding filament diameter was 32 μm.

INTRODUCTION

During the past few decades, various manufacturing methods have been developed to produce textiles suitable for geotechnical engineering applications. Needle punched nonwoven (NPNW) geotextiles are amongst the more common geotextiles used in various field applications. NPNW geotextiles consist of spatially curved filaments that are often assumed to be randomly oriented and isotropically distributed. Due to difficulties in direct observation, the micromechanical behavior of the internal geotextile structure has received limited attention. In this study, the effects of interface shearing against geomembranes on the geotextile microstructure is discussed in terms of tensile stress-strain-diameter response of the filaments as a function of boundary load conditions.

TENSILE PROPERTIES OF SINGLE GEOTEXTILE FILAMENTS

Most previous studies into the interaction between geotextiles and geomembranes have been limited to mechanical responses from large-scale perspectives. For example, Frost and Lee (2001) investigated the role of geomembrane textures on the evolution of interface friction against NPNW geotextiles, and quantified the degree of wear of geomembrane surface textures in terms of surface roughness parameters. Similarly, while Hebeler et al. (2005) studied geotextile-geomembrane behavior in terms of "hook and loop" interaction, their experimental efforts focused on global rather than filament level response. It is obvious that the interface resistance is determined by the combined response of textures and filaments, however the sensitive unbonded nature of the filaments in nonwoven geotextiles have rendered the direct measurement of shear induced changes in their structure impractical to date.

The sample preparation and image analysis techniques used in this study enable the internal structure at geotextile-geomembrane interfaces to be observed (Kim and Frost, 2005; 2006). In order to quantitatively analyze the localized interlocking between geotextile filaments and geomembrane texture elements, the ability to characterize the tensile properties of single filaments is essential. Tensile testing with single filaments is also potentially useful for designing new products and for predicting material durability.

Various techniques have been developed to characterize the tensile properties of single filaments and fibers. Typical test methods can be categorized into two types: (1) constant-rate-of-elongation (CRE) tests (Hindman, 1948); (2) constant-rate-of-loading (CRL) testes (Krais, 1928; de Meulemeester and Nicoloff, 1936). Due to creep effects, the two methods are known to provide difference results if the stress-strain responses are non-linear. It is known that the CRE method shows higher strength values at low strain and lower values at large strain because of the greater amount of cumulative creep (Morton and Hearle, 1993). Specific test procedures and analysis methods are described in ASTM D 3822 and D 3379.

Even for natural fibers with low homogeneity and isotropy, fiber diameter or fineness, is known to be an important parameter that influences various physical properties of fibers and textiles including stiffness, torsional rigidity, reflection of light, absorption of liquids, vapors, cohesion, and twist (Morton and Hearle, 1962; 1993). One of the most popular and traditional methods of measuring a fiber diameter is to use the projected surface image under a microscope. If the fiber has an oval cross sectional shape, this method is achieved by dispersing a fiber 0.8 mm long in a suitable mounting medium and then observing the specimen in random directions. Other methods include the gravimetric (ASTM, 1954), air-flow (Lord, 1955), and vibroscope methods (Gonsalves, 1947).

Materials Tested

Materials used in this study include two polypropylene (PP) geotextiles, one polyethylene (PE) geotextile, and a textured HDPE geomembrane that are all widely used in practice. The geotextiles are needle punched nonwoven types and their physical properties are listed in Table 1.

Table 1. Physical properties of the geotextiles.

Type	Mass per unit area[1] (g/m^2)	Tensile properties[2]		Puncture strength[3]	Trapezoidal tear strength[4]	Apparent opening size[5]
		σ_y (N)	ε_y (%)	(N)	(N)	(mm)
NPNW PP[6]	270	955	50	525	420	0.180
NPNW PP	405	1,420	50	835	555	0.150
NPNW PE[7]	271	1,023	60	444	356	0.210

Notes: [1]ASTM D 5216. [2]ASTM D 4632; [3]ASTM D 4833; [4]ASTM D 4632; [5]ASTM D 4751; [6]Polypropylene; [7]Polyethylene. Data from manufacturers literature.

Table 2. Physical properties of the geomembrane.

Type	Thickness [1] (mm)	Density [2] (g/cm^3)	Tensile Properties [3]			
			σ_y (N/mm) [4]	σ_b (N/mm)	ε_y (%)	ε_b (%)
Textured HDPE	1.5	0.94	16	23	13	150

Notes: [1]ASTM D 5199; [2]ASTM D 1505; [3]ASTM D 1603; [4]N/mm-width. σ_y =stress at yield; σ_b=stress at break; ε_y=strain at yield; ε_b=strain at break. Data from manufacturers literature.

The geomembrane has a nominal thickness of $1.5\,mm$ and yield tensile strength of $16\,N/mm-width$. It has a carbon black content of 2% and surface texture that is generated by the coextruding process. The surface roughness profile of the geomembrane measured using a stylus profilometer indicates that the sample is categorized as a moderately textured geomembrane based on the description proposed by Dove and Frost (1996). Detailed information about the selected geomembrane is shown in Table 2.

Experimental Setup and Test Method

Tensile properties of single geotextile filaments were measured using an experimental device at the Georgia Institute of Technology for measuring and recording the stress-strain response of filaments. The device had a force resolution of 0.0002 grams, maximum force of $35N$ (3500 gram-force), and strain resolution of $1\times10^{-6}\,mm$. A single fiber is centerline mounted using glue on a paper tab that has a slot at the center. Figure 1a presents a schematic diagram of a mounted specimen. The filament-mounted tab is gripped with a set of stationary jaws (Figure 1 b) and then strained until the specimen is exposed to a small load less than one tenth of gram-force (Figure 1c). The tab is initially pulled using delicate control of the tensile force to ensure the axial alignment of the filament specimen. After applying this initial force, the paper tab is cut gently at the middle points of either side, ensuring that the force applied to the filament does not exceed the allowable variation range. The gage length (net measurement length of the filament) is 25 mm, and the extension rate is controlled to a constant value of 0.1 mm/sec. Data are collected at the rate of 10 points per second (100 points per 1 mm extension). All other sample preparation and measurements are conducted based on the procedures described in ASTM D 3379.

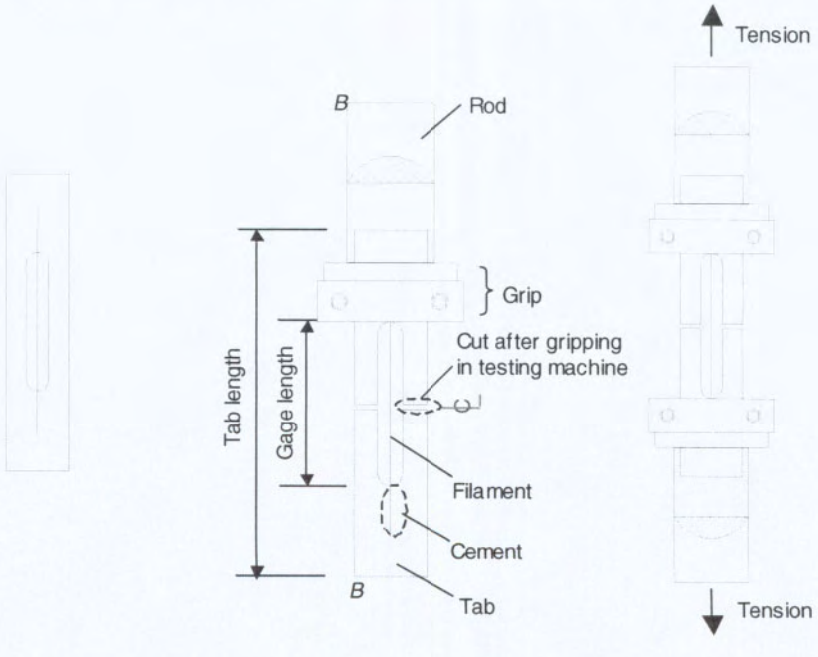

(a) (b) (c)

Figure 1. Specimen mounting method of a single filament: (a) tab and filament, (b) tab and filament in grip; (c) testing configuration.

Observing the change of filament diameter under tensile strain is required in order to be able to evaluate the subsequent shear induced change of filament sizes. Observing the surface image of a filament under a microscope is a widely used method to acquire the nominal diameter in practice. However, maintaining the required optical focus on a filament during tension testing is very difficult. This is because an optical microscope usually does not satisfy the two requirements for focusing at the same time: (a) a large range of measurement depth; (b) sufficient reflection of the light from the filament surface into the eyepiece of the microscope. Delicate focusing is essential to quantitatively and accurately measure the changing diameter of a filament in space and has technical limitations with conventional methods.

To overcome such measurement difficulties, the diameters (d) of single filaments were monitored at various strain levels using a helium neon gas deflectometer. This method is based on Bragg's law of diffraction (1913) as shown in equation 1.

$$d = \frac{m\lambda D}{\Delta y} \tag{1}$$

where, λ is the wavelength of the laser beam, D is the distance between the filament and the image wall that the deflected lights reach, Δy is the interval of the reflected light element in which the center and n th bright zone of the reflected light image are measured, and m is a constant determined by the interval of the bright span of the reflected image.

Figure 2 shows a schematic diagram of the experimental setup that includes a deflectometer and tensile strength facilities. For example, if the nearest bright point from the center image is selected among the detected points then m is set as 0.5. Similarly, m is 1.0 and 1.5 for the second and third points of bright zone. Helium neon gas which has a wavelength of 632.8 nm is used for the test. An important advantage of this method, particularly in this study was that the measurements could be conducted during the tensile straining of filaments by recording the reflected beam images on the wall with a video camera.

Measurement Parameters

The tensile behavior of single fibers and filaments can be expressed using various quantitative descriptors. The definitions and terminology illustrated in ASTM are summarized below (ASTM D 123, D3822, D3379), where tex is a unit of linear density that is equal to the mass in grams of a 1,000 meter long fiber. Denier (den) is another unit of linear density that is equal to the mass in grams of a 9,000 meter long fiber. Other definitions include:

- Breaking force, *BF* (*mN* or *gf*): maximum force applied to a fiber to carry the fiber rupture.
- Breaking tenacity, *BT* (gf/den): tenacity at breaking force.
- Breaking toughness, *BTO* (joule/den): energy absorbed to a specimen until rupture.
- Chord modulus, *CM* (*cN/tex* or *gf/den*): ratio of the change in stress to the change in strain between two specified points on a stress-strain curve.

- Elongation at peak, *EP*(%).
- Initial modulus, *IM* (*cN/tex* or *gf/den*): ratio of the change in stress to the change in strain of the initial straight portion of the stress-strain curve.
- Linear density, *LD* (*tex* or *denier*): mass per unit length.
- Tangent modulus, *TM* (*cN/tex* or *gf/den*): the ratio of change in stress to change in strain derived from the tangent to any point on the stress-strain curve of a tensile test.
- Tenacity (specific stress), *TN* (*gf/den*): tensile stress expressed as force per unit linear density of the unstrained specimen.
- Tensile stress at specific elongation, *TSSE* (*cN/tex*).
- Toughness (work per unit volume; work per unit mass; work of rupture), *TO* (*Joules/gf/kilometer*): capacity of a material to absorb energy required to a strain.
- Yield point, *YP* (%): the point beyond which work is not completely recoverable and permanent deformation takes places.

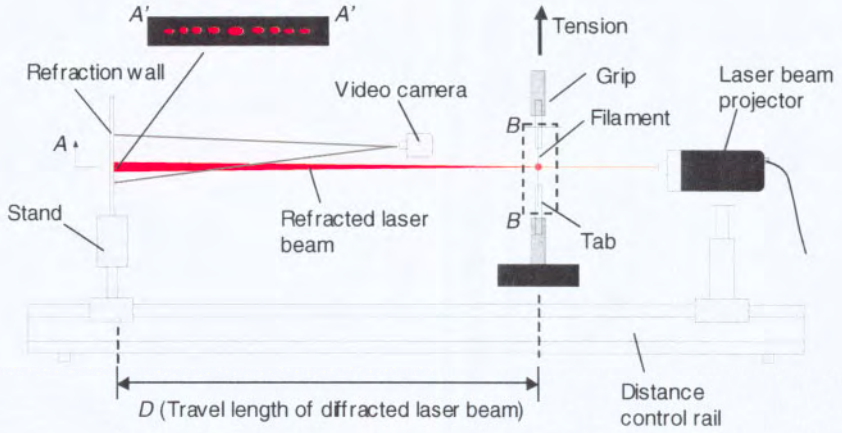

(a)

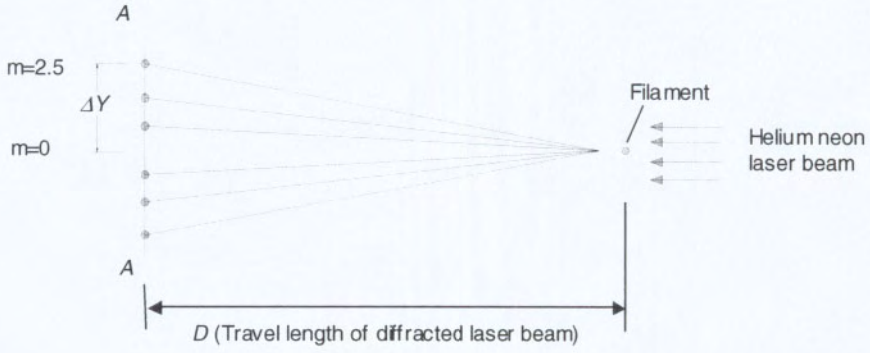

(b)

Figure 2. Schematic diagram of filament property measurement: (a) experimental setup (side view); (b) Bragg's law of diffraction (plan view).

SHEAR RESPONSE OF GEOTEXTILE-GEOMEMBRANE INTERFACES

The shear failure of geotextile-geomembrane interfaces in the field is known to be accompanied with excessive internal strain of the geotextiles (Mitchell and Seed, 1990; Seed and Mitchell, 1990; Villard et al., 1999). In order to model such a mechanism, a new shear device was used in this study as shown in Figure 3. A geomembrane specimen, 200 mm wide by 290 mm long, is positioned on a platform mounted on a set of linear bearing rails with the manufacturing machine

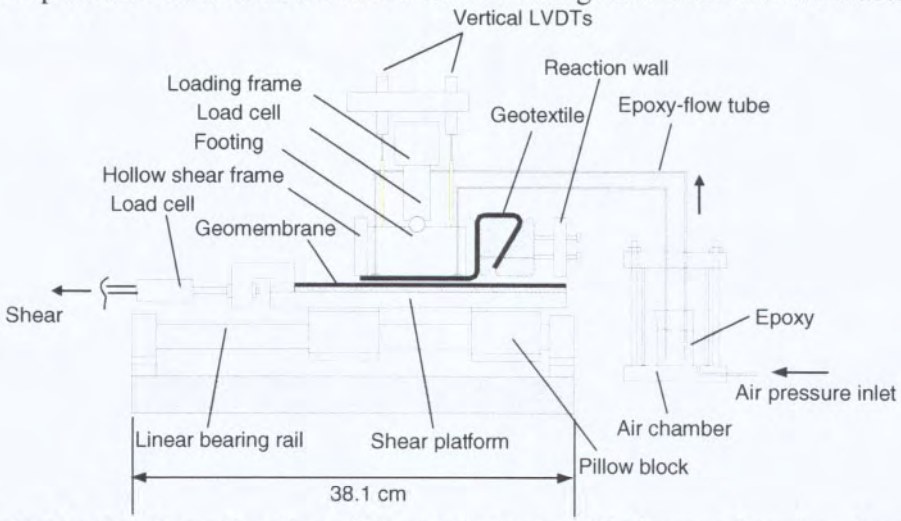

direction parallel to the shear direction. The geotextile is folded around wedge-shaped plates on the leading edge of the hollow shear frame and secured by pressure fastening the wedges to a reaction wall, while the shear frame is held in a plane above the platform base by two rigid shafts installed on either side of the shear platform so that error caused by the contact between the shear box and geomembrane is avoided. (Kim and Frost, 2005).

Figure 3. Schematic diagram of the interface shear device (Kim and Frost, 2005).

Typical results of interface shear resistance using geotextile A and the textured geomembrane are shown in Figure 4a. The corresponding vertical displacements that occurred during the initial compression and shear displacements are illustrated in Figure 4b. The specimen showed a dilation under a low normal stress of 10 kPa (A3 in Figure 4b) during shearing while the samples at 100 kPa and 300 kPa resulted in residual settlements after the peaks due to filament rearrangement and the localized filament-texture interactions.

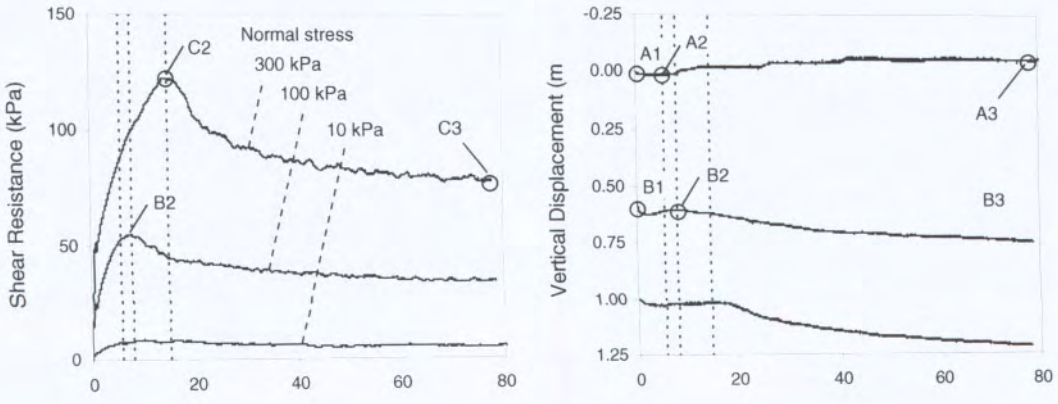

(a) (b)

Figure 4. Interface shear response of the geotextile against a moderately textured geomembrane: (a) shear resistance; (b) vertical displacement.

DIGITAL IMAGE ANALYSIS

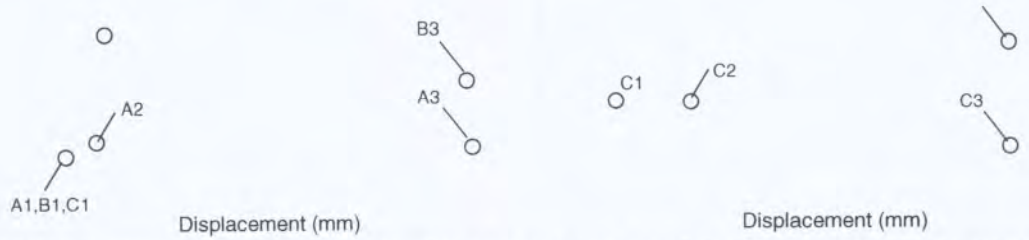

The geotextile-geomembrane layered specimens were encapsulated by low-viscosity epoxy resin at compressed/sheared states as shown in Figure 4. The initial unsheared compressed states of the specimens are marked as A1, B1, and C1 for normal stress states of 10, 100, and 300 kPa, respectively. Specimens were also prepared at peak strain (A2, B2, and C2), and at pseudo residual states (A3, B3, and C3) corresponding to displacements of about 80 mm.

The flow of epoxy resin into the geotextile pores was controlled using constant air pressure of 7 kPa (Figure 3). The selected epoxy resin is known to have appropriate properties for sensitive sample preservation satisfying critical requirements including optical clarity, hardness, bonding strength, and low volume change (Jang et al., 1999). The specimens were cured at room temperature for 24 hours. After being cured, the specimens were sectioned as appropriate to observe the internal structure of the filament-texture interfaces under a digital optical microscope. The tri-sector sampling method (Gokhale and Drury, 1994) was applied to the compressed specimens to obtain representative 3-D information from the section images (Figure 5a). In order to identify the effects of shear on the geotextile microstructure, two orthogonal viewing planes (Vaughan, and Brown, 1996) were observed including the shear surfaces (face I) and the cross-shear surfaces (face II) of the specimens as illustrated in Figure 5b.

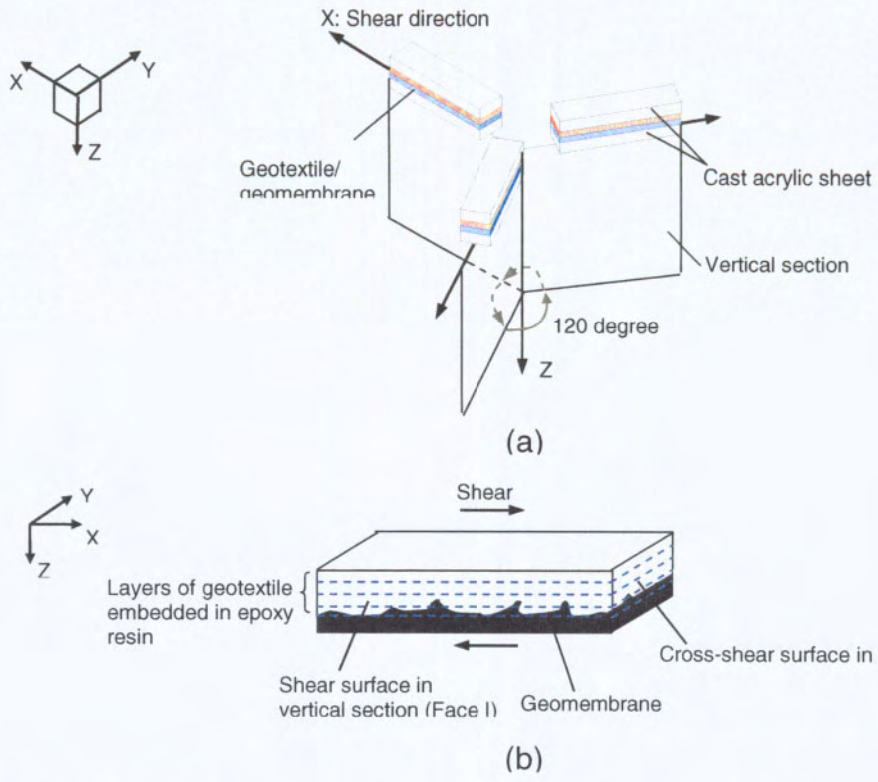

Figure 5. Sampling methods: (a) tri-sector sectioning method used for compressed specimens; (b) orthogonal viewing planes method used for sheared specimens.

TEST RESULTS

Tensile Behavior of Geotextile Filaments

The typical tensile behavior of single geotextile filaments is shown in Figure 6. The tensile force versus strain had a nonlinear elasto-perfect plastic form for the two PP geotextiles, resulting in nearly constant resistances after peak until they reached rupture at elongations of 62% and 57%, respectively (Figure 6a). The change of filament diameter is also shown as a function of displacement (Figure 6b). The diameter of the filament from geotextile A decreased rapidly under initial tensile loading and the slope of the stress-strain curves changed with the axial tensile strain. The filament from geotextile B resulted in a similar trend of stress-strain response and constant decrease of diameter with tensile force. The filament from geotextile C made from polyethylene demonstrated a different response. Its initial modulus was relatively high and then decreased at an elongation of about 0.5 mm. This specimen resulted in a constant increase of tensile force until the break point without yielding. Parameters obtained from the tests are summarized in Table 3. Geotextile A was selected for further study using image analysis techniques since it had a relatively large filament thickness and showed a large and constant rate of change of diameter with tensile strain (i.e., about 15 μm or 35% strain at failure).

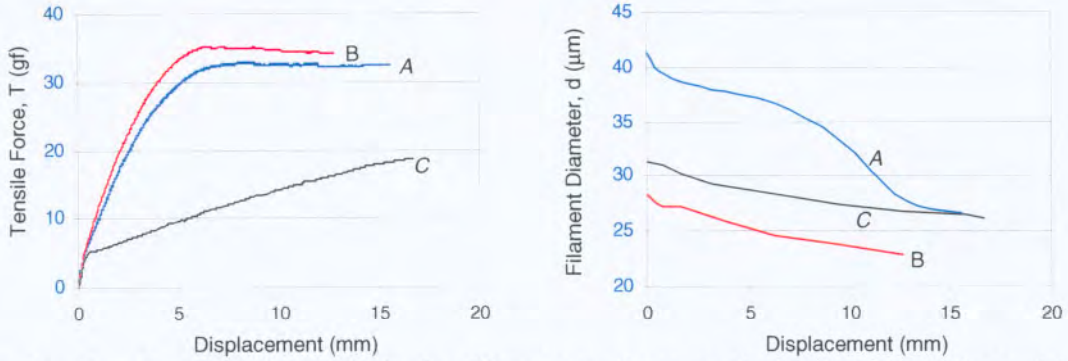

Figure 6. Tensile behavior of single filaments: force-strain-diameter relation: (a) force-displacement; (b) diameter-displacement.

Table 3. Tensile properties of single filaments of NPNW geotextiles.

Property	Geotextile		
	A	B	C
Breaking force, *BF* (*gf*)	33.0	35.3	18.7
Breaking tenacity, *BT* (*gf/den*)	28.9	66.2	28.5
Breaking toughness, *BTO* (*joules/den*)	383	696	204
Chord modulus, *CM* (*gf/den-mm*)	5.3	12.9	1.9
Elongation at peak, *EP* (%)	62.3	51.1	66.7
Initial Diameter, *d* (μm)	41.3	28.3	31.2
Initial modulus, *IM* (*gf/den-mm*)	342	750	667
Linear density, *LD* (*denier*)	1.145	0.533	0.656
Tangent modulus, *TM* (*gf/den-mm*)	13.7	30.0	26.7
Yield point, *YP* (%)	28.0	26.5	3.3

Filament Size Distribution

Synthetic fibers can have various cross section shapes such as three-lobal, three-sided, round and hollow. Other forms include four-, five-, or multi-lobal, and ribbon-shaped. In textile and fiber engineering fields, fibers with a certain cross section shape are often selected to obtain the required visual effect and performance. For example, hollow fibers are often used since they present more volume and increased stiffness compared to their mass per unit volume (Lunenschloss and Albrecht, 1985). Geotextile A which was selected for additional image analysis in this study had cross-sections of semi-round shape (Figure 7) so that the filament size could be expressed in terms of the width orthogonal to the longest length of the sectioned filament features.

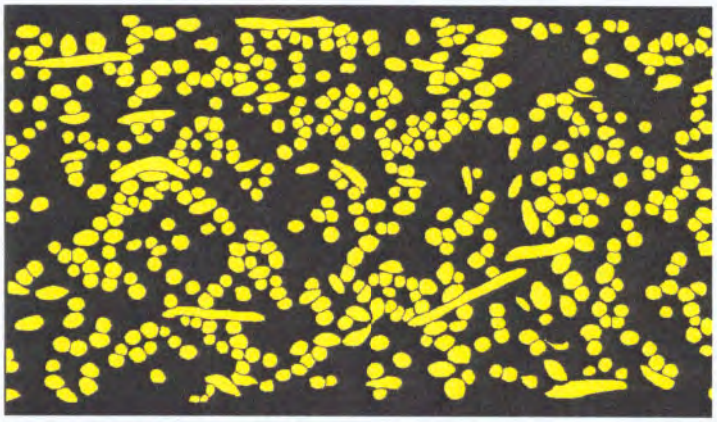

Image size: 1.993 mm (W) x 1.144 mm (H)
Loading: compression to 300 kPa
Filament area fraction: 0.331

Figure 7. Cross section view of a NPNW geotextile.

Results of the filament size distribution obtained from the vertical sections of the specimens are illustrated in Figure 8. The distribution of initial filament sizes at low normal stress of 10 kPa (A1 in Figure 4) is shown in Figure 8a. Theoretical curves shifted by decrease of filament size by 3 and 6 μm were also illustrated where all the filament sizes are assumed to decrease in the same ratio. Symbol F_i defines herein a cumulative percent frequency of filaments smaller than i μm in diameter. Similarly, D_j indicates a filament diameter corresponding to cumulative frequency of j %.

Figure 8b shows the effect of normal stress on filament size distribution. A slight decrease of about 1 μm is found for the diameter corresponding to the 50% cumulative frequency of filaments (D_{50}). The cumulative frequency of filaments smaller than 40 μm increased by 7% as the load increased from 10 to 300 kPa. This relatively small difference is considered to be a result of pulling of filaments as the geotextile strains in the horizontal direction under increased vertical normal loading.

Figure 8c presents the change of filament size due to shear against the textured geomembrane. The data were obtained from the shear surface (face I in Figure 5) under a normal stress of 100 kPa. The filament size corresponding to 50% frequency (D_{50}) decreased by about 6 μm at the

peak stain. At pseudo residual displacement, the value of D_{50} had recovered by $3\,\mu m$, but was still smaller than the initial value at a normal stress of 100 kPa by about $3\,\mu m$. At both the peak and residual shear states, 90% of filaments remained smaller than $37\,\mu m$. The filaments under 300 kPa had slightly smaller diameters compared to the specimens under 100 kPa (Figure 8d). A relatively small change of filament size of about 1.5 μm was found after peak as the specimen was displaced to pseudo residual state of 80 mm. This lower amount of recovery after peak shear

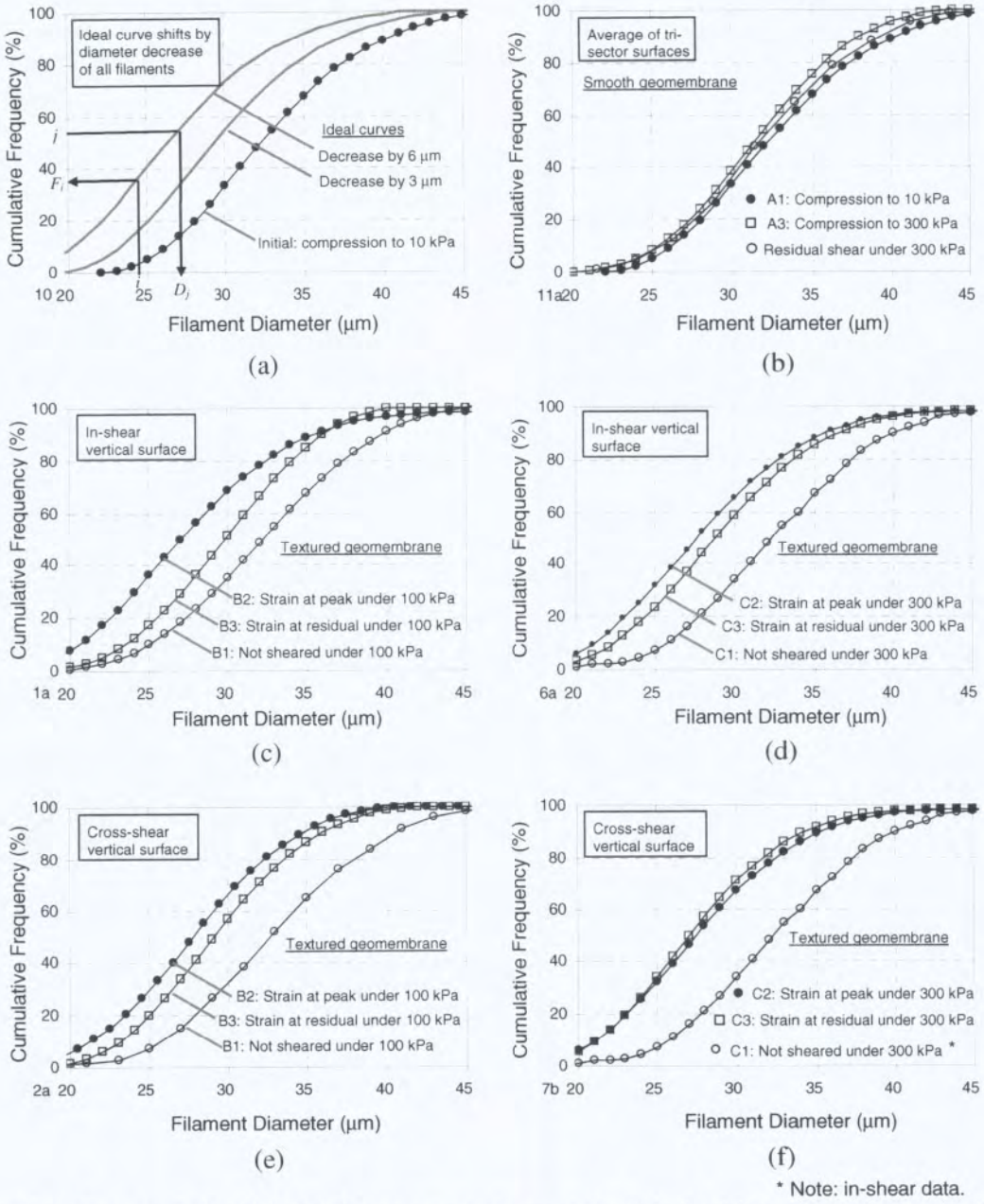

is considered as a result of the higher contact stress at the interlocking points between the deformed geomembrane textures and more densely compressed filaments.

Figure 8. Results of filament size distribution measured from vertical sections with various boundary conditions: (a) normal stress on a smooth geomembrane with theoretical curves; (b)

effect of normal stress; (c) and (d) effects of shear on a textured geomembrane-shear surface (I); (e) and (f) effects of shear on a textured geomembrane: cross-shear surface (II).

Friction is typically divided into two components: sliding and deformation (Bowden, 1952). The relatively small change in the distribution of filament sizes against a smooth geomembrane as shown in Figure 8b indicates a typical sliding friction response while the dominant change at different load stages (Figure 8d) suggests a deformation friction in which the geomembrane surface deforms and geotextile filaments strain.

The results from the counter shear surfaces (face II in Figure 5) which is orthogonal to the shear direction are illustrated in Figure 8e and f. A lower frequency of filaments smaller than $50\,\mu m$ (F_{50}) was found at peak strain under 100 kPa compared to the result from the shear surface (face I). A small change was found after peak strain with the value of D_{50} increasing to $29\,\mu m$. Similar to the results from the in-shear surface in Figure 8d, the change of distribution after peak strain was smaller for specimens at the higher normal stress of 300 kPa (Figure 8f). When compared to the changes in single filament diameters measured using the helium neon gas deflectometer, the observed changes in diameter under normal and shear loading suggest that tensile forces in individual filaments may be approaching yield loads at peak.

CONCLUSIONS

The tensile properties of filaments in needle-punched nonwoven geotextiles were measured though an experimental program and quantified in terms of the stress-strain-diameter response as well as other quantitative parameters. The experimental setup using a helium neon deflectometer enabled tracking of the complete tensile response of filaments as a function of shear displacement. Using digital image analysis techniques, the change of filament size during interface shearing was quantified. The interface shearing of a needle-punched non-woven geotextile against a textured geomembrane resulted in distinct reduction of filament size distribution. The maximum change of filament diameter was observed at peak shear. The test results showed the impact of the concentrated normal stress and micromechanical interlocking between the geomembrane textures and geotextile filaments during interface shearing.

This study resulted in a number of findings of importance to practitioners. A method to enable changes in geotextile filament diameter under different boundary load conditions was developed and implemented. Use of this method can lead to a better understanding of the long-term behavior of geosynthetics. As field applications involving geotextiles result in larger loads being transmitted to interfaces, understanding not only how the geotextile sheet is behaving but what tensile force individual filaments within the geotextile are being subjected to becomes increasingly important. Manufacturers can also use this insight to implement processes that can produce filaments that lead to enhanced long-term performance of geotextiles.

REFERENCES

Bowden, F. P. (1952) "Introduction to the Discussion: The Mechanism of Friction," Proceedings of the Royal Society of London. Series A, Mathematical and Physical Sciences, Vol. 212(1111), pp. 440-449.

De Meulemeester, D. and I. Nicoloff (1936) "Stress-extension recording dynamometer for textile fibres," Textile Institute Journal, Vol. 27(3), pp. 84-87.

Dove, J. E., and Frost, J.D. (1996) "A Method for Measuring Geomembrane Roughness," Geosynthetics International, Vol. 3, pp. 369-392.

Frost, J.D., and Lee, S.W. (2001) "Microscale Study of Geomembrane-Geotextile Interactions, Geosynthetics International," Vol. 8, No. 6, pp. 577-597.

Hindman, H. (1948) "Instron tensile tester," American Society of Mechanical Engineers-Advance Papers, Vol. 48, A-68, 3p.

Gokhale, A.M., and Drury, W.J. (1994) "Efficient Measurement of Microstructural Surface Area Using Trisector," Metallurgical and Materials Transactions A, Vol. 25A, pp. 919-928.

Gonsalves, V. E. (1947) "Determination of denier and strength of single filaments by vibroscope and Heim tensile tester," Textile Research Journal, Vol. 17(7), pp. 369-375.

Hebeler, G. H., Frost, J.D., and Myers, A.T. (2005) "Quantifying Hook and Loop Interaction in Textured Geomembrane-Geotextile Systems," Geotextiles and Geomembranes, Vol. 23(1), pp. 77-105.

Jang, D. J., Frost, J.D., and Park, J.Y. (1999) "Preparation of Epoxy Impregnated Sand Coupons for Image Analysis," Geotechnical Testing Journal, GTJODJ, Vol. 22(2), pp. 147-158.

Kim, D., and Frost, J.D., (2005) "Multi-Scale Assessment of Geotextile-Geomembrane Interaction," NAGS 2005/GRI 19 Conference, Las Vegas, USA, 8p.

Kim, D., and Frost, J.D. (2006) "Microscopic Investigation of Geotextile-Geomembrane Interface," Special Issue of Geosynthetics International (Accepted).

Krais, P. (1928) "The tensile testing of single fibres," Textile Institute Journal, Vol. 19(1), pp. 32-36.

Lunenschloss, J. and Albrecht, W. (1985) Non-Woven Bonded Fabrics, translator: Hock, J.; translation editor, Sharp, D., Ellis Horwood, 549p.

Lord, E. (1955) "Air flow through plugs of textile fibres (1)," Journal of Textile Institute, Vol. 46(3), pp. 191-213.

Mitchell, J. K., Seed, R.B., and Seed, H.B. (1990) "Kettleman Hills Waste Landfill Slope Failure. I: Liner System Properties," Journal of Geotechnical Engineering, Vol. 116(4), pp. 647-668.

Morton, W.E., and Hearle, J.S.W. (1962) Physical Properties of Textile Fibres, Manchester & London, The Textile Institute, Butterworths, 1st Edition, 608p.

Morton, W.E., and Hearle, J.S.W. (1993) Physical Properties of Textile Fibres, Manchester & London, The Textile Institute, Butterworths, 3rd Edition, 725p.

Park, Y. (2006) Personal Communication, Florida State University, FL.

Seed, R. B., Mitchell, J.K., and Seed, H.B. (1990) "Kettleman Hills Waste Ladnfill Slope Failure, Failure. II: Stability Analysis," Journal of Geotechnical Engineering, Vol. 116(4), pp. 669-690.

Vaughan, N.P. and R.C. Brown (1996) "Observations of the microscopic structure of fibrous filters," Filtration and Separation, Vol. 33(8), pp. 741-748.

Villard, P., J. P. Gourc, et al. (1999) "Analysis of geosynthetic lining systems (GLS) undergoing large deformations," Geotextiles and Geomembranes, Vol. 17(1), pp. 17-32.

CONTACT:

Duhwan Kim
Georgia Institute of Technology
210 Technology Circle
Savannah, GA 31407
Phone: 404-610-5700
Email: duhwan.kim@ce.gatech.edu

Effect of Wet-Dry Cycles on Capillary Break Formation in Geosynthetic Drainage Layers

John S. McCartney, The University of Texas at Austin; Jorge G. Zornberg, The University of Texas at Austin

ABSTRACT

This study investigates the impact of wet-dry cycles on the formation of a capillary break at the interface between a compacted clay layer and a geosynthetic drainage layer. To highlight the importance of this issue in practice, field monitoring data from a vegetated landfill test cover is presented showing how the behavior of the cover was altered by the capillary break effect. The landfill cover, consisting of a 1.17-m thick low plasticity clay layer over a geosynthetic drainage layer, experienced an increase in available moisture storage due to the capillary barrier effect. Negligible amounts of water were observed to flow from the soil into the geosynthetic drainage layer during a six year period. To interpret this behavior, two infiltration/evaporation column tests were performed on compacted clay underlain by geosynthetic drainage layers. A 1.35 m-long soil column was used to infer moisture and suction profiles during wetting and drying from the surface. The results indicate formation of a capillary break during infiltration and limited moisture removal during evaporation. A 0.125 m-long soil column was used to investigate the influence of wet-dry cycles on the formation of a capillary break. The capillary break effect was observed to occur during repeated wetting cycles, with breakthrough occurring at the same suction value on each cycle. These results indicate that a capillary break effect can be used in landfill covers to provide an increase in moisture storage during wet seasons if adequate moisture is removed from the interface during dry seasons.

INTRODUCTION

Geosynthetic drainage layers consisting of a geonet sandwiched between two nonwoven geotextiles are often used to provide drainage of water from soil profiles. Geotechnical applications involving geosynthetic drainage layers include leachate collection and leak detection systems in landfills, drainage components of lysimeters for performance evaluation of alternative landfill covers, sub-base separation systems in roadways, and drainage systems for mechanically stabilized earth walls. When saturated, the permittivity and transmissivity of geosynthetic drainage layers are typically higher than that of the soil being drained, and do not have a significant impact on the flow of water through the system. The behavior of a saturated system can be characterized using only the hydraulic conductivity values of the soil and geosynthetic drainage layer. When the system is slightly unsaturated (e.g., when suction value at the interface is between 1 kPa and 10 kPa), geosynthetic layers are practically non-conductive to water while in this range most fine-grained soils have hydraulic conductivity close to their saturated value. Depending on the soil, the geosynthetic drainage layer may have a significant impact on the flow of water through an unsaturated system.

Hydraulic properties that are useful to interpret the interaction between unsaturated soils and geosynthetics include the water retention curve (WRC) and the hydraulic conductivity function (K-function). Due to their uniform and relatively large pore size, nonwoven geotextiles will retain water at saturation until the suction applied to a boundary of the geotextile increases to

about 1 kPa, at which point air enters the geotextile and water drains. This suction value is referred to as the air-entry suction. For imposed suctions slightly greater than the air-entry suction, a sharp decrease in moisture content from full saturation to residual water retention has been observed (Stormont et al. 1997; Morris 2000; Stormont and Morris 2000; Knight and Kotha 2001; McCartney et al. 2005; Bouazza et al. 2006). At residual water retention, the hydraulic conductivity of a nonwoven geotextile predicted from the shape of the WRC using the van Genuchten-Mualem model (1980) is less than 10-11 m/s. Measurements of the K-function for unsaturated geotextiles were made by Morris (2000) and Stormont et al. (2001), and indicate that the van Genuchten-Mualem model is acceptable for prediction of the K-function shape.

The contrast in hydraulic conductivity between nonwoven geotextiles and unsaturated clay has been shown to cause a capillary barrier effect (Henry and Holtz 2001; McCartney et al. 2005; Iryo and Rowe 2005). A capillary break effect occurs when water will not flow across the interface between a fine grained material (e.g., clay) and an underlying dry, coarse grained material (e.g., a nonwoven geotextile). The water in the small pores of the fine-grained material must increase in pressure in order to displace air in the larger pores of the coarse-grained material. This effect prevents a measurable amount of water from flowing from a clay layer into a geotextile until the suction at their interface is reduced to a critical value. This critical suction is referred to as the water entry or breakthrough suction. The capillary barrier effect also causes an increase in moisture storage of the clay, in excess of the volume that would be stored during flow under a unit hydraulic gradient (i.e., water flow driven by self-weight).

This study investigates the hydraulic interaction between unsaturated, low plasticity, compacted clay and a geosynthetic drainage layer. To highlight the motivation of this research, monitoring results are presented from an evapotranspirative landfill test cover in which the interaction between a geosynthetic drainage layer and an unsaturated soil played an important role in the behavior of the cover. An experimental study in the laboratory was conducted to interpret the capillary break effect in soil-geosynthetic columns during cycles of infiltration and evaporation. The results from the column tests are used to interpret the behavior noted in the field monitoring results under controlled conditions, and provide guidance on the use (or prevention) of the capillary break in unsaturated soils and geosynthetic drainage layers.

MOTIVATION: GEOSYNTHETICS IN EVAPOTRANSPIRATIVE COVERS

An evapotranspirative landfill cover consists of a hydraulic barrier consisting of a vegetated, compacted clay layer placed atop waste. The cover functions by storing infiltrated water in the soil until it may be subsequently removed by evapotranspiration, which prevents percolation of water into underlying waste (Zornberg and McCartney 2006). An evapotranspirative landfill test cover, consisting of a 1.17-m-thick monolithic layer of low plasticity clay atop a geosynthetic drainage layer, was constructed in 1997 to investigate the behavior of this system under atmospheric boundary conditions. The system is underlain by a 60-mil geomembrane placed on a 3% grade in order to collect the water that passes through the system (referred to as percolation). The combination of a geosynthetic drainage layer and geomembrane is referred to as a lysimeter. The soil was vegetated with Cheatgrass, a local plant with a rooting length of 0.5 m (less than the thickness of the cover). A schematic of the cover is shown in Figure 1. The cover was instrumented with a weather station to measure precipitation, air temperature, and wind speed. The cover also has a vertical nest of 6 horizontally-oriented water content

reflectometer (WCR) probes, which are used to infer the volumetric moisture content. The depth of each probe is shown in Figure 1. More information on WCR probes can be found in McCartney and Zornberg (2006). The test cover was monitored until 2003.

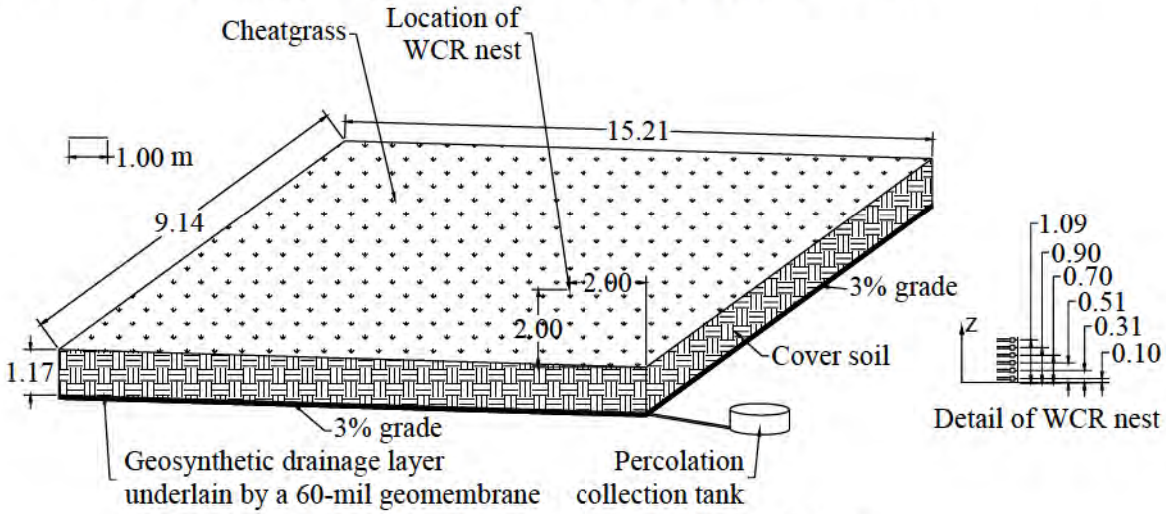

Figure 1: Schematic of the landfill test cover

An important finding from the monitoring program was that the percolation collected from the lysimeter was negligible (less than 0.1% of the precipitation). However, investigation of the moisture content profiles inferred using the WCR probes indicated that infiltration fronts reached the base of the cover during significant rainfall events. For example, the moisture content profiles shown in Figure 2(a) illustrate the migration of a wetting front through the cover during a particularly wet spring season. The infiltration front progressed through the cover at a moisture content of 20%, but after reaching the base the moisture content near the geosynthetic drainage layer increased to approximately 28%. This observation indicates that ponding of water occurred about the geosynthetic drainage layer, which is evidence of a capillary break effect. Also, a small volume of percolation was collected at the end of May 1999, indicating that breakthrough occurred after ponding was observed. The original intent of the geosynthetic drainage layer was to facilitate collection of the percolation, not to impact the hydraulic performance of the cover. However, the final design of the cover incorporated a geosynthetic drainage layer to cause a capillary break and to provide separation of the cover soil from the waste. Another important finding from the moisture profiles is that the cover "recovered" after ponding occurred. Specifically, the soil dried over the course of six months due to a combination of evapotranspiration and lateral drainage, as shown in Figure 2(b). More importantly, ponding and recovery trends were observed to occur on two other occasions during the monitoring period.

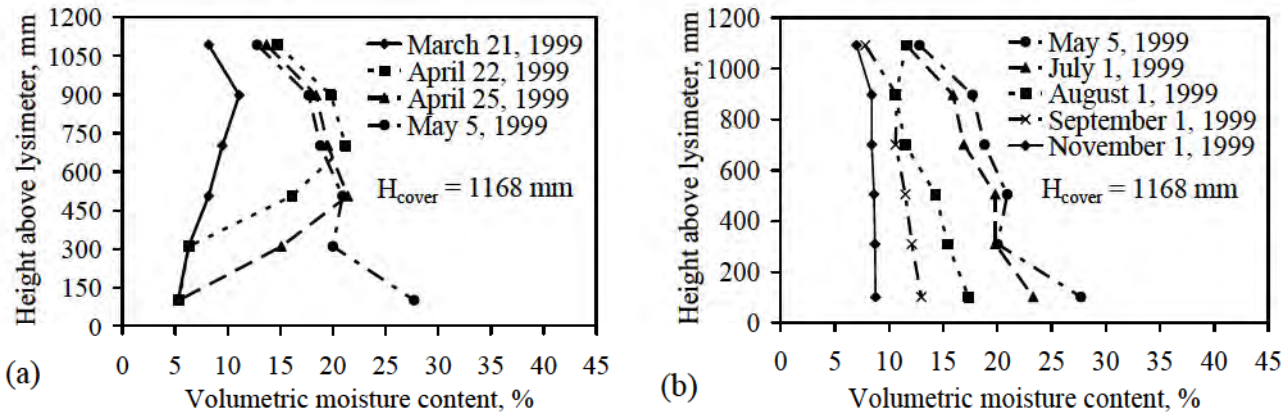

Figure 2: Moisture content profiles: (a) Wet season; (c) Dry season

MATERIALS

Geosynthetic Drainage Layer

The geosynthetic drainage layer used in the laboratory component of this study is a GSE Fabrinet® geocomposite, which is composed of a 200-mil geonet sandwiched between two 6 oz/yd^2 nonwoven geotextiles (GSE 2004). The thickness of the geocomposite as a whole is 12.5 mm. The porosity of a nonwoven geotextile is necessary to calculate its degree of saturation from measured values of gravimetric moisture content. The nonwoven geotextile components of the geocomposite have a thickness t of 2.56 mm, a mass per unit area μ of 20 kg/m^2, and a fiber density ρ_f of 910 kg/m^3. The porosity of the nonwoven geotextile was calculated to be 0.99 using the following expression (Koerner 2005):

$$\eta = 1 - \frac{\mu}{t\rho_f} \tag{1}$$

Compacted Clay

The low plasticity clay (CL) used in this study has a specific gravity of 2.71, an average plasticity index of 12, and an average liquid limit of 27. The same soil used in the field study was used in the laboratory tests. The specified range of relative compaction in the field was 70 to 80% of the maximum standard proctor dry density (1902 kg/m^3). In the laboratory and field, the clay was compacted at the optimum water content of 11.5%. The compaction energy was controlled in the field using a lightweight roller, and was controlled in the laboratory using a piston compactor.

Hydraulic Properties

The hanging column and pressure plate methods (Wang and Benson 2004) were used to define drying-path WRCs for the nonwoven geotextile component of the geosynthetic drainage layer and for specimens of the clay at relative compactions of 70% and 80%. The WRC results shown in Figure 3(a) indicate that the nonwoven geotextile drains from saturation to residual conditions at a suction value of 0.2 kPa, while the clay drains gradually. The density has only a slight impact on the WRC of the clay. The hydraulic conductivity of saturated soil and geosynthetic drainage layer specimens was assessed using a flexible-wall permeameter. The specimens were back-pressure saturated with tap water as the permeating fluid. An effective stress of 7 kPa was used, along with an average hydraulic gradient of 2.0. The K-functions shown in Figure 3(b) for the different materials were predicted from the WRC using the van Genuchten-Mualem model (1980). The hydraulic conductivity of the geotextile is higher than that of the clay when saturated, but is lower for suction values greater than 2 kPa.

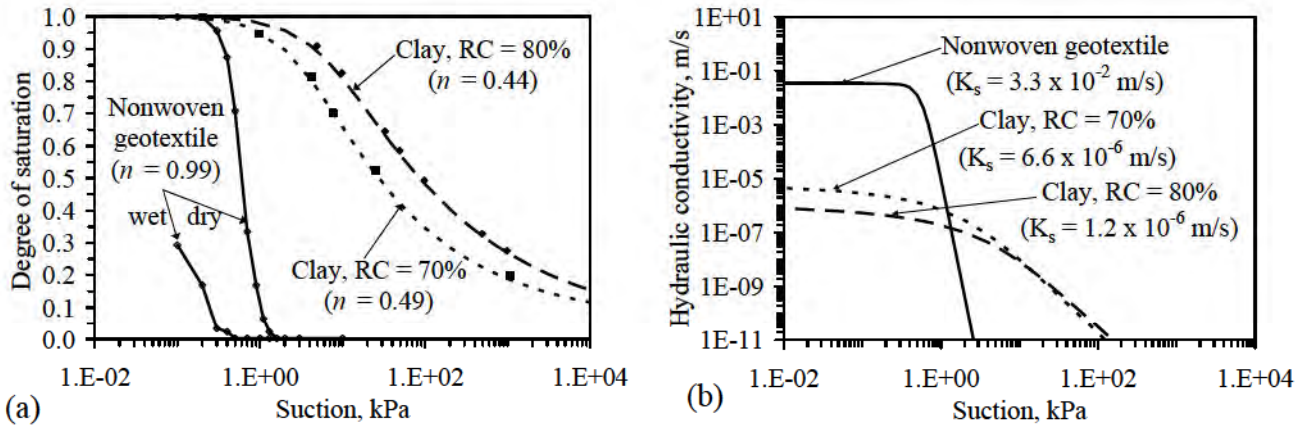

Figure 2: Hydraulic properties; (a) Water retention curves and porosities; (b) Predicted K-functions

LABORATORY TESTING PROGRAM

Soil Profiles

To investigate the behavior noted in the field program in a controlled setting, two soil-geosynthetic profiles were constructed in 203-mm diameter cylindrical columns. The columns are clear PVC tubes mounted with an "o"-ring seal onto a perforated acrylic disc, supported by a wooden platform. Tensioned wires were used to confine the tubes to the acrylic disc. Profile A is a 1350-mm-thick clay layer placed at a relative compaction of 70% above a geosynthetic drainage layer. The thickness of the soil in Profile A allows full-scale simulation of the moisture content and suction profiles in an evapotranspirative cover. Profile B is a 125-mm-thick clay layer placed at a relative compaction of 80% above a geosynthetic drainage layer. This profile is used to investigate the influence of wet-dry cycles on capillary break formation.

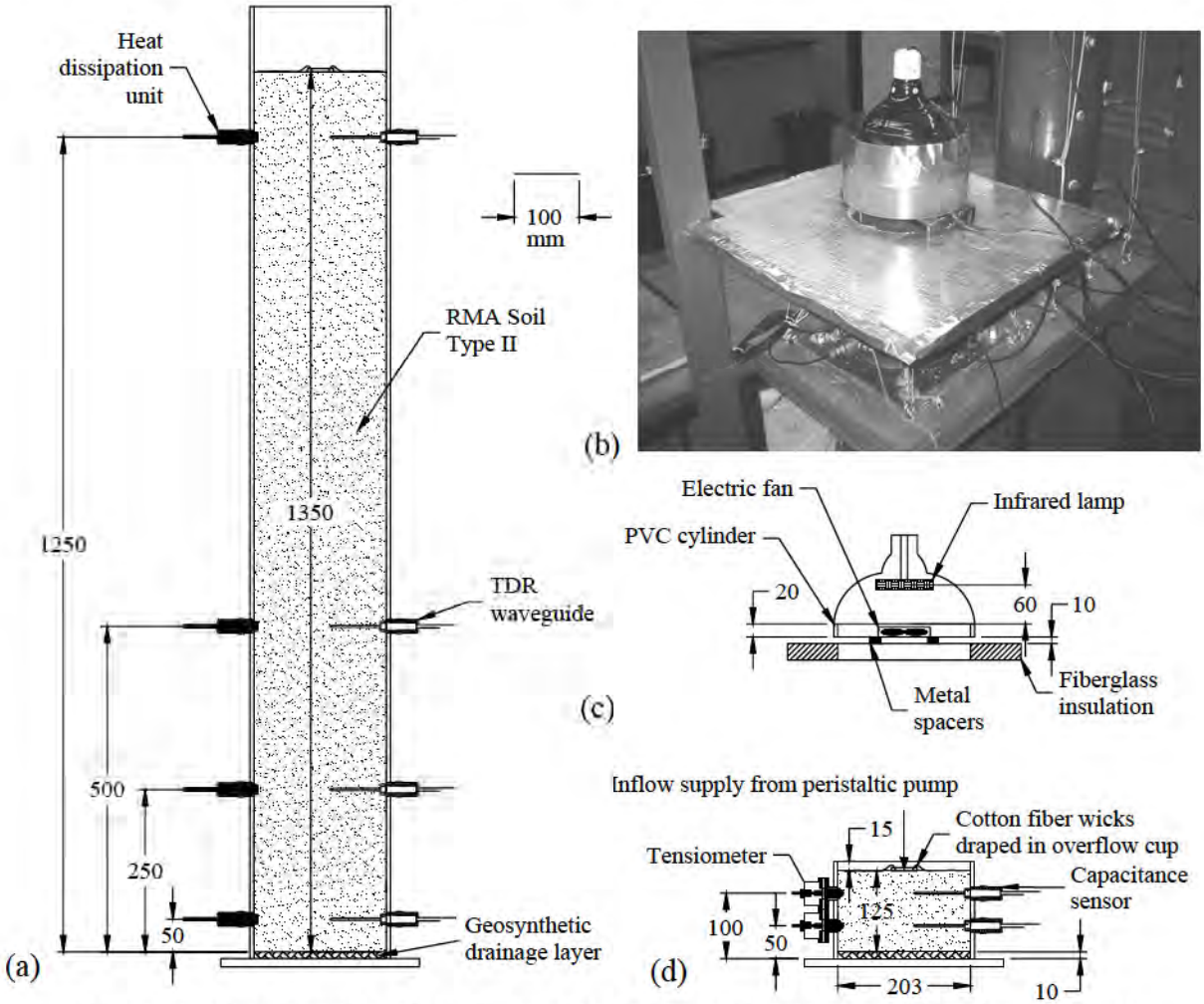

Figure 4: (a) Schematic of Profile A; (b) Picture of Evaporation setup for Profile B; (c) Schematic of Evaporation setup; (d) Schematic of Profile B

The profiles are shown in Figure 4. During infiltration, water is supplied to a reservoir on the surface of the soil profile via a peristaltic pump. The water is then distributed from the reservoir to the soil surface using a system of cotton fiber wicks. Outflow was measured using a tipping

bucket rain gauge mounted below the acrylic disc. During evaporation, an infrared lamp and a fan were used to induce drying from the soil surface, shown in Figure 4(c). This approach was not intended to replicate the actual energy supplied to the soil surface in the field to cause evaporation. Instead, this approach was used to provide a simple, yet controlled means of inducing drying of the soil. A sheet of fiberglass insulation with a hole having the same diameter as the column was placed on top of the column to limit heating of the column sides.

Monitoring System

Volumetric moisture content profiles in the columns were inferred using time domain reflectometry (TDR) and capacitance probes. The MiniTRASE© TDR system, developed by SoilMoisture, Inc. was used in Profile A, while ECH_20-TE© capacitance probes, developed by Decagon, Inc., were used in Profile B. The ECH_20-TE© probes also measure temperature and electrical conductivity. For calibration, the probes were embedded horizontally in clay specimens having a range of compaction moisture contents. The calibration relationships for two relative compactions obtained at room temperature are presented in Table 1. Linear relationships were obtained between the inferred quantities (dielectric permittivity for TDR and raw moisture content for the ECH_20-TE©) and actual volumetric moisture content values for the range of compaction conditions in the calibration program.

Table 1: Calibration equations for moisture content monitoring systems

System	Relative compaction (%)	Moisture content range (%)	Equation
TRASE TDR	70	10 to 49	$\theta_a = 14.9K_a^{0.5} - 23.4$
	80	8 to 44	$\theta_a = 12.0K_a^{0.5} - 17.0$
ECH_20-TE	70	10 to 49	$\theta_a = 1.1\theta_i - 3.9$
	80	8 to 44	$\theta_a = 0.9\theta_i - 0.3$

θ_a = Actual volumetric moisture content

θ_i = Inferred volumetric moisture content

K_a = Inferred dielectric permittivity

Suction was measured using heat dissipation units (HDUs) in Profile A and using flushing tensiometers in Profile B. HDUs infer suction by measuring the change in temperature of a low-air entry ceramic in contact with the clay during an imposed heat pulse (Flint et al. 1999). For the same heat pulse, the temperature change for a dry ceramic will be greater than for a wet ceramic because of variation in the ceramic's thermal conductivity with water content. As the suction between the soil and ceramic is continuous, the temperature response can be correlated with the suction in the ceramic, providing a soil-independent calibration. The HDUs were calibrated using the method described by Flint et al. (1999), and the same calibration equation used in that study was used in this study. The HDUs were found to be useful for measurement of suction values greater than 20 kPa. Tensiometers are a commonly used approach to directly measure suction. A miniature pore pressure transducer is used to monitor changes in pressure inside a water reservoir in hydraulic contact with the soil through a high-air entry ceramic (Ridley and Burland 1995). As a soil dries, water is drawn from the reservoir through the ceramic, causing a negative pressure in the reservoir. The tensiometers used in this study were

designed for this project, and include flushing ports. The flushing ports aid in initial saturation of the ceramic and removal of air bubbles in the case that cavitation occurs. The tensiometers were calibrated by applying pressures ranging from -100 to 100 kPa to the transducer. These tensiometers are useful for measurement of suction values less than 200 kPa.

Profile Preparation

The soil was placed into the columns in 25 mm lifts using a piston compactor. An relative compaction of 70% was obtained using a pressure of 10 psi and a 40-mm diameter piston and a relative compaction of 80% was obtained using a pressure of 15 psi and a 40-mm diameter piston. The walls of the cylinder were greased to minimize side-wall leakage. The sensors were placed at the elevations noted in Figures 4(a) and 4(d). The moisture content sensors and HDUs were placed in the middle of lifts during compaction, shown in Figure 5(a), while the tensiometers were screwed into the column after compaction, as shown in Figure 5(b).

(a) 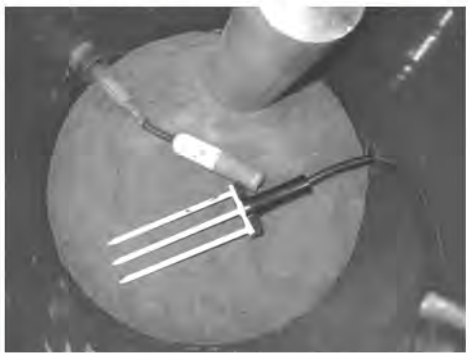 (b) 

Figure 5: (a) Soil profile A during compaction; (b) Soil profile B after compaction

Test Procedures. The infiltration stages involved imposing a steady flow rate, measuring the volumetric moisture content and suction changes with time as the wetting front progresses through the soil. An infiltration stage was completed when the outflow discharge velocity was the same as the inflow discharge velocity. The soil surface was covered to maintain a constant relative humidity (~96%) during infiltration. The evaporation stages involved measurement of the surface temperature and relative humidity as well as internal profiles of temperature, moisture content, and suction. The geometry, soil conditions, stage duration, and boundary conditions are summarized in Table 2. The stage names include the profile name, the cycle number, and the stage type (i for infiltration or e for evaporation). The infiltration rates were selected to be less than the hydraulic conductivity of the clay when saturated. The suction at the soil surface was inferred from the relative humidity using the equation in Table 2.

Table 2: Details of the laboratory column testing program

Profile name	Length	Relative compaction	Compaction water content	n	$K_{s,system}$	Stage name	Stage description	Duration	Infiltration rate	Evaporation surface suction
	(mm)	%	(%)		(m/s)			(hrs)	(m/s)	(kPa)
A	1350	70	11.5	0.49	6.20E-06	A1(i-1)	Infiltration	2423	3.4E-09	N/A
						A1(i-2)	Infiltration	683	6.5E-08	N/A
						A1(e)	Evaporation	2179	N/A	3.0E+05
						A2(i)	Infiltration	819	3.4E-08	N/A
						A2(e)	Evaporation	857	N/A	3.0E+05
B	125	80	11.5	0.44	1.20E-06	B1(i)	Infiltration	135	8.0E-09	N/A
						B1(e)	Evaporation	101	N/A	3.0E+05
						B2(i)	Infiltration	93	8.0E-09	N/A
						B2(e)	Evaporation	174	N/A	3.0E+05
						B3(i)	Infiltration	596	8.0E-09	N/A

Note: N/A is not applicable

$$\text{Boundary Suction} = -\frac{\rho_w RT}{M_w}\ln\left(\frac{R_h}{100\%}\right)$$

where ρ_w = water density, R = universal gas constant, T = temperature in K, M_w = molecular mass of water vapor, and R_h = relative humidity in percent

RESULTS

Profile A

The inflow and outflow data in Profile A during the infiltration stages are shown in Figure 6(a). The amount of moisture leaving the columns during the evaporation stages was not measured. The progress of the wetting front shown in Figure 6(b) indicates that the initial wetting front reached the base of the profile in 1400 hrs, even though capillary breakthrough did not occur until 1874 hrs. Less time was required to cause capillary breakthrough during infiltration Stage A2(i). This occurred because the moisture removed during evaporation Stage A1(e) was not sufficient to return the soil profile to its original moisture content. Accordingly, infiltration and evaporation Stages A2(i) and A2(e) are not discussed in this paper.

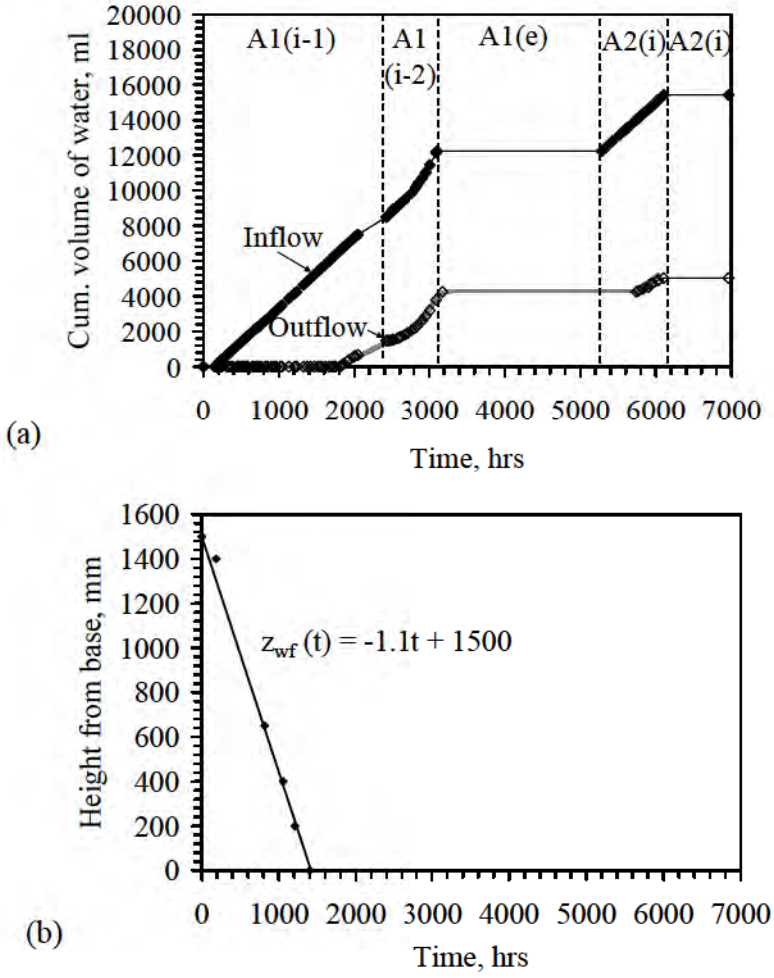

Figure 6: Profile A: (a) Cumulative inflow and outflow; (b) Initial wetting front

The suction time series for Profile A are shown in Figure 7(a). The HDUs were responsive to changes in suction during the initial infiltration stage. During this stage, HDU A1 shows a drop in suction from a value of approximately 100 kPa to 30 kPa. As the infiltration passes through the soil profile, the other HDUs showed subsequent drops in suction to approximately 20 kPa. The HDUs are not able to measure suction values less than 20 kPa, so the suction in the bottom portion of the profile after 2000 hrs is not certain. However, the upper HDU shows a decrease in

suction during Stage A1(i-2), and an increase in suction from 30 kPa to 49 kPa during Stage A1(e). The evaporation front did not progress to the depths of the lower HDUs.

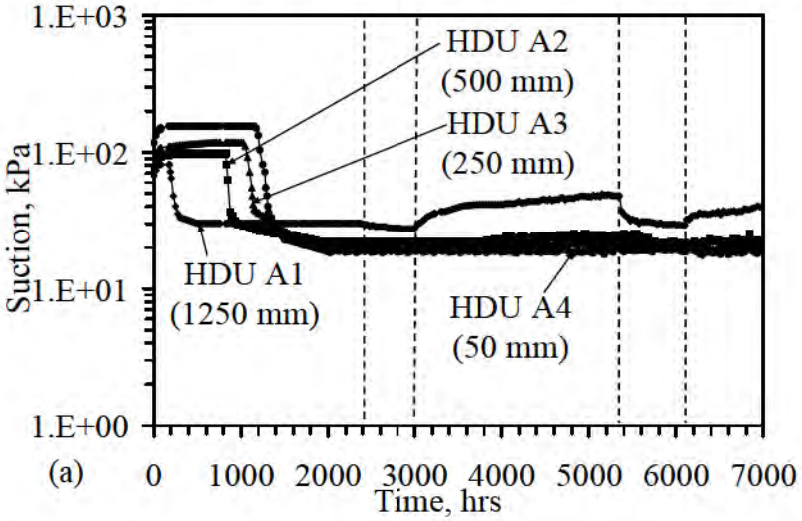

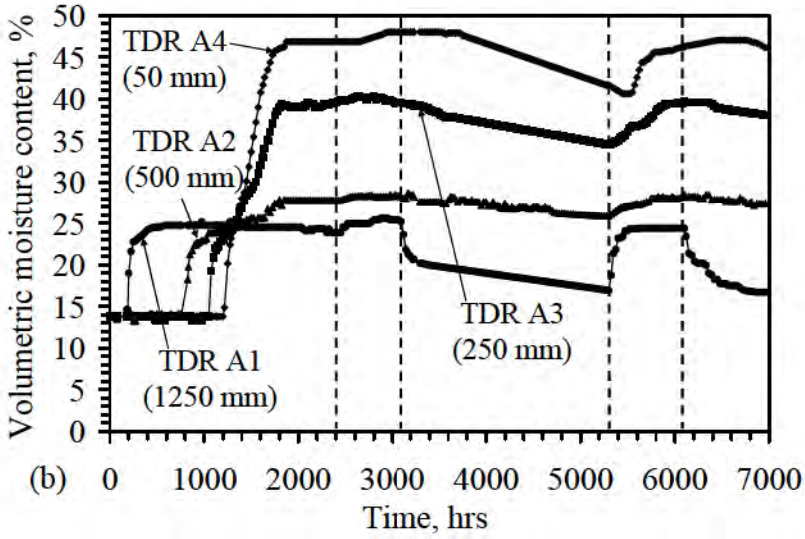

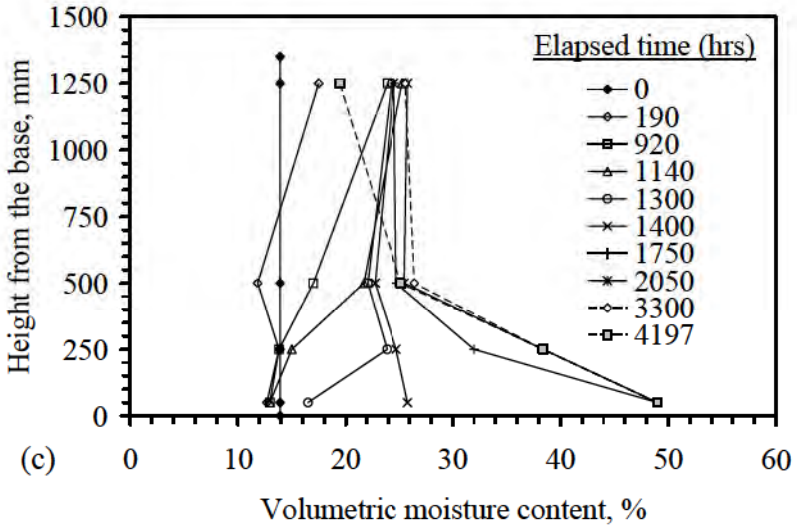

Figure 7: Profile A: (a) Suction; (b) Moisture content; (c) Moisture content profiles

The moisture content time series shown in Figure 7(b) indicate progression of the infiltration front through the soil profile during Stage A1(i-1) at a moisture content of 24%. Unlike the suction time series, the moisture content data allows closer investigation of the behavior of the soil profile after the infiltration front reaches the base of the profile. Specifically, an increase in moisture content from 24% to 47% occurred after the wetting front reached the base of the profile (TDR A4, z = 50 mm). TDR A3 (z = 250 mm) and TDR A2 (z = 500 mm) also showed increases in moisture content (although less significant), while TDR A1 (z = 1250 mm) did not show an increase in moisture content. The moisture content at the base of the profile was close to saturation when capillary breakthrough occurred at t = 1824 hrs. The moisture profiles with depth during Stage A1(i-1), shown in Figure 7(c), indicate that ponding occurred in the profile. The shapes of these profiles are similar to those from the field study shown in Figure 2(a). The moisture content profiles during Stage A1(i-1) indicate that the capillary break effect was the cause of the accumulation of water at the base of the covers observed in Figure 2(a).

During the first evaporation stage (t = 3100 hrs), the moisture content near the surface of the profile (z = 1250 mm) decreases from 24% to 20% during the first 100 hrs of evaporation, followed by a more gradual decrease to 16% over 3 months. HDU A1 indicates that the suction at this depth also increased to 49 kPa during this stage. Slight decreases in moisture content were also noted at the depths of the other TDR waveguides during this stage. However, these decreases were most likely due to gravity drainage, not evaporation. Measurements of moisture content obtained by gravimetric sampling indicate that the drying front progressed only 700 mm into the cover (*i.e.*, z = 650 mm) during the 3 month-long Stage A1(e). The field data in Figure 2(b) showed a uniform decrease in moisture content throughout the depth of the cover during 7 months. Differences in the rates and depths of drying in the field and laboratory are due to differences in the energy supplied to the soil to cause evaporation, as well as due to the added contributions of transpiration and lateral drainage to moisture removal in the field.

Profile B

Inflow and outflow during the different stages for Profile B are shown in Figure 8(a). Three infiltration stages were conducted to evaluate the formation of a capillary break during infiltration. The intermediate evaporation stages were used to dry the soil profile. The infiltration stages were stopped when steady-state flow was observed, while the evaporation stages were stopped when the moisture content in the top of the profile reached the initial value.

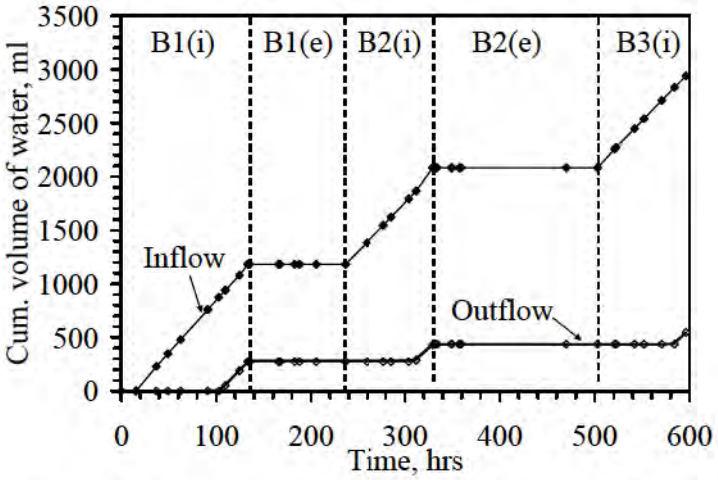

Figure 8: Cumulative inflow and outflow in Profile B

The changes in temperature and relative humidity at the surface are shown in Figure 9(a), and changes in temperature at the depths of the capacitance sensors are shown in Figure 9(b). The infrared lamp led to an increase in surface temperature from 23 to 44 °C and a decrease in surface relative humidity from 96 to 13%. This corresponds to a steady-state suction boundary condition at the surface of $3x10^5$ kPa. The temperature in the soil increased significantly during early stages of evaporation, but reached a steady-state profile after 40 hrs of evaporation.

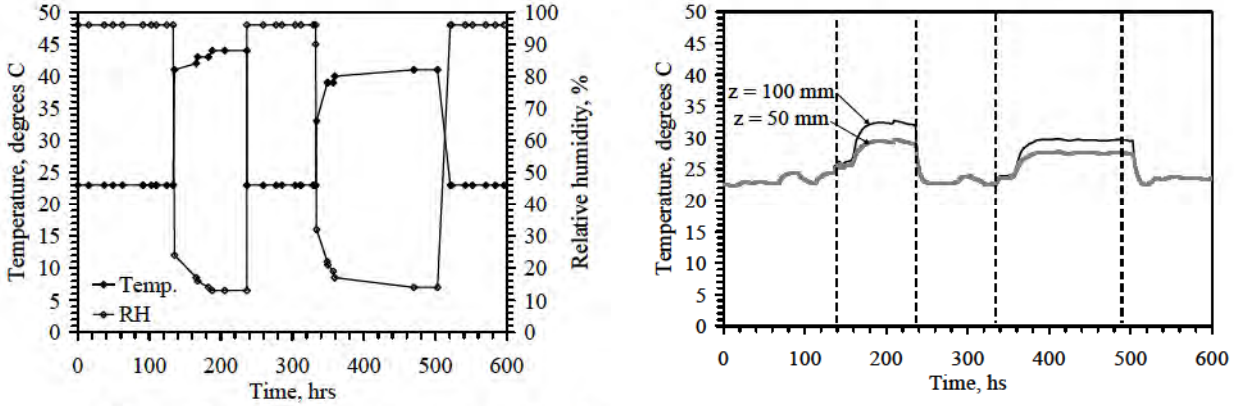

Figure 9: (a) Surface temperature and relative humidity; (b) Internal temperature

The bottom boundary in Profile B (i.e., the geosynthetic drainage layer) has a significant effect on the suction and moisture content profiles in the soil due to its short length. Accordingly, this profile is useful to investigate the impact of the interface on the soil. The suction time series for Profile B are shown in Figure 10(a). The tensiometers are able to measure suction values less than 20 kPa, so they were more useful than the HDUs in interpreting the suction at capillary breakthrough. However, the tensiometer at a height of 100 mm was affected by vibrations from the fan, so it does not yield reliable results at low suctions. The tensiometer at a height of 50 mm was assumed to be representative of the suction at the interface. During Stage B1(i), the tensiometers were equilibrating with the initial suction in the soil when the infiltration front passed their locations. Although they had not fully equilibrated with the initial suction after about 25-45 hours, the tensiometers showed a smooth decrease in suction that is consistent with trends in moisture content measured using the capacitance sensors. The initiation of outflow (i.e., capillary breakthrough) for each infiltration stage is denoted in Figure 10(a) with arrows. Breakthrough occurred in Stage B1(i) after 104 hrs, at a suction of 3.64 kPa. After breakthrough, the tensiometers showed further decreases in suction. After reaching steady state outflow, evaporation was started. Suction increased asymptotically with time during Stage B1(e), and Tensiometer B-1 approached the suction value measured before the first infiltration front passed through the profile. After this point, infiltration was started again. Despite different durations of the evaporation stages evaluated for this profile (and corresponding differences in moisture removal), breakthrough occurred at approximately the same suction.

The moisture content time series for Profile B are shown in Figure 10(b). In general, the trends in moisture content measured using the capacitance sensors are consistent with the trends in suction measured using the tensiometers. The moisture content of the wetting front is indicated by the first bend in the moisture content time series after infiltration starts (point A). The moisture content at the wetting front is approximately 24% for each infiltration stage. Unlike the moisture content time series for Profile A, the upper portion of the profile did not remain at the moisture content of the wetting front due to the shorter height of this column. Instead, the moisture content of the entire profile increased. This is because ponding of water above the geosynthetic drainage layer affected the entire height of the profile. Capillary breakthrough occurred at a moisture content of 40%, slightly after the second bend in the moisture content time series (point B). A significant decrease in moisture content from 43% to 25% occurred during the first 20 hrs of drying in Stage B1(e). A less significant decrease in moisture content from 25% to 21% was observed over the next 80 hrs of drying. The imposed suction boundary condition caused a gradient in moisture content (and suction) with height in the specimen. Based on the value of moisture content at $z = 50$ mm after 240 hrs of testing, it is likely that the moisture content at the soil-geosynthetic interface did not return to its original value. However, after subsequent wetting in Stages B2(i) and B3(i), the moisture content at breakthrough was similar to that observed during Stage B1(i).

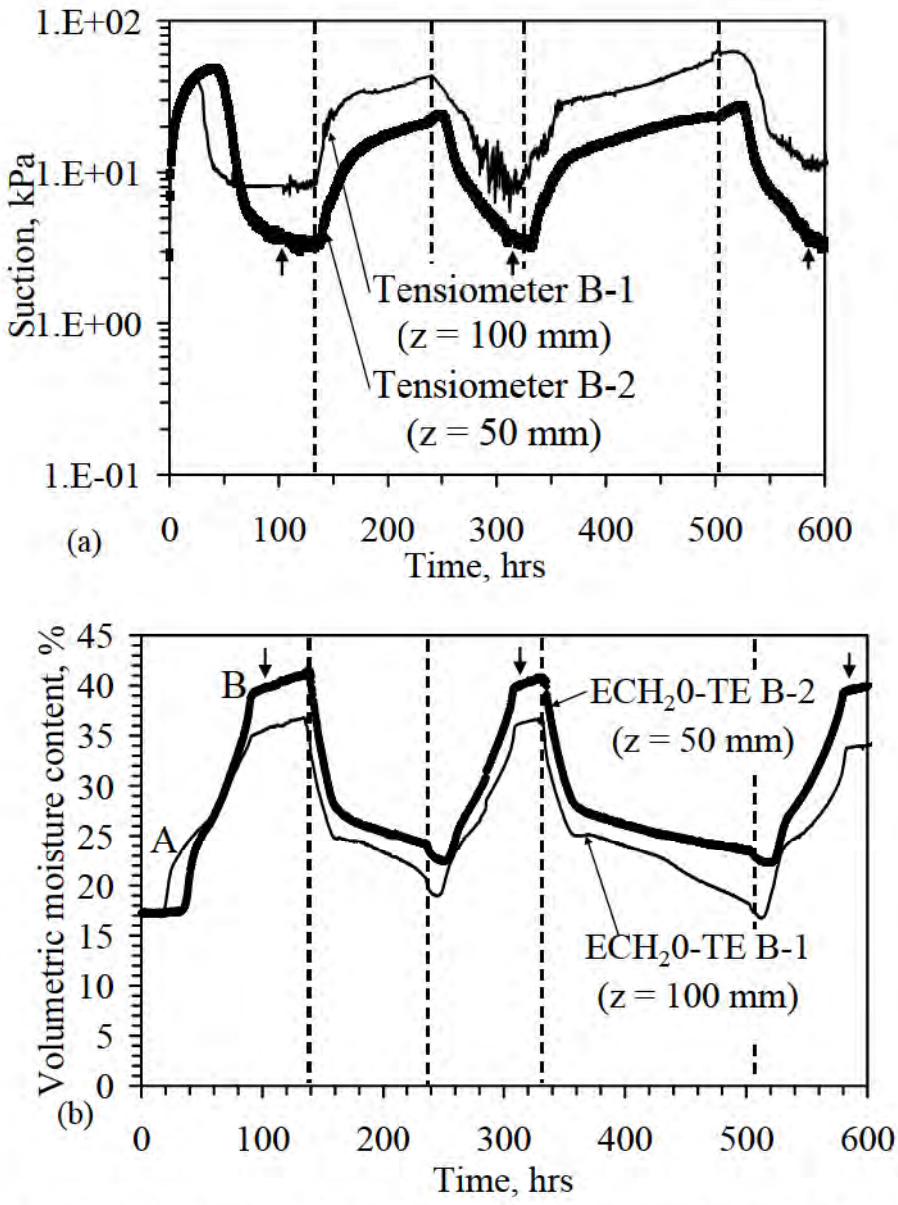

Figure 10: Profile B: (a) Suction; (b) Moisture content (Arrows denote breakthrough)

After the evaporation boundary condition was removed (i.e., at t = 240 hrs), the capacitance sensors tended to show a decrease in moisture content. This was attributed to temperature effects. These temperature effects altered both the suction and moisture content measurements, and tended to be more relevant during the evaporation stages (under a surface temperature of 40 °C). A third evaporation stage was conducted for Profile B (outside the scope of this study) to help shed light into the temperature dependence of the sensors. During this extra stage, the temperature was cycled with time by shutting the infrared lamp on and off, as shown in Figure 11(a). The corresponding changes in suction and moisture content are shown in Figure 11(b). At high temperatures, the suction is 8% greater than at room temperature, and moisture content is 5% smaller than at room temperature. Nonetheless, as the main interest of this study is the behavior of the soil near the interface during infiltration (i.e., capillary breakthrough), the

measurements of the sensors during evaporation are deemed acceptable. During infiltration, the system is at room temperature, so the error in the suction and moisture content is the same as the error obtained during the calibration program, approximately 0.1%.

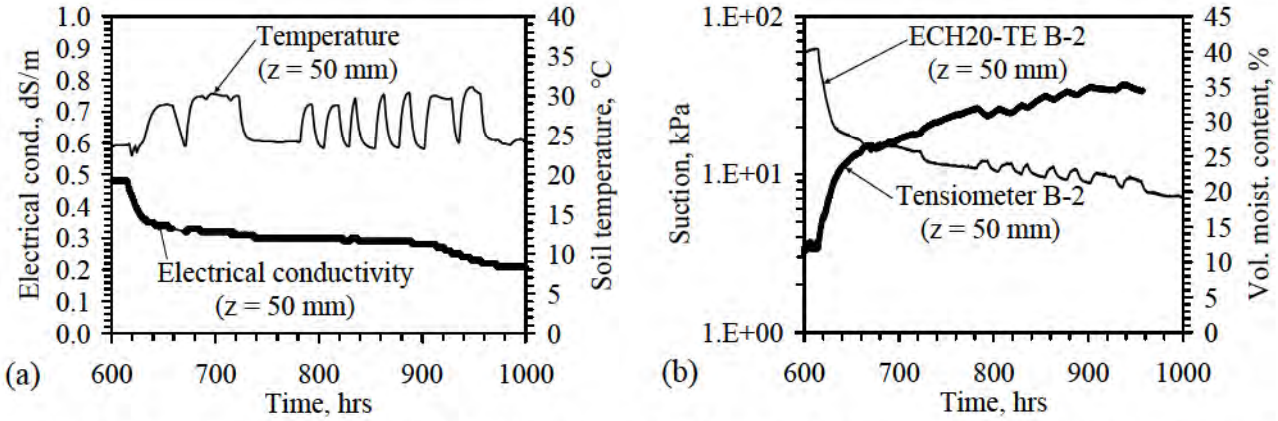

Figure 11: Temperature effects: (a) Temperature and EC; (b) Moisture content and suction changes

DISCUSSION

The results obtained during the infiltration and evaporation stages for Profiles A and B are summarized in Table 3. The results from the two profiles can be compared in spite of their differences in density and length. The moisture content and suction at the infiltration front are similar (24% and 20 to 30 kPa, respectively) as the inflow rates applied to the profiles are similar. Also, breakthrough occurred at a similar degree of saturation (94%) for both profiles. The breakthrough suction for each wet/dry cycle in Profile B is approximately 3.7 kPa. These values are consistent with the transition of the geotextile WCR from residual conditions to saturated conditions [Figure 3(a)]. This signifies that the WCRs can be used to estimate the breakthrough suction for unsaturated soil-geosynthetic system. The speed of the wetting fronts tended to increase with time because the profiles had not returned to their original moisture content after the end of each evaporation stage. Similar conclusions can be made about the time required to reach steady-state infiltration. The speed of the evaporation front in Profile B was calculated from the difference between times at which the capacitance sensors responded to the evaporation boundary condition. The calculated speeds were similar for both evaporation stages in Profile B. The evaporation fronts in Profile A only passed 500 to 700 mm into the profile, so a speed was not calculated. A capillary break effect was not obvious during Stage A2 in Profile A.

Table 3: Summary of column test results

Column name	Wet-dry cycle	Depth of evaporation front (mm)	Speed of wetting front (m/s)	Suction at wetting front (kPa)	Moisture content at wetting front (%)	Time until steady state infiltration (hrs)	Breakthrough suction (kPa)	Breakthrough moisture content (%)	Speed of evaporation front (m/s)
A	A1	700	2.7E-07	30.1	24.7	1874	?	46.2	?
	A2	500	1.0E-06	29.6	24.4	453	?	45.6	?
B	B1	125	9.6E-07	21.1	24.3	105	3.64	40.2	3.5E-06
	B2	125	1.5E-06	25.0	24.1	75	3.74	40.5	3.1E-06
	B3	125	1.8E-06	25.8	24.2	83	3.64	39.6	N/A

The transient WRCs for Profile B, shown in Figures 12(a) and 12(b), were obtained from the capacitance sensor and tensiometer data. The left-most point on the WRCs at z = 50 mm are similar for both cycles, corresponding to breakthrough. The wetting and drying paths follow the shape of the drying-path WRC obtained for the clay with a relative compaction of 80% [see Figure 3(a)]. This has practical significance, because it is common to obtain only the drying WRC in practice. Accordingly, this indicates that the breakthrough suction for a soil-geosynthetic drainage layer interface may be estimated using only the drying-path WRCs. The drying path WRC is the most commonly obtained information for unsaturated soils. Hysteresis is not significant (except at z = 100 mm in Cycle 1, likely due to errors in the tensiometer near saturation), and less hysteresis is observed in Cycle 2 than in Cycle 1.

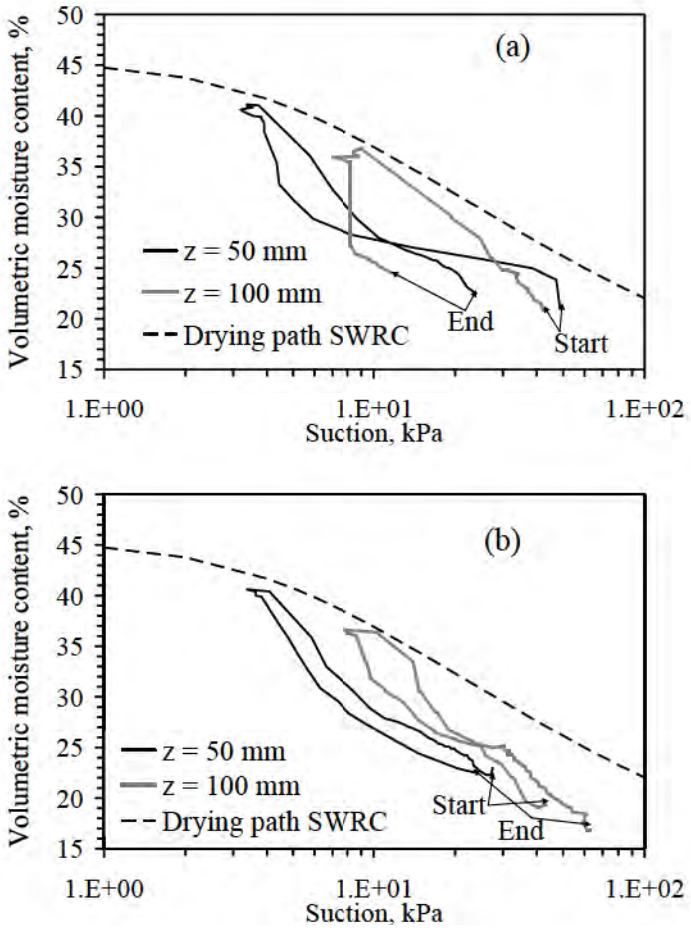

Figure 12: Transient WRCs for Profile B: (a) Cycle 1; (b) Cycle 2

CONCLUSIONS

The results of this study indicate that the capillary break effect is the cause of moisture accumulation above the interface between an unsaturated soil and a geosynthetic drainage layer observed in the field. Further, during infiltration after repeated wet-dry cycles, capillary breakthrough occurred at the same suction and moisture content. This finding implies that landfill cover systems using geosynthetic drainage layers, like the test cover described herein, can rely on the capillary break effect to provide additional moisture storage during significant storms. However, this also implies that drainage systems for retaining walls or roadways may need to approach saturation before functioning as drains. This may have implications on stability and deformations. Comparison of the results from Profiles A and B indicate that the repeated effectiveness of a capillary break relies on removal of water from the soil-geosynthetic interface. Landfill covers with a capillary break should be designed to either promote lateral drainage from the base of the cover, or to facilitate evapotranspiration through the use of plants.

ACKNOWLEDGEMENTS

Funding was provided by the NSF under Grant CMS-0401488. This support is gratefully appreciated.

REFERENCES

Bouazza, A., Nahlawi, H., Kodikara, J., and Delage, P. (2006). "Water retention curves of a non woven polyester geotextile." *UNSAT'06*. ASCE Geotech. Sp. Pub. 147(2):1651-1658.

Flint, A.L., Campbell, G.S., Ellet, K.M., and Calissendorff, C. (2002). "Calibration and temperature correction of heat dissipation matric potential sensors." *SSSA*. 66:1439-1445.

GSE, Inc. (2004). "GSE Fabrinet Geocomposite – Product Data Sheet." Houston, TX.

Henry, K.S. and Holtz, R.D. (2001). "Geocomposite capillary barriers to reduce frost heave in soils." *Can. Geotech. J.* 38:678-694.

Iryo, T. and Rowe, R.K. (2005) "Infiltration into an embankment reinforced by nonwoven geotextiles" *Can. Geotech. J.* 42(4):1145-1159.

Lu, N. and Likos, W. (2004). *Unsaturated Soil Mechanics*. John Wiley and Sons. New York.

Knight, M.A. and Kotha, S.M. (2001). "Measurement of Geotextile-Water Characteristic Curves Using a Controlled Outflow Capillary Pressure Cell." *Geosyn. Int.*, 8(3):271-282.

Koerner, R.M. (2005). *Designing With Geosynthetics*. 5th Edition. Prentice Hall, NJ.

McCartney, J.S., Kuhn, J.A., and Zornberg J.G. (2005). "Geosynthetic drainage layers in contact with unsaturated soils." *16th ISSMGE*. 12-16 Sept. Osaka, Japan.

McCartney, J.S., and Zornberg, J.G. (2006). "Correction of Lightning Effects on Water Content Reflectometer (WCR) Soil Moisture Data." *Vadose Zone J.* 5:673–683.

Zornberg, J.G. and McCartney, J.S. (2006). "Chapter 34: Evapotranspirative Cover Systems for Waste Containment." *Handbook of Groundwater Eng, Vol. 2*. CRC Press. Boca Raton.

Ridley, A.M. and Burland, J.B. (1995). "A pore pressure probe for the in-situ measurement of soil suction". *Proc. Of Conf. on Advances in Site Investigation Practice*. I.C.E., London.

Stormont, J.C., Henry, K.S. and Evans, T.M. (1997). "Water retention functions of four nonwoven polypropylene geotextiles." *Geosyn. Int.* 4(6):661-672.

Stormont, J.C. and Morris, C.E. (2000). "Characterization of unsaturated nonwoven geotextiles." *Advances in Unsaturated Geotechnics*. ASCE Geotech. Sp. Pub. 99:153-164.

Stormont, J. C., Ray, C., and Evans, T. M., (2001). "Transmissivity of a Nonwoven Polypropylene Geotextile Under Suction," *Geotech. Test. J.* 24(2):164–171.

van Genuchten, M. (1980). "A closed-form equation for predicting the hydraulic conductivity of unsaturated soils." *SSSA*. 44:892-898.

CONTACT:
John McCartney
The University of Texas at Austin
Department of Civil, Architectural, and Environmental Engineering
1 University Station
Austin,TX 78712-0280
Phone: 512-232-3595
Email: jmccartney@mail.utexas.edu.